Faculty of Engineering and Science

Strength and Durability of Concrete Incorporating Industrial Wastes, Marine Sand and Seawater Exposed to Marine Environment

Matthew Ting Zhi Yeon

0000-0001-7407-4705

This thesis is presented for the Degree of
Doctor of Philosophy
of
Curtin University

May 2021

Declaration

To the best of my knowledge and belief this thesis contains no material previously published by any other person except where due acknowledgment has been made. This thesis contains no material which has been accepted for the award of any other degree or diploma in any university.

Name: Matthew Ting Zhi Yeon

Date: 26th May 2021

Publication

Ting, M. Z. Y., Wong, K. S., Rahman, M. E., & Meheron, S. J. 2020. Deterioration of marine concrete exposed to wetting-drying action. Journal of cleaner production, 278, 123383 (https://doi.org/10.1016/j.jclepro.2020.123383).

Ting, M. Z. Y., Wong, K. S., Rahman, M. E., & Joo, M. S. 2020. Mechanical and durability performance of marine sand and seawater concrete incorporating silicomanganese slag as coarse aggregate. Construction and Building Materials, 254, 119195 (https://doi.org/10.1016/j.conbuildmat.2020.119195).

Ting, M. Z. Y., Wong, K. S., Rahman, M. E., & Joo, M. S. 2021. Prediction model for hardened state properties of silica fume and fly ash based seawater concrete incorporating silicomanganese slag. Journal of building engineering, 41, 102356 (https://doi.org/10.1016/j.jobe.2021.102356).

Presentation

Ting, M. Z. Y., Wong, K.S., Rahman, M. E. (2018). "Review on Marine Sand Seawater Concrete" One Curtin International Postgraduate Conference(OCPC) 2018, 26 – 28 Nov, 2018, Miri, Sarawak, Malaysia

<u>Attribution Statement:</u>

In relation to this thesis work, the co-authors of the published papers are supervisors in guiding the candidate through the research period. The attribution statement for publication of journal articles is given:

Matthew Ting Zhi Yeon: Conceptualization, Investigation, Data analysis and interpretation, Writing of original draft, Visualization.

Wong Kwong Soon: Conceptualization, Review & editing, Supervision, Funding acquisition, Project administration.

Muhammad Ekhlasur Rahman: Conceptualization, Review & editing, Supervision.

Meheron Selowarajoo: Conceptualization, Review & editing, Supervision.

Acknowledgement

First of all, I wish to express my deepest gratitude to Dr. Wong Kwong Soon, my main supervisor, who has given me great support during my study and research. His patience, encouragement, advice and guidance on knowledge development and problem-solving skills have helped me to complete this research work and writing thesis. He also provided me with his selfless assistance whenever I was confronted with issue and problem.

I would also like to thank my co-supervisors, Dr. Muhammad Ekhlasur Rahman and Ir. Meheron Selowarajoo, for their guidance and support over these years. Dr. Muhammad has always been concerned about my research progress and has given me his feedback on every work and shared his valuable experience with me. Ir. Meheron has been very supportive of the project, in which his guidance inspired me to complete my work.

I want to thank the lab technicians and officers Ms. Henrietta, Mr. Mohd Hidayat, Mr. Anthony, Mr. Arif, Mr. Martin, Ms. Marilyn and Mr. Kelvin for their assistance in carrying out laboratory work.

Special thanks go to my friends Mr. Wong Sen Kai, Mr. Chester Chia, Mr. Tan Wei Li, Mr. Kerk Yu Xuan, Mr. Tan Lai Hin and Mr. Ng Yeong Sheng who helped me to prepare concrete specimens and assisted me to conduct experiment.

With my greatest appreciation, I would like to acknowledge the research grant from Curtin University Malaysia and Novakey Developer Sdn. Bhd. for providing funding and materials of the research project. I would like to extend my thanks to Mr. Ting Seng Kung from the funder for all his support and encouragement of this project.

Last but not the least, I want to express my deepest gratitude to my family, who have been caring for and supporting me over the course of my study. Without their precious encouragement, I would not have been able to complete the study.

Abstract

Phenomenal global warming and consequent seawater level rise are shrinking more coastal land. As a result, concrete is increasingly being used as a construction material in maritime structures to counter sea action. The use of locally available materials in concrete production, such as marine sand and seawater, reduces the need for material transportation and thus saves cost and time. Concrete production costs can be reduced even further by utilizing industrial wastes such as silicomanganese (SiMn) slag, fly ash (FA) and silica fume (SF) as alternative materials. In hostile marine environment, concrete is susceptible to deterioration, which can be exacerbated by wetting-drying action (WDA). Limited research has been conducted on the synergy of two deterioration mechanisms, particularly between sulphate attack and cyclic loading. Furthermore, the role of WDA in the synergistic deterioration has never been investigated. Against this backdrop, this research aims to develop concrete mix design that incorporates marine sand, seawater, SiMn slag, FA and SF for application in marine environments subjected to WDA.

Concrete mix design incorporating SiMn slag, marine sand and seawater as full replacements for coarse aggregate, fine aggregate and tap water has been developed using the ACI 211 guidelines and their effects on the concrete strength and durability has been investigated. Subsequently, the concrete was incorporated with FA and SF as partial cement replacement. The effect of FA and SF on workability, strength and durability was measured experimentally, and the results were statistically evaluated using analysis of variance (ANOVA). The Response Surface Method (RSM) was then used to optimize the replacement contents of FA and SF. Afterwards, experiments were conducted to investigate the performance of optimized concrete subjected to sulphate attack, cyclic loading and WDA. Sulphate profile, mass and volume change, compressive strength, splitting tensile strength, scanning electron microscope (SEM) analysis and compressive fatigue behavior of concrete were evaluated in the experiments. A numerical model was then developed using ABAQUS software to simulate the cyclic loading of concrete deteriorated by sulphate attack and WDA using Concrete Damaged Plasticity (CDP) model. The model was used to predict the fatigue life of concrete exposed to long-term sulphate attack and WDA.

The experimental results demonstrated that SiMn slag, marine sand and seawater can be used as alternative concreting materials. Although the compressive strength decreased by 7.6%–8.3% and splitting tensile strength decreased by 11.9%–14.5%, the concrete had a comparable durability to control concrete, which was normal limestone concrete. Based on the RSM optimization, the incorporation of 16.3% FA and 11.5% SF improved the strength and durability of the concrete. The compressive and splitting tensile strengths of the optimized concrete were 4.2%–5.1% and 1.6%–7.6% higher, respectively, than those of control concrete containing limestone aggregate. The sorptivity decreased by 27.3%–45.5% and the chloride permeability decreased by 24%–54.2%. The optimized concrete was also more resistant to the deterioration caused by sulphate attack and WDA. The compressive strength of concrete at 150 days of WDA in 20% Na_2SO_4 solution was 0.67–0.7 times that of 0-day WDA, and these values were greater than 0.63–0.64 for normal concrete. Furthermore, the cyclic loading test results showed that sulphate attack and WDA weakened the concrete, leading to a 49.7% increase in residual displacement and a 1.5% decrease in elastic modulus. The numerical analysis revealed that long-term exposure to sulphate attack and WDA reduced the concrete fatigue life considerably. After 20, 35 and 50 years of exposure and hence deterioration, the fatigue life of concrete loaded at 55% of design compressive strength was reduced to 2549 cycles, 1556 cycles and 334 cycles, respectively, for the SiMn slag concrete optimized with FA and SF.

Contents

List of Figures

List of Tables

Nomenclature

The section presents the list of nomenclature used in the thesis.

Alphabet Notations

A	Constant for damage factor of compressive strength
A_g	Area of cross section
B	Constant for damage factor of tensile strength
C	Concentration of sulphate solution
D	Concrete damage parameter
D_{WDA}	Damage factor caused by sulphate attack and WDA
d_c	Compressive damage parameter
d_s	Diameter of specimen
d_t	Tensile damage parameter
E_C	Elastic modulus of concrete
$E_{C,LS}$	Elastic modulus of limestone concrete
$E_{C,SM}$	Elastic modulus of SiMn slag concrete
E_o	Initial modulus of elasticity
f_c'	Design compressive strength
f_{cr}'	Required compressive strength
$f_{c,LS}$	Compressive strength of limestone concrete
$f_{c,SM}$	Compressive strength of SiMn slag concrete
f_{ct}	Uniaxial tensile strength
$f_{ct,d}$	Degraded uniaxial tensile strength
$f_{ct,o}$	Undamaged uniaxial tensile strength
f_{cy}	Cylinder compressive strength
$f_{cy,d}$	Degraded cylinder compressive strength
f_{cu}	Cube compressive strength
$f_{cu,o}$	Undamaged cube compressive strength
f_d	Degraded concrete strength
f_o	Undamaged concrete strength
f_{st}	Splitting tensile strength
I_t	Current at t minute

i	Water absorption
K_c	Ratio of tensile to compressive meridian
M_d	Mass of concrete at d day of exposure
M_o	Mass of concrete before exposure
m_a	Apparent mass
m_b	Saturated mass after boiling
m_d	Dry mass
m_t	Mass at time t
m_s	Saturated mass
P	Applied load
Q	Charge
S_{max}	Upper stress level
S_{min}	Lower stress level
$S_{c,LS}$	Sorptivity of limestone concrete
$S_{c,SM}$	Sorptivity of SiMn slag concrete
T	Exposure time
V_c	Volume of cement
V_d	Volume of concrete at d day of exposure
V_{fa}, $V_{fa,new}$	Volume of fine aggregate
V_o	Volume of concrete before exposure
V_{scm}	Volume of supplementary cementitious materials
W_c, $W_{c,new}$	Weight of cement
W_{ca}	Weight of coarse aggregate
W_{fa}, $W_{fa,new}$	Weight of fine aggregate
W_{scm}	Weight of supplementary cementitious materials
W_w	Weight of water
x	Design variable
x_i	Design variable in linear term
x_j	Design variable in quadratic term
x_h	Design variable in higher-order polynomials term
y	Response variable

Greek Symbols

β_1	Parameter for stress-strain curve
β_i	Coefficient of regression for linear term
β_j	Coefficient of regression for quadratic term
β_h	Coefficient of regression for higher-order polynomials term
ε	Random error
$\varepsilon_{0.5}$	Strain at 50% of peak stress at descending branch
ε_{cr}	Tensile strain at peak stress
ε_{in}	Inelastic strain
ε_o	Strain at peak stress
ε_{pl}	Plastic strain
ρ_c	Density of concrete
ρ_w	Density of water
$\bar{\sigma}$	Effective stress
σ_{b0}	Biaxial strength
σ_c	Compressive stress
σ_{c0}	Uniaxial strength
σ_t	Tensile stress

Abbreviation

ACI	American Concrete Institute
AFm	Aluminate ferrite monosulfate
AS	Australian Standard
ASTM	American Society for Testing and Materials
ANN	Artificial Neural Network
ANOVA	Analysis of variance
BS	British Standard
BS EN	British standard implementation of English language versions of European standard
C-A-H	Calcium aluminate hydrate
C-S-H	Calcium silicate hydrate
CCD	Central Composite Design
CDM	Continuum damage mechanics
CDP	Concrete damaged plasticity
DT	Decision tree
EFNARC	European Federation of National Associations Representing for Concrete
EDX	Energy dispersive X-ray
FA/B	Fly ash-to-binder ratio
FA	Fly ash
FM	Fracture mechanics
FRP	Fiber reinforced polymer
FTA	Freezing-thawing action
GGBS	Ground granulated blast furnace slag
ITZ	Interfacial transition zone
JASS	Japanese Architectural Standard Specification
LP	Linear programming
M-S-H	Magnesium silicate hydrate
MC	Mass concrete
MK	Metakaolin

ML	Machine learning
MWP	Marble waste powder
OPC	Ordinary Portland cement
RAC	Recycled aggregate concrete
RC	Reinforced concrete
RCA	Recycled coarse aggregate
RCPT	Rapid chloride penetration test
RDME	Relative dynamic modulus of elasticity
RILEM	Union of Laboratories and Experts in Construction Materials, System and Structures
RSM	Response Surface Method
SF/B	Silica fume-to-binder ratio
SCM	Supplementary cementitious material
SEM	Scanning electron microscope
SF	Silica fume
SiMn	Silicomanganese
SP	Superplasticizer
SR	Sulphate-resisting
W/B	Water-to-binder ratio
WDA	Wetting-drying action
XRD	X-ray powder diffraction

Chapter 1. Introduction

1.1 Research Background

1.1.1 Deterioration of Concrete in Marine Environment

Maritime structures, such as breakwater, groin, seawall and jetty, are susceptible to material deterioration, especially due to wear and tear caused by the hostile environment. Meanwhile, phenomenal global warming and a consequent rise in seawater level are causing the earth landmass to shrink. Approximately 70% of the earth surface is covered by water which is mainly ocean (NOAA, 2018). Maritime structures are increasing in number because more coastal defense has to be constructed to counter the onslaught of sea action (Arns et al., 2017). In this regard, concrete has been widely used as construction material for maritime structures due to its better corrosion resistance than other materials like steel (Chilana et al., 2016).

The proximity of coastal regions to the marine environment can be up to 10 km from the coastline (Pratolongo et al., 2019). The marine aerosol, formed due to breaking wave, contains salt that is carried inland by the wind. Within this vicinity, a hostile marine environment will cause concrete to deteriorate. This can result in overall structural failure and even catastrophic loss in the extreme case (Ibrion et al., 2020). Mitigation measures such as increasing concrete cover and strength, the use of stainless steel and various maintenance methods considerably increase the life-cycle cost (Val and Stewart, 2003). Concrete deterioration rate decreases with increasing distance from the coastline and is very much dependent on wind conditions such as wind speed and direction (Meira et al., 2007).

There are two mechanisms of concrete deterioration, namely chemical and physical deterioration. Chemical deterioration, such as chloride attack, sulphate attack and carbonation, arises from the chemical reaction between deleterious components of seawater and cement hydration products, causing concrete degradation. Conversely, physical deterioration impairs the exterior of concrete and causes superficial damage. This form of degradation includes salt crystallization, freezing-thawing action and wave erosion. Both types of degradation adversely affect the long-term strength and durability of concrete, reducing the service life of structure.

Maritime concrete can be classified as mass concrete (MC) or reinforced concrete (RC) depending on its application (Alexander and Nganga, 2016). MC is unreinforced concrete whereas RC is reinforced with steel bars. MC is used for gravity-stabilizing purpose, such as coastal armoring, and is prone to physical deterioration. The durability issue of MC is associated with degradation of concrete and is critical if its strength is compromised. In this connection, physical deterioration, particularly the wave action, can exert cyclic loading on the concrete, resulting in fatigue damage. Conversely, the corrosion of embedded steel in RC creates a more serious durability issue. Intrusion of deleterious compounds as well as subsequent reactions with the concrete matrix which cause changes in properties, can reduce passivity of steel and lead to corrosion (Zhang et al., 2010).

Maritime structure can be subjected to four different exposure conditions, including submerged, splash, tidal and atmospheric zones as illustrated in Figure 1.1(a) (Song et al., 2008). In atmospheric and submerged zones, on account of low chloride content and less oxygen exposure respectively, concrete is less prone to corrosion. Concrete corrosion in tidal and splash zones occurs more intensely due to the high chloride and oxygen contents as well as the alternating wetting-drying process. In this context, wetting-drying action (WDA) facilitates the deterioration of concrete. It induces accumulation of chloride and increases intrusion (Chen et al., 2016). The WDA also increases moisture transfer into concrete and accelerates the deterioration process (Zhang et al., 2011). In the tidal zone, concrete experiences a regular WDA caused by sea tide. In the splash zone, concrete is exposed to more cycles of WDA caused by wave, making it more vulnerable to damage.

1.1.2 Wetting-Drying Action on Concrete

Wetting-drying action (WDA) has also brought about weathering and degradation of coastal structures for decades. Past research concentrated on the wetting-drying effects of rock and soil used for coastal defense. For example, the WDA can weaken the inter-granular bonds of clay-bearing rock, causing the rock to transform into a soil-like material over time (Gokceoglu et al., 2000). Rao et al. (2001) also showed that the lime-stabilized soil could be deteriorated by the same mechanism, causing it to lose cementation and increase porosity. The degradation of rock and soil will eventually lead to problems such as erosion, slope failure and embankment collapse.

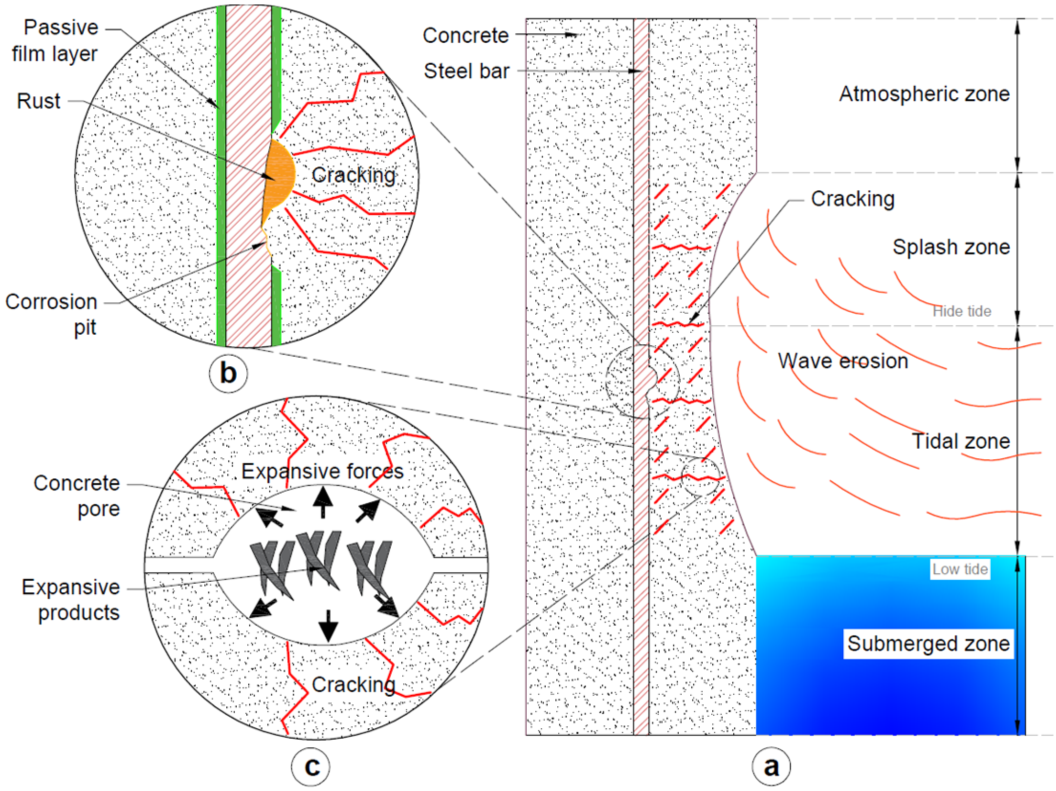

Figure 1.1: Concrete exposed to deterioration in marine environment: (a) Element of concrete structure, (b) steel corrosion and (c) damage by expansion (Mehta and Monteiro, 2006)

Over the past two decades, the WDA studies have focused on concrete structures due to the rapid advancement of concrete technology. The earlier research in this field analyzed the contributing factors. Sahmaran et al. (2007) investigated the effect of WDA exposure duration on the degradation of concrete strength. Medeiros et al. (2013) studied the effects of cycle number, structure height and location on chloride intrusion into concrete. Besides, Ryu et al. (2011) determined the effects of rainfall duration, intensity and relative humidity on moisture transfer. Also, Yu et al. (2015) incorporated factors of temperature, relative humidity and exposure time variables to develop chloride diffusion model.

Concrete structure in service is generally subjected to loading such as permanent and imposed loads. In this connection, the research has been further expanded to include cases with loading effects. For instance, Wu et al. (2016) and Chen et al. (2017) studied the transport and intrusion behavior of chloride into concrete subjected to compression. The chloride intrusion into concrete under tensile loading was studied by Fu et al. (2016). Several researches also examined the cases of flexural loading (Gao et al., 2013; Ye et al., 2016b; Zhang et al., 2017). Chen et al. (2017) simulated the actual permanent and imposed loads in a structure by applying short-term and long-term flexural loadings on concrete.

Recent studies have enhanced concrete performance under WDA through incorporation of mineral admixtures such as granulated blast furnace slag (Qi et al., 2017), fly ash (Hoy et al., 2017), metakaolin (Valipour et al., 2017), palm oil fuel ash (Mohammadhosseini et al., 2017) and silica fume (Farahani et al., 2015). New research interest used fiber reinforced polymer (FRP) composite in concrete due to its higher corrosion resistance and strength-to-weight characteristics. Zhang et al. (2016a) strengthened concrete beam with carbon FRP fabrics, while Tang et al. (2020) used glass FRP sheets. Garzon-Roca et al. (2015) replaced steel bars with carbon FRP bars.

1.1.3 Consideration in Current Standard

Concrete specification for maritime application has been widely discussed in various standards and literature (Giza and Burke, 2013). Table 1.1 summarizes the specification for marine concrete adopted by Australian Standard (AS), British Standard (BS) and American Concrete Institute (ACI). AS 3600 (2018) specifies the concrete of maritime structure to have a minimum service life of 50 years, while the BS 6349-1-4 (2013) recommends a design life up to 100 years to ensure a safe and durable structure. ACI 357R-84 (1997) does not have any provision for design life of marine concrete, but ACI 365.1R-17 (2017) provides a guideline for predicting the service life of concrete based on exposure conditions. The AS, BS and ACI specify a minimum compressive strength of 50 MPa, 40 MPa and 42 MPa respectively for concrete structures in tidal and splash zones. A minimum cover of 65 mm for concrete in immersed, tidal and splash zones is specified in the standards. AS and ACI allows for a reduced cover of 50 mm for concrete in atmospheric zone. The minimum concrete cover is to provide a protective layer against chloride intrusion and to prevent the corrosion of steel reinforcement.

The standards also provide the prescriptive requirements of binder type, minimum binder content and maximum water-binder (W/B) ratio for concrete in maritime applications. Generally, the binder recommended by the standards is ordinary Portland cement (OPC). AS specifies the use of sulphate-resistant (SR) cement for concrete exposed to sulphate attack caused by sodium sulphate and magnesium sulphate. BS provides provision for the use of pozzolans such as fly ash and ground granulated blast furnace slag. ACI allows the use of pozzolans that conform to ASTM C618 (2019) to improve concrete resistance against sulphate attack and corrosion. Furthermore, both BS and ACI specify a minimum binder content of 360 kg/m^3 and 356 kg/m^3 respectively, to ensure that the concrete can achieve the required strength. Both standards also restrict the W/B ratio below 0.4 and 0.45 respectively, to minimize pore formation due to excess water.

Table 1.1: Concrete specification for maritime application

Specification	**Australian Standard (AS 3600, 2018)**	**British Standard (BS 6349-1-4, 2013)**	**American Concrete Institute (ACI 357R-84, 1997)**
Design life	50 years	50 to 100 years	-
Minimum compressive strength	50 MPa	40 MPa	42 MPa
Minimum concrete cover for immersed, tidal and splash zones	65 mm	65 mm	65 mm
Minimum concrete cover for atmospheric zone	50 mm	65 mm	50 mm
Binder type	• OPC • Cement – Type SR	• OPC – Type I and II • Pozzolans – fly ash and ground granulated blast furnace slag	• OPC – Type I, II and III • Pozzolans – conformed to ASTM C618 (2019)
Binder content	-	360 – 380 kg/m^3	356 – 415 kg/m^3
W/B ratio	-	0.35 – 0.4	0.4 – 0.45

Marine concrete is designed for high strength and durability. Strength is required to resist abrasion and erosion. Durability, measured by permeability, has a bearing on concrete degradation. There is limited guideline in the existing standards for designing high durability concrete. The concrete mix proportion guidelines provided by ACI 211.4R-93 (1998), BS 8500-2 (2015) and IS (IRC44, 2017) emphasize on the design of high strength concrete. High strength concrete is perceived to possess less porosity because of its lower water demand. It contains less unreacted water that contributes to pore development and hence boosts durability (Kim et al., 2014).

Researchers adopt various performance-based methods for specifying the requirement of concrete in marine environment. The assessment is mainly based on the durability performance of concrete. For example, Luping and Gulikers (2007) adopted chloride diffusion approach to evaluate the service life of RC structure up to 10 years. The ionic diffusion model developed by Li et al. (2016a), describes the transport of ion into concrete in freezing-thawing environment. Water penetration properties such as permeable pore, water absorption and sorptivity were also used by researchers to assess concrete performance (Andrews-Phaedonos, 1996; Medeiros and Helene, 2009). Neville (1995) classified concrete with a water absorption of less than 10% as durable concrete. Another performance-based method is the rapid chloride penetration test (RCPT) and as described in ASTM C1202 (2012) , it defines the concrete permeability limit based on charge transfer. RILEM TC 246-TDC also established test methods for assessing the durability of concrete subjected to both environmental action and mechanical load (Yao et al., 2017).

Even though the performance-based design method is commonly used, there is a limited standard procedure for carrying out the mix design of marine concrete, particularly that exposed to WDA. Designers are more inclined to carry out the design based on experimental results. The variation in WDA characteristics at different sites can result in unique laboratory works.

1.1.4 Sustainable Local Materials for Concrete

1.1.4.1 Marine Sand and Seawater

Concrete demand is increasing rapidly due to the robust growth of the construction industry. More recently, construction activities have expanded to coastal areas due to land reclamation projects in countries with limited land (Limeira et al., 2012). In this connection, concrete ingredients, especially sand and freshwater, are consumed in enormous quantities, which can eventually lead to depletion of resources, unless new sources are found. Furthermore, these materials are not locally available and the necessary transportation cost has incurred extra project expenses. A more economical and innovative solution is to use marine sand and seawater as replacing materials, since they are abundant in coastal regions.

The incorporation of marine sand and seawater has already been practiced in concrete construction due to the ease of extraction, reduced transportation need and hence cost saving (Huiguang et al., 2011; Katano et al., 2013). However, the presence of salt especially chloride can cause steel corrosion of reinforced concrete, cracks in concrete through expansion and subsequently deterioration of the concrete. Therefore, to make full use of marine sand and seawater successfully, suitable methods for mitigating corrosion in concrete must be searched and developed.

To address corrosion issue, desalting treatment can be employed on marine sand and seawater to reduce salt content to a threshold level (Xiao et al., 2017). This method is generally not recommended in practice due to high operating cost and additional requirement of exquisite quality control and management. Another more feasible solution is to incorporate mineral admixture that can improve concrete performance. Extensive research has shown that permeability of concrete can be minimized by adding admixtures such as metakaolin and silica fume as they refine micro-pores in concrete (Karthikeyan and Nagarajan, 2016; Shi et al., 2015). Corrosion of reinforcing steel in concrete can be minimized as a result of lower oxygen ingress. Moreover, a more effective approach is to replace conventional steel bars with non-corrodible reinforcement such as fiber reinforced polymers (Li et al., 2018a; Li et al., 2016b). In this case, corrosion will not be an issue as corrodible steel is absent.

Since the use of marine sand and seawater in concrete is impeded by steel corrosion, research into the respective effects of these materials on concrete performance has not gained momentum. These materials, however, can be used without much refinement in mass concrete for foundation, maritime structure and retaining wall, where steel reinforcement is not required. This necessitates further research into the effects of marine sand and seawater in concrete.

1.1.4.2 Silicomanganese Slag

Apart from using locally available materials, incorporation of industrial waste in producing concrete has the benefit of lowering manufacturing cost. Silicomanganese (SiMn) slag, as shown in Figure 1.2, is a waste produced during extraction of silicon and manganese metals from ores for use as alloying elements in steel (Ding and Olsen, 2000). Production of SiMn is economically preferred and adapted because it results in less manganese loss as metal inclusion in steelmaking (Olsen and Tangstad, 2004). As a result, a large amount of SiMn slag has been produced. Statistics showed that the smelting plants from Samalaju Industrial Park in Malaysia have already produced 400,000 tonnes of SiMn slag, which is disposed of in landfill (Wong, 2018). This waste disposal method not only causes environmental pollution, but it is also costly and takes up a lot of space. There is an urgent need to conduct further research to use SiMn slag in the context of environmental sustainability and efficient waste recycling. One viable option is to use it as a component in concrete.

Figure 1.2: Silicomanganese slag

To date, several researches have been performed to utilize SiMn slag as a partial cement replacement in concrete (Frias et al., 2009; Frias et al., 2006; Nath and Kumar, 2016). However, to substitute SiMn slag for cement, additional grinding process is required which can eventually increase the production cost (Kim et al., 2011). Therefore, it is more cost-effective if SiMn slag can be used directly as coarse aggregate in concrete without further treatment. There has been limited research into using SiMn slag to replace gravel as coarse aggregate for concreting. Additional cost savings can be realized by using locally available materials such as marine sand and seawater. From the perspective of sustainability and cost-effectiveness, full replacement of the conventional materials is beneficial. Hence, as shown in this research, it is innovative for the concreting materials of SiMn slag, marine sand and seawater to be used to replace ordinary materials of gravel, river sand and tap water respectively.

1.2 Aim and Objectives

The aim of this research is to develop concrete mix design that incorporates marine sand, seawater, silicomanganese (SiMn) slag, fly ash (FA) and silica fume (SF) for application in marine environments subjected to wetting-drying action (WDA). The following are the research objectives:

1. To investigate the effect of the use of marine sand, seawater and SiMn slag on the strength and durability of concrete.
2. To optimize FA and SF as ternary binder with cement in concrete containing marine sand, seawater and SiMn slag, based on workability, strength and durability.
3. To assess the durability and compressive cyclic behavior of the optimized concrete subjected to sulphate attack and WDA.
4. To develop a numerical model to predict the fatigue life of concrete subjected to sulphate attack and WDA.

1.3 Scope of Work

This project is designed to produce the concrete incorporated with marine sand, seawater and SiMn slag through experimental works. FA and SF are also incorporated as supplementary cementitious materials to enhance the concrete performance. Optimization of FA and SF is performed by using the Response Surface Method (RSM). Accelerated experiments are then carried out to simulate the marine environment in order to assess the durability of optimized concrete. In the experiment, the concrete is exposed to sulphate attack and WDA. The compressive cyclic behavior of deteriorated concrete is also evaluated by conducting cyclic loading test. To widen the horizon of the experiment, numerical model is developed to further assess the cyclic behavior of concrete exposed to sulphate attack and WDA.

In objective one, experimental works were conducted to study the effect of using marine sand, seawater and SiMn slag to replace river sand, tap water and limestone on strength and durability of concrete. Six concrete mixtures were designed in accordance with the ACI standard. Each concrete mixture was used to study the effect of each material replacement type and also the effect of material combinations. The compressive and splitting tensile strength tests were performed for all concrete mixtures. Assessment on durability properties including water absorption, pore volume, sorptivity, chloride permeability and sulphate resistance was also carried out. Microstructural analysis using scanning electron microscope-energy dispersive X-ray (SEM-EDX) technique was conducted to examine the interfacial transition zone (ITZ) of cement paste and aggregate.

In objective two, the effect of FA and SF as binary and ternary binders on the strength and durability of concrete incorporating marine sand, seawater and SiMn slag was investigated. Twenty-one concrete mixtures were developed and their workability, strength and durability were experimentally evaluated. Concrete workability was assessed through slump test. Compressive and splitting tensile strengths were also determined. Sorptivity and chloride permeability tests were carried out to evaluate concrete durability. The replacement levels of FA and SF were limited to 30% and 40% respectively. The test results were statistically evaluated by using the RSM. Prediction models were developed and used to optimize the replacement levels of FA and SF in terms of workability, strength and durability. The optimum FA and SF replacement levels were also validated by conducting experiments. In addition, the models developed on the basis of SiMn slag concrete were used in conjunction with established relationships to predict the properties of limestone concrete.

In objective three, experiment was conducted to replicate marine environment for assessing the durability of optimized concrete. Three concrete mixtures, which were control concrete, SF-optimized concrete and FA-SF-optimized concrete, were included in this experiment. For comparison, three similar concrete mixtures with limestone aggregate as replacement of SiMn slag was also included in the test program. In the experiment, the concrete was exposed to sulphate attack and WDA. The effects of different sulphate concentrations (5%, 12.5% and 20%) and exposure periods (30, 60, 90, 120 and 150 days) were studied. The deteriorated concrete properties including compressive strength, splitting tensile strength, mass loss, volume change and microstructure were determined. Furthermore, the compressive cyclic behavior of the deteriorated concrete was examined by performing cyclic loading test. In the test, the effects of upper stress level and loading frequency were investigated.

In objective four, numerical model was developed for the cyclic loading of concrete by using the finite element analysis software ABAQUS. A material constitutive model, Concrete Damaged Plasticity (CDP), was used for numerical modelling. The effects of sulphate attack and WDA were considered in the CDP model by modifying the concrete properties using the experimental results obtained from objective three. The numerical model was developed and calibrated based on the test results. The model was then validated against the cyclic loading test results. Parametric studies were carried out to further investigate the effects of compressive strength, lower stress level and specimen size. The fatigue life of concrete exposed to long-term sulphate attack and WDA was also predicted by using the developed model.

1.4 Research Significance

The following summarizes the significance of the research works.

1) Based on the outcomes of this study, SiMn slag, a byproduct of iron smelting plant, can be used as an alternative coarse aggregate in concrete. This can eliminate the need to dispose of SiMn slag in landfill. The use of SiMn slag in concrete works is not only a more appropriate waste management measure, but also a sustainable way of reusing industrial waste, which contributes significantly to environmental conservation. To date, there has been limited research on the use of SiMn slag as coarse aggregate.
2) This research also investigates the use of marine sand and seawater in the manufacture of concrete. Although marine sand and seawater contain salts that cause steel corrosion, they can undeniably be used in mass concrete where steel reinforcement is not required. Marine sand and seawater are locally available in abundance in coastal regions. Utilization of the local materials can reduce the cost of transportation and hence, the construction cost of maritime structures. In addition, no literature on the interaction of these materials with SiMn slag in concrete has been published. In this context, further comprehensive research is essential in this field.
3) Numerous studies have been conducted to investigate the effects of FA and SF. However, the published literature shows inconsistent findings due to variations of material properties and concrete proportions used in the studies. The proportions of FA and SF yielding the optimum concrete performance are also inconsistent, particularly in the ternary blended concrete. Therefore, further investigation is still required to examine the effect of FA and SF in binary and ternary blended concrete and ultimately to determine the optimum replacement levels to improve the performance of SiMn slag concrete.

4) This research utilizes the RSM, a more appropriate and comprehensive optimization method, to optimize the replacement levels of FA and SF. There is limited published literature on the use of RSM for the optimization of FA and SF. Moreover, this study has shown that the prediction models developed on the basis of SiMn slag concrete can be used to predict the properties of other types of concrete containing FA and SF when the relationships between concrete types are established. In this regard, it is not necessary to repeat the tedious experiment if FA and SF are used in other types of concrete.
5) The published literature has widely discussed the effect of sulphate attack and WDA on the concrete properties including physical properties, strength and durability. However, limited research has been carried out on the cyclic behavior of concrete after the deterioration. In marine environment, the deteriorated concrete is also subjected to cyclic loading such as wave action. This study thus examines the deterioration mechanism of concrete subjected to combined actions of sulphate attack, WDA and compressive cyclic loading.
6) Cyclic loading of concrete is numerically modelled using the ABAQUS to study the fatigue behavior of concrete subjected to sulphate attack and WDA. The deterioration of concrete caused by sulphate attack and WDA is considered in the material constitutive model by modifying the concrete properties. By using the numerical model, parametric studies can be carried out without conducting the otherwise costly and time-consuming experiments. In this regard, the effects of related parameters of cyclic loading can be further studied and the model can be used to predict fatigue life of concrete due to long-term deterioration.

1.5 Thesis Outline

The chapter outlines for this thesis are presented as follows.

Chapter 2 is devoted to the literature review on the incorporation of concrete materials such as marine sand, seawater, SiMn slag, FA and SF, as well as the relevant optimization methods for the design of concrete mixture. The deterioration of concrete exposed to WDA in marine environment and the effect of cyclic loading on concrete are also reviewed.

Chapter 3 develops the mix design of concrete incorporating marine sand, seawater and SiMn slag. This section also investigates the strength and durability of the developed concrete.

Chapter 4 presents the optimization of FA and SF in the concrete incorporated with marine sand, seawater and SiMn slag. The experimental results are statistically analyzed based on the analysis of variance (ANOVA). The optimization is carried out by using the RSM.

Chapter 5 elaborates the experimental investigation on the durability of optimized concrete subjected to sulphate attack and WDA. This section also investigates fatigue behavior of the deteriorated concrete through laboratory works.

Chapter 6 delves into the numerical simulation of compressive cyclic loading on concrete deteriorated by sulphate attack and WDA. The validation of numerical model with experimental results is shown. The outcomes of parametric study and fatigue life prediction of concrete exposed to long-term deterioration using the model are presented.

Chapter 7 concludes the findings of this research. The recommendations for future study are also provided in this section.

Chapter 2. Literature Review

Section 2.4 of this chapter has been published in the journal paper entitled "Deterioration of marine concrete exposed to wetting-drying action" (Journal of Cleaner Production, Q1, https://doi.org/10.1016/j.jclepro.2020.123383).

2.1 Introduction

This chapter presents literature review related to this research work. The literature review begins with the investigation of the effect of alternative concreting materials used in this project. The materials include FA and SF as supplementary cementitious materials, marine sand as fine aggregate, seawater as mixing water as well as SiMn slag as coarse aggregate. The effect of these materials on the strength and durability is discussed. Optimization techniques related to the design of concrete proportion are then elaborated to identify the appropriate method for optimizing concrete performance. Deterioration mechanism of concrete exposed to WDA in marine environment is subsequently reviewed. Research related to cyclic loading on concrete is also discussed before the end of this chapter.

2.2 Sustainable Concreting Material

Due to high consumption as well as increasing demand in construction industry, the source of conventional concreting materials is depleting (Monteiro et al., 2017). The search for alternative materials, such as industrial wastes, is vital in order to mitigate environmental impact. As binder, coarse aggregate, fine aggregate and water are the main components of concrete, effort must be made to seek for their respective replacements. This study aims to produce sustainable concrete by substituting FA and SF for binder, SiMn slag for coarse aggregate, marine sand for fine aggregate and seawater for freshwater. Therefore, physical property and chemical composition of these materials and their effects on the strength and durability of concrete are reviewed to ensure their effective incorporation.

2.2.1 Supplementary Cementitious Material

FA and SF can be used as supplementary cementitious materials to partially replace cement. The use of FA and SF is becoming increasingly popular due to their sustainability benefits. Cement production is one of the major sources of carbon dioxide (CO_2) emissions, which has accounted for 2.4% of global CO_2 emissions (Gibbs et al., 2000). Both industrial wastes, FA and SF, are therefore recommended to partially replace cement in order to reduce carbon footprint. In addition, extensive research shows that FA and SF are capable of enhancing concrete properties. But, their replacement levels are constrained by physical and chemical properties.

2.2.1.1 Characteristic of Fly Ash

FA is a powdery residue produced in coal-fired power plant during coal combustion. Table 2.1 summarizes the chemical composition and physical properties of FA as used by various researchers. Based on chemical composition, FA can be divided into two classes, class C and class F. ASTM C618 (2019) specifies the class C FA as having a composition of 50% to 70% SiO_2, Al_2O_3 and Fe_2O_3, while the class F FA has more than 70% of these components. The oxide compounds usually exist as alumino-silicate minerals such as quartz, mullite and hematite, which are amorphous in nature (Hemalatha and Ramaswamy, 2017). The minerals have a poorly arranged atomic structure and are pozzolanic in nature. Pozzolanic reaction occurs when alumina (Al_2O_3) and silica (SiO_2) components of FA react with calcium hydroxide ($Ca(OH)_2$) from cement hydration to form hydrate as shown in Eq. 2.1 to Eq. 2.3 (Papadakis, 1999; Zeng et al., 2012).

$$1.5Ca(OH)_2 + SiO_2 \rightarrow C_{1.5}SH_{1.5} \qquad \text{Eq. 2.1}$$

$$Al_2O_3 + 4Ca(OH)_2 + 9H_2O \rightarrow C_4AH_{13} \qquad \text{Eq. 2.2}$$

$$Fe_2O_3 + Al_2O_3 + 8Ca(OH)_2 + 18H_2O \rightarrow C_8AFH_{26} \qquad \text{Eq. 2.3}$$

In cementitious mixture, FA can only induce a pozzolanic reaction if there is sufficient $CaOH_2$, which is also a secondary product of cement hydration. As a result, the pozzolanic reaction is at a lower rate as it occurs after the hydraulic reaction. Its effect on the hardened state properties of concrete is only evident over time. Nonetheless, class C FA contains a higher amount of lime (CaO) which has a self-cementing property and does not require activator. As such, class C FA usually provides better concrete properties at an early age (Ponikiewski and Gołaszewski, 2014; Sumer, 2012).

The specific gravity of FA ranges from 1.84 to 2.64, which is approximately 15% to 40% lower than that of ordinary Portland cement (OPC), as shown in Table 2.1.

Replacing cement with FA, especially in large quantity, will result in a lower concrete density. Besides, the fineness of FA used in the literature ranges from 1900 cm^2/g to 6628 cm^2/g. FA with higher fineness has a higher rate of pozzolanic reaction due to its larger surface area to provide packing and nucleation effects (Bagheri et al., 2013). Itskos et al. (2010) have shown that FA with particle size ranging from 7 μm to 150 μm exhibits better pozzolanic property. The fine FA comprises more amorphous phases that are more reactive.

Table 2.1: Chemical composition and physical property of FA from literature

Literature	Chemical composition (%)					Physical property	
	CaO	SiO_2	Al_2O_3	Fe_2O_3	Class	Specific gravity	Fineness (cm^2/g)
Siddique (2004)	5.6	55.3	25.7	5.3	F	2.72	-
Oner et al. (2005)	2.1	55.6	25.2	6.5	F	2.09	3355
Erdem and Kirca (2008)	5.5	54.3	19.1	14.6	F	1.92	5540
Gesoglu et al. (2009)	4.2	56.2	20.2	6.7	F	2.25	2870
Nochaiya et al. (2010)	15.2	39.8	21.5	13.7	F	-	-
Siddique (2011a)	2.2	58.6	28.2	3.4	F	2.13	-
Sumer (2012)	1.6	58.6	23.4	7.0	F	2.34	3350
Bagheri et al. (2013)	0.7	58.7	31.4	3.7	F	2.22	4096
	2.0	58.8	32.2	3.8	F	2.24	6628
Kwan and Chen (2013)	4.8	56.5	26.5	5.3	F	2.52	3590
Kondraivendhan and Bhattacharjee (2015)	1.3	61.0	27.8	4.5	F	2.13	-
Sankar et al. (2020)	7.0	46.9	26.5	11.4	F	3.10	-
Mustapha et al. (2021)	4.8	51.8	26.5	8.5	F	2.10	-
Padavala et al. (2021)	2.3	55.6	26.6	9.5	F	2.34	-
Erdem and Kirca (2008)	29.2	37.3	19.3	4.8	C	2.62	3900
Radlinski and Olek (2012)	16.2	41.4	20.0	6.0	C	2.56	-
Sumer (2012)	15.1	46.4	13.9	8.3	C	1.84	2850
Ponikiewski and Gołaszewski (2014)	22.4	40.2	24.0	5.9	C	2.64	1900 & 4060

2.2.1.2 Characteristic of Silica Fume

SF is a waste produced from the reduction of quartz with coal during manufacturing of ferrosilicon and silicon metals. Table 2.2 presents the chemical composition and physical property of SF found in the published literature. SF has a high content of silica (SiO_2) which ranges from 86% to 99%. But, it contains less alumina (Al_2O_3) and iron oxide (Fe_2O_3) than the FA. As such, the pozzolanic reaction of SF is only contributed by the reaction between the SiO_2 and $Ca(OH)_2$, as shown in Eq. 2.1. Besides, SF contains a low CaO content ranging from 0.3% to 1.7% and thus has no self-cementing property. The chemical composition of SF is similar to that of class N pozzolan, in which the sum of SiO_2, Al_2O_3 and Fe_2O_3 accounts for more than 70% of total composition, as defined by ASTM C618 (2019) .

SF has a more constant specific gravity of between 2.2 and 2.25 as reported in the literature. The specific gravity of SF is lower than that of OPC and FA. This is due to its higher content of SiO_2, which has a lower density than other oxide such as CaO, Al_2O_3 and Fe_2O_3 (Siddique, 2011b). In addition, SF has a fineness of between 14000 cm^2/g and 21080 cm^2/g, which is approximately 4 times finer than FA. The SF can therefore fill the particle gap in cement and densify the cementitious matrix (Gesoglu et al., 2009). Pozzolanic reaction of SF also occurs at a faster rate due to the larger surface area, but may require more water (Gonen and Yazicioglu, 2007). In this regard, SF is often considered as a better supplementary cementitious material than FA since it exhibits better pozzolanic property due to its higher silica content and particle fineness.

Table 2.2: Chemical composition and physical property of SF from literature

Literature	Chemical composition				Physical property	
	CaO	SiO_2	Al_2O_3	Fe_2O_3	Specific gravity	Fineness (cm^2/g)
Mazloom et al. (2004)	1.7	91.7	1.0	0.9	-	14000
Bhanja and Sengupta (2005)	-	90.9	-	-	-	18000
Gonen and Yazicioglu (2007)	0.7	91.0	0.6	0.2	2.20	14400
Erdem and Kirca (2008)	0.3	86.2	0	0.4	2.23	-
Tanyildizi and Coskun (2008)	0.7	91.0	0.6	0.2	2.20	-
Gesoglu et al. (2009)	0.5	90.4	0.7	1.3	2.20	21080
Nochaiya et al. (2010)	0.3	95.3	0.6	0.3	-	-
Radlinski and Olek (2012)	0.7	93.1	0.6	0.4	2.20	-
Bagheri et al. (2013)	0.5	94.3	1.1	0.7	2.21	-
Ahmad (2017)	-	99.0	0.8	-	-	-
Sankar et al. (2020)	0.6	91.5	0.6	1.6	2.20	20000
Tripathi et al. (2020)	0.5	89.8	1.4	1.8	2.25	-
Mustapha et al. (2021)	0.1	96	0.1	0.6	2.1 – 2.4	-
Padavala et al. (2021)	1.1	91.1	1.3	1.2	2.42	20000

2.2.1.3 Effect of Fly Ash on Concrete Property

FA has physical property and chemical composition that are different from those of OPC. The replacement of OPC with FA can affect the concrete properties, such as workability, strength and durability. Several studies have been conducted to investigate the effect of FA on these properties in order to determine the optimum FA replacement level.

The effect of FA on concrete workability reported in the published literature is presented in Figure 2.1(a). Most of the studies show that FA has a beneficial effect on the workability. Bagheri et al. (2013) demonstrated that concrete with up to 30% FA content exhibited higher workability due to lower water demand. The workability improved further with the use of finer FA as a result of better particle packing. Siddique (2004) observed that incorporation of FA up to 50% significantly improved the concrete slump. Gesoglu et al. (2009) found that an optimum FA replacement of 40% improved slump flow by 9% compared to the control. Siddique (2011a) showed that the use of FA with a replacement level between 15% and 35% could produce self-compacting concrete that fulfilled all the requirements stated in the EFNARC standard. Kwan and Chen (2013) also noticed an improvement in flow rate of mortar with an increase in FA content of up to 60%. This was ascribed to the ball bearing effect of the spherical FA particles, which reduced friction inside the cementitious matrix.

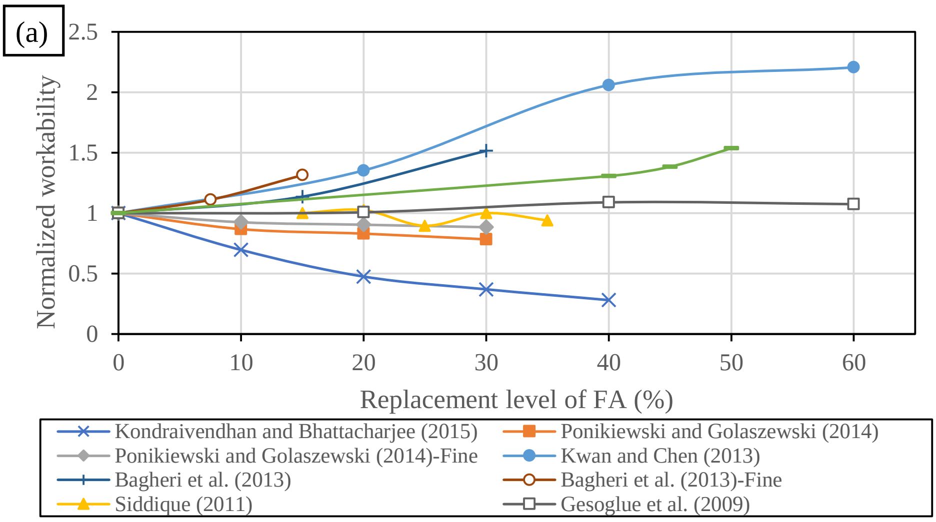

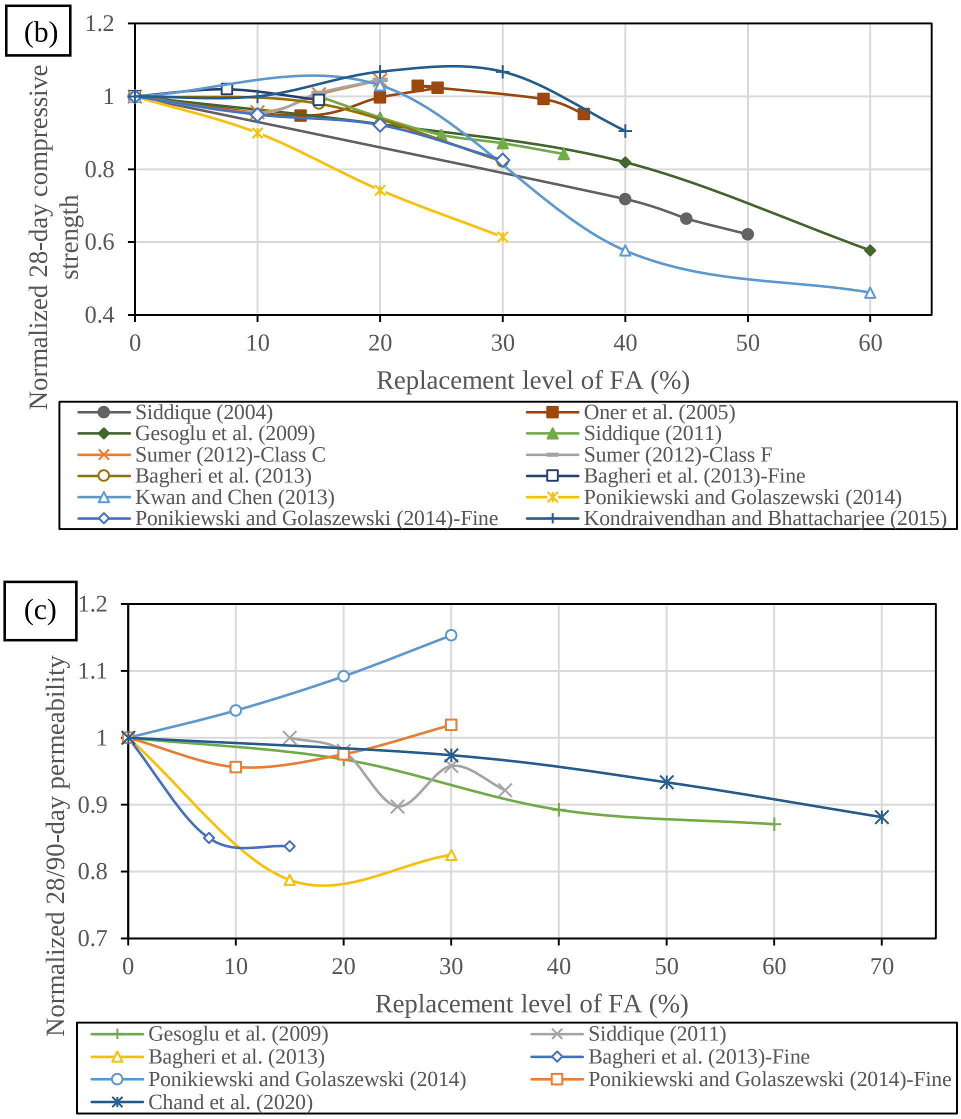

Figure 2.1: Effect of FA on normalized (a) workability, (b) compressive strength and (c) permeability based on literature

Conversely, Kondraivendhan and Bhattacharjee (2015) found that concrete workability decreased with the addition of FA due to its larger surface area, which had a higher demand for water. Ponikiewski and Gołaszewski (2014) also noted that FA had a negative effect on concrete workability. This was due to the increased concrete viscosity with the addition of FA, which shortened the setting time and accelerated the loss of workability.

Several studies have also been performed to investigate the effect of FA on concrete strength. Figure 2.1(b) summarizes the variation of 28-day compressive strength with FA replacement level. In general, the compressive strength decreased with an increased FA content. Kwan and Chen (2013) reported that the use of up to 40% of

FA increased the 28-day compressive strength by 11%, but any further FA addition decreased the strength. An optimum replacement level of 40% for FA was reported by Oner et al. (2005). Siddique (2011a) demonstrated that the concrete containing 15%–35% of FA had a comparable strength to normal concrete. Sumer (2012) found a lower compressive strength with the incorporation of class F FA at 28 and 90 days. However, he noted that class C FA produced a higher strength concrete than the control. This was due to the higher calcium content of class C FA that promoted faster concrete cementation.

Ponikiewski and Gołaszewski (2014) showed that FA concrete had a lower early strength. Kondraivendhan and Bhattacharjee (2015) reported that the strength gain of FA concrete was more prominent after 90 days of curing. Siddique (2004) found that FA concrete experienced approximately 39% and 45% of strength gain from 28 to 365 days. This was attributed to the lower rate of pozzolanic reaction of FA. Pozzolanic reaction took place later than cement hydration because the reaction required $Ca(OH)_2$ from hydration to form hydrates to gain strength.

As for the FA effect on durability, Figure 2.1(c) presents the graphs of normalized concrete permeability against FA replacement level. Siddique (2011a) observed a decrease in chloride permeability when the FA content was between 15% and 35%, with an optimum level of 25%. Gesoglu et al. (2009) showed that the substitution of OPC by up to 60% of FA decreased chloride and water permeability almost twice. Chand et al. (2020) demonstrated that the use of 70% FA in concrete decreased chloride penetration by 12%. The reduction in permeability was due to the denser packing of cementitious matrix by the spherical FA particles, which reduced the size of concrete pore. The interfacial transition zone (ITZ) between cement paste and aggregate was also strengthened by FA.

In addition, Bagheri et al. (2013) also found the chloride permeability of FA concrete decreased and this effect became more pronounced at a later age. The results also showed that the use of finer FA was less effective than normal FA in terms of durability. In contrast, Ponikiewski and Gołaszewski (2014) demonstrated that the fine FA could better reduce chloride and water permeability of concrete at an optimum dose of 10%. Meanwhile, the use of normal FA at a replacement level between 0% and 30% resulted in a higher permeability than control concrete at all ages. The fine FA filled the particle gap in OPC and produced concrete with a lower porosity. High surface area of fine FA also accelerated pozzolanic reaction that densified the microstructure of concrete.

Based on the literature review, the incorporation of FA with a replacement level of between 20% and 60% could improve concrete workability. Most studies report that FA contributes to inferior strength at an early age, but it increases strength at a later stage. In terms of strength, the optimum replacement level of FA ranges from 20% to 40%. The literature also shows that FA has a positive effect on concrete durability and its optimum content is between 7.5% and 25%.

2.2.1.4 Effect of Silica Fume on Concrete Property

As SF has a high fineness and pozzolanic property, its incorporation into concrete will alter the workability, strength and durability. The effect of SF on the concrete properties is different from that of FA due to their distinct chemical compositions and physical properties.

The influence of SF on the concrete workability presented by the published literature is shown in Figure 2.2(a). The literature indicates that the workability generally decreases with the incorporation of SF. Bagheri et al. (2013) found that the addition of up to 10% of SF increased water demand of concrete. Gonen and Yazicioglu (2007) showed that the use of 10% SF reduced the concrete slump by 28%. Mazloom et al. (2004) used a greater amount of superplasticizer to achieve the target slump when the SF content was increased. It was noted that the superplasticizer had to be increased from 1.6% to 2.7% of total binder content when SF replacement level was 15%. Furthermore, Tripathi et al. (2020) reported a 42% reduction in concrete slump when the SF replacement level was increased to 25%. This was ascribed to the very fine size of SF particle having a larger surface area that required higher water demand. The addition of SF also increased the cohesiveness of concrete and thus reduced its workability (Bagheri et al., 2013).

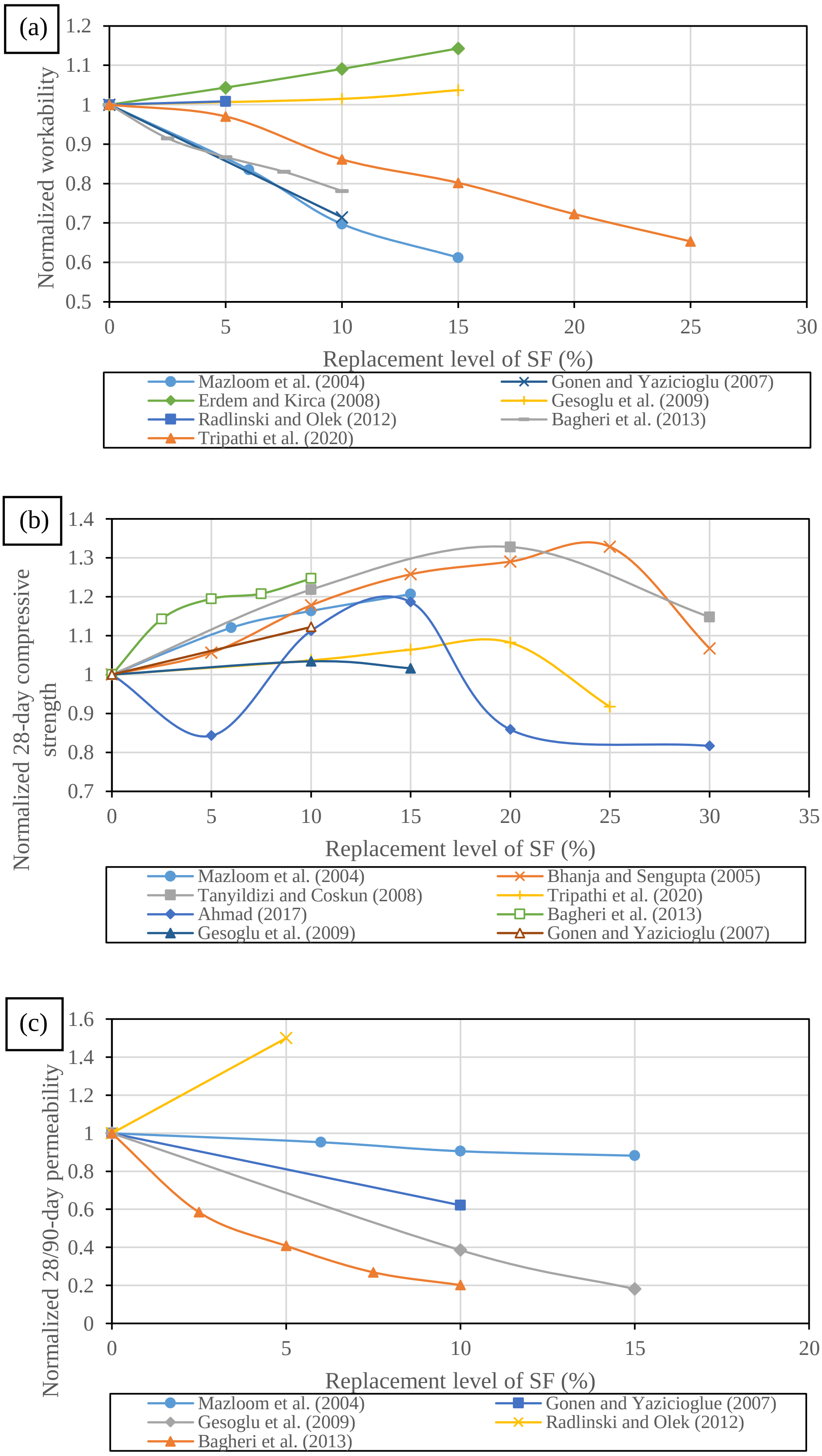

Figure 2.2: Effect of SF on normalized (a) workability, (b) compressive strength and (c) permeability based on literature

Nevertheless, some studies indicate that SF can increase concrete workability. Radlinski and Olek (2012) showed a slight decrease in superplasticizer dosage with the addition of 5% SF. Gesoglu et al. (2009) demonstrated that the slump flow properties of concrete improved by adding 0–15% of SF. All the SF concrete also complied with the EFNARC requirements for self-compacting concrete. Erdem and Kirca (2008) noted a decline in water demand in SF concrete. The water demand decreased with an increase of up to 15% in SF replacement level. The water-reducing effect of SF was ascribed to its spherical particle, which acted as a ball bearing, to minimize inter-particle friction.

With respect to strength, the literature generally shows that SF improves concrete strength as shown in Figure 2.2(b). Ahmad (2017) found that 28-day compressive strength increased by 19% with an optimum SF replacement level of 15%. But, further addition of SF reduced the strength below that of the control concrete. The higher SF volume produced more cohesive concrete that affected the homogeneity of mixture. Tripathi et al. (2020) found that the compressive strength of concrete increased with an SF content of up to 20%, but decreased with further addition. Tanyildizi and Coskun (2008) reported an optimum SF content of 20%, while Bhanja and Sengupta (2005) observed an optimum value of 25% in terms of compressive and splitting tensile strengths.

Furthermore, Bagheri et al. (2013) found that, unlike FA, SF concrete could achieve a higher strength than control concrete at both early and later ages. Mazloom et al. (2004) demonstrated that the compressive strength of SF concrete was 15%, 20% and 19% higher than that of the control at 7, 28 and 90 days, respectively. This was attributed to the smaller particle size of SF, which had a larger surface area that accelerated the pozzolanic reaction. The fine SF also served as filler to improve the bonding of cement paste with aggregate (Gonen and Yazicioglu, 2007).

The durability of concrete has been improved by the incorporation of SF as shown in Figure 2.2(c). Mazloom et al. (2004) observed that the penetration of water into concrete decreased with an increase of up to 15% in SF content. The pore size and porosity of SF concrete were smaller than those of normal concrete. Gonen and Yazicioglu (2007) showed that the SF concrete had 4% porosity and 38% capillary absorption lower than the control. Gesoglu et al. (2009) also found a reduced chloride and water permeability of concrete with the use of 15% SF. This was because SF was finer in size and could fill the gaps within the paste matrix to minimize the capillary pores of concrete (Bagheri et al., 2013). Radlinski and Olek (2012) recorded a 50% higher sorptivity of SF concrete at 28 days, but comparable sorptivity to control concrete at 180 days. This indicated that pozzolanic reaction of SF became more complete in the long term.

In summary, the concrete workability decreases with an increase in SF content. But, SF has an advantageous effect on both early and late concrete strength with an optimum replacement level of between 15% and 25%. SF also improves the concrete durability by minimizing the permeability with an optimum content ranging from 10% to 15%. The optimum SF replacement level is generally lower than that of FA due to its higher silica content. The dosage is also restricted by the lower workability of concrete caused by it.

2.2.1.5 Synergistic Effect of Fly Ash and Silica Fume in Concrete

The published literature also studied the synergy of FA and SF in ternary blended concrete. As for workability, Bagheri et al. (2013) found that combined FA and SF reduced the water demand in concrete except when SF content is more than 7.5%. Gesoglu et al. (2009) demonstrated that the ternary blend of FA and SF had better slump flow properties than the binary blend. The flow time of SF concrete was decreased by 25% with the incorporation of FA at a replacement level of 45%. Padavala et al. (2021) discovered that the slump value of concrete increased with FA and SF contents. This was because FA and SF were spherical, providing a ball bearing effect for inter-particle lubrication. Radlinski and Olek (2012) showed that the dosage of superplasticizer in ternary blended concrete was 2.5% lower than that in control concrete. However, with a rise in SF content, Nochaiya et al. (2010) observed a decrease in concrete slump. The slump was lower than in the control concrete when the SF content was higher than 10%. The larger surface area of SF increased water demand, but the ball bearing effect of FA reduced inter-particle friction.

As for strength, the literature shows different effects due to the different properties of FA and SF used. Gesoglu et al. (2009) reported that the compressive strength of ternary blended concrete was lower than that of binary blended concrete. Concrete containing 30% FA and 10% SF had a 4.5% lower strength than concrete containing 40% FA. However, Gonen and Yazicioglu (2007) showed that adding 10% SF increased the compressive strength of FA concrete by 11.3%. Besides, Radlinski and Olek (2012) demonstrated that SF was able to compensate slightly for the lower early strength of FA concrete, but the strength was still below that of the control. However, the synergistic effect of FA and SF became evident at a later age when it achieved comparable strength to SF concrete. Bagheri et al. (2013) found that when the FA content was below 15%, the use of 2.5%–7.5% SF could produce concrete with a comparable early strength to that of control. This was attributed to fine SF that exhibited better pozzolanic property than FA (Nochaiya et al., 2010). Khan and Ali (2019), on the other hand, demonstrated that when the SF content was 15%, the incorporation of 5%–15% FA increased the 28-day compressive strength by 15%–28%. Sankar et al. (2020) showed that the use of 5%–25% FA improved the strength of concrete containing 15% SF. The increase in strength was due to the pozzolanic reaction of FA.

The synergy of FA and SF also affects concrete durability. Gonen and Yazicioglu (2007) showed that the ternary blended concrete has lower porosity than binary blended concrete. Its capillary absorption was slightly higher than that of SF concrete, but lower than that of the control concrete. Radlinski and Olek (2012) reported that ternary blended concrete had a higher sorptivity than binary blended and control concrete at 7 and 28 days, but attained a lower sorptivity at 180 days. Bagheri et al. (2013) found that when FA content was below 30%, the incorporation of 2.5%–7.5% of SF could further reduce the diffusion of chloride into concrete. The ternary blended concrete had a chloride penetration resistance comparable to that of SF concrete at an early age, but it outperformed SF concrete at a later age. Gesoglu et al. (2009) demonstrated that using less than 15% SF could reduce the sorptivity of FA concrete by as much as 12.3%. The pozzolanic reaction of FA and SF produced more calcium silicate hydrate (C-S-H) to fill capillary pores of concrete. The fine SF particles also served as filler to densify the concrete microstructure (Nochaiya et al., 2010).

According to the literature review, the high water demand of SF concrete can be overcome by using a ternary mixture with FA. The use of FA and SF as ternary blend in concrete also improves the strength and durability. However, the published literature does not provide the optimum combination of FA and SF owing to incomprehensive study. Further investigation is still required and it is recommended that an effective optimization tool be used to evaluate the optimum content of FA and SF.

2.2.2 Marine Sand and Seawater Concrete

The consumption of river sand and freshwater in large scale for concreting has caused environmental issues such as material depletion, environmental degradation, pollution and climate change (Blankendaal et al., 2014; Xiao et al., 2017). Sand extraction in river can lead to negative impact on the river ecosystem, riverine transportation and flood mitigation system. Freshwater consumption can become a problem, particularly if the source is remote and supplies are scarce. Furthermore, the transportation of these materials incurs extra project cost. In this connection, the use of marine sand and seawater in the manufacture of concrete is an innovative solution, particularly for the maritime structures.

2.2.2.1 Characteristic of Marine Sand

Marine sand contains salt that can cause corrosion of steel in concrete. In general, the sand will be desalted using freshwater. Standards such as JASS 5 by Architectural Institute of Japan (2015) , BS EN 12620 by British Standard (2013) and JGJ206-2010 by China Architecture & Building Press (2010) , have provided guidelines for the desalination of marine sand for use in building and construction. The standards also set out requirements for the use of desalted marine sand to ensure safety and durability of structure. However, the desalting process requires high operating cost and exquisite quality control and may not be feasible due to freshwater scarcity. As a result, the use of unwashed marine sand in coastal projects is particularly appealing.

Though both marine sand and river sand typically exhibit similar mineral compositions and geological properties, marine sand can contain impurities such as salt and seashell (Dong et al., 2016). Chloride from salt in marine sand is harmful to steel as it causes corrosion. The content of chloride in marine sand can range between 0.03% and 0.13% of the total sand weight and it also depends on salinity of seawater (Li et al., 2018b; Tang et al., 2018). Dias et al. (2008) showed that the threshold chloride content in sand was below 0.3% when the embedded steel was safe from corrosion. Besides, marine sand exhibits higher density than river sand due to the presence of seashell which is mainly made up of calcium carbonate ($CaCO_3$) (Xiao et al., 2017). Seashell is generally not harmful to concrete and can be removed by sieving. Xiao et al. (2017) found that seashell flakes could provide better bond strength of concrete and reduce porosity.

The particle size distribution of marine sand used by various researchers is shown in Figure 2.3. These sands are generally close to the limits specified by the ASTM C33 (2012) standard. Compared to these sands, the marine sand sampled from Tanjung Lobang Beach located in Miri, Malaysia was finer and its grading fell outside the standard limit. The sand is also finer than the river sand supplied by Hollystone Quarry Sdn. Bhd. from Baram, Miri. The marine sand is therefore not suitable for use as fine aggregates and because of its high water demand, it affects concrete workability. It should be further processed by mixing with coarser sand such as quarry dust.

The use of marine sand in concrete requires careful quality control and monitoring. Yepez and Yepez (2017) highlighted the role of marine sand in the failure of RC structure in Ecuador following the Mw 7.8 Pedernales earthquake in 2016. Fine aggregate of concrete of the damaged and collapsed buildings was primarily made up of marine sand. The sand exhibited low fineness modulus of 1.1 and also contained impurities such as granulometric materials, organic matter and chloride. These components from the sand have weakened the bonding of cementitious materials, increased the concrete porosity as well as created a corrosive environment for embedded steel. Although the direct use of marine sand is cost-effective and environmental friendly, consideration should also be given to the strength and durability of concrete.

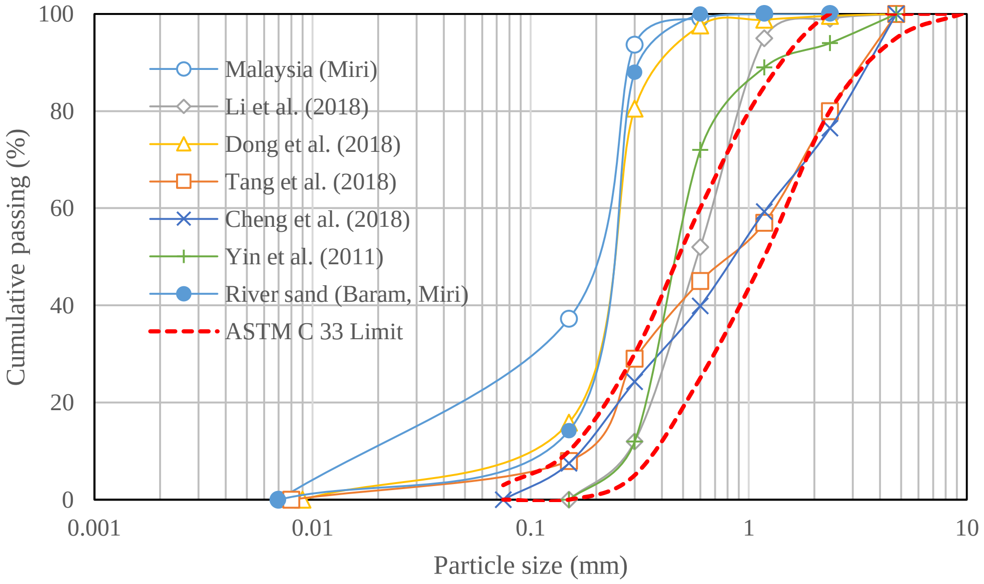

Figure 2.3: Comparison of particle size distribution of marine sand and river sand with the standard distribution of ASTM C33

2.2.2.2 Composition of Seawater

Seawater contains salt and is thus denser than freshwater. It is typically alkaline and has a pH value ranging from 8.08 to 8.33 due to the dissolved rock minerals collected during runoff (Marion et al., 2011). Table 2.3 presents the normal seawater composition at various locations investigated by Lenntech (2018). Seawater contains high amount of chloride (Cl^-) and sulphate (SO_4^{2-}), which are the main ions that cause degradation of concrete. As compared to freshwater, seawater has a marginally higher density of 1022–1025 kg/m^3. Concrete can be exposed to seawater in two ways, namely as an ingredient in concrete mixing and through physical contact in maritime applications. The presence of the two ions in seawater can have an adverse effect on the fresh and hardened state properties of concrete (Katano et al., 2013; Xiao et al., 2017).

Table 2.3: Composition of seawater from literature

Literature	**Composition (g/L)**							**Density (kg/m^3)**	**pH value**
	Cl^-	**SO_4^{2-}**	**HCO^{3-}**	**Na^+**	**Mg^{2+}**	**Ca^{2+}**	**K^+**		
Mohammed et al. (2004)	17.1	2.4	-	9.3	1.2	-	-		
Otsuki et al. (2011)	17.1	2.4	-	10.1	1.2	-	-	1024	8.03
Younis et al. (2018)	18.6	2.4	-	-	-	-	-	-	8.20
Montanari et al. (2019)	19.9	2.7	-	10.7	1.4	-	-	1025	-
Lenntech (2018) • Typical seawater	19.0	2.6	0.1	10.6	1.3	0.4	0.4	-	-
• Eastern Mediterranean	21.2	3.0	0	11.8	1.4	0.4	0.5	-	-
• Arabian Gulf at Kuwait	23.0	3.2	0.1	15.9	1.8	0.5	0.5	-	-
• Red Sea at Jeddah	22.2	3.1	0.1	14.3	0.7	0.2	0.2	-	-

2.2.2.3 Workability of Marine Sand Concrete and Seawater Concrete

The effect of marine sand and seawater on the fresh properties of concrete has been studied by several researchers. As for the use of marine sand in concreting, Limeira et al. (2012) found that the flowability of mortar decreased when the sand content increased. A dosage of 2% superplasticizer was required to compensate for the reduced flow rate. Cheng et al. (2018) showed that the slump of marine sand concrete was 40 mm lower than that of river sand concrete. The marine sand used in these studies exhibited a fine grading. The loss of workability was therefore caused by a higher water demand of the sand. Nevertheless, Hasdemir et al. (2016) found that workability of concrete made up of marine sand was higher than that of sands sampled from inland of Marmara region in Turkey. This was because this type of marine sand contained less fine material such as clay and had a lower water absorption.

The shell from marine sand also has a negative effect on concrete workability. Yang et al. (2010) used an additional 0.6% water-reducing admixture when the fine aggregate of concrete is 20% substituted by seashell. Safi et al. (2015) demonstrated that concrete slump decreased with the increasing seashell content. The workability of concrete was reduced by 13.3% when fine aggregate was completely replaced by seashell. The reduction of workability was mainly attributed to the irregular shape of seashell which impeded fresh concrete flow.

As for the effect of seawater, Katano et al. (2013) observed a 15.2% decrease in the slump value of concrete compared to the use of freshwater. Younis et al. (2018) found that the slump flow of seawater concrete was 20% lower than that of freshwater concrete. The setting time of seawater concrete was also reduced by 30%, indicating a higher rate of workability loss. Ghorab et al. (1990) stated that the initial and final setting times for seawater concrete were 24% and 22% lower than that of freshwater concrete. This was attributed to the acceleration of cement hydration promoted by chloride from seawater. Sodium chloride (NaCl) from seawater can react with calcium hydroxide ($Ca(OH)_2$) from cement hydration to form calcium chloride ($CaCl_2$) as shown in Eq. 2.4. $CaCl_2$ plays an important role in accelerating the cement hydration (Bortoluzzi et al., 2009; Kishar et al., 2013). As such, the workability of seawater concrete decreased due to the accelerated hydration. Nevertheless, Nishida et al. (2013) showed that seawater had negligible effect on the concrete workability.

$$Ca(OH)_2 + 2NaCl \rightarrow CaCl_2 + 2Na^+ + 2OH^- \qquad \text{Eq. 2.4}$$

The majority of the studies indicate that marine sand and seawater have a negative impact on concrete workability.

2.2.2.4 Strength of Marine Sand Concrete and Seawater Concrete

Several studies have been performed on the strength of concrete incorporating marine sand. Karthikeyan and Nagarajan (2016) found that the incorporation of marine sand with a content of up to 20% increased the compressive, splitting tensile and flexural strength of concrete, but the strength decreased with further addition. Tang et al. (2018) showed that the compressive and flexural strengths of marine sand concrete were 15.9% and 20% respectively, lower than those of river sand concrete. Yepez and Yepez (2017) found that 15 to 40 years old marine sand concrete had a compressive strength of 20.5 MPa to 23.3 MPa. The strength barely met the minimum strength limit of 21 MPa specified by ACI 318 (2008). The low concrete strength was caused by the organic content of marine sand, which increased the concrete porosity. Ratnayake et al. (2014) also found that marine sand concrete had a 10% lower compressive strength than river sand concrete.

Past studies have also found the beneficial effect of marine sand. Limeira et al. (2011) demonstrated that the addition of up to 50% of marine sand produced concrete with higher compressive and flexural strength at 7 and 28 days. Partial replacement with marine sand, which was finer, filled the gap between aggregate particles, which improved concrete compaction. The presence of chloride ions in marine sand can also increase bonding strength of concrete (Dong et al., 2016). Cheng et al. (2018) reported that the early compressive strength of marine sand concrete was 34% higher than normal concrete, but it was 6% lower at a later age. This was due to the water contained in porous sand, which provided internal curing and promoted early strength development.

As for the effect of seawater, Katano et al. (2013) observed that it improved concrete compressive strength substantially. Shi et al. (2015) showed that seawater concrete exhibited higher compressive strength at all ages due to the accelerated hydration caused by chloride. Wegian (2010) found that seawater concrete had higher early-age compressive, splitting tensile and flexural strength, but lower long-term strength than control concrete. The increase in strength was due to the chloride from seawater, which could react with cement hydrate to form Friedel’s salt and facilitate early hydration in concrete (Ogirigbo and Ukpata, 2017). Islam et al. (2012) noted a 10% lower late-age compressive strength due to gradual loss of hydration product caused by salt crystal formation.

There is limited literature on the combined use of marine sand and seawater in concrete. Tjaronge et al. (2014) have shown that concrete made from marine sand and seawater can achieve a target 28-day compressive strength and also result in homogeneous compaction. The literature review has indicated contradictory findings with regard to the strength of marine sand concrete and seawater concrete. Further research is essential to iron out the discrepancy.

2.2.2.5 Durability of Marine Sand Concrete and Seawater Concrete

The effect of marine sand on concrete durability has been reported by several researchers. Huiguang et al. (2011) found that marine sand improved concrete resistance against chloride penetration due to a lower clay content. Liu et al. (2016) stated that chloride in marine sand could reduce concrete porosity and enhance the carbonation resistance. Cheng et al. (2018) also observed a decrease in chloride penetration into marine sand concrete due to less porosity resulting from internal curing by water stored in sand. Tang et al. (2018) noted that marine sand concrete had a higher resistance to sulphate attack than river sand concrete. Limeira et al. (2011) demonstrated that various types of marine sand decreased concrete sorptivity by 1.7% to 23.3%. The concrete microstructure was refined by smaller marine sand and became more compact. However, Ratnayake et al. (2014) found that marine sand sampled from Muthurajawela in Sri Lanka had a chloride content higher than the threshold, causing steel corrosion.

As for concrete mixed with seawater, pore structure analysis conducted by Tjaronge and Irfan (2015) implied that seawater could provide good bonding between cement matrix and aggregate. Shi et al. (2015) showed that concrete mixed with seawater exhibited better chloride penetration resistance. This was due to accelerated hydration caused by chloride in seawater, which reduced concrete pore diameter. Younis et al. (2018) found that seawater concrete had a comparable chloride penetration resistance to freshwater concrete. Seawater concrete had a lower pore volume and a smaller pore size. The microstructure was more compact and dense with C-S-H.

With respect to the combined use of marine sand and seawater in concrete, Li et al. (2018b) found that the resulting concrete had a higher thermal expansion that caused a higher residual strain than control concrete. This was due to impurities such as salt and shell debris in marine sand and seawater, which exhibited different thermal expansion property. But, the concrete had a similar residual strength to that of concrete made from freshwater and river sand. Katano et al. (2013) incorporated both marine sand and seawater to study concrete durability, but the investigation was focused on the effect of seawater. It was shown that seawater reduced the permeability of marine sand concrete by almost two times.

When compared to strength, relatively less research has been performed on the durability of marine sand concrete and seawater concrete. The literature review shows that marine sand and seawater generally improve concrete durability.

2.2.3 Silicomanganese Slag Concrete

SiMn slag is a by-product of the smelting of silicon and manganese for use as alloy in manufacturing steel. The production of SiMn alloy generates about 1.2 times the SiMn slag from electric arc furnace, and this creates problems in waste management (Kim et al., 2011). Storing a large amount of waste at the smelting plant is space-consuming and environmental unfriendly. This waste is commonly disposed of in landfill and sometimes used as road paving materials (Oliveira et al., 2017). Using SiMn slag to replace concrete components is a promising strategy for concrete industry from the perspective of cost-effectiveness and environmental sustainability.

2.2.3.1 Characteristic of Silicomanganese Slag

SiMn slag is a type of steel slag produced with the use of lime (CaO), dolomite (MgO) and other auxiliary materials in steel manufacturing (Dong et al., 2020). The mineral composition of SiMn slag is identical to cement clinker, which includes silicon dioxide (SiO_2) and calcium oxide (CaO) (Chen et al., 2020). Table 2.4 presents the chemical composition of SiMn slag used by various researchers. SiMn slag comprises 17%–30% of CaO, 36%–44% of SiO_2, 10%–26% of Al_2O_3 and 10%–12% of MnO. Due to the presence of CaO, it exhibits a mild cementing property. Besides, SiMn slag will also exhibit pozzolanic property if the content of SiO_2 and Al_2O_3 are from amorphous minerals. Therefore, ground SiMn slag is suitable for use as a supplementary cementitious material in concrete.

The physical property of SiMn slag, when used as an ingredient, can affect the mechanical and durability properties of concrete. Table 2.5 presents the physical property of SiMn slag used by various researchers. The specific gravity of SiMn slag is close to 3, which is due to the main compositions of heavy CaO, SiO_2 and Al_2O_3. However, the physical property of SiMn slag can vary when different cooling methods are used. Choi and Kim (2020) used three cooling methods, namely rapid cooling by air (A), by water (W) as well as by combination of air and water (AW), in producing SiMn slag aggregate. W and AW methods produced porous SiMn slag that had a lower specific gravity of 1.05 and a higher water absorption of 28.5%. If the standard air cooling method was used, the slag exhibited a lower water absorption of between 0.12% and 0.6% (Choi and Kim, 2020; Shareef et al., 2015).

As for the shape of SiMn slag, it is usually less flaky and less elongated with a higher angularity. However, depending on the crushing process, the shape can change and the bulk density can be affected. The bulk density can vary from 1625 to 3000 kg/m^3 as shown in Table 2.5. The surface of SiMn slag is typically rough and hard compared to conventional aggregates such as limestone and basalt (Dong et al., 2020). Shareef et al. (2015) reported that SiMn slag had higher crushing and impact values than the natural aggregate.

From the literature review, SiMn slag has a chemical composition suitable for use as supplementary cementitious material in concrete. Based on the physical property, SiMn slag can be used as coarse aggregate in concrete.

Table 2.4: Chemical composition of SiMn slag from literature

Literature	Chemical composition (%)					
	CaO	SiO_2	Al_2O_3	Fe_2O_3	MnO	MgO
Frias et al. (2006) & Frias et al. (2009)	25.2	42.6	12.2	1.0	9.9	4.2
Allahverdi and Ahmadnezhad (2014)	29.3	38.2	14.8	1.8	10.3	2.8
Anudeep et al. (2015)	17.6	43.5	18.5	0.6	11.5	6.5
Nath and Kumar (2016)	26.2	40.3	14.6	0.8	10.1	5.7
Nath and Kumar (2017)	17.7	36.4	25.9	1.2	11.2	4.3
Navarro et al. (2017)	29.1	36.5	9.9	0.9	12.2	4.7

Table 2.5: Physical property of SiMn slag from literature

Literature	Specific gravity	Water absorption (%)	Crushing value (%)	Impact value (%)	Bulk density (kg/m^3)
Anudeep et al. (2015)	1.57	-	-	-	3000
Shareef et al. (2015)	2.7	0.12	26.8	25.4	1625
Nath and Kumar (2016)	2.9	-	-	-	-
Nath and Kumar (2017)	3.02	-	-	-	-
Nath and Kumar (2019)	2.94	-	-	-	-
Choi and Kim (2020)	1.05 – 2.88	0.6 – 28.5	-	-	433 – 1857

2.2.3.2 Silicomanganese Slag as Binder of Concrete

Several studies have used SiMn slag to partially replace cement in concrete. Nath and Kumar (2016) showed that mortar incorporated with SiMn slag could achieve a comparable 28-day compressive strength to normal mortar, although a lower strength was observed at an early age. This was due to less active pozzolanic reaction of SiMn slag in the early stage. Nevertheless, calcium manganese oxide hydrate was formed by the hydration of SiMn slag in the later stage. Frias et al. (2009) found that the blend of cement and SiMn slag in a small amount (5%–15%) increased the mortar resistance to aggressive solutions such as NaCl, Na_2SO_4 and seawater. This was due to the refinement of pore structure of cementitious mixture induced by the pozzolanic reaction of SiMn slag.

Allahverdi and Ahmadnezhad (2014) reported that the compressive and flexural strength of mortar decreased with the use of 15% SiMn slag. Ground SiMn slag exhibited a moderate pozzolanic property compared to other pozzolans such as FA and SF. However, Frias et al. (2006) showed that SiMn slag had higher pozzolanic activity than FA but lower than SF. According to the findings, mortar containing up to 15% of SiMn slag had lower compressive strength at 7 and 28 days, but similar strength at a later age, when compared with the control. This was due to impurities such as manganese and sulphate ions in SiMn slag that delayed hydration process.

Research has also been conducted to use SiMn slag as alkali-activated binder. Navarro et al. (2017) used a mixture of sodium silicate and sodium hydroxide solution to activate the cementitious property of SiMn slag. The paste made from alkali-activated

SiMn slag could achieve a compressive strength of more than 45 MPa and a low shrinkage of between 1.5% and 3%. Nath and Kumar (2017) developed an alkali-activated cement by using the blend of SiMn slag and FA. The investigation showed that the compressive strength increased with SiMn slag content. This was attributed to the high reactivity of SiMn slag to form more C-S-H gel for providing a better bonding property. CaO in SiMn slag also provided cementitious property to induce faster hydration. Nath and Kumar (2019) showed that mortar made with alkali-activated SiMn slag exhibited a more compact microstructure than the normal mortar.

SiMn slag as cement replacement can produce concrete with improved strength and durability. But, the use of SiMn slag as cement replacement involves an additional preparation process, such as grinding and sieving, which increases production cost. Therefore, the use of SiMn slag as aggregate in concrete might be more cost-effective.

2.2.3.3 Silicomanganese Slag as Aggregate of Concrete

SiMn slag has been used as fine aggregate in concrete by several researchers. Anudeep et al. (2015) replaced up to 50% of river sand with fine SiMn slag and found that the workability decreased with SiMn slag content. This was due to large surface area and high water absorption exhibited by SiMn slag. Because of poor workability, the concrete compressive and splitting tensile strength decreased by 43.5% and 20.6% respectively. Choi and Kim (2020) used three types of SiMn slag as fine aggregate (A1, A2 and A3) which were produced with different cooling methods. A1, A2 and A3 aggregates had a bulk density of 433 kg/m^3, 838 kg/m^3 and 1857 kg/m^3 respectively. The mortar strength decreased in the order of use of aggregates A3, A2, and A1. This was due to a more porous aggregate at a lower bulk density, which weakened the cementitious bond. Mortar containing A3 aggregate had a strength higher than the control at all replacement levels. A3 aggregate had a more even particle size distribution, lower shrinkage and less porosity.

SiMn slag has also been used as coarse aggregate in concrete. Shareef et al. (2015) compared the compressive strength of concrete made with natural aggregate (B1), quartzite (B2) and SiMn slag (B3), with the latter two being used in full replacement. Concrete made with B3 aggregate had a compressive strength 6.2% and 20.8% lower than concrete made with B1 and B2 aggregates, respectively. This was attributed to the lower crushing value and impact strength exhibited by SiMn slag aggregate, which resulted in weaker concrete. The SiMn slag also had a lower surface roughness that weakened the cement paste bonding. Oliveira et al. (2017) suggested that SiMn slag was suitable for use as cement, aggregate, rail ballast and road paving material.

From the literature review, the use of SiMn slag as coarse aggregate is more cost-effective due to less preparation work. However, there is limited investigation on the use of SiMn slag as coarse aggregate in concrete work. Further research is required to determine the effect of SiMn slag used as a coarse aggregate on the strength and durability of concrete.

2.2.4 Microstructural Analysis

2.2.4.1 Microstructure of Marine Sand and Seawater Concrete

The literature review shows that marine sand has a substantial impact on the hardened state properties of concrete. In this consideration, the effect of marine sand on the concrete microstructure is discussed in this section. Xu et al. (2019) found that marine sand concrete had a compact interfacial transition zone (ITZ) with less visible micro-crack, resulting in improved mechanical properties. This was attributed to lower fineness modulus of marine sand, which contained less free water to form pores in the concrete. He et al. (2020) discovered that the salt in marine sand could react with hydration product to form ettringite, resulting in a denser concrete microstructure. Yang et al. (2019) demonstrated that, even though the marine sand had larger void sizes than river sand, the voids were filled by the cement paste.

As for the effect of seawater, Younis et al. (2018) showed that cementitious paste made from seawater had less pores of smaller size than freshwater concrete. This was ascribed to pore filling by Friedel’s salt as a result of the reaction between chloride and hydration product (Xu et al., 2019). Besides, Li et al. (2015) demonstrated that seawater concrete had a comparable microstructure to the freshwater concrete and its microstructure could be improved by adding 5% metakaolin. However, Younis et al. (2020) observed more micro-cracks and fissures in seawater concrete than in freshwater concrete. The defects in seawater concrete were caused by salt crystallization and gypsum formation. According to the literature review, the effect of seawater on the concrete microstructure is inconsistent, necessitating further investigation.

2.2.4.2 Microstructure of Fly Ash and Silica Fume Concrete

The effect of FA on the concrete microstructure is also studied. According to Jiang et al. (2017b) and Papadakis et al. (1999), FA concrete had less $Ca(OH)_2$ morphology but more C-S-H gel due to the FA pozzolanic reaction and hence had a denser microstructure than normal concrete. At an early age of concrete, the unreacted FA particles were visible as glassy spheres under the magnification of a scanning electron microscope (SEM). At 180 days, FA particles were not found on the microstructure as a result of the complete pozzolanic reaction.

Regarding the effect of SF, Zhang et al. (2016b) found that the ITZ of SF concrete was substantially refined and densely surrounded by hydration products. The pozzolanic reaction of SF began at its surface and eventually penetrated into the particle. Rostami and Behfarnia (2017) also discovered that the addition of 10% SF strengthened the microstructure of concrete. The fine SF particles filled the concrete pore, and the subsequent pozzolanic reaction produced more C-S-H gel to densify the concrete microstructure. Nochaiya et al. (2010) demonstrated that the incorporation of SF into FA concrete reduced the $Ca(OH)_2$ content of concrete, indicating that SF promoted faster pozzolanic reaction. In summary, the literature review shows that both FA and SF can improve the microstructure of concrete.

2.2.4.3 Microstructure of SiMn Slag Concrete

The past research on the concrete microstructure has focused on the use of SiMn slag as binder replacement. According to Nath and Kumar (2017), SiMn slag improved the particles bridging and bonding in the cementitious paste. It was also shown that increasing the SiMn slag content improved the matrix compactness and pozzolanic reaction. Nasir et al. (2019) demonstrated that the inclusion of SiMn slag as alkaline-activated binder densified the microstructure of concrete. The SiMn slag concrete had less cracks and smaller crack widths, which resulted in improved mechanical properties. The pozzolanic reaction of SiMn slag produced calcium manganese hydrate, which could refine microstructure of concrete (Nath and Kumar, 2019). Based on the literature review, there has been relatively little work done to reveal the microstructure of SiMn slag concrete, especially when the SiMn slag is used as coarse aggregate.

2.2.5 Summary

Based on the literature review, partial replacement of OPC with FA and SF can improve workability, strength and durability of concrete. Despite several studies, the optimum replacement levels of SF and FA, especially in the ternary system, are not conclusive due to insufficient experimental planning. The findings are inconsistent due to variation of material property and concrete mix design used in the studies. Further research is therefore still needed. In this regard, it is recommended that an appropriate optimization tool be used to systematically determine the optimum contents of FA and SF in concrete.

The use of marine sand and seawater in concrete, due to their ample availability, is beneficial for construction works in the coastal region. The effects of marine sand and seawater on concrete properties have been separately investigated and the findings are inconsistent in the published literature. There is limited research on the combined use of marine sand and seawater. Thus, further study is necessary to resolve the discrepancy and fill the knowledge gap.

SiMn slag can be used as a partial replacement of cement in concrete. However, additional grinding and sieving works are required, which increases the production cost. Therefore, the incorporation of SiMn slag as coarse aggregate in concrete is more cost-effective as the processing work is less. There is also limited knowledge on the use of SiMn slag as coarse aggregate. Therefore, further research work is needed, especially when SiMn slag is incorporated with FA, SF, marine sand and seawater into the production of concrete.

2.3 Optimization of Concrete Mixture

An optimization method is required to determine the optimum combination of FA and SF that produces concrete with the best strength and durability. In the optimization process, the replacement levels of FA and SF are design variables. The optimization objective is to maximize the strength and minimize the permeability of concrete. The decision-making process is more complex when it includes more than one variables and multi-objective problems. Optimization tool is therefore needed in this study. The use of optimization tool can more effectively evaluate the non-linear effect of FA and SF on concrete strength and durability. Several commonly used optimization methods are therefore reviewed in order to select the most suitable methodology for optimizing the contents of FA and SF in concrete.

2.3.1. Optimization Method

The optimization process is formulated by three components, which are decision, objective and constraint. The decision refers to variables manipulated by decision-maker in order to achieve the desired output. The objective is the quantification of output and the constraint is a boundary condition that determines the validity of solution. The three components are used to develop mathematical expression for variables and outputs. Several optimization methods have been used to solve concrete mix design problems. Linear programming, statistical, machine learning and physics-based models are among the approaches used.

2.3.1.1. Linear Programming Model

Linear programming (LP) model is used to optimize the objective as a linear function of decision variable. It is suitable for solving the optimization problem with a simple equality constraint. The LP model makes use of various mathematical techniques such as linear algebra, multivariable calculus, numerical analysis and computational mathematics (Arsham, 2011). It is ideal for optimizing the objective related to maximizing and minimizing linear variable, especially when resource is scarce. An example of LP model is the optimization of the ingredient cost in concrete. Yeh (2007) optimized the cost of OPC, FA, slag, water, SP, coarse and fine aggregates in concrete, while setting the strength, workability and ingredient content as constraints. Ahmad (2007) also adopted LP model to determine the minimum cost of concrete mixture by varying the contents of cement and aggregate. The LP model is simple and most frequently used for cost optimization which is essentially a linear relationship. Nevertheless, most of the optimization problems in concrete are non-linear. Therefore, the LP model is not suitable for modeling the non-linear relationship of concrete properties such as the strength and durability.

2.3.1.2. Statistical Model

Statistical model is another optimization approach that correlates decision variable with objective using mathematical equation. The statistical model is used when data on decision variable is available, but the mathematical relationship is not known. In statistical modelling, the data is analyzed using probability function (Kuhn and Johnson, 2013). The mathematical relationship equation is determined by maximizing the probability function and minimizing the norm of residuals. The developed equation can predict the outcome based on decision variable, which is useful for optimization. For a simple relationship, the equation can be linear. The statistical model also reflects a more complex and non-linear relationship in the form of quadratic and higher-order polynomial equations. The accuracy of optimization improves with the increased polynomial order.

The statistical model has been used by researchers to evaluate concrete property. Nehdi and Summer (2002) used factorial experiment to optimize the contents of FA and SF in ternary blended concrete. However, the analysis was not conclusive due to a limited number of experiment performed over a wide range of replacement levels of FA and SF. Muthukumar et al. (2003) optimized silica aggregates in polymer concrete using the Box-Behnken design method. A total of 54 concrete mixtures of various variable combinations were used. The developed statistical model had a high correlation coefficient of 0.96 was fit for optimization.

In short, the statistical model is suitable for optimizing the objective related to strength and durability of concrete, which is a complex relationship, as the data can be obtained from the experiment.

2.3.1.3. Machine Learning Model

Machine learning (ML) model is a set of algorithms with learning capability that can be trained to evaluate the relationship of data. The ML model learns from a collection of training data and predicts the outcome. Explicit equation such as polynomial equation is not required to describe a complex relationship. The ML model has been explained in detail by DeRousseau et al. (2018).

Several studies have been carried out to use the ML model for the optimization of concrete mixture. Siddique et al. (2011) used the Artificial Neural Network (ANN) method to model non-linear relationship between variables such as cement content, FA content, bottom ash content, W/B ratio and SP dosage, and compressive strength. In the study, data from the published literature was used to develop the ANN model. The developed model was used to predict experimental result with a good correlation coefficient of 0.9. Erdal (2013) optimized the compressive strength of high performance concrete by using the Decision Tree (DT) method. The variables included contents of OPC, FA, slag, water, SP, coarse aggregate and fine aggregate. The DT model had well predicted the compressive strength with R^2 values between 0.937 and 0.952.

In summary, the ML model is a better option if the performance of statistical model is not adequate to describe the complex relationship. But, the ML model requires a great deal of experimental data for model development and is also more computationally expensive.

2.3.1.4. Physics-based Model

Physics-based model is a mechanistic optimization method that uses the underlying physics principle to establish the relationship between decision variable and objective. The physics-based model is more efficient when the relationship of variable and objective can be interpreted based on physics theory. Roshavelov (2005) used particle packing model to optimize the effect of binder content, W/B ratio, coarse-to-fine aggregate ratio and aggregate particle distribution on the rheological property of concrete. The study used the principle of aggregate packing to correlate rheological property with aggregate particle size distribution. Chidiac and Mahmoodzadeh (2009) optimized the fresh property of concrete by establishing its relationship with plastic viscosity and yield stress. The physics-based model is not commonly used to optimize concrete property as the available mechanistic model for concrete mix design is limited.

2.3.1.5. Selection of Optimization Tool

The LP model is not applicable to the optimization related to concrete strength and durability as their relationship to the contents of FA and SF is non-linear. The ML model can solve problem of complex relationship, but requires more data and is too computationally expensive for optimization process. The physics-based model is not appropriate for the optimization of concrete mix design, as there is limited mechanistic approach for describing concrete properties such as strength and durability. Based on the literature review, the statistical model, which can describe non-linear relationship between variable and objective, is ideal for optimizing the replacement levels of FA and SF in concrete.

2.3.2. Response Surface Method

Response Surface Method (RSM) is a statistical model used to construct the mathematical equation describing multiple responses over a number of variables (Whitcomb and Anderson, 2004). The RSM establishes a polynomial relationship between the responses and the variables, including their influence and significance to the model. The established relationship can be used to predict and optimize the response. The development of RSM model requires the collection of experimental data. An appropriate polynomial equation is subsequently developed based on the data. The equation that has high fitness and low residual value is fit for prediction and optimization of response.

The RSM has been used in numerous studies to model concrete property based on various variables. Sonebi (2004) used RSM to examine the effect of cement content (60–216 kg/m^3), FA content (183–317 kg/m^3), W/B ratio (0.38–0.72) and SP dosage (0%–1%) on eleven fresh properties and compressive strength of concrete. The relationships between the responses and variables were analyzed using polynomial regression. The FA content was found as the primary factor influencing the concrete fresh properties and strength. Lotfy et al. (2014) used RSM to derive statistical models for eight fresh properties and four hardened properties of concrete based on three parameters, which were binder content (410–550 kg/m^3), W/B ratio (0.3–0.4) and SP dosage (0.3%–1.2%). The models were fit for optimization of concrete properties that met three classes of self-compacting concrete requirements, including standard condition, pumping application and congested situation. Bayramov et al. (2004) optimized the ductile behavior of steel fiber reinforced concrete using the three-level factorial RSM. The variables were volume fraction (0.26%, 0.45%, and 0.64%) and aspect ratio (55, 65, and 80) of fiber. Based on the statistical modelling on cost and ductility, the optimum content was 0.558% for the volume fraction and 75.87 for the aspect ratio.

Kockal and Ozturan (2011) investigated the effect of sintering parameters on the specific gravity, water absorption and crushing strength of FA aggregate by using the RSM based on historical data. The parameters included sintering temperature (1100–1200 ^{o}C), binder type (bentonite, glass powder) and binder content (0%–10%). The relationship of these variables with specific gravity and water absorption was a quadratic equation, while the relationship with crushing strength was a two-factor-interaction (2FI) equation. The FA aggregate made up of 10% bentonite and 10% glass powder at temperature of 1200 °C yielded the highest desirability. Aldahdooh et al. (2013) used RSM to optimize the contents of cement (up to 1062.13 kg/m^3) and SF content (up to 268.53 kg/m^3) in ultra-high performance concrete. By maximizing compressive strength and targeting a workable flow, the optimum content was 720.49 kg/m^3 for cement and 214.25 kg/m^3 for SF.

Study has also been performed to use RSM for optimizing the replacement level of supplementary cementitious material in ternary blended concrete. Guneyisi et al. (2014) used the RSM to optimize replacement levels of metakaolin (MK) (0%–10%) and FA (0%–20%) in high performance concrete. The optimum combination of MK and FA was 13% and 10% respectively in terms of strength and durability. Rezaifar et al. (2016) optimized the substitution of crumb rubber (CR) (4.39%–25.6%) for fine aggregate and MK (2.92%–17.07%) for cement in hybrid blended concrete. The mixture containing 3.3% of CR and 19.5% of MK achieved the lowest water absorption. The developed statistical model was experimentally validated to have an error below 10%.

2.3.3. Summary

The statistical model is ideal for optimizing the replacement levels of FA and SF as ternary blended cement in this study. The relationship of FA and SF contents with concrete strength and durability is non-linear. Using the statistical model, the relationship between variable and objective can be expressed as polynomial equation that is suitable for optimization purpose. Response Surface Method (RSM) is a statistical model suitable for experimental design, mathematical formulation and optimization. From the literature review, there is limited research on the use of RMS in the optimization of replacement levels of ternary blended cement, in particular FA and SF. Further study to expand the knowledge in this research field is therefore warranted.

2.4 Concrete Deterioration in Marine Environment

The adverse effect of hostile marine environment on concrete structure has inevitably resulted in huge economic loss and, in extreme case, may contribute to catastrophic failure. Concrete is susceptible to weathering, particularly under wetting-drying action

(WDA), although its current state of the art is quite well established. The diverse characteristics of WDA at different site locations have compromised the reliability of laboratory works. The objective of this section is to review the impact of WDA on concrete and to provide an overview of the research trend, aiming to identify the research gap. Concrete deterioration mechanisms in marine environment in respect of WDA are identified. The influential factors of WDA are analyzed. The physical and mechanical properties of concrete exposed to WDA are discussed.

2.4.1. Concrete Deterioration Mechanism

Concrete performance deteriorates in aggressive marine environment and WDA can further aggravate it. The deterioration can be due to chemical and physical mechanisms. The following further elaborates the chemical and physical deterioration mechanisms of concrete in combination with the WDA.

2.4.1.1. Chemical Deterioration

2.4.1.1.1. Chloride Attack

Chloride from seawater causes corrosion of steel in reinforced concrete. In alkaline environment of concrete, the surface of steel is surrounded by a thin passive oxide film which stabilizes the metal and prevents ionization. If the concentration of invading chloride reaches a threshold level, it reacts with and destroys the oxide film, exposing the steel to oxygen and water to cause corrosion (Khan et al., 2017). The deterioration process commences with localized corrosion and formation of rust. It causes approximately 2 to 6 times volume expansion of steel to exert stress which causes concrete cracking and performance loss as illustrated in Figure 1.1(b) (Apostolopoulos et al., 2019). Both bound and free chlorides exist in concrete. Bound chloride is immobilized in alkaline environment and is not deleterious to steel, while free chloride penetrates into concrete to cause corrosion.

The WDA increases the rate of chloride attack on concrete. Significant increment of chloride concentration can be found at the concrete surface after long-term exposure to WDA (Qi et al., 2018). The increased chloride concentration on concrete surface results in expansion of convection zone which is also referred to the depth of maximum chloride concentration. This zone is equivalent to loss of concrete cover for steel protection. Table 2.6 compares the convection zones of concrete under WDA and full immersion exposures which have been determined by researchers. Full immersion refers to the test conducted in fully immersed environment without being subjected to drying phase. The result shows comparatively deeper convection zone for concrete under WDA exposure than the fully immersed condition. The intrusion rate of chloride is increased by WDA through the following mechanisms: (i) chloride penetrates into concrete by sorption during initial wetting stage, (ii) water evaporates during drying stage while chloride only permeates by means of diffusion, and (iii) chloride further accumulates and penetrates through capillary suction during the subsequent wetting stage. The alternating WDA has consequently induced a steep concentration gradient which amplifies the diffusion rate.

Table 2.6: Convection zone for chloride intrusion into concrete

Literature	Convection zone (WDA exposure)	Convection zone (full immersion)*
Chrisp et al. (2002)	25–30 mm	N.D.
Simcic et al. (2015)	4–8 mm	N.D.
Ye et al. (2016a)	5–12 mm	N.D.
Wu et al. (2016)	10–15 mm	5–10 mm
Paul et al. (2016)	10–15 mm	0–5 mm
Qi et al. (2018)	2.5–7.5 mm	N.D.
Wang et al. (2018a)	2–6 mm	N.D.
*Concrete was fully immersed throughout testing period without being subjected to drying phase. N.D. – Not determined in the study		

2.4.1.1.2. Sulphate attack

Sulphate is another element of seawater which brings about durability problem to concrete. It reacts with calcium aluminate hydrate (C-A-H) and $Ca(OH)_2$ to form ettringite and gypsum which are expansive (Roziere et al., 2009). Figure 2.4(a) quantifies the reaction of sulphate attack. The ettringite and gypsum increase with duration of WDA, while the portlandite decreases. The accumulation of ettringite and gypsum exerts stress on concrete pore, causing it to crack and disintegrate as illustrated in Figure 1.1(c). The dissolution of $Ca(OH)_2$ and C-A-H also leads to loss of concrete strength. It can reduce concrete alkalinity and thereby reduces the corrosion resistance of steel. Concrete experiences more severe deterioration in the presence of magnesium sulphate (Jiang and Niu, 2016). Cation-exchange reaction can occur, by which magnesium (Mg) ion replaces Ca ion from C-S-H to form magnesium silicate hydrate (M-S-H). M-S-H does not provides cementation which results in further strength loss (Cheng et al., 2020a).

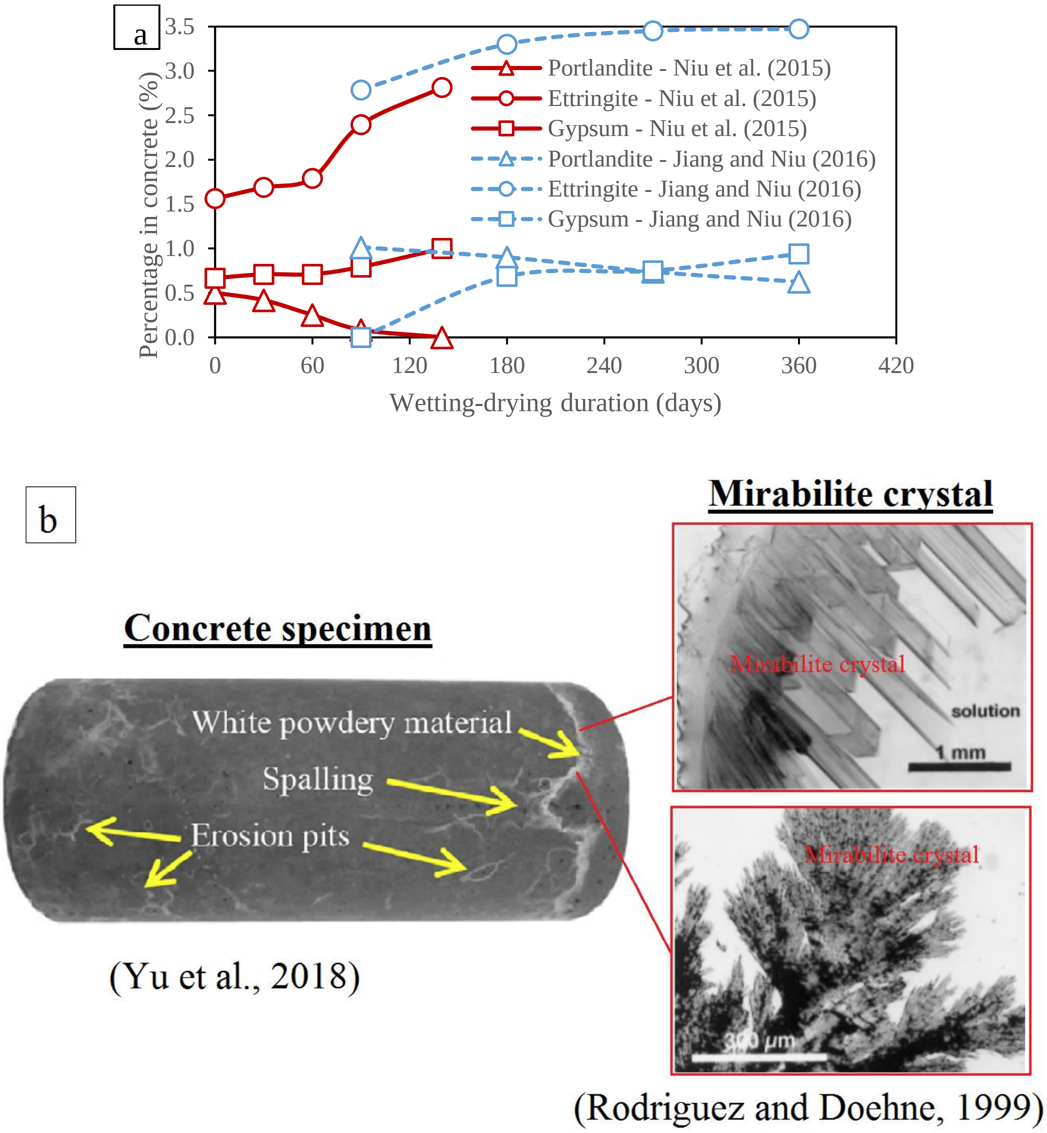

(Yu et al., 2018)

(Rodriguez and Doehne, 1999)

Figure 2.4: (a) Relative composition of ettringite, gypsum and portlandite in concrete (Jiang and Niu, 2016; Niu et al., 2015), (b) Mirabilite crystal (Rodriguez and Doehne, 1999; Yu et al., 2018)

The WDA intensifies the sulphate attack on concrete deterioration. It increases the rate of capillary absorption and diffusion which facilitates sulphate penetration. The drying stage from WDA also causes concrete shrinkage and then micro-cracking. However, Wu et al. (2017) and Yu et al. (2018) claimed that the subsequent wetting stage could partially heal the cracks. Once re-wetted, the damaged C-S-H absorbs water, and swells to close the cracks. The crystallization of sulphate-based salt due to WDA also causes concrete damage. The precipitated salts exist in the form of thenardite and mirabilite crystals as shown in Figure 2.4(b) (Zhongya et al., 2019). These crystals are usually needle-shaped and expansive which exert stress in the confined concrete pores (Jiang and Niu, 2016) as shown in Figure 2.4(b).

The deterioration caused by sulphate attack exhibits in two stages which are enhancing and weakening stages. The findings have been confirmed in the separate studies carried out by Gao et al. (2013), Zhang et al. (2017) and Yu et al. (2018). The enhancing stage is attributed to the filling of concrete pores by ettringite and gypsum which improves the mechanical properties. The weakening stage is caused by expansion of ettringite and gypsum which induces concrete damage. Some studies, however, describe the sulphate attack as three stages of deterioration mechanism. A damaging stage which occurred prior to the enhancing stage was noted by Qi et al. (2017). The damaging stage was due to negative impact of WDA such as shrinkage cracking caused by repeated drying. After weakening stage, Mullauer et al. (2013) found that in the third stage, concrete would not undergo further deterioration. This was ascribed to exhaustion of reactants for formation of expansive products. Zhongya et al. (2019) discovered an incubation stage in between the enhancing and weakening stages under WDA in the actual environment. The stress generated by gradual formation of expansive products within this period was not sufficient to cause deterioration. This indicated that the accelerated laboratory test could alter the deterioration process.

2.4.1.1.3. Carbonation

In humid marine environment, moisture absorbed by concrete contains dissolved carbon dioxide (CO_2) which initiates carbonation. CO_2 is highly reactive with calcium elements such as $Ca(OH)_2$ and C-S-H in hydrated cementitious matrix. The chemical reaction of carbonation is presented as Eq. 2.5 and Eq. 2.6 (Samimi et al., 2018). The products of these two reactions are calcium carbonate. This leads to dissolution of portlandite and depletion of bonding medium, resulting in instability of anhydrous phase of cement paste (Chang and Chen, 2006). The alkalinity of concrete gradually decreases with the reduction of hydroxide concentration which destroys the passivity of embedded steel, leading to corrosion.

$$Ca(OH)_2 + CO_2 + H_2O) \rightarrow CaCO_3 + 2H_2O \qquad \text{Eq. 2.5}$$

$$\text{C-S-H} + 2CO_2 \rightarrow SiO_2 + 2CaCO_3 + H_2O \qquad \text{Eq. 2.6}$$

Research shows that the WDA intensifies deteriorating effect of concrete carbonation. Jerman et al. (2019) found that WDA caused microstructure of cementitious matrix to become coarser which speeded up intrusion of CO_2. Chang et al. (2018) showed that the accelerated capillary suction induced by WDA and the direct penetration of CO_2 into concrete during drying period caused more severe carbonation. Ye et al. (2016b) discovered that the carbonation was speeded up in chloride environment. However, Kuosa et al. (2014) demonstrated that the presence of chloride could retard concrete carbonation. The hygroscopic characteristic of chloride created water film to block concrete pores. Salt crystallization caused by WDA also filled up concrete pore and slowed down carbonation.

Carbonation can alter concrete property and negatively affect deterioration from chloride attack (Chang, 2017). Carbonation reduces chloride binding capacity of concrete which converts bound chloride to free chloride and accelerates steel corrosion. The bound chloride, existed as Friedel's salt in concrete, is decomposed during carbonation and is prevented from formation. This is due to the reduction of pH which gradually alters the surface charge of C-S-H and reduces its ability to bind chloride (Saillio et al., 2014). The carbonation also widens the chloride convection zone as shown in Figure 2.5. Ye et al. (2016b) found pronounced increment in the depth of chloride convection zone in concrete after being carbonated. Chang et al. (2018) demonstrated that under accelerated carbonation, the location of chloride maximum progressed deeper into concrete. Within the carbonated zone, concrete pores are refined which reduces chloride intrusion, but this tends to accumulate chloride at the carbonation front. The bound chloride is also decomposed into free chloride. This consequently leads to high concentration gradient and hastens chloride diffusion.

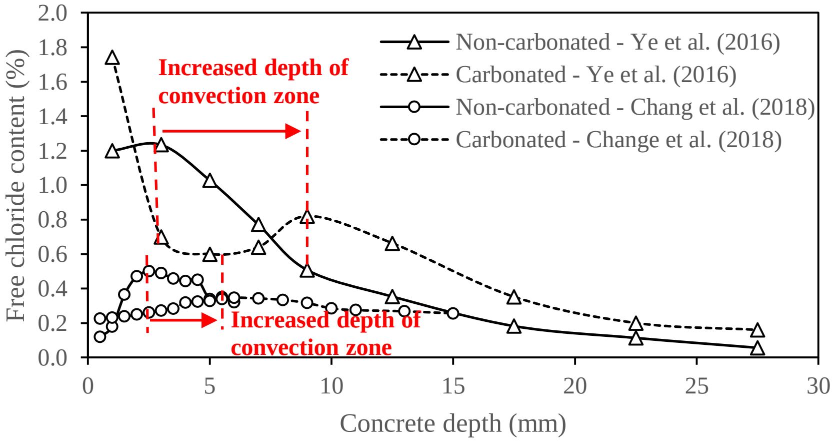

Figure 2.5: Chloride ingress profile before and after carbonation (Chang et al., 2018; Ye et al., 2016b)

2.4.1.2. Physical Deterioration

2.4.1.2.1. Salt crystallization

In the absence of chemical interaction, salt crystallization occurs in saline environment and physically damages concrete. The damage is caused by internal stress arising from the formation of salt crystals in concrete pores when the pore solution becomes supersaturated (Thaulow and Sahu, 2004). Salt crystallization happens in two circumstances which are evaporation of pore solution with the capillary rise and WDA (Nadelman and Kurtis, 2019). A schematic illustration of the first mechanism is shown in Figure 2.6. Concrete in the close vicinity of salt source becomes saturated as the moisture is transferred through capillary suction. Concrete surface becomes drier when the surface is further away from the source as a result of evaporation. The concentration of pore solution increases and salt begins to precipitate after reaching the saturation point. Alternating cycles of WDA, on the other hand, causes repetitive exchange of pore solution and accumulates salt solution in concrete whereby crystallization takes place after saturation point. The salt precipitated on concrete surface is termed as efflorescence, while that formed within concrete pore is subflorescence which is the cause of concrete distress (Lee and Kurtis, 2017). Concrete is damaged through bulging when the pressure exerted by subflorescence exceeds tensile strength.

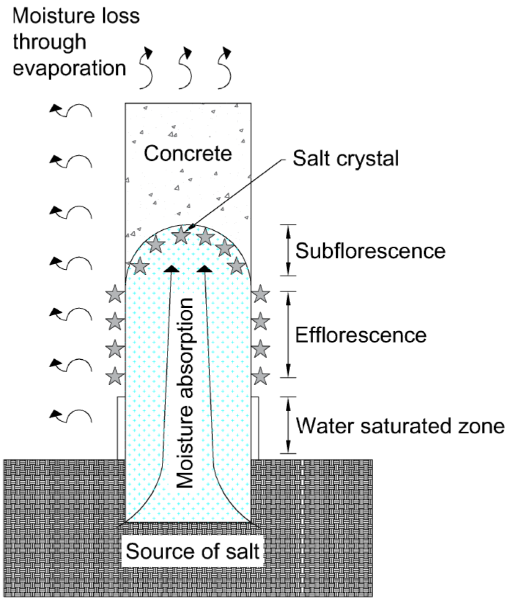

Figure 2.6: Salt crystallization by capillary rise and evaporation (Lee and Kurtis, 2017; Nadelman and Kurtis, 2019)

Saline environments such as salt-bearing soil, saline groundwater and seawater mainly contains chloride and sulphate salts. The damage by sulphate salt is more severe than chloride salt and it is receiving greater attention. Nadelman and Kurtis (2019) noticed the formation of micro-cracks and layers of efflorescence on mortar surface which were caused by crystallization of sulphate salt. Steiger and Asmussen (2008) found that sodium sulphate crystallized to form thenardite and mirabilite which caused damage to concrete. The phase conversion between thenardite and mirabilite could also result in concrete scaling (Haynes et al., 2008).

Some studies, on the contrary, shows that other types of salt cause more severe deterioration of concrete. Gentilini et al. (2012) found more significant destruction of specimen by chloride salt, while the sulphate salt appeared to provide stiffening effect. This was due to the chemical reaction of sulphate with cement hydrate, forming ettringite and gypsum, which strengthened concrete by filling up pores. Lee and Kurtis (2017) discovered that the damage of mortar caused by nitrate salt is more severe than sulphate salt. The samples exposed to sulphate salt were not damage, although heavy efflorescence was observed. This could be due to insufficient exposure duration to the salt. The result discrepancy could also be due to different source of salt used which exhibits different phase-transition characteristic with distinct crystallization behavior (Haynes et al., 2010).

2.4.1.2.2. Freezing-thawing action

Freezing-thawing action (FTA) is a physical concrete deterioration mechanism occurs in wet and cold climate. Its occurrence is caused by crystallization of solvent inside capillary cavity of concrete. Liquid in pore at freezing temperature transforms to ice and expands to exert pressure on concrete. The damage depends on concrete pore characteristics such as size, volume and continuity. FTA is less destructive if the concrete possesses adequate pores which are interconnected and big enough to provide room for uniform expansion and thus less stress in concrete (Cai and Liu, 1998). Otherwise, internal cracking and spalling of concrete can occur, resulting in loss of mechanical properties and even further intrusion of deleterious substances (Wang et al., 2014).

Salt-containing seawater can alter deterioration mechanism of FTA on concrete. Miao et al. (2002) found more damage was experienced by concrete exposed to FTA with sulphate solution. Sun et al. (2002) found the damage caused by FTA with chloride solution was twice than that with water. The differential thermal expansion of salt solution and cementitious matrix causes superficial spalling of concrete (Wang et al., 2014). Chemical deterioration of concrete, such as sulphate attack, can also take place which is in synergy with FTA. However, Jiang et al. (2015) discovered that FTA with salt solution caused less damage than that with fresh water. The salt lowered freezing point of pore solution which made the damage less severe.

In actual environment, concrete experiences FTA during winter and WDA during rest of the year. Hamze (2014) found that the combined FTA and WDA had significant effect on causing micro-cracks. Liu et al. (2018) demonstrated that the combined FTA, sulphate attack and carbonation caused more severe damage to concrete with increased pore degradation. Nevertheless, the study related to combined effect of WDA and FTA is still limited and indeed required investigation.

2.4.1.2.3. Erosion by wave action

Wave action can also cause physical concrete damages such as wear and tear. Wave often carries debris such as silt, sand, gravel, rock and ice. It can cause two types of action which are hydrodynamic force and abrasion by water-borne debris (Dandapat and Deb, 2016). The latter action causes more damage to concrete (Kryzanowski et al., 2009). The erosion of concrete due to abrasion occurs in three stages. During initial stage, concrete is subjected to weak pre-abrasion by hydraulic pressure of flowing water, whereby concrete surface is slightly stripped off. Drifting water-borne debris follows on to exert prising force which generates more drastic damage such as superficial cracking. Combination of both actions abrades and scours off the mortar layer, disintegrating coarse aggregate and interfacial transition surface. Cavitation force from implosion of air bubble during wave striking can also induce destructive wearing damage on concrete (Horszczaruk, 2005). Concrete consequently loses mechanical strength and shield against corrosion.

Research in this domain has made assessment on hydraulic structures subjected to abrasion. Abrasion resistance is often related to the strength of concrete. Kryzanowski et al. (2009) used compressive strength, tensile strength, elastic modulus and aggregate strength to assess abrasion resistance of concrete. Horszczaruk (2005) demonstrated that concrete compressive strength could accurately estimate the abrasion resistance.

Liu et al. (2006) found that splitting tensile strength was more effective in predicting abrasion. The abrasion resistance of concrete also depends on other factors. Dandapat and Deb (2016) showed that concrete made from coarse aggregates having larger size, less angularity and flakiness exhibited stronger abrasion resistance. Cai et al. (2016) discovered that wave abrasion force increased when impinging angle increased from 0 to 90^o as this caused greater concrete deformation. Higher impinging velocity of wave could further aggravate the damage. The degradation of concrete can occur together with other types of mechanism. Rosenqvist et al. (2017) showed that both leaching and FTA could cause superficial concrete damage and debilitate the abrasion resistance.

2.4.1.3. Summary of Concrete Deterioration Mechanism

Mass concrete (MC) is prone to deterioration only if the mechanisms, such as sulphate attack, salt crystallization, FTA and erosion, causes loss of mechanical properties. The main concern for reinforced concrete (RC) is corrosion of steel bar whereby carbonation and chloride attack come into play. However, other deterioration mechanisms that are critical to MC also have an impact on providing means for intrusion of chloride and carbon dioxide. The deleterious compounds, which include chloride, sulphate and carbon dioxide, enter the concrete through capillary pore to actuate deterioration. The intrusion of these compounds can be minimized by reducing size, number and continuity of pore. The damage caused by physical deterioration can be mitigated by improving the concrete mechanical properties, especially the tensile strength, which prevents disintegration of concrete. The WDA has great influence on the deterioration mechanisms of concrete. It increases intrusion rate of deleterious compounds into concrete which escalates the deterioration processes. Research concentrates on a single deterioration mechanism. In actual weathering scenario, however, there is occurrence of synergy between two or more mechanisms. It is recommended to study synergetic effect of various combinations, especially the combination of chemical and physical deteriorations.

2.4.2. Influential Factor of WDA

The characteristics of WDA have bearing on the intrusion of deleterious compounds into concrete. The characteristics vary with site location, climate and exposure conditions. Researchers have reproduced the characteristics in laboratory with the aim to study the influences of WDA on concrete performance. Accelerated test is also used to shorten the study period. This can lead to inaccurate prediction if irrelevant method is used. The influential factors of WDA are reviewed based on the experiments performed by various researchers.

2.4.2.1. Phenomenon of Wetting and Drying

The alternating wetting and drying of marine concrete is caused by tidal phenomenon. The characteristics of tide, particularly tidal cycle and tidal range, has great influence on WDA behavior. Tidal phenomenon can be classified into three types which are diurnal, semidiurnal and mixed tides. Diurnal tide exhibits one cycle of low and high tides per day, while semidiurnal tide displays two cycles per day (NOAA, 2019). Mixed tide is the case of semidiurnal tide having different amplitude of crest and trough. The tidal range can vary from near 0 to 12 m (Trenhaile, 2011). Considering the effects of tidal cycle and range, wetting and drying periods can vary in different tidal situations.

Researchers adopted various wetting and drying periods in their laboratory tests to simulate WDA at the field as shown in Table 2.7. Wu et al. (2016) conducted wetting-drying test by following the tidal conditions of Bohai Sea, East Sea and Yellow Sea in China, in which concrete was exposed to 8 hours of both wetting and drying for one tidal cycle. Yu et al. (2018) used wetting-drying period from Chinese Standard: GB/T 50082-2009 (Standard, 2009) which adopted 16 hours of wetting, 2 hours of room temperature drying and 6 hours of oven drying at 60 ^{o}C. Niu et al. (2015) also used the same laboratory condition for simulating deterioration of shotcrete in a tunnel construction site of Western China. This exposure condition has included an oven drying period which is used to boost water evaporation and shorten test duration. Backus et al. (2013) used period of 1-day wetting and 6-day drying which they claimed this scenario as splash zone. Zhongya et al. (2019) adopted a regime of 8-day wetting and 7-day drying and compared with continuous immersion and actual wetting-drying environment of Chongqing, China. The study showed that the adopted conditions for laboratory test could shorten test period, but slightly change the actual degradation process.

2.4.2.2. Ion Type and Concentration

Concrete deterioration by WDA is also influenced by compositions of seawater especially chloride and sulphate, and their concentrations. Chloride and sulphate contents vary with salinity of seawater. Salinity is the total amount of non-carbonate salts which exist in combination with sodium, potassium and magnesium ions (Effler et al., 1986). The seawater has an average salinity of 3.5% and the salt exists mostly as sodium chloride (Lehigh, 2011). Researchers thus use this concentration of chloride solution in their studies as shown in Table 2.7. The commonly used sulphate concentration is 5%. It is assumed that this concentration can result in noticeable damage to concrete and is suitable for laboratory test. The ASTM C1012 (2018) standard also recommends this concentration of sulphate solution for testing. Some studies also increase ion concentration to perform accelerated test. The chloride and sulphate concentrations have been increased up to 10% and 15% respectively. Yuan et al. (2016) showed the test duration was reduced by a factor of two if sulphate concentration at saturation point had been used. Different types of sulphate also cause different extent of concrete degradation. Jiang and Niu (2016) and Cheng et al. (2020b) demonstrated that concrete damage by $MgSO_4$ solution was more severe than Na_2SO_4 solution. An additional deterioration caused by cation-exchange reaction which replaced Ca ion in C-S-H with Mg ion, resulting in strength loss of concrete.

Researchers also use a composite solution containing chloride and sulphate salts as occurred in seawater. Jiang and Niu (2016) used composite solution of 10% Na_2SO_4 and 3.5% NaCl which reduced concrete deterioration. The presence of chloride reduced diffusion of sulphate as the Friedel’s salt was formed from chloride to fill up pores in concrete which delayed sulphate attack. Cheng et al. (2020b) also found reduced chloride intrusion with the co-existence of sulphate. The intruded chloride amount could be further reduced if the sulphate concentration increased (Chen et al., 2016). The modification of charge-equilibrium and mass-equilibrium status of ions in composite solution reduced the activity of chloride ion. The formation of ettringite by sulphate also refined and densified concrete pores, limiting penetration of chloride. The findings show that the concrete deterioration by composite solution, which better represent the actual situation, is lower than that with a single salt.

2.4.2.3. Temperature in Drying Stage

Concrete gradually loses its moisture through water evaporation in drying stage of WDA. As the ambient temperature increases, the relative humidity decreases which induces faster drying of concrete. The continual sun exposure raises concrete temperature up to 30–50 ^{o}C (Guan, 2011; Tan et al., 2014). Researchers also include an oven drying stage in their experiments to consider this effect. The temperature used can range from 45 to 80 ^{o}C as shown in Table 2.7. Higher temperature is used to increase water evaporation rate which substantially reduces test period.

Some studies, however, indicate that the elevated temperature can lead to negative consequences. It causes concrete shrinkage and then micro-cracking which affects intrusion behaviors and test result (Yu et al., 2018). The elevated concrete temperature also induces greater moisture transfer and increases chloride content and penetration depth (Oh and Jang, 2007). Farahani et al. (2015) discovered that chloride diffusion rate increased by two times when temperature was raised from 28.5 to 34.5 ^{o}C. The increased temperature provided more energy for chloride diffusion. Alhozaimy et al. (2012) found that steel corrosion became more severe when temperature was increased from 30 to 40 ^{o}C, but decreased corrosion for the temperature range of 40 to 50 ^{o}C. The increased corrosion was due to catalytic effect provided by higher temperature for chloride to destroy steel passivity. The decreased corrosion was attributed to the lower oxygen solubility and the increased concrete pore discontinuity at this high temperature. Thus, postulation of using elevated temperature in WDA experiment remains controversial as it can alter the deterioration mechanism.

2.4.2.4. External Loading

Concrete in service is subjected to stresses such as compression and tension which can affect the WDA test results. The stresses modify concrete pore characteristics and change the intrusion behavior. The resultant strain and the induced crack allow for further penetration of deleterious components into concrete.

Studies have also incorporated the loading effect on deterioration of concrete subjected to WDA. Gao et al. (2013) found that, with flexural loading, more severe deterioration was experienced by concrete subjected to WDA. The concrete deterioration also increased with flexural stress ratio (Ye et al., 2016b). This was due to the enlarged concrete pore under tensile strain increased the ingress of corrosive compounds. The damage caused by long-term flexural loading was also more severe than the short-term loading since the former caused permanent deformation such as creep (Chen et al., 2017). Fu et al. (2016) showed that cyclic uniaxial tensile loading had caused fatigue damage to concrete which increased the chloride intrusion by a factor of three. Paul et al. (2016) stated that the cracked concrete was intruded with significantly higher chloride than non-cracked concrete. The development of micro-cracks caused by flexural and tensile stress had speeded up the intrusion of corrosive compounds.

The effect of compressive stress in WDA on concrete has also been studied. Zhang et al. (2017) pointed out that in the compression zone of concrete under flexural loading, concrete was actually strengthened. Wu et al. (2016) also observed similar scenario when concrete was compressively loaded. The compression closed the concrete pores and reduced permeability. But, the growth of salt crystal in pores could induce higher stress under compressive loading in the long term, causing greater damage to concrete (Chen et al., 2017).

2.4.2.5. Summary of Laboratory-simulated WDA Exposure Condition

The influential factors of WDA such as wetting-drying periods, ion type, ion concentration, temperature and condition of external loading have significant impact on concrete deterioration mechanisms. Table 2.7 summarizes these influential factors that are used by researchers to duplicate WDA in actual environment. The wetting period can range from 0.3 hour to 1080 hours, while the drying period at ambient temperature ranges from 0.7 hour to 1172 hours. Some studies include an oven drying period of 5 hours to 168 hours in order to accelerate the test. The oven drying temperature varies from 45 to 80 ^{o}C. As for ion type in corrosive solution, the study mainly includes NaCl, Na_2SO_4 and $MgSO_4$ and composite of them. The simulated external loadings are compression, tension and flexural bending.

The WDA tests performed by researchers have achieved the objectives of respective studies. However, the laboratory experiments have inherent limitations such as difficulties in simulating the actual site situation, shortening the test period using accelerated test and predicting the long-term concrete durability. Further research is still required to improve the experiments.

Table 2.7: Laboratory-simulated field exposure conditions of WDA on concrete

Literature	Phenomenon of wetting and drying			Ion type and concentration		Drying temperature		External loading		Site location (which WDA was duplicated)
	Wetting period (hours)	Room drying period (hours)	Oven drying period (hours)	Solution type	Concentration (%)	Room temperature (°C)	Oven temperature (°C)	Loading type	Stress ratio	
Ye et al. (2016a)	24	48	-	NaCL	5	35 ± 0.5	-	-	-	-
Chrisp et al. (2002)	48	1176	-	NaCl	5.8	22 ± 2	-	-	-	-
Simcic et al. (2015)	0.3	0.7	-	NaCl	10	20 ± 2	-	-	-	-
Wu et al. (2016)	8	8	-	NaCl	3	-	-	Compressive	0, 0.3, 0.5, 0.7	Bohai Sea, East Sea and Yellow Sea in China
Paul et al. (2016)	72	96	-	NaCl	3.5	-	-	-	-	-
Qi et al. (2018)	21	6	45	NaCl	3.5	20 ± 2	60	Flexural	0, 0.3, 0.5	-
Wang et al. (2018b)	12	12	-	NaCl	3.5	20 ± 2	-	-	-	-
Qi et al. (2017)	21	6	45	Na_2SO_4	5	20 ± 2	60	-	-	-
Tang et al. (2018)	16	2	6	Na_2SO_4	0, 5, 10	20 ± 2	80 ± 5	-	-	-
Chen et al. (2016)	21	6	45	Na_2SO_4 (Na_2SO_4 + NaCl)	5 (10 + 5), (10 + 5)	20 ± 3	60	-	-	-
Yuan et al. (2016)	16	2	8	Na_2SO_4	0, 3, 7, saturated	-	70	-	-	-
Cai et al. (2019)	12	6	6	Na_2SO_4	5	20	45	-	-	-

Table 2.7: Laboratory-simulated field exposure conditions of WDA on concrete (continued)

Jiang and Niu (2016)	168	192	-	Na_2SO_4 $MgSO_4$ ($MgSO_4$ + NaCl)	10 10 (10 + 3.5)	20 ± 3	-	-	-	-
Zhongya et al. (2019)	192	-	168	Na_2SO_4	0, 2.1, 15	-	45 ± 2	-	-	General use, Chongqing China
Zhang et al. (2019)	24	144	-	Na_2SO_4	5	20	-	-	-	-
Yu et al. (2018)	16	2	6	Na_2SO_4	0, 5	20 ± 2	80 ± 2	-	-	Standard (GB/T 50082-2009)
Niu et al. (2015)	16	2	6	Na_2SO_4	10	20 ± 2	60	-	-	Tunnel construction site in Western China
Zhang et al. (2017)	72	96	-	Na_2SO_4	5	23 ± 1	-	Flexural	0.4	-
Chen et al. (2017)	21	6	45	(Na_2SO_4 + NaCl)	(5 + 5)	20	60	Short-term flexural Long-term flexural	0, 0.35, 0.5 0.35, 0.5, 0.7	-

Table 2.7: Laboratory-simulated field exposure conditions of WDA on concrete (continued)

Cheng et al. (2020b)	18	1	5	NaCl (NaCl + $MgCl_2$) (NaCl + Na_2SO_4) (NaCl + $MgCl_2$ + Na_2SO_4)	3.3 (2.7 + 0.5) (3.3 + 0.4) (3.3 + 0.5 + 0.4), (3.2 + 0.5 + 0.4)	20 ± 2	60	-	-	-
Li et al. (2020)	720-1080	0.5	96	Na_2SO_4	0, 3, 5, 10	20 ± 2	40 ± 2	-	-	-
Gao et al. (2013)	21	6	45	Na_2SO_4	5	20 ± 3	60	Flexural	0, 0.2, 0.4, 0.6	-
Jerman et al. (2019)	48-72	48-72	-	Water	-	25	-	-	-	-
Malheiro et al. (2014)	24	144 (CO_2 environment)	-	NaCl	3.5	20	-	-	-	-
Ye et al. (2016b)	96	48, 48 (CO_2 environment), 96 (CO_2 environment)	48	NaCl	15	20 ± 5	60	Flexural	0, 0.3, 0.6	-
Backus et al. (2013)	24	144	-	NaCl	3.2	20 ± 1	-	-	-	Extreme splash zone
Chang et al. (2018)	24	144, 144 (CO_2 environment)	-	NaCl	3.5	20 ± 1	-	-	-	-

2.4.3. Physical Property of Concrete Exposed to WDA

2.4.3.1. Physical Appearance

Concrete with aesthetic exterior look is indicative of its reasonably good performance. Assessment of concrete physical appearance is beneficial in early detection of concrete deterioration and hence mitigation can be expediently provided for prior to catastrophic failure.

Researchers assess concrete deterioration through its physical appearance. Yu et al. (2018) found that mortar surface was severely damaged after being exposed to 270 days of WDA in 5% Na_2SO_4 solution. The surface was covered with white powdery efflorescence and erosion pit, which gradually led to spalling and delamination. Jiang and Niu (2016) investigated the effect of solutions respectively comprising 10% Na_2SO_4 (S1), 10% $MgSO_4$ (S2) and composite of 10% Na_2SO_4 plus 3% NaCl (S3) on concrete physical appearance. Concrete exposed to S1 experienced some surface delamination and cracks near the edges. The damage on concrete exposed to S2 was more severe, wherein the surface was peeled off, uncovering coarse aggregate. Minimal scaling of surface was observed in concrete exposed to S3. The magnesium sulphate caused more severe damage to concrete, but chloride if combined with sulphate could reduce the effect. Chen et al. (2016) also found that the concrete exposed to composite solution containing chloride was not damaged. The chloride ion was capable of delaying formation of corrosion products as discussed in Section 2.4.2.2.

Effect of FA and SF on physical appearance was studied by Zhongya et al. (2019). The concrete incorporated with FA and SF suffered more severe physical damage than normal concrete. The damages such as spalling and chipping of mortar occurred along corners and edges of concrete. Although addition of FA and SF refined concrete pore structure, salt crystals formed had indeed increased pressure in the pores and caused more damage.

2.4.3.2. Volume Expansion

Concrete swells and expands after being deteriorated in marine environment. Zhongya et al. (2019) studied the concrete expansion exposed to full immersion (E1), indoor WDA (E2) and actual WDA (E3) using Na_2SO_4 solution for 720 days. The length of concrete increased with exposure time and the highest volume expansion was found to be 1.0%, 1.6% and 1.4% for E1, E2 and E3 respectively. The WDA aggravated volume expansion of concrete. Expansion in E2 was higher than E3 because in the actual field situation, less cycles of WDA had been experienced by concrete. Yu et al. (2018) investigated the effect of four exposure conditions on the mortar expansion for 270 days which were Condition 1 (0% Na_2SO_4 with full immersion), Condition 2 (0% Na_2SO_4 with WDA), Condition 3 (5% Na_2SO_4 with full immersion) and Condition 4 (5% Na_2SO_4 with WDA). There was no noticeable volume change observed from mortar in Condition 1, while the mortar under Condition 2 experienced slight but minimal reduction of volume which was caused by shrinkage during drying. Expansions of mortar were 0.8% and 1.4% for Condition 3 and Condition 4 respectively. The WDA had pronounced effect in accelerating concrete deterioration and then increased volume expansion.

2.4.3.3. Mass Change

Mass change of concrete is also measured to determine extent of concrete deterioration caused by WDA. Chen et al. (2016) reported the concrete mass increased with a maximum gain of 1.75%. The mass gain was caused by salt crystallization and formation of ettringite and gypsum. Cheng et al. (2020b) also noticed mass gain of mortar up to 2.74%. The mass gain was caused by continuous hydration produced more C-S-H which had higher surface area and increased water imbibition up to its saturation point. Qi et al. (2017) substituted aggregate of concrete with recycled coarse aggregate. The recycled aggregate concrete (RAC) at replacement level up to 50% exhibited smaller mass gain than normal concrete, but significantly higher mass gain at higher replacement level. RAC possessed higher water absorption property whereby higher replacement level could increase mass gain. At low replacement level, RAC absorbed mixing water which in turn reduced effective w/b ratio and concrete strength increased. The concrete was less vulnerable to deterioration and hence exhibited lower mass gain.

Mass of concrete could also decrease when subjected to WDA. Tang et al. (2018) studied mass change of concrete exposed to 0%, 5% and 10% Na_2SO_4 solutions. The concrete exposed to 5% and 10% Na_2SO_4 solutions exhibited mass gain, the mass reduced in 0% solution. The mass loss was due to surface damages such as peeling and chipping of mortar layer caused by WDA. The mass gain in 5% and 10% Na_2SO_4 solution was ascribed to formation of ettringite and gypsum. Jiang and Niu (2016) noticed that concrete mass loss occurred in two stages which were steady and escalated stages. Concrete experienced constant mass loss during steady stage and after 150 days of exposure, it lost mass rapidly. Mortar layer gradually disintegrated to cause weight loss in escalated stage.

The contradiction in concrete mass change (i.e. mass gain or loss) described in the above literature is attributed to the difference in concrete mechanical properties. Higher strength concrete can resist damage caused by sulphate attack and salt crystallization, particularly the internal stress resulted from expansive products. Concrete mass increases with the accumulation of the products. Low strength concrete is more prone to the damage. The expansive products cannot be accumulated in the concrete, but can cause severe physical scaling and weight loss.

2.4.3.4. Summary of Concrete Physical Property Deterioration

The sulphate attack and salt crystallization under the influence of WDA are the main deterioration mechanisms which change the physical properties of concrete. Concrete surface is physically damaged with forming of efflorescence initially, followed by gradual delamination and peeling of mortar, which further cause detachment of coarse aggregate. This leads to cover loss and further disintegration of concrete.

Concrete can also experience volume expansion after exposing to the long-term deterioration mechanisms. Review of the literature shows this type of expansion is minimal with value in the range of 0.8–1.6%. But, the expansion of concrete volume in a restrained structure can be detrimental as it induces stress to cause concrete cracking.

Mass change of concrete caused by the deterioration mechanisms depends on its strength. Concrete with high strength experiences mass increase, but low strength concrete suffers mass loss. The change of concrete physical properties in respect of their appearance, volume and mass changes can be used as material deterioration indicators.

2.4.4. Mechanical Property of Concrete Exposed to WDA

2.4.4.1. Compressive Strength

The influence of WDA deteriorates the mechanical properties of concrete, of which the compressive strength is the most important assessment criterion used for concrete performance. The following investigates the deterioration of compressive strength associated with WDA.

Yu et al. (2018) investigated compressive strength of mortar under the influence of WDA and sulphate solution. The compressive strength increased for 150 days but decreased significantly afterward. Li et al. (2020) found that the strength reduction started after 6 months of WDA. The formation of ettringite and gypsum from sulphate solution densified microstructure initially, but their subsequent accumulation caused strength reduction. The reduction was more severe under WDA. The WDA also caused formation of salt crystals in the pores when the solution became supersaturated during drying process. Internal stress was induced, causing damage and hence loss of strength. Zhongya et al. (2019) also studied compressive strength of concrete exposed to full immersion (E1), indoor WDA (E2) and actual WDA (E3) using sulphate solution. The strength of concrete exposed to E1 increased throughout exposure period, but slightly reduced towards the end of test period. The reduction was more prominent with the use of higher sulphate concentration. Concrete with E3 exposure exhibited similar trend as E1, but the strength loss occurred earlier with higher severity. The WDA accelerated the strength loss. The concrete exposed to E2 deteriorated two times faster than that in E3 exposure. The actual WDA could be imitated in laboratory with accelerated rate in the aspect of compressive strength.

Tang et al. (2018) found that the compressive strength of concrete exposed to WDA using tap water reduced by 29% after 140 days. Although the sulphate deterioration was not involved in the test, the damage could be caused by shrinkage of concrete during drying cycles. Tap water also contained mineral by which salt crystallization had occurred to deteriorate concrete. Jiang and Niu (2016) investigated the effect of different sulfate solutions which were Na_2SO_4 (S1), $MgSO_4$ (S2) and composite of Na_2SO_4 plus NaCl (S3) on concrete compressive strength. In all cases, the strength slightly increased initially. It was followed by a constant reduction, then an accelerated reduction towards the end of test period. The strength reduced in the increasing order of S3, S1 and S2. The S3 contained chloride which delayed sulphate attack. Mg ion from S2 induced cation-exchange reaction which reduced C-S-H for bonding.

2.4.4.2. Tensile Strength

Tensile strength is an essential mechanical property to prevent cracking of concrete. It can be assessed from both splitting test and flexural test. Limited research related to this property has been done. Tang et al. (2018) investigated the effect of WDA on concrete flexural strength. The flexural strength reduced when concrete was exposed to WDA using sulphate solution. The flexural strength reduction was greater than that of compressive strength. Concrete cracking as a result of sulphate attack and salt crystallization caused more loss of concrete capacity to resist tensile stress.

2.4.4.3. Modulus of Elasticity

Relative dynamic modulus of elasticity (RDME) is also used to assess weathering of concrete subjected to WDA. It is the elasticity of concrete under dynamic loads such as longitudinal and flexural vibrations.

Jiang and Niu (2016) studied the effect of WDA on RDME of concrete exposed to sulphate solution. The RDME loss occurred in three stages which were steady-decreasing, constant and rapid-decreasing stages. The damage in first stage was caused by WDA and salt crystallization. In the second stage, concrete pores were densified by formation of ettringite and gypsum. The accumulation of these products induced stress which accelerated RDME loss in the last stage. Tang et al. (2018) determined the effect of sulphate concentration on concrete RDME. The RDME loss was higher when the sulphate concentration became higher as this produced more corrosion products. The study also showed that the RDME loss reduced with the use of coral reef sand as fine aggregate. Higher porosity of the sand had provided more space for ettringite and gypsum expansion.

Qi et al. (2017) used recycle coarse aggregate (RCA) to improve the concrete resistance against sulphate attack subjected to WDA. The incorporation of RCA at low replacement level of 30% to 50% reduced the RDME loss of concrete. The higher water absorption of RCA had reduced the effective w/b ratio of concrete and increased strength. The RDME loss increased for the replacement level higher than 50%. The high porosity of RCA overwhelmed the positive effect and reduced the mechanical strength. The study also showed that the addition of mineral admixtures such as grounded blast furnace slag (GBFS) and FA reduced concrete permeability and hence loss of RDME. Chen et al. (2016) demonstrated that the incorporation of 50% GBFS and 30% FA reduced RDME loss. The GBFS and FA improved the RDME of concrete by 15.7% and 18.7% respectively as the cementitious matrix was densified by pozzolanic reaction and secondary hydration.

Gao et al. (2013) studied the effect of long-term flexural loading on concrete subjected to sulphate attack under influence of WDA. The application of 40% ultimate flexural loading caused slight reduction of concrete RDME. Higher loading level at 60% resulted in concrete cracking which escalated the deterioration and hence further RDME loss. The incorporation of GBFS into concrete slightly improved the RDME, while FA incorporation showed better improvement. Chen et al. (2017) also found greater RDME loss at higher level of applied flexural loading. The difference of RDME between tension zone and compression zone was compared. The RDME loss in tension zone was greater than that in compression zone. The tension induced cracking to cause concrete degradation, whereas compression prevented cracking.

2.4.4.4. Summary of Concrete Mechanical Property Deterioration

Concrete mechanical properties such as compressive strength, tensile strength and elastic modulus are damaged under the influence of WDA in marine environment. The deteriorating effect is mainly caused by sulphate attack and salt crystallization. The loss of mechanical properties is also highly dependent on applied external stress. Tensile stress induces concrete cracking, while compressive stress closes concrete pore to reduce damage. The incorporation of GBFS and FA improves the mechanical properties and shields concrete against weathering.

The published literature concerning the effect of WDA on tensile strength is limited. The tensile strength is perceived to be closely related to compressive strength as concrete having high compressive strength usually possesses higher tensile strength. This leads to misconception that WDA has similar impact on tensile strength to that on compressive strength. It is recommended to further conduct research in this area since their relationship is not linear.

2.4.5. Summary

Research gaps and limitations related to concrete deterioration under the influence of WDA are identified. The research trends are recommended as follows.

1. The current research focuses on a single deterioration mechanism and also multiple mechanisms, but only between chemical types such as chloride attack and carbonation, as well as chloride attack and sulphate attack. Physical weathering of concrete can occur simultaneously to cause scaling and cracking of its surface, degrading the shielding layer and making it more susceptible to chemical deterioration. For example, salt crystallization causes significant physical and mechanical damages to concrete which can aggravate chemical deterioration such as sulphate attack.

2. The study has been carried out on the WDA in combination with external loading such as compression, tension and short-term and long-term flexural loading. However, maritime structure is susceptible to cyclic loading caused by wind loading, wave action and earthquake. It is recommended to study the cyclic behavior of concrete after it has been deteriorated by WDA.

3. Researchers have performed experiments to simulate wetting-drying environment, of which the behaviors of WDA vary differently from their respective laboratory works. Validation has not been conducted to prove the relevance and accuracy of the simulated environment. It is suggested to compare the experimental results with real-time wetting-drying phenomenon, so as to establish the relationship between laboratory and actual conditions.

4. Further investigation is recommended to study the effect of WDA on tensile strength of concrete as the research is limited in current literature.

2.5 Cyclic Loading on Concrete

Apart from material degradation, the maritime structure is also subjected to damage caused by cyclic loading such as wind and wave actions. Cyclic loading is a series of load repetitions that can be constant or varying in loading magnitude and frequency. Although the applied load is lower than compressive strength, concrete exposed to cyclic loading can still experience a progressive material damage. The damage includes cracking and stiffness reduction of concrete, which can ultimately lead to fatigue failure (Lee and Barr, 2004). Concrete resistance to fatigue damage can be further aggravated by the maritime deterioration mechanism. Consideration of cyclic loading on concrete is also an important aspect of the study of concrete performance in marine environment. In this context, past research work on the fatigue behavior of concrete is reviewed in the following section.

2.5.1. Fatigue Behavior of Concrete

Concrete fatigue is a process of progressive change in the internal material structure that leads to permanent damage when continual cyclic loading is applied. The fatigue of concrete is associated with the development of micro-crack and the increase in irreversible strain. At macro level, this deteriorates mechanical property of concrete that leads to a fracture when the accumulated damage exceeds the fatigue strength (Xiao et al., 2013). Concrete can fail due to fatigue when subjected to cyclic loading, even if the applied load is lower than the compressive strength. Concrete fatigue strength is defined as stress limit that concrete can endure for a given number of cycles before failure. The fatigue strength of concrete in the structural design is limited to 60% of the compressive strength (Jiang et al., 2017a).

2.5.1.1. Type of Cyclic Loading

Cyclic loading is categorized into two types, which are low-cycle and high-cycle loadings. Low-cycle loading is the situation when fewer loading cycles are applied, but with higher stress. ACI 215R-74 (1997) specifies the low-cycle fatigue as concrete failure within 100 cycles of load applied. The failure is usually caused by high stress loading such as earthquake. On the other hand, high-cycle loading is a loading condition with a high number of cycles at a low stress level. High-cycle fatigue is caused by traffic load and wind action. The failure typically occurs after subjected to 10^2 to 10^7 cycles of loading (Lee and Barr, 2004). In the case of low-cycle loading, the failure mechanism of concrete is governed by mortar cracking that subsequently leads to more severe macro-cracks in the concrete matrix (Hsu, 1984). As for the high-cycle loading, failure is manifested as progressive development of cracking between the bonding of composites in concrete.

2.5.1.2. Cyclic Loading Test of Concrete

Concrete cyclic loading test is generally conducted for various loading arrangements such as compression, tension and bending. The commonly used fatigue test is the flexural test due to simple set-up and popular application (Boulekbache et al., 2016; Fischer and Li, 2002). The compression fatigue test is also widely used (Jiang et al., 2017a; Xiao et al., 2013). Comparatively less research has been done on the tension fatigue test due to the difficulty in setting up the test (Fu et al., 2016). Research also covers the fatigue test of concrete subjected to biaxial loading, lateral loading and non-proportional loading (Wang and Song, 2011). ACI 215R-74 (1997) provides guideline on fatigue capacity of concrete in the event that experiment cannot be performed. The standard defines the fatigue capacity of concrete subjected to compression, tension and flexure at 55% of compressive strength as 10^7 loading cycles.

2.5.1.3. Fatigue Life of Concrete

The fatigue life of concrete is assessed by using the fatigue (S-N) curve, also known as the Wholer curve. An example of S-N curve for concrete is shown in Figure 2.7. The variation of fatigue behavior in concrete is greater than that in ferrous material due to the heterogeneous property exhibited by concrete. Statistical and probabilistic methods are therefore ideal for the interpretation of fatigue test results. Using the repeated test results, the relationship can be established between the probability of failure and the number of cycle for a given loading condition. The curves b, c and d in Figure 2.7 represent 80%, 50% and 5% probability of failure for loading on concrete at a lower-to-upper loading stress ratio of 0.15, respectively. The S-N curve shows the effect of upper loading stress on the number of cycles resulting in fatigue failure. Meanwhile, the effect of lower loading stress can be evaluated using the constant life diagrams such as Goodman curve and Smith curve (Lee and Barr, 2004). The curves graphically illustrate the concrete fatigue affected by the corresponding loading parameters.

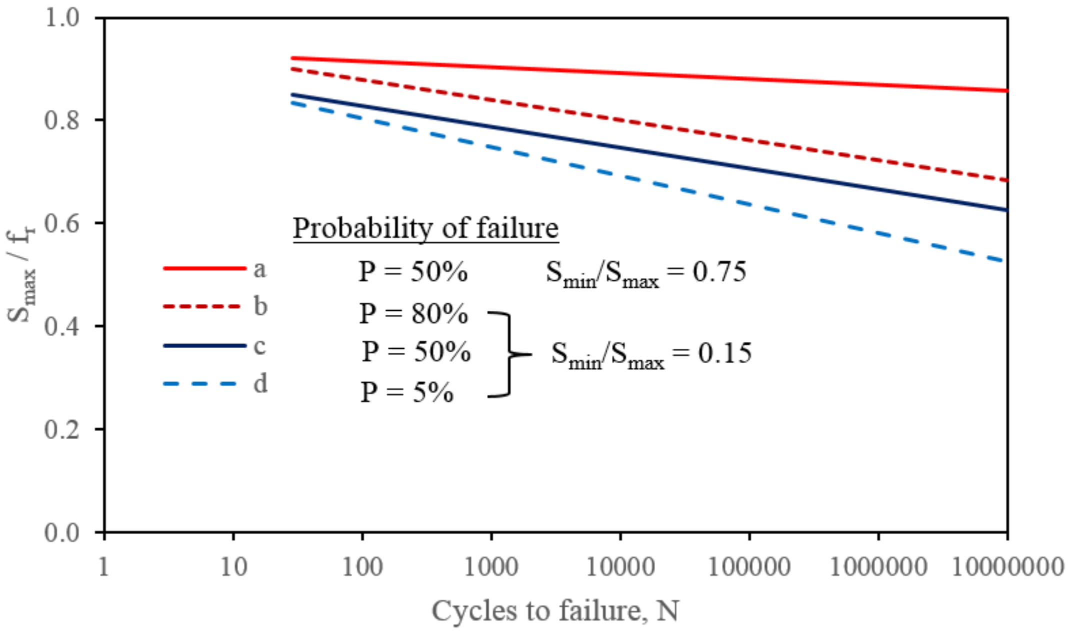

Figure 2.7: Typical S-N curve of concrete (ACI 215R-74, 1997)

2.5.1.4. Fatigue Failure Mechanism of Concrete

Concrete is a composite material that exhibits heterogeneous property. It is flawed with void, micro-crack and impurity. In such a situation, failure mechanism of concrete due to cyclic loading can be divided into three consecutive phases over the service life (Rezazadeh and Carvelli, 2018). The first phase is the rapid increase in concrete damage due to the internal flaw that occurs between 0%–10% of fatigue life. The second phase occurs during the longer fatigue life of between 10%–90% where a slow and reduced rate of damage, usually known as micro-cracking, is experienced by concrete. The third phase corresponds to the rapid increase in damage that occurs when the micro-cracks transform into unstable macro-cracks, leading to concrete failure.

2.5.2. Fatigue Damage Model of Concrete

The fatigue test for concrete necessitates a considerable amount of experimental effort and time, making it more expensive than other tests for evaluating concrete mechanical property. The heterogeneous property of concrete, as well as its high sensitivity to experimental set-up and loading condition, makes obtaining test results difficult. The use of numerical method such as fatigue damage model is therefore cheaper and more feasible for evaluating concrete fatigue behavior. In this study, several fatigue damage models are reviewed in order to identify a more effective numerical method for modelling cyclic loading of concrete.

2.5.2.1. Fracture Mechanics-Based Model

Fracture mechanics is a study of material failure based on the mechanism of crack propagation. The fracture mechanics-based (FM) model is often used to study tensile failure of concrete. In the model, Young's modulus (E) and Poisson's ration (v) are used to define linear property of concrete, while the non-linear portion is represented by fracture parameters, which are fracture energy (G_f) and tensile strength (f_t). The constitutive relation of cyclic loading in terms of stress-strain curve based on the FM model is shown in Figure 2.8. Monotonic loading is illustrated as line OABCD. In the cyclic loading, strain gap exists at zero stress level after unloading, which represents the closing and opening of micro-crack in concrete. The value of strain gap is evaluated using parameters g_o and g_c. After each cyclic loading, the stress-strain curve shifts to the right, indicating the irrecoverable damage to concrete. FM model, however, is not suitable for the analysis of high-cycle fatigue, because it explains only the evolution of existing crack but not the new crack initiation (Schafer et al., 2019).

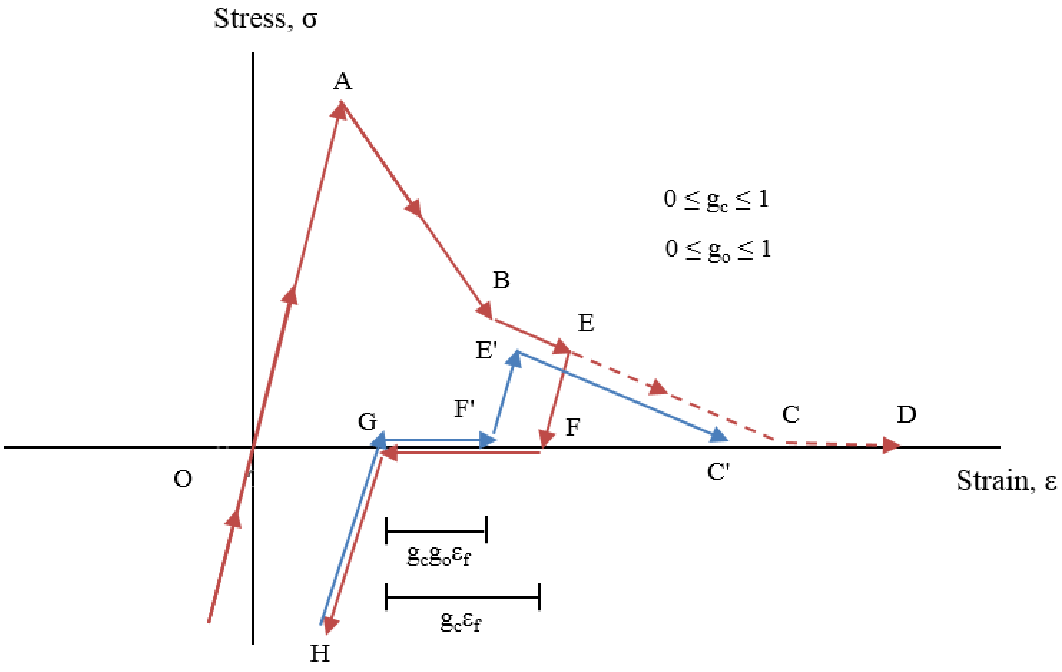

Figure 2.8: Constitutive relation of cyclic loading based on fracture mechanics (Gylltoft, 1984; Schafer et al., 2019)

2.5.2.2. Continuum Damage Mechanics Model

Continuum damage mechanics (CDM) model couples the framework of thermodynamics and continuum mechanics in simulating the micro-crack development, macro-crack formation and material rupture (Yadav and Thapa, 2020). The CDM model simulates irreversible material damages in terms of brittle, creep, ductile and fatigue failures. The development of various fatigue models using the CDM has been reported by Xiao et al. (1998). In the CDM model, the damage parameter (D) of a material is represented by the ratio of micro-crack area to total cross-sectional area as shown in Eq. 2.7, where D = 0 corresponds to the undamaged state, and D = 1 corresponds to the failure state.

$$\mathrm{D} = \frac{\mathrm{A_c}}{\mathrm{A_g}} \qquad \text{Eq. 2.7}$$

where A_g refers to the total area of cross section and A_c is the area of micro-crack.

In cyclic loading, the damage parameter is incorporated as an increasing variable into the damage evolution model that determines the equivalent stress as shown in Eq. 2.8.

$$\frac{\mathrm{dD}}{\mathrm{dN}} = \frac{\mathrm{B}}{\mathrm{q}(1-\mathrm{D})^{2\mathrm{q}}}\left({\sigma_\mathrm{M}}^{2\mathrm{q}} - {\sigma_\mathrm{m}}^{2\mathrm{q}}\right) \qquad \text{Eq. 2.8}$$

where B and q are material constants defined in the report by Xiao et al. (1998), σ_M is maximum equivalent stress and σ_m is minimum equivalent stress. By solving the damage evolution model with geometrical and equilibrium equations and applying boundary conditions, the stress and damage of concrete is then numerically determined. The constitutive equation of CDM model can be used in conjunction with finite element method to determine the fatigue damage of concrete.

2.5.2.3. Concrete Damaged Plasticity Model

Concrete damaged plasticity (CDP) model is a continuum model for describing concrete damage based on the irrecoverable and non-linear characteristics of material. The CDP model considers the inelastic strain of concrete subjected to multiaxial loading and provides better dilatancy control than CDM model (Wu et al., 2006). In the model, the concrete strain, based on the principle of incremental plasticity, is divided into elastic strain (ε_{el}) and inelastic strain (ε_{pl}) as shown in Eq. 2.9. The inelastic strain refers to the irreversible deformations normally caused by micro-cracking. The model adopts two damage parameters, one of which represents compressive damage while the other represents tensile damage. The two damage parameters are similarly defined in Eq. 2.7. The parameters are incorporated into the CDP model to represent the stiffness degradation of concrete as shown in Eq. 2.10.

$$\varepsilon = \varepsilon_{el} + \varepsilon_{pl} \qquad \text{Eq. 2.9}$$

$$\sigma = (1 - D)\, E_o\, (\varepsilon - \varepsilon_{pl}) \qquad \text{Eq. 2.10}$$

The CDP model also adopts the stiffness recovery parameter to simulate opening and closing of crack due to stress reversal in cyclic loading. Concrete stiffness degraded by damage is restored during load conversion between compression and tension. By combining the above constitutive relation with an appropriate yield function, such as Drucker-Prager yield criterion, the CDP model simulates the fatigue damage of concrete (Xiao et al., 2016).

2.5.3. Summary

The FM model can be used to simulate cyclic loading on concrete, but is more suitable for tensile loading only. The model takes into account the evolution of existing crack, but not the new formation. Both the CDM and CDP models can also be used for the simulation of cyclic loading on concrete. The CDM model incorporates damage parameter into damage evolution model to consider the defect such as micro-crack in concrete. But, the CDP model, which considers the plastic behavior and the stiffness recovery, provides better dilatancy control and is more ideal for modelling concrete fatigue damage.

2.6 Concluding Remark

Chapter 2 presents the literature review of sustainable concreting materials, concrete optimization methods, deterioration of concrete exposed to WDA in marine environment and cyclic loading on concrete.

The use of SiMn slag, an industrial waste, to replace conventional coarse aggregate of concrete is more sustainable and cost-effective, as additional material processing and handling are not necessary. The production cost of concrete can be further reduced if locally available materials such as marine sand and seawater at coastal area are utilized for construction. From the perspective of sustainability and cost-effectiveness, full replacement of the conventional materials is beneficial. Therefore, this study investigates the innovative use of SiMn slag, marine sand and seawater to replace ordinary materials of gravel, river sand and tap water respectively. There is minimal research on the use of these materials in concrete work, in particular the substitution of SiMn slag as a coarse aggregate.

FA and SF, which are industrial waste, will contribute to environmental sustainability if used to replace cement. Based on the literature review, the partial substitution of FA and SF as ternary blended cement in concrete enhances the workability, strength and durability of concrete. But, the optimum replacement levels of FA and SF in the published literature are not consistent due to the variation of material properties and concrete mix proportions. Further investigation is still needed to iron out the inconsistency of experimental results with regard to the effect of FA and SF on concrete properties. In addition, past study on FA and SF in ternary blended cement is not conclusive due to insufficient experimental planning. It is therefore recommended that the RSM, a statistical optimization method, be used to systematically determine the optimum replacement levels of FA and SF in this research.

Concrete exposed to marine environment is susceptible to physical and chemical deterioration mechanisms, which are aggravated by WDA. Sulphate attack and salt crystallization are the main deterioration mechanisms for mass concrete. Past research has focused on the deterioration of concrete subjected to WDA, combined with external loading, including compression, tension and short-term and long-term flexural loading. However, limited research is performed on the deterioration of concrete subjected to WDA combined with cyclic loading. Therefore, this research work investigates the concrete performance exposed to sulphate attack combined with WDA and cyclic compressive loading.

In order to minimize cost and experiment time, the numerical model is used as an alternative to laboratory cyclic loading test. Several fatigue models have been reviewed to determine an effective numerical model for simulating concrete cyclic loading. The CDP model, which uses damage parameter and inelastic strain to simulate concrete fatigue failure, is considered to be the most applicable model and is therefore adopted in this study.

Chapter 3. Strength and Durability of Concrete Incorporated with Silicomanganese Slag, Marine Sand and Seawater

This chapter has been published in the journal paper entitled "Mechanical and durability performance of marine sand and seawater concrete incorporating silicomanganese slag as coarse aggregate"(Construction and Building Materials, Q1, https://doi.org/10.1016/j.conbuildmat.2020.119195).

3.1. Introduction

This chapter studies the effect of using silicomanganese (SiMn) slag, marine sand and seawater as alternative concreting materials on the strength and durability of concrete. SiMn slag is used to substitute limestone as a coarse aggregate. Marine sand and seawater are used to replace river sand and freshwater respectively. The full replacement of these materials is beneficial in terms of sustainability and cost-effectiveness. Experiments were planned and conducted to investigate the effects of single and combined substitutions of the materials. Concrete strengths, including compressive and splitting tensile strengths, were evaluated at 7, 28 and 90 days of age. The durability properties of concrete, such as water absorption, sorptivity, chloride permeability and sulphate resistance, were assessed at 28, 90 and 180 days. SEM and EDX analyses were conducted to examine the interfacial transition zone of concrete. The results of the experiments were analyzed and the discussion was elaborated.

3.2. Material and Test Method

3.2.1. Material

3.2.1.1. Cement

Ordinary Portland cement (OPC) graded as CEM 1 42.5 N was used as a binder in this study. It complied with the specifications stated in ASTM C150 (2012) . The chemical composition of OPC is shown in Table 4.1. In general, the OPC consisted mainly of 68.97% of calcium oxide (CaO), 16.29% of silicon dioxide (SiO_2), 4.17% of aluminium oxide (Al_2O_3) and 3.51% of ferric oxide (Fe_2O_3).

3.2.1.2. Coarse Aggregate

Coarse aggregates used in this research included crushed limestone (B1) and crushed SiMn slag (B2) which had nominal sizes of 19.0 mm and 25.0 mm respectively. Particle size distribution of the two types of aggregate is presented in Figure 3.1. Both aggregate size distribution curves were within the upper and lower bounds as specified in ASTM C33 (2012) . Specific gravities of the aggregate B1 and B2 were determined as 2.64 and 2.97 respectively as presented in Table 3.1. As shown in Table 3.2, the SiMn slag contained 41.49% of silicon dioxide (SiO_2) and 13.95% of aluminium oxide (Al_2O_3) respectively, suggesting that it could cause a pozzolanic reaction in concrete.

3.2.1.3. Fine Aggregate

Two types of sand, river sand and marine sand, were used as fine portion of aggregate in concrete. The marine sand was sampled at Tanjung Lobang Beach in Miri, Malaysia. Due to highly fine property of the sand, quarry dust retrieved from quarrying waste was used to replace 30% sand by volume in order to ensure desirable concrete workability. Particle size distributions of blended river sand (C1) and blended marine sand (C2) together with upper and lower size distribution limits of ASTM C33 (2012) are shown in Figure 3.1. Grading curve of C1 was close to the ASTM limit while it was slightly beyond the limit for C2, which indicated higher proportion of fine particle. The grading of C2 aggregate can be further improved by blending with a higher percentage of quarry dust. However, it was not done due to economic reason and hence C2 aggregate was still adopted for this study despite its non-conformation with recommended grading. Table 3.1 presents the physical properties of fine aggregates. The chemical composition of marine sand is shown in Table 3.2. The marine sand primarily composed of 95.5% SiO_2.

Table 3.1: Physical properties of coarse and fine aggregates

Properties of aggregates	**Aggregate types**			
	B1	**B2**	**C1**	**C2**
Fineness modulus	6.75	9.25	3.18	2.59
Specific gravity	2.64	2.97	2.67	2.70
Water absorption (%)	0.66	0.21	-	-
Flatness ratio	0.68	0.55	-	-
Elongation ratio	0.68	0.59	-	-
Aschenbrenner & Zingg catergory	Equidimensional	Flaky and elongated	-	-
Abrasion resistance (%)	12	22	-	-

Table 3.2: Chemical compositions of SiMn slag and marine sand and comparison with conventional aggregates

Chemical composition	**SiMn slag**	**Marine sand**	**Conventional aggregates**	
			Limestone (Yılmaz and Olgun, 2008)	**River sand (Hussain et al., 2018)**
Silicon dioxide (SiO_2)	41.49	95.5	2.58	88.6
Calcium oxide (CaO)	21.04	0.04	52.39	0.07
Aluminium oxide (Al_2O_3)	13.95	0.79	0.64	-
Manganese oxide (MnO)	8.12	-	-	-
Magnesium oxide (MgO)	4.61	0.39	0.64	-
Ferric oxide (Fe_2O_3)	4.47	0.57	0.33	0.53
Potassium oxide (K_2O)	1.35	0.15	0.11	2.93

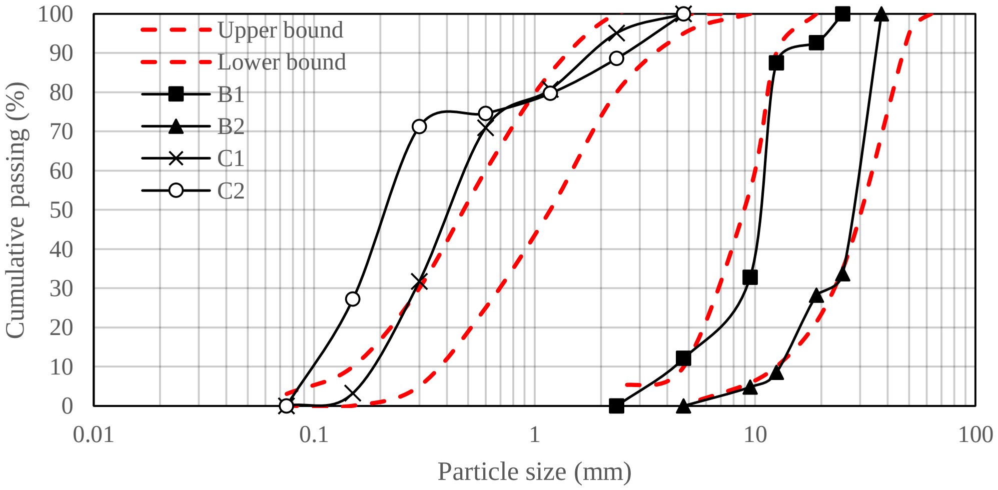

Figure 3.1: Particle size distribution of coarse and fine aggregates

3.2.1.4. Mixing Water

For mixing water, tap water (D1) and seawater (D2) were used. Seawater was sampled from the sea near the shore of Tanjung Lobang Beach. The seawater was stored in tightly closed polyethylene containers and put in a fridge at a temperature of 5±2.5 °C to minimize microbial activity. Table 3.3 summarizes chemical composition of the seawater. The seawater was slightly alkaline with a pH of 8.1 at room temperature (26 °C). The main compositions of seawater were Na^+, Cl^- and SO_4^{2-} which accounted for approximately 95% of the total salt content. The seawater composition was identical to that of the standard seawater presented by Lenntech (2018). In addition, the determination of seawater composition is shown in Appendix B.

Table 3.3: Chemical compositions of seawater

Density (26 ± 0.5 °C)	**pH (26 ± 0.5 °C)**	**Chemical compositions (mg/l)**					
		Na^+	**Mg^{2+}**	**Ca^{2+}**	**K^+**	**Cl^-**	**SO_4^{2-}**
1.01 g/cm^3	8.1	17840	460	613	456	19675	1730

3.2.1.5. Superplasticizer

Superplasticizer (SP), sodium naphthalene sulphonate formaldehyde was used as chemical admixture for ensuring sufficient workability of concrete. It was classified as a Type A (water-reducing) chemical admixture in accordance with the ASTM C494 (2019) standard.

3.2.2. Concrete Mixing Method

Concrete mixing was carried out using a 0.1m^3 capacity laboratory mixer with a mixing speed of 25 rpm. The mixing process began with the dry mixing of cement, coarse aggregate and fine aggregate for 1 minute. The water and SP were then slowly added to the mixture for the next 1 minute of mixing. The mixing process continued for 1 to 3 minutes, until a uniform mixture was obtained. The opening of the mixer was covered with a plastic sheet during the mixing process to avoid material spillage. Concrete was casted into steel moulds in three layers and compacted using a vibrating table. The casted specimens were covered with a plastic sheet and placed in the curing room at 27±1 °C for 1 day. The specimens were then removed from the moulds and cured by fully submerging them in water until the time of testing. Figure 3.2 depicts the stages for the preparation of concrete specimens. Three replicates of concrete specimens were prepared and the average value of each concrete property was used for analysis. The specimens of each concrete mixture were prepared from the same batch to reduce the test inconsistency.

Figure 3.2: Concrete specimens (a) mixing, (b) casting, (c) demoulding and (d) curing

3.2.3. Test Method

3.2.3.1. Slump Test

The slump test was conducted in accordance with ASTM C143 (2015) to determine the workability of concrete after mixing. Slump cone with a height of 300 mm, a bottom diameter of 200 mm and a top diameter of 100 mm was used for the test. Before testing, the slump cone was moisturized with a wet cloth and then firmly placed on a smooth plate. During the test, the slump cone was filled with three layers of concrete, and each layer was pounded 25 times with a 16 mm diameter steel rod. The excess concrete on the top surface of slump cone was removed by the rolling action of steel rod. Then, the slump cone was raised slowly. After the concrete slump stopped, the reduction of concrete height from the top of cone to the top of slump was measured. An example of concrete slump test is shown in Figure 3.3.

Figure 3.3: Concrete slump test

3.2.3.2. Compressive Strength Test

Cylinder and cube compressive strengths were determined for each type of mix. Cylindrical moulds with dimensions of 100 mm x 200 mm and cube moulds with dimensions of 100 mm were used respectively. The use of these mould sizes was in accordance with the Indian Standard (IS: 10086-2008), which required that the mould size be 4 times larger than the maximum aggregate size (19–25 mm) used. The specimens were cured for 7, 28 and 90 days and tested by using 3000kN semi-auto compression testing machine in accordance with the ASTM C39 (2012) . Figure 3.4 illustrates the experimental set-up of compression test for the specimen.

Figure 3.4: Compressive strength test

3.2.3.3. Splitting Tensile Strength Test

Splitting tensile test was used to evaluate the concrete tensile strength. In carrying out the test, cylindrical concrete specimens with a size of 100 mm x 200 mm were prepared. The splitting tensile strengths of all mixes were measured at concrete ages of 7, 28 and 90 days. The specimens were tested in accordance with the ASTM C496 (2012) requirement. The experimental set-up of splitting tensile test is shown in Figure 3.5. The splitting tensile strength of concrete is calculated using Eq. 3.1.

$$f_{st} = \frac{2P}{\pi l d_s} \qquad \text{Eq. 3.1}$$

where f_{st} is splitting tensile strength, P is the maximum applied load at failure, l is the specimen length and d_s is the specimen diameter.

Figure 3.5: Splitting tensile test

3.2.3.4. Water Absorption and Permeable Pore Test

Water absorption and permeable pore volume of concrete were measured based on the ASTM C642 (2012) test method. 50 mm concrete cubes were prepared and tested at the age of 28, 90 and 180 days respectively. In the test, the dry mass of specimen (m_d) was measured after drying at a temperature of 110 °C in the oven. The saturated mass of specimen (m_s) was measured after 48 hours of immersion in water at room temperature. Both m_d and m_s were taken only if the difference between two successive values after repetition was less than 0.5%. After immersion, the saturated mass after boiling (m_b) was determined by boiling and cooling the specimen for 5 hours and 14 hours respectively. Then, the apparent mass (m_a) of the specimen in water was determined. Water absorption and permeable pore volume of concrete can be calculated using Eq. 3.2 and Eq. 3.3 respectively.

$$\text{Water absorption, \%} = \frac{m_s - m_d}{m_d} \times 100 \qquad \text{Eq. 3.2}$$

$$\text{Volume of permeable pore, \%} = \left(1 - \frac{m_d - m_a}{m_b - m_d}\right) \times 100 \qquad \text{Eq. 3.3}$$

3.2.3.5. Sorptivity Test

The rate of water absorption of concrete, often referred to as sorptivity, was assessed by carrying out uni-directional water absorption test. The test was conducted in accordance with ASTM C1585 (2012) standard. Cylindrical specimens with height of 100 mm and diameter of 50 mm were trimmed from a 100 x 200 mm concrete cylinder using wet cutting method. The specimens were dried in the oven at 50±1 ^{o}C for 7 days until a constant mass was reached. Side and top surfaces of the specimens were sealed with an epoxy coating. The test started by placing the specimens on support rods in a plastic tray, exposing the unsealed bottom surface to water. The water level was maintained at 2±1 mm during the test period. Figure 3.6 shows the schematic of the sorptivity test. Changes in the mass of specimens were recorded for 8 days. Water absorption (i) of specimens was calculated using Eq. 3.4. The sorptivity of concrete was determined from the slope of water absorption curve against the square root of time. The test was conducted on concrete specimens after 28, 90 and 180 days of curing.

$$i = \frac{m_t}{A_g \times \rho_w} \qquad \text{Eq. 3.4}$$

where m_t is the mass change of specimen at time t, A_g is the area of specimen exposed to water and ρ_w is the density of water.

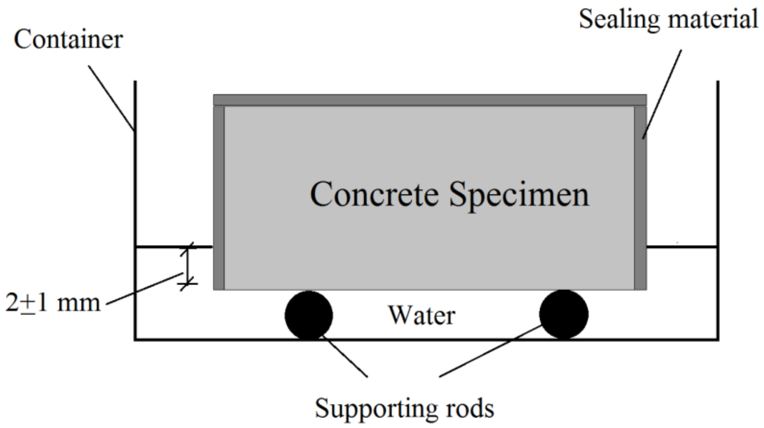

Figure 3.6: Schematic of sorptivity test

3.2.3.6. Rapid Chloride Ion Penetration Test

Concrete permeability for each mix was also examined by rapid chloride ion penetration test (RCPT). The test procedure recommended by ASTM C1202 (2012) was used for this study. Cylindrical concrete specimens with dimension of 100 mm x 50 mm were prepared and tested for 28, 90 and 180 days. The specimen with side surface sealed with an epoxy coating was conditioned in a desiccator using vacuum pump. The specimen conditioning consisted of 3 hours of dry vacuum, 1 hour of vacuum in water and 18 hours of soaking in water. After standard conditioning, the specimen was connected to two test cells, one cell containing 3.0% sodium chloride (NaCl) solution and the other cell containing 0.3 N sodium hydroxide (NaOH) solution. Electrical current of 60±0.1 volt was applied across the specimens for 6 hours. The current was recorded every 30 minutes and the total charge (Q) was determined by integrating the current versus time plot using Eq. 3.5. Table 3.4 presents the guideline for assessing concrete permeability through the use of flow charge. Figure 3.7 shows the setup of a rapid chloride ion penetration test.

$$Q = 900\,(I_0 + 2I_{30} + 2I_{60} + \ldots + 2I_{300} + 2I_{330} + I_{360}) \qquad \text{Eq. 3.5}$$

where I_0 is the current immediately after voltage is applied and I_t is the current at t min after voltage is applied.

Table 3.4: Concrete permeability based on RCPT (ASTM C1202, 2012)

Charge passed (coulombs)	Permeability of concrete
> 4,000	High
2,000–4,000	Moderate
1,000–2,000	Low
100–1,000	Very low
< 100	Negligible

Figure 3.7: Rapid chloride ion penetration test

3.2.3.7. Resistance to Sulphate Attack Test

Sulphate immersion test was conducted for each concrete mix to evaluate its resistance to sulphate attack. The test was conducted in accordance with the ASTM C1012 (2012) guideline. 100 mm concrete cubes were casted, cured for 7 days and then immersed in 5% sodium sulphate solution for 7, 28 and 90 days. The containers used for sulphate immersion were stored in the curing room at a temperature of 27±1 ^{o}C. The containers were covered with caps during the test in order to minimize evaporation. Concrete compressive strength at each immersion durations was measured. Subsequently, the reduction of compressive strength due to sulphate attack was determined relative to the compressive strength of concrete immersed in water.

3.2.3.8. Scanning Electron Microscope Analysis

Concrete specimen, with a length of 10 mm, a width of 10 mm and a thickness of 5 ± 2 mm, was trimmed from 100 mm cube using a wet cutting method. The specimen was immersed in ethanol for 24 hours to terminate the hydration process. It was then dried in the oven at 50 ^{o}C for 48 to 72 hours until it reached a constant weight. The microstructure image of the specimen was taken using the Thermo Scientific Quattro environmental scanning electron microscope (SEM). SEM analysis was conducted at 7 days for Mix 6 (B2/C2/D2) and at 28 days for Mix 1 (B1/C1/D1), Mix 5 (B1/C2/D2) and Mix 6 (B2/C2/D2).

3.3. Concrete Mix Design

The purpose of this research is to develop a concrete that is durable in the hostile marine environment. There is a minimal standardized method for the design of concrete with high durability. Instead, the existing ACI, BS and IS standards provide mix design for high strength concrete. High strength concrete typically has better durability due to lower water demand and hence less porosity. Therefore, in this study, ACI mix design method is adopted to initiate laboratory work. The ACI method also provides guideline for the use of supplementary cementitious materials studied at the later stage of study in Chapter 4.

3.3.1. ACI Mix Design Algorithm

The ACI Committee 211 has provided guideline for the proportioning of high strength concrete as set out in the ACI 211.4R-93 (1998) standard. The absolute volume method is used by the ACI standard, which determines the proportions of cement, aggregate and water based on their absolute volume in one cubic yard of concrete. Figure 3.8 provides an overview of the mix design process for ACI method. A mix design calculation using this method is shown in Appendix A. The procedures for developing the high strength concrete are presented below.

Step 1: Target slump and strength

The first step in the proportioning of concrete mix is to determine the target slump and strength of concrete. The concrete slump recommended by the standard is between 50 mm and 100 mm. This is meant to provide a better consolidation of concrete containing a high quantity of coarse aggregate and cementitious material. If a superplasticizer is used, the minimum slump can be reduced to 25 mm. The range of concrete strength design for cylindrical specimens with an aspect ratio of 0.5 is between 48 MPa and 82 MPa. The ACI standard recommends the use of higher strength ($f_{cr}^{'}$) during the mix development by factoring the target compressive strength (f_c') using Eq. 3.6. This is to account for the strength variability of concrete, which can typically be 10% lower due to environmental factors and the quality of raw materials.

$$f_{cr}{}' = \frac{f_c{}' + 9.65}{0.9} \qquad \text{Eq. 3.6}$$

where f_{cr}' is required compressive strength and f_c' is design compressive strength.

Step 2: Calculation of coarse aggregate content

The weight of coarse aggregate in one cubic yard of concrete can be determined from Eq. 3.7. CAF is the coarse aggregate factor that considers the size effect of aggregate and it is further elaborated in ACI 211.4R-93 (1998). The recommended maximum coarse aggregate size is between 9.5 mm and 25 mm, whereby the use of smaller size aggregate will result in better particle packing and thus higher strength concrete. DRUW refers to the dry-rodded unit weight of coarse aggregate and is measured in accordance with ASTM C29 (2017) . The proportioning method is only appropriate for fine aggregate with a fineness modulus of between 2.5 and 3.2, which can provide adequate lubrication and compaction of concrete.

$$W_{ca} = \text{CAF} \times \text{DRUW} \qquad \text{Eq. 3.7}$$

where W_{ca} is weight of coarse aggregate, CAF is coarse aggregate factor and DRUW is dry-rodded unit weight.

Step 3: Calculation of water and cement contents

The water content of concrete is estimated based on the slump and coarse aggregate size. Meanwhile, the water-to-cement (w/c) ratio is determined by the compressive strength and coarse aggregate size. ACI 211.4R-93 (1998) provides design data for the determination of water content and w/c ratio. The cement content can then be determined from Eq. 3.8.

$$W_c = \frac{W_w}{\text{w/c ratio}} \qquad \text{Eq. 3.8}$$

where W_c is weight of cement and W_w is weight of water.

Step 4: Calculation of fine aggregate content

The volume of fine aggregate is determined from Eq. 3.9 based on the absolute volume method. The fine aggregate volume can be converted into unit weight using Eq. 3.10.

$$V_{fa} = 1 - \frac{1}{1000}\left(\frac{W_c}{SG_c} + \frac{W_{ca}}{SG_{ca}} + \frac{W_w}{SG_w}\right) \qquad \text{Eq. 3.9}$$

$$W_{fa} = V_{fa} \times SG_{fa} \times 1000 \qquad \text{Eq. 3.10}$$

where V_{fa} and W_{fa} are volume and weight of fine aggregate and SG_c, SG_{ca}, SG_w and SG_{fa} are specific gravity of cement, coarse aggregate, water and fine aggregate respectively.

Extra Step: Addition of Supplementary Cementitious Material

The ACI standard provides guideline for proportioning the concrete mix design containing supplementary cementitious material (SCM). The weight of SCM is determined using Eq. 3.11. It is then subtracted from the weight of cement as shown in Eq. 3.12. The volumes of cement and SCM are determined using Eq. 3.13 and Eq. 3.14 respectively. Subsequently, the volume and weight of fine aggregate in Step 4 is re-calculated by replacing Eq. 3.9 with Eq. 3.15 and Eq. 3.10 with Eq. 3.16.

$$W_{scm} = RL \times W_c \qquad \text{Eq. 3.11}$$

$$W_{c,new} = W_c - W_{scm} \qquad \text{Eq. 3.12}$$

$$V_{c,new} = \frac{W_{c,new}}{1000 \times SG_c} \qquad \text{Eq. 3.13}$$

$$V_{scm} = \frac{W_{scm}}{1000 \times SG_{scm}} \qquad \text{Eq. 3.14}$$

$$V_{fa,new} = 1 - \frac{1}{1000}\left(\frac{W_{ca}}{SG_{ca}} + \frac{W_w}{SG_w}\right) - V_{c,new} - V_{scm} \qquad \text{Eq. 3.15}$$

$$W_{fa,new} = V_{fa,new} \times SG_{fa} \times 1000 \qquad \text{Eq. 3.16}$$

where W_{scm}, $W_{c,new}$ and $W_{fa,new}$ are the newly calculated weights of SCM, cement and fine aggregate, V_{scm}, $V_{c,new}$ and $V_{fa,new}$ are the newly calculated volumes of SCM, cement and fine aggregate and RL is the replacement level of SCM.

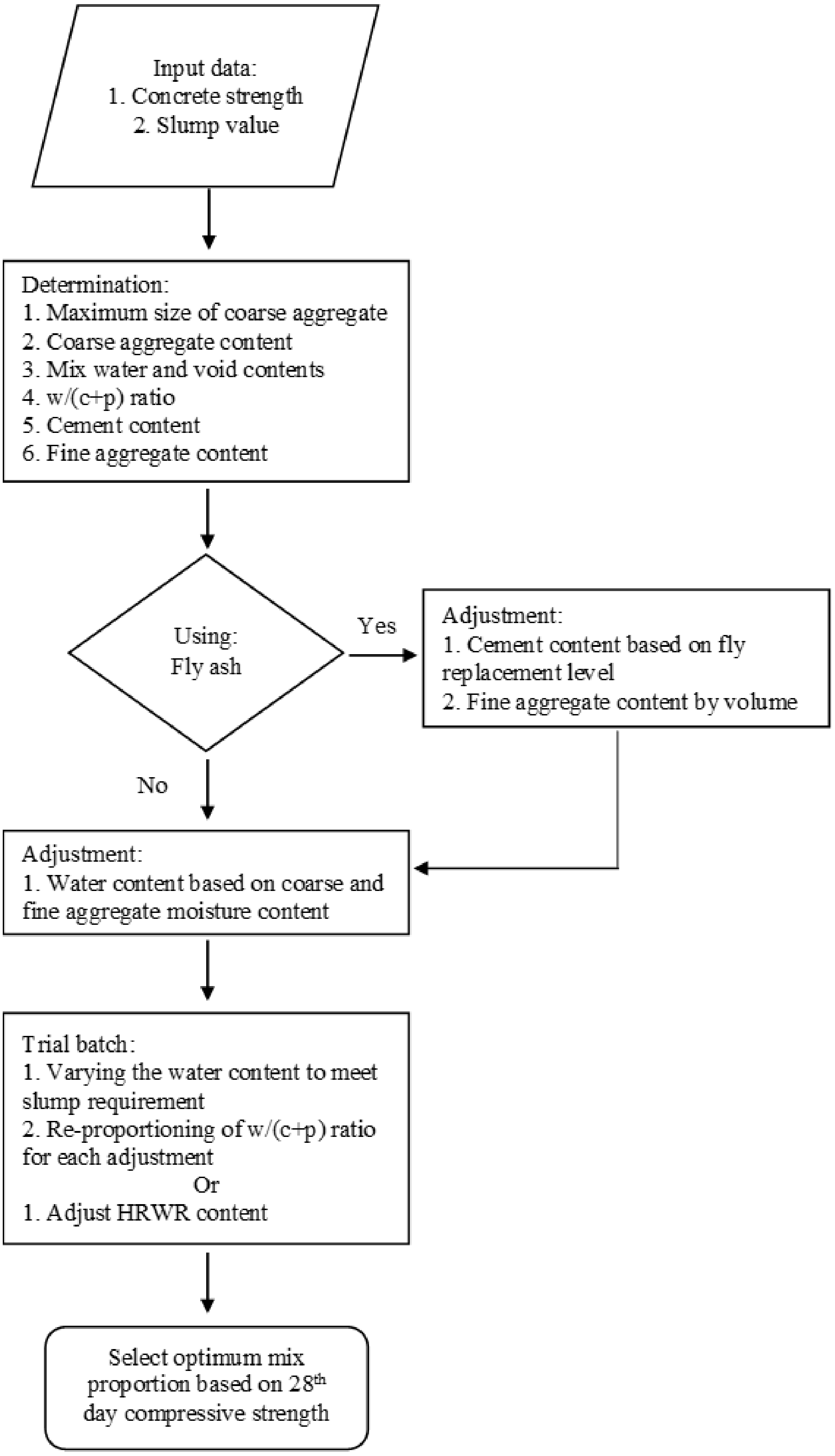

Figure 3.8: ACI high strength concrete mix design procedure

3.3.2. Trial Concrete Mix Design

Concrete mix with $f_c^{'}$ of 50 MPa and slump of 100 mm was developed using the ACI mix design algorithm. Table 3.5 presents the trial mix design for concrete consisting of cement as binder, limestone as coarse aggregate, marine sand as fine aggregate and tap water. However, the workability of the concrete was far below than that of the target, which resulted in an inhomogeneous mixture. This also caused the 28-day compressive strength of concrete to be 22% lower than the design strength. The poor workability was due to the high water demand of fine marine sand. The distribution of its particle size was outside the standard limit. In this regard, two rectification methods were proposed, namely increase in SP dosage and hybridization of marine sand with quarry dust, in order to improve concrete workability.

Table 3.5: Trial concrete mix design

Concrete component	**Content**
w/c ratio	0.32
Cement	550 kg/m^3
Limestone	965 kg/m^3
Marine sand	745 kg/m^3
Tap water	176 kg/m^3
SP	4.4 kg/m^3 (0.8% of binder content)
Concrete property	**Result**
Slump	10 mm
Compressive strength at 7 days	29.76 MPa
Compressive strength at 28 days	38.92 MPa

3.3.2.1. Increase in SP Content

Sodium naphthalene sulphonate formaldehyde is used as an SP in this research. This type of SP contains naphthalene-sulphonate monomers that are crosslinked by formaldehyde to form polymers with surfactant properties. The negatively charged backbone of polymers adsorbs on to the positively charged cement particles which facilitates the dispersion of particles and increases concrete workability (Cheah et al., 2019). In this section, the SP dosage has been raised from 0.8% to 1.0%, 1.5%, 2.0% and 3.0% in order to improve concrete workability. The slump and compressive strengths at 7 and 28 days are determined and shown in Table 3.6. Concrete with 0.8% to 2.0% SP had a similar compressive strength, but there was a slight improvement in strength with 3% SP. Besides, the slump of concrete increased marginally with an increase in SP dosage. Concrete with 3% SP achieved the highest slump value of 31 mm, but was still far below the target slump of 100 mm. The use of high SP dosage in concrete is not recommended since it may increase the setting time and hence affect the strength development. Based on the results, a 1% SP dosage is recommended in terms of effectiveness of strength and workability.

Table 3.6: Effect of SP content on slump and compressive strengths of concrete

SP content (%)	Slump (mm)	7-day Compressive strength (MPa)	28-day compressive strength (MPa)
0.8	10	29.8	38.9
1.0	18	30.4	40.3
1.5	20	29.5	38.8
2.0	21	30.2	40.1
3.0	31	32.6	41

3.3.2.2. Hybridization of Marine Sand and Quarry Dust

The use of marine sand increases the water demand due to its high fineness and poor particle grading. Quarry dust is a byproduct of stone crushing and has a size appropriate for use as fine aggregate of concrete. Therefore, marine sand is partially replaced by quarry dust to improve the particle grading. Figure 3.9 presents the particle size distribution for the mixture of marine sand with a volume of 20%, 30%, 40% and 50% respectively replaced by quarry dust. Although all the mixtures were outside the limit of the ASTM C33 standard, the particle grading improved with an increase in the amount of quarry dust being replaced. Besides, the fineness modulus of marine sand also increased with the addition of quarry dust as shown in Table 3.7, indicating a higher average particle size.

Table 3.7: Effect of hybridization on slump and compressive strength

Mixture	Fineness modulus	Slump (mm)	7-day compressive strength (MPa)	28-day compressive strength (MPa)
MS100% (QD0%)	1.89	10	29.8	38.9
MS80% (QD20%)	2.32	34	38.7	46.3
MS70% (QD30%)	2.59	78	43.7	48.1
MS60% (QD40%)	2.65	82	44.5	48.4
MS50% (QD50%)	2.95	91	44.8	50.0

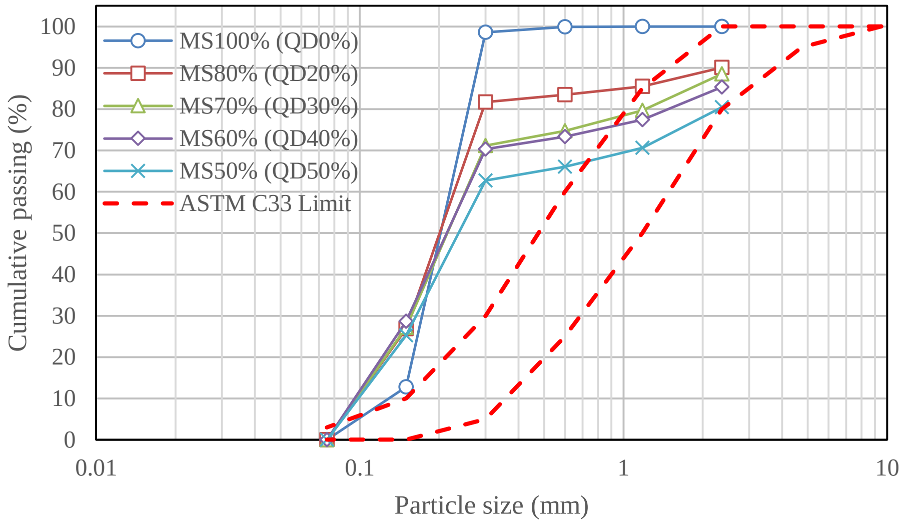

Figure 3.9: Grading for mixture of marine sand and quarry dust

In this context, the concrete for the experiment was produced using mixtures of marine sand and quarry dust. The contents of other concrete components as shown in Table 3.5 were used. The slump and compressive strength of the concrete were determined as shown in Table 3.7. The concrete slump increased significantly with the increased amount of quarry dust. Concrete containing 50% marine sand and 50% quarry dust achieved the highest slump of 91 mm, which was close to the target value. This was due to the larger particle size of quarry dust, which had a smaller total surface area requiring lower water demand.

The compressive strength of concrete also increased significantly with an increase in the quarry dust replacement. Hybridization of marine sand and quarry dust resulted in higher strength improvement compared to the use of more SP. The compressive strengths of concrete containing 30%, 40% and 50% quarry dust were 48.1 MPa, 48.4 MPa and 50 MPa respectively and were close to the design strength. Since the concrete strengths were comparable, the mixture of 70% marine sand and 30% quarry dust was used for economic reason in the subsequent study. Furthermore, this mixture had a particle grading close to the standard limit and a fineness modulus higher than 2.5. Although the slump was not achieved, it could be improved by the increasing the SP dosage up to 1% as previously discussed.

3.3.3. Final Concrete Mix Design

As described in the previous section, the concrete mix design was developed using the ACI algorithm. The trial concrete mix design was modified as a result of the unsatisfactory slump and compressive strength. In this context, quarry dust was used to replace 30% of sand by volume in order to improve particle grading and reduce water demand. Furthermore, a 1% SP content was used to ensure desirable concrete workability. Table 3.8 shows the concrete mix proportion designed for the study of this chapter. Six types of concrete mix were proposed to study the effect of SiMn slag, marine sand and seawater on the hardened concrete properties. Hereafter, abbreviation of "Mix (B/C/D)" was used to indicate different type of materials used for three components of concrete, whereby B denoted coarse aggregate, C denoted fine aggregate and D denoted mixing water. Mix 1 (B1/C1/D1) was control mix which contained conventional materials of limestone, river sand and tap water as mixing ingredients. For all the mixes, water to cement ratio was kept constant at 0.32.

Table 3.8: Concrete mix proportion for investigating the effectiveness of SiMn slag, marine sand and seawater

Components	**Proportions (kg/m^3)**					
	Mix 1 (B1/C1/D1)	Mix 2 (B2/C1/D1)	Mix 3 (B1/C2/D1)	Mix 4 (B1/C1/D2)	Mix 5 (B1/C2/D2)	Mix 6 (B2/C2/D2)
Cement	550	550	550	550	550	550
Limestone	965	0	965	965	965	0
SiMn slag	0	1115	0	0	0	1115
River sand	520	520	0	520	0	0
Marine sand	0	0	515	0	515	515
Quarry dust	167	167	173	167	173	173
Tap water	176	176	176	0	0	0
Seawater	0	0	0	176	176	176
Superplasticizer	5.5	5.5	5.5	5.5	5.5	5.5
Note:						
B1 – Limestone, B2 – SiMn slag, C1 – River sand, C2 – Marine sand, D1 – Tap water, D2 – Seawater						

3.4. Results and Discussions

3.4.1. Concrete Workability

Figure 3.10 shows the slump values which measure the workability of concrete of different mixes. The slump values of all concrete were in the range of 77 mm to 121 mm which indicated ample workability suitable for concrete pumping (ACI 304.R-96, 1996) . Control mix, Mix 1 (B1/C1/D1) was noted to exhibit the highest slump value. Meanwhile, incorporation of SiMn slag as coarse aggregate replacement, as in Mix 2 (B2/C1/D1), reduced the slump value significantly by 36%. This was attributed to poor particle size distribution exhibited by SiMn slag. Referring to Figure 3.1, approximately 70% of SiMn slag aggregate was retained on 25 mm sieve. Hence, there was a lack of finer particle to lubricate aggregate skeleton for achieving desirable concrete workability. Partial replacement of coarse aggregate by SiMn slag may result in well graded aggregate and hence better workability, but further investigation is required.

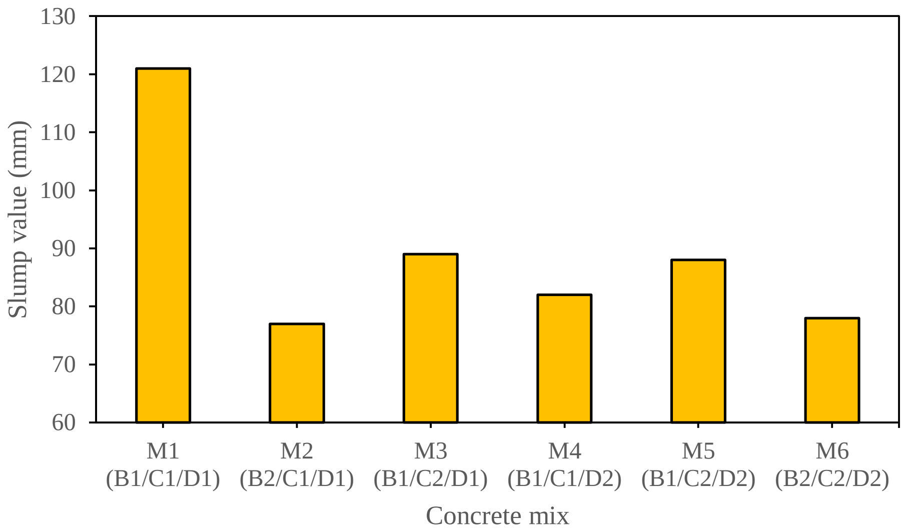

Figure 3.10: Workability of concrete for different mixtures

Mix 3 (B1/C2/D1) concrete, manufactured with marine sand, showed 26% lower slump value compared with the control mix using river sand. This was due to fine property of marine sand which possessed higher net particle surface area. This increased water demand and hence additional water was required for achieving comparable workability to the control concrete. Fineness modulus of marine sand and river sand were determined as 2.59 and 3.18 respectively, indicating lower average aggregate size exhibited by marine sand. Mix 3 (B1/C2/D1) can achieve better workability by replacing marine sand with more quarry dust as this increases fineness modulus of aggregate which exhibits less water demand. Nevertheless, this will contribute to the drawback of cost increase.

Replacement of tap water with seawater in Mix 4 (B1/C1/D2) showed 32% lower slump value than control mix. The result was in line with finding of Younis et al. (2018) that concrete mixed with seawater required extra 15% superplasticizer to achieve comparable workability to control concrete. The presence of salt in seawater reduces concrete setting time whereby concrete losses its workability at higher rate. Furthermore, the use of marine sand and seawater as in Mix 5 (B1/C2/D2) showed 27% reduction of slump value, while further incorporation of SiMn slag as in Mix 6 (B2/C2/D2) exhibited 36% reduction. In short, although concrete incorporated with SiMn slag, marine sand and seawater exhibited lower slump value, it can still provide satisfactory workability in practice.

3.4.2. Effect on Compressive Strength

Cylinder and cube compressive strength of concrete at 7-day, 28-day and 90-day ages is illustrated in Figure 3.11 and Figure 3.12 respectively. The compressive strength of all concrete samples increased orderly with curing age. Both types of concrete strength exhibited similar trend lines. By using the experimental data, relationship between cylinder and cube compressive strengths was analyzed through linear regression method. The resultant relationship is presented as Eq. 3.17:

$$\mathrm{f_{cy}} = 0.6945\mathrm{f_{cu}} + 0.12 \qquad \text{Eq. 3.17}$$

where $\mathrm{f_{cy}}$ and $\mathrm{f_{cu}}$ are cylinder and cube compressive strength respectively.

The cylinder strength was normalized by dividing it with the cube strength as illustrated in Figure 3.13 and the cylinder to cube strength ratio was determined as 0.70. The result was also well compared to the British Standard (BS EN 206-1, 2000) and published literature (Elwell and Fu, 1995; Neville, 1966). Concrete strength ratio calculated from the British Standard was 0.83 (BS EN 206-1, 2000) . Meanwhile, Neville (1966) provided a more comprehensive cylinder and cube strength relationship that took into consideration the different shapes and sizes of concrete samples, giving a 0.61 strength ratio. Also, (Elwell and Fu, 1995) claimed that concrete cylinder to cube strength ratio ranged from 0.60 and 0.90. Replacement of British Standard by Eurocode for concrete design has advocated use of concrete cylinder strength rather than cube strength (Mosley et al., 2012). In this connection, Eq. 3.17 can be beneficial in converting cube strength into cylinder strength.

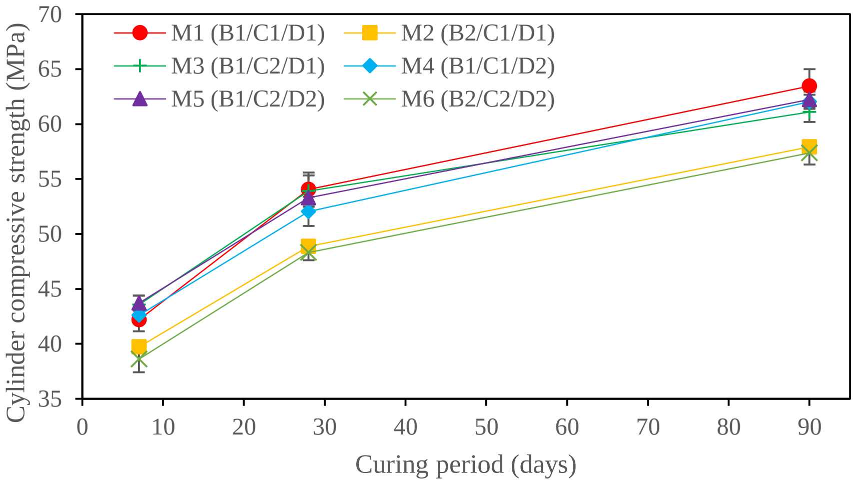

Figure 3.11: Variation of cylinder compressive strength with curing period

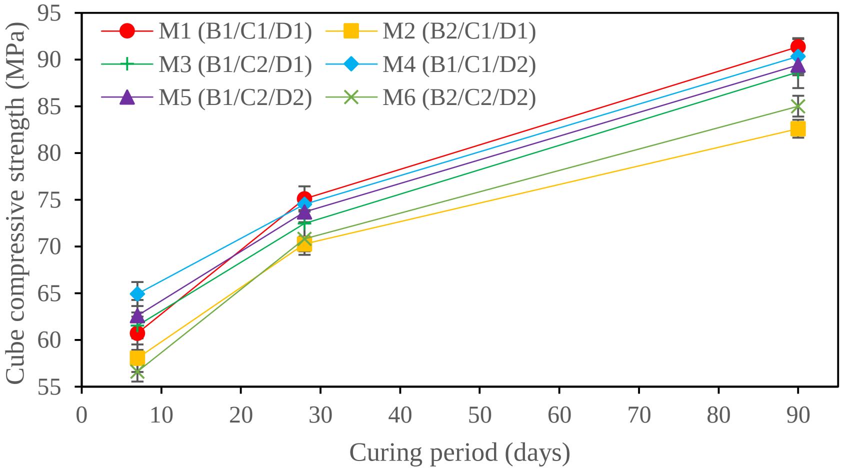

Figure 3.12: Variation of cube compressive strength with curing period

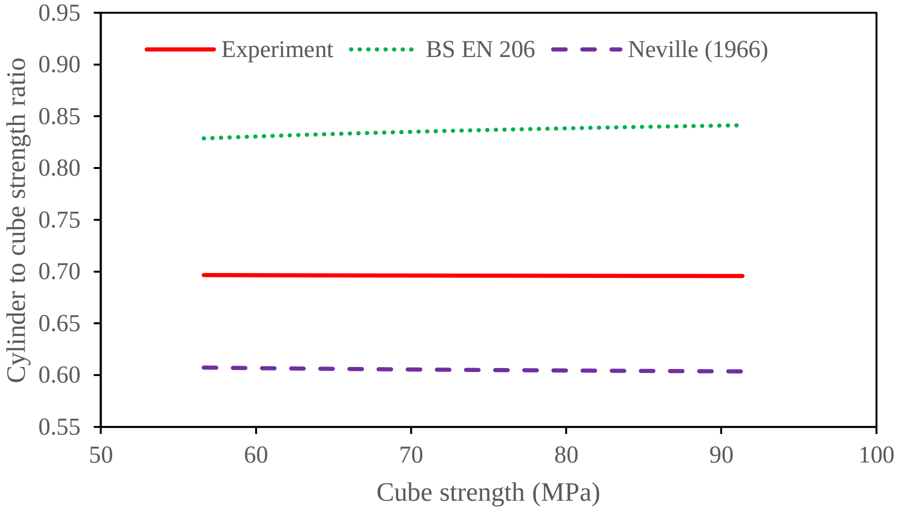

Figure 3.13: Correlation between cylinder and cube compressive strength

Table 3.9 presents variation of concrete compressive strength for all mixes with respect to the control. Utilizing SiMn slag as coarse aggregate in concrete generally decreased compressive strength regardless of age. Reduction of compressive strengths was computed as 5.1%, 8.0% and 9.2% at 7, 28 and 90 days respectively for Mix 2 (B2/C1/D1), while it was 7.6%, 8.2% and 8.3% respectively for Mix 6 (B2/C2/D2). As shown in Table 3.1, SiMn slag aggregate exhibited high flatness and elongation ratio which was categorized as elongated and flaky aggregate, while limestone aggregate belonged to equidimensional category. Therefore, the reduction of compressive strength was attributed to angular shape and smoother surface of SiMn slag which weakened its bonding with cement paste. Similar observation was reported in study conducted by Kazjonovs et al. (2010), whereby steel punch was used as coarse aggregate. In this case, flaky steel punch exerted high and concentrated stress on concrete interface which resulted in brittle failure at relatively low load.

Table 3.9: Compressive strength variation with respect to control mix

Concrete age	**Variation of compressive strength (%)**				
	Mix 2 (B2/C1/D1)	Mix 3 (B1/C2/D1)	Mix 4 (B1/C1/D2)	Mix 5 (B1/C2/D2)	Mix 6 (B2/C2/D2)
7 days	-5.1	2.3	4.0	3.4	-7.6
28 days	-8.0	-1.9	-2.2	-1.6	-8.2
90 days	-9.2	-3.3	-1.7	-2.0	-8.3

For concrete containing marine sand and seawater, as in Mix 3 (B1/C2/D1), Mix 4 (B1/C1/D2) and Mix 5 (B1/C2/D2), 7-day compressive strength increased by 2.3%, 4.0% and 3.4% respectively. The strength increase can be attributed to formation of Friedel’s salt which resulted from reaction between free chloride and aluminate ferrite monosulfate (AFm) hydrate (Ogirigbo and Ukpata, 2017; Shi et al., 2016). The Friedel’s salt can fill up pores and provide blocking effect which reduces concrete porosity and densifies pore structure. As a result, the concrete exhibited higher strength. The results tied well with previous studies performed by Katano et al. (2013), Shi et al. (2015) and Wegian (2010), wherein higher early strength was observed due to Friedel’s salt. Meanwhile, for long-term compressive strength, slight reduction was observed for all concrete mixes containing marine sand and seawater. For example, the reductions at 90 days for Mix 3 (B1/C2/D1), Mix 4 (B1/C1/D2) and Mix 5 (B1/C2/D2) were 3.3%, 1.7% and 2.0% respectively. The strength deterioration was attributed to gradual crystallization of salt from marine sand and seawater within the concrete pore at a later age. Accumulation of salt crystals can cause concrete expansion which develops micro-crack, resulting in strength reduction (Zhang et al., 2017). The decrease of long-term strength caused by excessive salt content is verified by sulphate salt immersion test, the results of which are presented later. Besides, Mix 6 (B2/C2/D2) concrete exhibited similar compressive strengths to Mix 2 (B2/C1/D1) concrete at all ages. This implies that marine sand and seawater do not bring about much negative effect to compressive strength on concrete batched with SiMn slag. As such, there is a potential for concrete manufactured with SiMn slag, marine sand and seawater to be used for commercial purpose from the perspective of compressive strength.

3.4.3. Effect on Splitting Tensile Strength

Development of concrete splitting tensile for all mixes is presented in Figure 3.14. The results showed that the strength ranged from 3.6 MPa to 4.6 MPa, 4.6 MPa to 5.2 MPa and 5.2 MPa to 6.4 MPa at 7 days, 28 days and 90 days respectively. All the concrete tensile strength increased orderly with curing time.

Overall result showed reduction of splitting tensile strength in concrete manufactured with SiMn slag. At 90-day age, the strength reduction was 17.5% and 14.5% for Mix 2 (B2/C1/D1) and Mix 6 (B2/C2/D2) respectively. Similar to compressive strength, the tensile strength decrease was due to flaky and elongated geometry exhibited by

SiMn slag which caused brittle and premature failure of concrete. It will be important that future research is extended to develop methods to produce round shaped SiMn slag for use as coarse aggregate in concreting. One possible method is by appropriate grinding and then screening, but extra cost and time may be incurred. Moreover, another reason was that smooth surface exhibited by SiMn slag had lessened adhesion and hence bonding of aggregate with cement paste. The results are in accordance with findings reported by Kazjonovs et al. (2010) who used smooth steel punch as coarse aggregate.

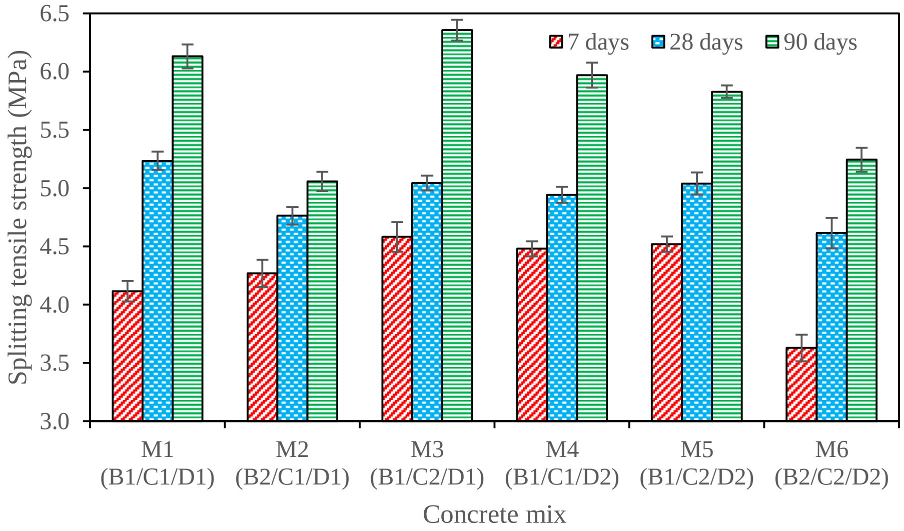

Figure 3.14: Splitting tensile strength of concrete incorporating SiMn slag, marine sand and seawater

Table 3.10: Splitting tensile strength variation with respect to control mix

Concrete age	**Variation of splitting tensile strength (%)**				
	Mix 2 (B2/C1/D1)	Mix 3 (B1/C2/D1)	Mix 4 (B1/C1/D2)	Mix 5 (B1/C2/D2)	Mix 6 (B2/C2/D2)
7 days	3.7	11.3	8.8	9.8	-11.8
28 days	-9.0	-3.6	-5.6	-3.7	-11.8
90 days	-17.5	3.7	-2.6	-4.9	-14.5

Marine sand and seawater improved concrete splitting tensile strength at 7-day age by 11.3%, 8.8% and 9.8% for Mix 3 (B1/C1/D2), Mix 4 (B1/C1/D2) and Mix 5 (B1/C2/D2) respectively. Similar to compressive strength, the strength increment at early age was due to pore refinement promoted by Friedel’s salt formation (Ogirigbo and Ukpata, 2017; Shi et al., 2016). Furthermore, Wegian (2010) also showed that concrete mixed with and cured in seawater possessed higher bonding strength and thus greater tensile strength. On long-term basis, concrete containing marine sand and seawater achieved comparable tensile strength to the control. Research performed by Wegian (2010) and Limeira et al. (2010) also indicated that marine sand and seawater had negligible effect on concrete tensile strength at later age.

The results of splitting tensile strength and compressive strength are generally similar. In this connection, correlation between tensile and compressive strength is established by using regression analysis based on experimental data. These two parameters can be as expressed as a power function shown as Eq. 3.18 below.

$$f_{st} = 0.2153 f_{cy}^{\ 0.7978} \qquad \text{Eq. 3.18}$$

where f_{st} is the splitting tensile strength and f_{cy} is the cylinder compressive strength.

The computed relationship has an acceptable R^2 value of 0.81. To show the validity of the equation, a comparison is made with Australian Standard (AS) and American Concrete Institute (ACI) as depicted in Figure 3.15. The AS 3600 (2018) provides a more conservative relationship between splitting tensile and compressive strength, while Eq. 3.18 shows closer relationship to that in ACI 318M-99 (2008) . This implies that incorporation of SiMn slag, marine sand and seawater has minimal effect on the relationship.

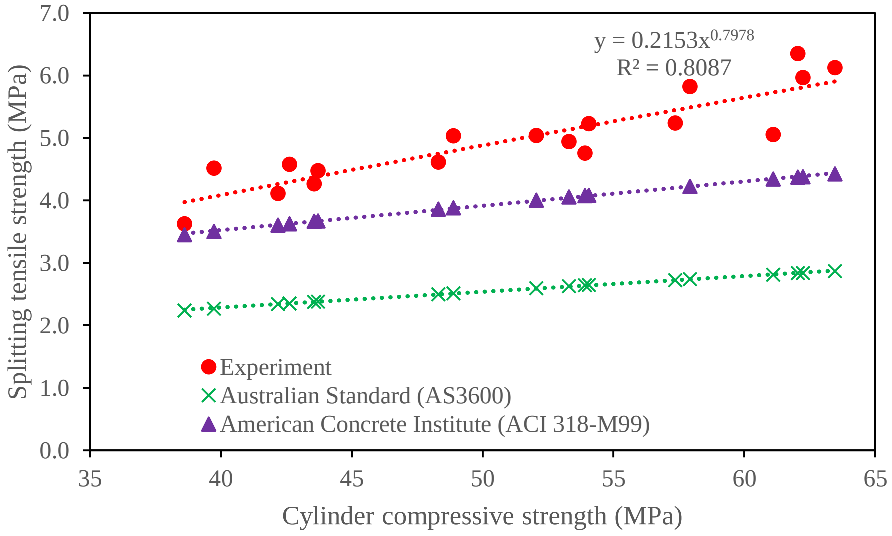

Figure 3.15: Correlation between splitting tensile and compressive strength

3.4.4. Water Absorption and Permeable Pore of Concrete

Figure 3.16 presents water absorption and permeable pore volume of concrete at 28 and 90 days. The water absorption ranged from 3.86% to 5.30%, 3.73% to 4.78% and 3.54% to 4.58% for 28-day, 90-day and 180-day ages respectively, while the concrete contained 11.25% to 14.03%, 10.79% to 13.04% and 10.01% to 12.14% pore volume respectively at these ages. The result generally indicated that water absorption increased with pore volume and vice versa. It also showed that water absorption and pore volume slightly decreased with concrete age. This was ascribed to more complete hydration of cement which produced increased calcium silicate hydrate (C-S-H) to fill up concrete pore.

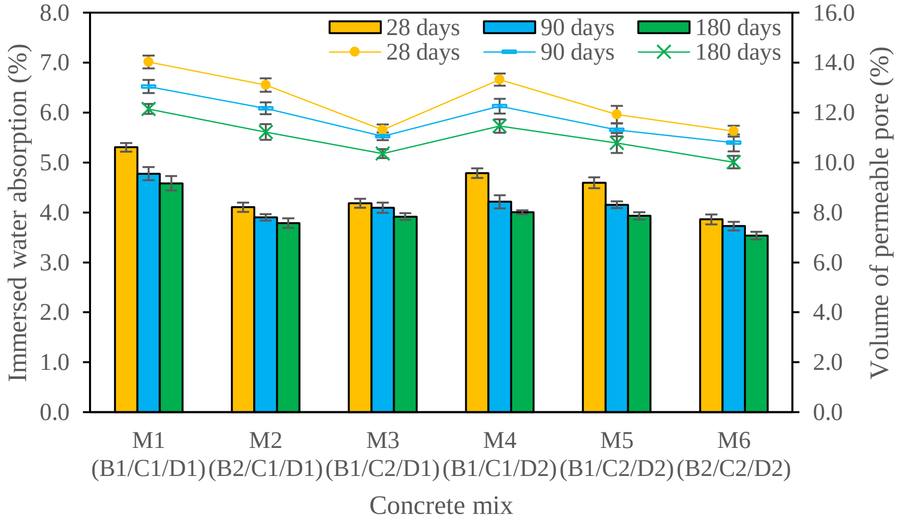

Figure 3.16: Immersed water absorption and volume of permeable pore of concrete incorporating SiMn slag, marine sand and seawater

The use of SiMn slag significantly reduced water absorption of concrete. This was due to lower water absorption capability of SiMn slag aggregate. As shown in Table 3.1, the SiMn slag and limestone aggregates were found to possess 0.21% and 0.66% water absorption respectively. In this regard, SiMn slag aggregate retains less amount of water and hence the resultant concrete exhibits lower water absorption. As for pore volume, it was reduced for concrete containing SiMn slag as well. This indicated that reduction of concrete water absorption was also attributed to lower porosity possessed by SiMn slag concrete. A similar observation was made in study conducted by Alsayed and Amjad (1996), whereby natural and crushed aggregates were used. Although the obtained water absorption values cannot unequivocally and directly measure concrete quality, they are still below 10% and hence within the range of good concrete defined by Neville (1995).

Water absorption and pore volume of concrete containing marine sand, as in Mix 3 (B1/C2/D1), decreased significantly at both 28-day and 90-day age. This was because of smaller particle size possessed by marine sand. In this regard, the fine marine sand can provide more densified microstructure. Cheng et al. (2018) also showed that marine sand minimized concrete porosity and hence capillary water absorption. As for the effect of seawater, Mix 4 (B1/C1/D2) concrete exhibited slightly lower water absorption and pore volume than the control. In alkaline environment of concrete, Friedel's salt could precipitate from AFm hydrate and chloride which was stable in high pH and able to fill concrete pores (Liu et al., 2014; Shi et al., 2015; Suryavanshi and Swamy, 1996). Although the study indicates that the porosity can be slightly reduced by Friedel's salt, the effect on permeability is not significant as shown in sorptivity test which will be explained and elaborated later. Also, the effect of seawater is not noticeable in Mix 5 (B1/C2/D2) as the pore refinement contributed by marine sand is more dominant.

From the results and explanation presented so far, it is logical that concrete incorporated with SiMn slag, marine sand and seawater exhibits the lowest water absorption and pore volume, as confirmed by test result of Mix 6 (B2/C2/D2). Nevertheless, water absorption and pore volume cannot best represent concrete durability as it only indicates water retention capacity. In fact, rate of water absorption is a better indicator of quality concrete. Therefore, concrete permeability has to be further assessed with sorptivity and rapid chloride ion penetration tests, the results of which are presented in the following section.

3.4.5. Effect on Sorptivity

Sorptivity test which measures rate of water absorption can more precisely evaluate concrete permeability. Water absorption curves of concrete of all mixes at 28-day, 90-day and 180-day ages in this research are depicted in Figure 3.17(a), Figure 3.17(b) and Figure 3.17(c) respectively. The curves consist of two stages which are initial and secondary stages, in which their slopes represent sorptivity of concrete as shown in Table 3.11. Initial sorptivity is greater as concrete pores are mostly empty at first and hence capillary flow occurs at faster rate, while the lower secondary sorptivity is due to slow filling of air void. As shown in the result, both types of sorptivity decreased with age for all concrete mixes. Similar to water absorption, more C-S-H was formed to densify concrete pore gradually as the concrete aged.

Table 3.11: Sorptivity at initial and secondary stages of concrete incorporating SiMn slag, marine sand and seawater

Concrete mix	**28 days**		**90 days**		**180 days**	
	Initial sorptivity (mm/sec$^{1/2}$)	Secondary sorptivity (mm/sec$^{1/2}$)	Initial sorptivity (mm/sec$^{1/2}$)	Secondary sorptivity (mm/sec$^{1/2}$)	Initial sorptivity (mm/sec$^{1/2}$)	Secondary sorptivity (mm/sec$^{1/2}$)
Mix 1 (B1/C1/D1)	0.0052	0.00095	0.0041	0.00085	0.0033	0.00075
Mix 2 (B2/C1/D1)	0.0070	0.00135	0.0043	0.00095	0.0036	0.00085
Mix 3 (B1/C2/D1)	0.0030	0.00055	0.0020	0.00050	0.0016	0.00040
Mix 4 (B1/C1/D2)	0.0055	0.00095	0.0050	0.00090	0.0043	0.00085
Mix 5 (B1/C2/D2)	0.0032	0.00060	0.0021	0.00055	0.0018	0.00045
Mix 6 (B2/C2/D2)	0.0048	0.00065	0.0035	0.00055	0.0031	0.00050

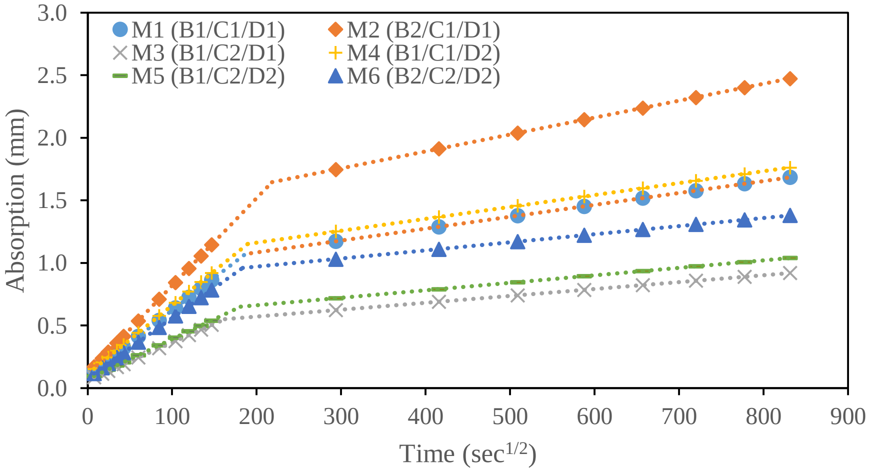

(a) 28 days

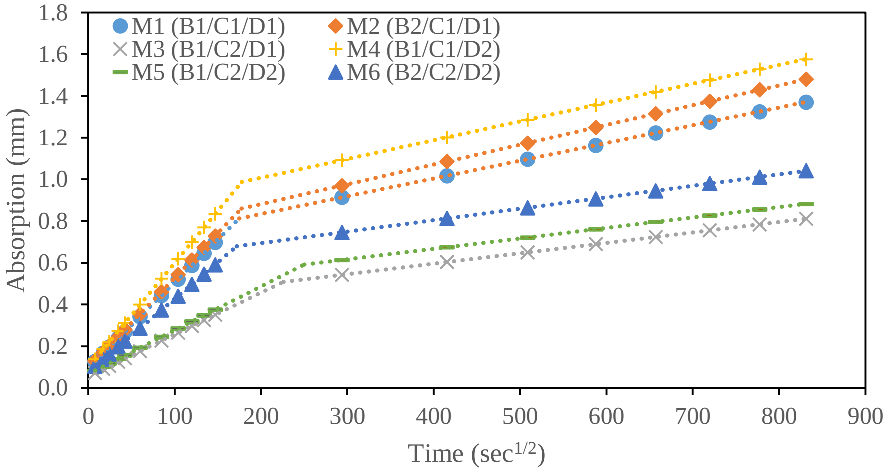

(b) 90 days

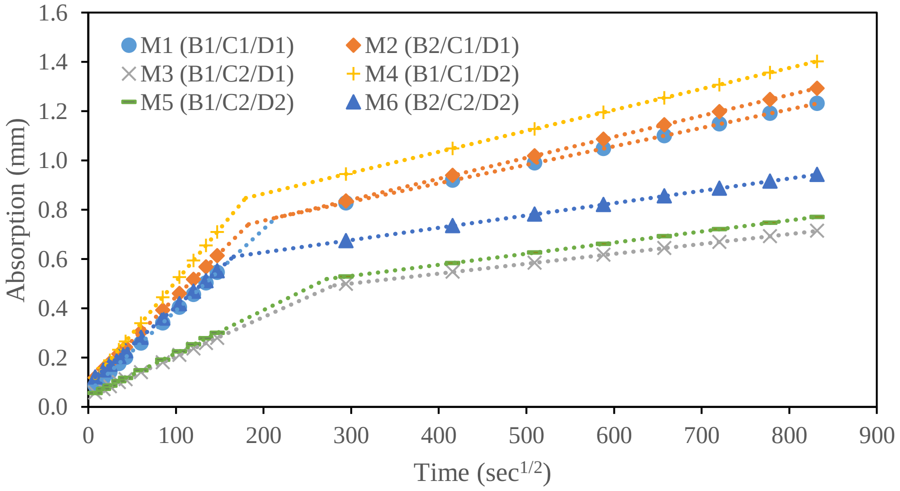

(c) 180 days

Figure 3.17: Cumulative absorption of concrete for different mixtures at (a) 28 days, (b) 90 days and (c) 180 days

Concrete casted with SiMn slag, as in Mix 2 (B2/C1/D1), exhibited higher sorptivity at 28-day age, but similar sorptivity at 90-day age when compared with control mix. Higher sorptivity at 28-day age was due to weaker bonding of smooth SiMn slag with cement matrix. According to Giaccio and Zerbino (1998), coarse aggregate possessing smooth surface will reduce concrete bonding strength and result in more porous interface. As a result, water ingress is higher. As for the improved sorptivity at 90-day and 180-day age, it might be attributed to weak pozzolanic reaction occurring within interfacial transition zone of the concrete. The mechanism of pozzolanic reaction involves formation of calcium silicate hydrate (C-S-H) or calcium aluminate hydrate (C-A-H) from reaction between calcium hydroxide and silicate or aluminate component (Sargent, 2015). Based on test result in Table 3.2, SiMn slag comprised 41% and 14% of silicon dioxide and aluminium oxide respectively. Although SiMn slag aggregate possesses relatively small specific surface area, it is still possible that small scale pozzolanic reaction can take place, especially on interface between the aggregate and cement paste. Study performed by Masateru et al. (2007) also showed that pozzolanic reaction which occurred on outer layer of coal fly ash aggregate, could refine its interface with cement matrix. As a result, some refinement may have been made on the concrete which reduces its porosity and hence sorptivity. As only a slight pozzolanic reaction occurs on interface between SiMn slag and cementitious matrix, improvement is not reflected in the compressive strength of concrete. Nevertheless, further investigation has to be carried out to confirm this finding.

The use of marine sand in Mix 3 (B1/C2/D1) significantly improved concrete durability as its sorptivity reduced by nearly half at all ages. This was because marine sand aggregate was smaller in size which provided more compacted concrete. Previous study conducted by Cheng et al. (2018) showed that marine sand could reduce porosity of cement paste, which optimized pore distribution, providing concrete with a denser microstructure. As shown in Mix 4 (B1/C1/D2), sorptivity of concrete mixed with seawater was almost the same as that of control mix. The result shows dissimilar effect as presented in the water absorption test. This implies that reduction of concrete porosity promoted by Friedel’s salt is not adequate to improve its permeability as it is also dependent on pore characteristics such as pore size and connectivity. The effect on permeability may not be detected and reflected in the test as variations of water absorption and porosity are small. The result was also confirmed by Mix 5 (B1/C2/D2) whereby seawater was used for casting. As for Mix 6 (B2/C2/D2), the result showed the ability of marine sand to offset drawback of SiMn slag aggregate on concrete sorptivity at 28-day age and even improve it at 90-day and 180-day ages. Overall, the use of SiMn slag, marine sand and seawater can produce concrete with lower sorptivity and hence make it more durable than normal concrete.

3.4.6. Effect on Rapid Chloride Ion Penetration

Alternatively, concrete permeability can also be measured based on its resistance to chloride ion penetration. Figure 3.18 summarizes chloride ion permeability of concrete of all the mixes at 28-day, 90-day and 180-day age. At 28-day age, concrete chloride penetration resistance which was measured as charge passed through it, ranged from 1885.6 to 2752.7 Coulomb (C). In this case, the concrete was graded as "moderate" permeability except for Mix 3 (B1/C2/D1) and Mix 5 (B1/C2/D2) which were graded as "low" permeability. The charge which passed through 90-day concrete ranged from 1421.8 to 1659.8 C and all concrete was classified as "low" permeability. As for 180-day age, the charge ranged from 758.3 to 1022.3 C and all concrete was graded as "very low" permeability except for Mix 2 (B2/C1/D1). This showed that concrete resistance to chloride ion penetration improved with curing. This was due to more complete hydration of cement which developed more C-S-H to fill concrete pore.

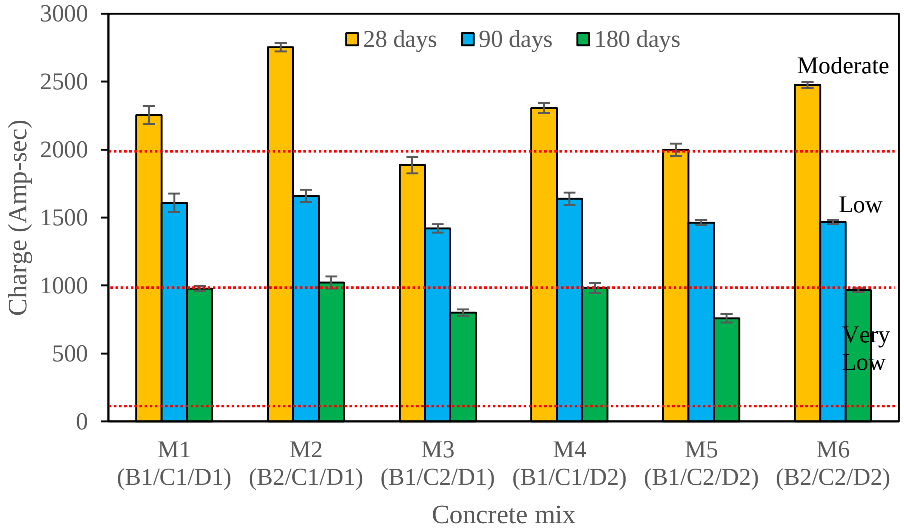

Figure 3.18: Chloride ion permeability of concrete incorporating SiMn slag, marine sand and seawater

Mix 2 (B2/C1/D1) concrete containing SiMn slag exhibited higher chloride permeability at 28-day age, but showed comparable permeability to control concrete at 90-day and 180-day age. The result showed the same trend as that of sorptivity test. Similarly, same explanation can be given to the improvement of concrete resistance to chloride ion penetration at later age, whereby weak pozzolanic reaction might have occurred to refine aggregate interface. In this case, chloride can also be bound onto extra C-S-H and C-A-H, improving chloride binding capacity of concrete.

Investigation by Frias et al. (2009) also showed that pozzolanic reaction resulted from SiMn slag enhanced concrete resistance against penetration of aggressive chemicals such as chloride, sulphate and seawater. Since both sorptivity and chloride penetration test results show that SiMn slag concrete possesses comparable permeability to normal concrete on long term, it has the potential to be used commercially.

As observed in Mix 3 (B1/C2/D1), the use of marine sand improved concrete resistance to chloride ion penetration at 28-day, 90-day and 180-day age. The finer particle size of marine sand reduced concrete pore volume and refined it into more compacted microstructure. According to Cheng et al. (2018), another possibility was that marine sand, being more fine and having higher surface area, can retain more water to promote hydration through internal curing. As for seawater, the test result of Mix 4 (B1/C1/D2) showed that it had negligible effect on chloride permeability of concrete. This also implied that the permeability reduction of Mix 5 (B1/C2/D2) concrete, which was made from both marine sand and seawater, was ascribed to the effect of marine sand. As for Mix 6 (B2/C2/D2), it had been shown that marine sand improved concrete resistance to chloride penetration as well.

In summary, the test results of chloride ion permeability of all mixes agree well with those of sorptivity. It has been proven that combining SiMn slag, marine sand and seawater for concreting can result in more durable concrete than conventional concrete.

3.4.7. Effect on Resistance to Sulphate Attack

Sulphate immersion test measures concrete resistance to sulphate attack in terms of compressive strength loss. Figure 3.19 depicts the loss of compressive strength for all concrete mixes at 7-day, 28-day and 90-day immersion periods. It was observed that loss of concrete compressive strength increased with immersion time. After 7 days of immersion, the strength loss ranged from 0.28% to 1.69% which was negligible. Meanwhile, strength loss after 28 days of immersion increased slightly to a range of 2.07% to 3.53%. Concrete strength loss after 90 days of immersion, which became more noticeable, was between 7.92% and 9.90%. The strength loss was attributed to the formation of expansive ettringite and gypsum due to reaction between sulphate and hydration products such as C-A-H and calcium hydroxide, which induced stress in concrete (Tang et al., 2018). Another deterioration mechanism was the formation of salt crystal within concrete pore which caused damage through expansion and subsequently led to the development of concrete micro-crack.

Although the variation between the mixes was minimal, it had been observed that SiMn slag exhibited slightly lower resistance to sulphate attack than the control for all immersion durations. As the test was carried out after 7-day of curing, initial lower hydration rate of SiMn slag concrete had made it more permeable to sulphate intrusion which caused more damage. It was also shown in Mix 3 (B1/C2/D1), Mix 5 (B1/C2/D2) and Mix 6 (B2/C2/D2) that marine sand could enhance concrete resistance to sulphate attack. As explained previously, finer marine sand had produced concrete with lower permeability that reduced sulphate ingression. Also, the result showed that seawater slightly reduced concrete damage caused by sulphate attack. This was due to the lower porosity of the concrete contributed by Friedel’s salt. On the whole, concrete incorporated with SiMn slag, marine sand and seawater displayed slightly higher resistance against sulphate attack.

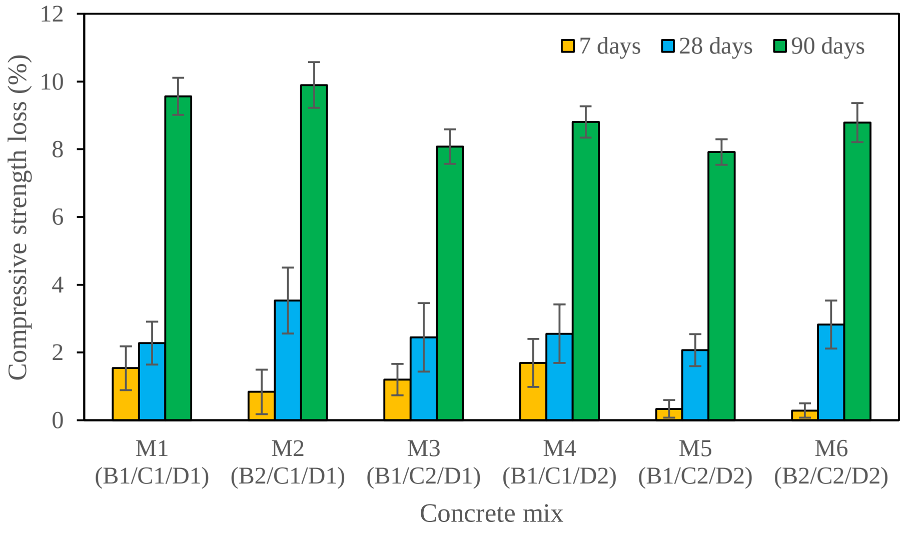

Figure 3.19: Loss of compressive strength for all concrete mixes

3.4.8. SEM Analysis

Scanning electron microscope (SEM) analysis has been conducted to assess the interfacial transition zone (ITZ) between cement paste and aggregate of concrete. The SEM images showing the ITZ for Mix 1 (B1/C1/D1) and Mix 5 (B1/C2/D2) concrete at 28-day age are presented in Figure 3.20 and Figure 3.21 respectively. Both concretes showed the presence of C-S-H as cloud-like morphology and $Ca(OH)_2$ as hexagonal plate-like crystals in the cement paste. The SEM images showed that Mix 5 (B1/C2/D2) concrete had a more uniform distribution of cement paste over the ITZ compared to control concrete, Mix 1 (B1/C1/D1). The void present in the ITZ of Mix 5 (B1/C2/D2) concrete was smaller and less than that of control concrete. This indicated that the marine sand in Mix 5 (B1/C2/D2) could improve the pore distribution and reduce the porosity of cement paste due to its finer property. The SEM analysis has confirmed the improved concrete strength and durability with the incorporation of marine sand.

SEM images for Mix 6 (B2/C2/D2) concrete at 7 days and 28 days are shown Figure 3.22 and Figure 3.23 respectively. More hexagonal plate-like crystals of $Ca(OH)_2$ were found in 28-day concrete than 7-day concrete. This indicated that the hydration of the cement became more complete with a longer period of concrete curing. Although $Ca(OH)_2$ is a secondary product of cement hydration and does not contribute to concrete strength, its existence may be an indication of a more complete reaction. In addition, 28-day concrete had a slightly less visible ITZ than 7-day concrete, indicating a more compact microstructure as a result of more complete hydration. The SEM analysis also showed that the use of SiMn slag aggregate in Mix 6 (B2/C2/D2) could produce concrete with an ITZ comparable to that of limestone in Mix 5 (B1/C2/D2). Besides, the SEM images of both SiMn slag concrete also confirmed the positive effect of marine sand on ITZ when compared to the control. In short, the findings of SEM analysis are consistent with those of strength and durability analyses and have validated the applicability of marine sand, seawater and SiMn slag as concreting materials.

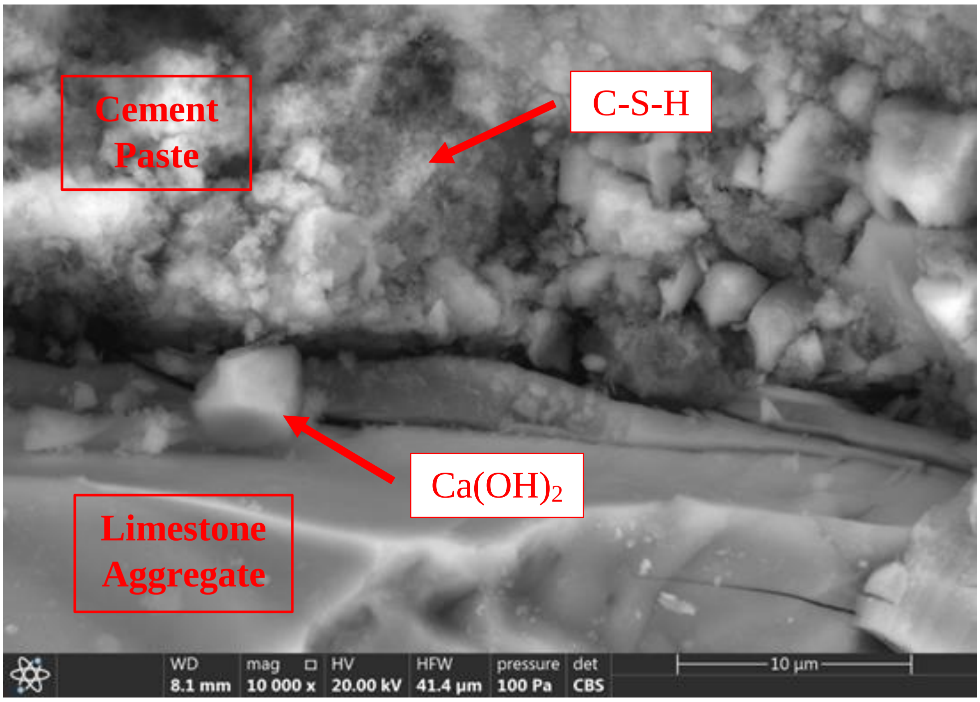

Figure 3.20: SEM image on ITZ of Mix 1 (B1/C1/D1) at 28 days

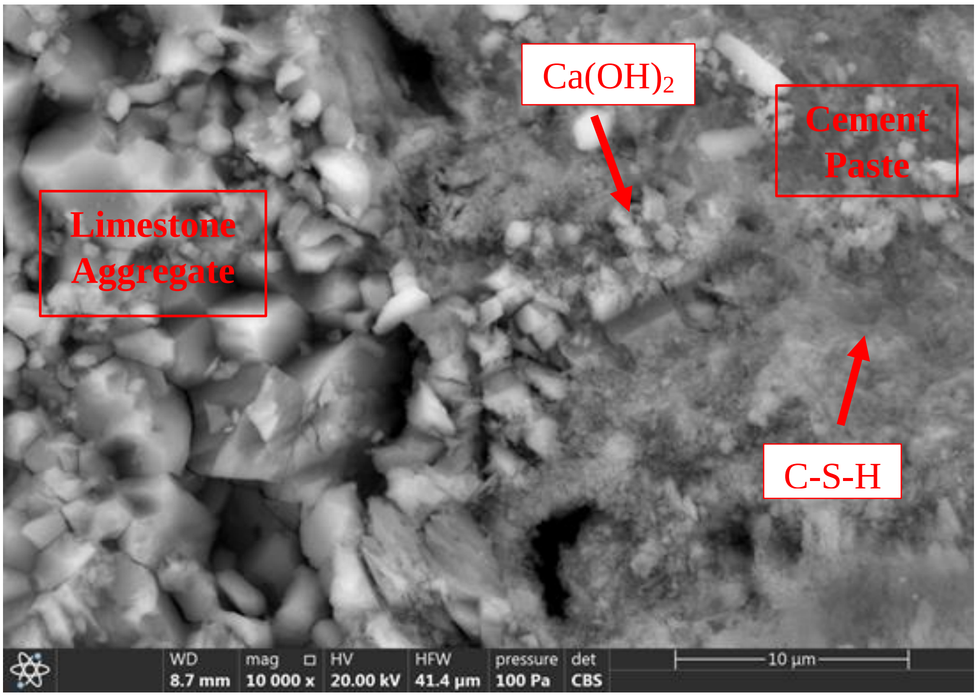

Figure 3.21: SEM image on ITZ of Mix 5 (B1/C2/D2) at 28 days

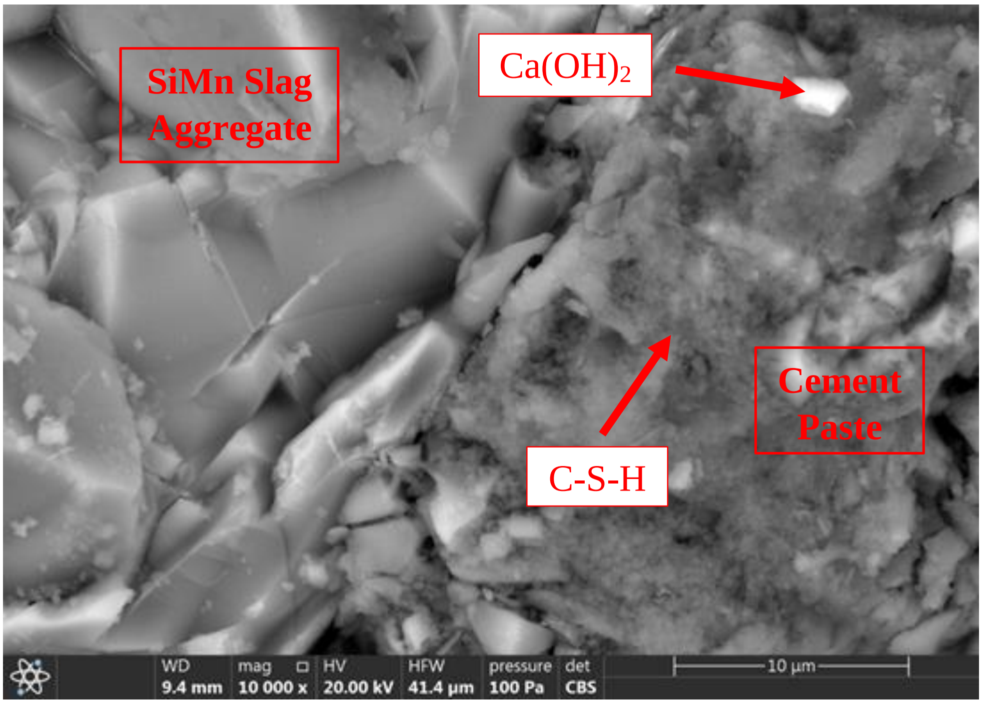

Figure 3.22: SEM image on ITZ of Mix 6 (B2/C2/D2) at 7 days

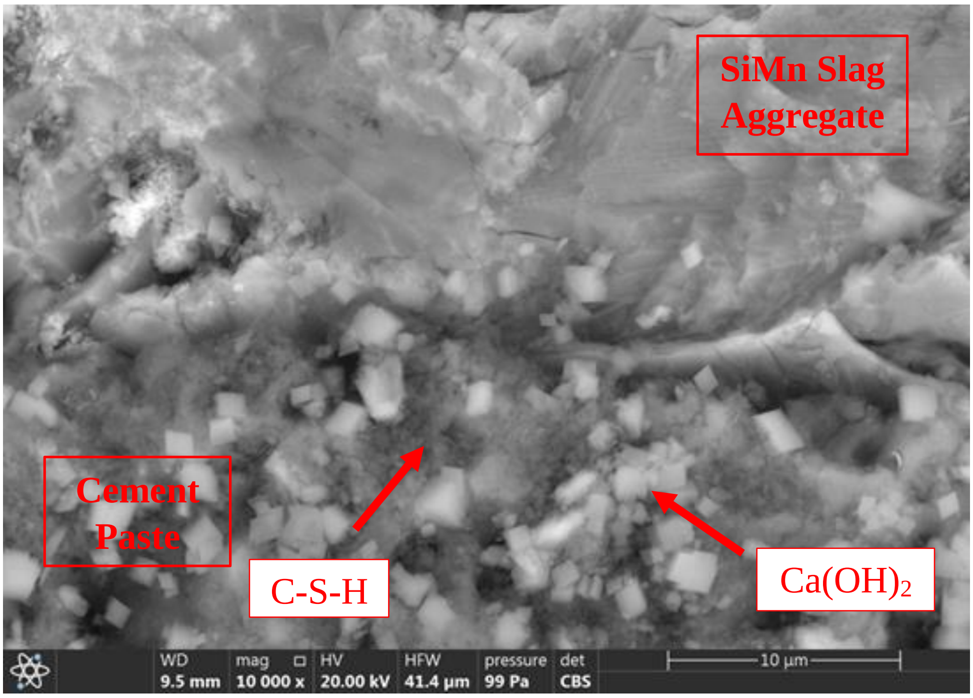

Figure 3.23: SEM image on ITZ of Mix 6 (B2/C2/D2) at 28 days

3.5. Concluding Remark

The result of this experimental investigation has provided a better insight into strength and durability of concrete containing SiMn slag, marine sand and seawater. In this regard, the following conclusions can be drawn:

1. Incorporation of SiMn slag as coarse aggregate for concreting had reduced concrete workability by 36% due to poor aggregate size grading. Marine sand and seawater also reduced concrete slump by 26% and 32% respectively.
2. The incorporation of SiMn slag slightly reduced the compressive and tensile strengths of concrete due to its flaky characteristic, but it was still a viable alternative to limestone aggregate. It also was demonstrated that concrete manufactured with marine sand and seawater achieved higher strength at early age, but lower late strength than conventional concrete.
3. SiMn slag concrete exhibited lower water absorption, with values of 4.1%, 3.9% and 3.8% at 28-day, 90-day and 180-day ages respectively, compared to control concrete with values of 5.3%, 4.8% and 4.6% at these ages, due to the lower water absorption characteristic of SiMn slag aggregate. Water absorption of the concrete could be further reduced to 3.9%, 3.7% and 3.5% at 28-day, 90-day and 180-day ages respectively by incorporating with marine sand and seawater which had characteristic of better filling up concrete pores.
4. Both sorptivity and rapid chloride penetration tests showed that incorporation of SiMn slag increased concrete permeability at 28-day age as compared to conventional concrete. However, similar permeability of these two types of concrete was shown by the tests at 90-day and 180-day ages. Also, the use of marine sand reduced concrete permeability and was able to offset the drawback of SiMn slag aggregate in the aspect of durability.
5. Sulphate immersion test demonstrated that the loss of concrete compressive strength due to sulphate attack was small after 7 days and 28 days of testing. But, the loss became more significant after 90-day immersion time with the highest loss value of 9.9%.
6. The SEM analysis showed that the use of marine sand produced concrete with a more compact ITZ and less void in the cement paste. As for the effect of SiMn slag, the results showed a proper bonding between cement paste and SiMn slag aggregate and had an ITZ similar to the limestone concrete.

Despite the slight reduction in the strength, it is possible to produce a more sustainable concrete with incorporation of SiMn slag, marine sand and seawater, as in Mix 6 (B2/C2/D2), for potential industrial use. In this regard, Mix 6 (B2/C2/D2) is used for the subsequent study in Chapter 4.

Chapter 4. Binders Optimization for Silicomanganese Slag Concrete Using Response Surface Methodology

This chapter has been published in the journal paper entitled "Prediction model for hardened state properties of silica fume and fly ash based seawater concrete incorporating silicomanganese slag" (Journal of Building Engineering, Q1, https://doi.org/10.1016/j.jobe.2021.102356).

4.1. Introduction

This chapter investigates the effect of fly ash (FA) and silica fume (SF) on workability, strength and durability of concrete through experiment and Response Surface Method (RSM). The aim of this study is to use the binary and ternary cement blends of FA and SF for compensating the drawback, in terms of strength and durability of concrete incorporated with silicomanganese (SiMn) slag, marine sand and seawater, also referred to as Mix 6 (B2/C2/D2) in Chapter 3. The study investigated the interactions between FA and SF in SiMn slag concrete by statistically evaluating the experimental results. The relationships were established between the replacement levels of FA and SF with concrete strength, durability and workability. Prediction model of the concrete properties was developed by using the RSM for optimization. The two-way analysis of variance (ANOVA) was used to evaluate the fitness of developed model for prediction and optimization. The outcomes of optimization were validated by conducting further experiments and SEM analysis. Furthermore, the prediction model was used to predict the properties of concrete produced from the limestone aggregate to demonstrate the applicability of the model.

4.2. Experimental Programme

The main objective of the research presented in this section is to further improve the SiMn slag concrete known as Mix 6 (B2/C2/D2) in Objective 1. The concrete was produced from cement as binder, SiMn slag as coarse aggregate, marine sand as fine aggregate and seawater. Similar concrete mix proportions have been used in this investigation, but with SF and FA as partial cement replacements.

4.2.1. Material

4.2.1.1. Cement

The same ordinary Portland cement (OPC) as described in Section 3.2.1.1 was used for the batching of concrete. The OPC used was graded as CEM 1 42.5. As shown in Table 4.1, the OPC consisted high amount of 68.97% of calcium oxide (CaO), which provided the cementing property in concrete when hydrated.

4.2.1.2. Fly Ash

FA used in this research was brown in colour as shown in Figure 4.2(a). The chemical composition of FA is presented in Table 4.1. It comprised 68% of the total of SiO_2, Al_2O_3 and Fe_2O_3 and was classified as class C FA according to ASTM C618 (2019) standard. The phase composition of FA has been determined using the XRD analysis as shown in Figure 4.1(a). The FA contained quartz (SiO_2), mullite ($2Al_2O_3.2SiO_2$) and gehlenite ($Ca_2Al[AlSiO_7]$), the findings of which were consistent with the chemical composition. Its specific gravity was 2.98.

4.2.1.3. Silica Fume

SF used in this research was a black powdery material as shown in Figure 4.2(b). The chemical composition of SF is presented in Table 4.1. The SF primarily contained silica with 96.21% of SiO_2. The specific gravity of this type of SF was 2.43. This was consistent with the phase composition. The SF contained quartz as shown in Figure 4.1(b). Amorphous silica and alumina were indicated as a broad hump in the XRD spectrum as shown in Figure 4.1.

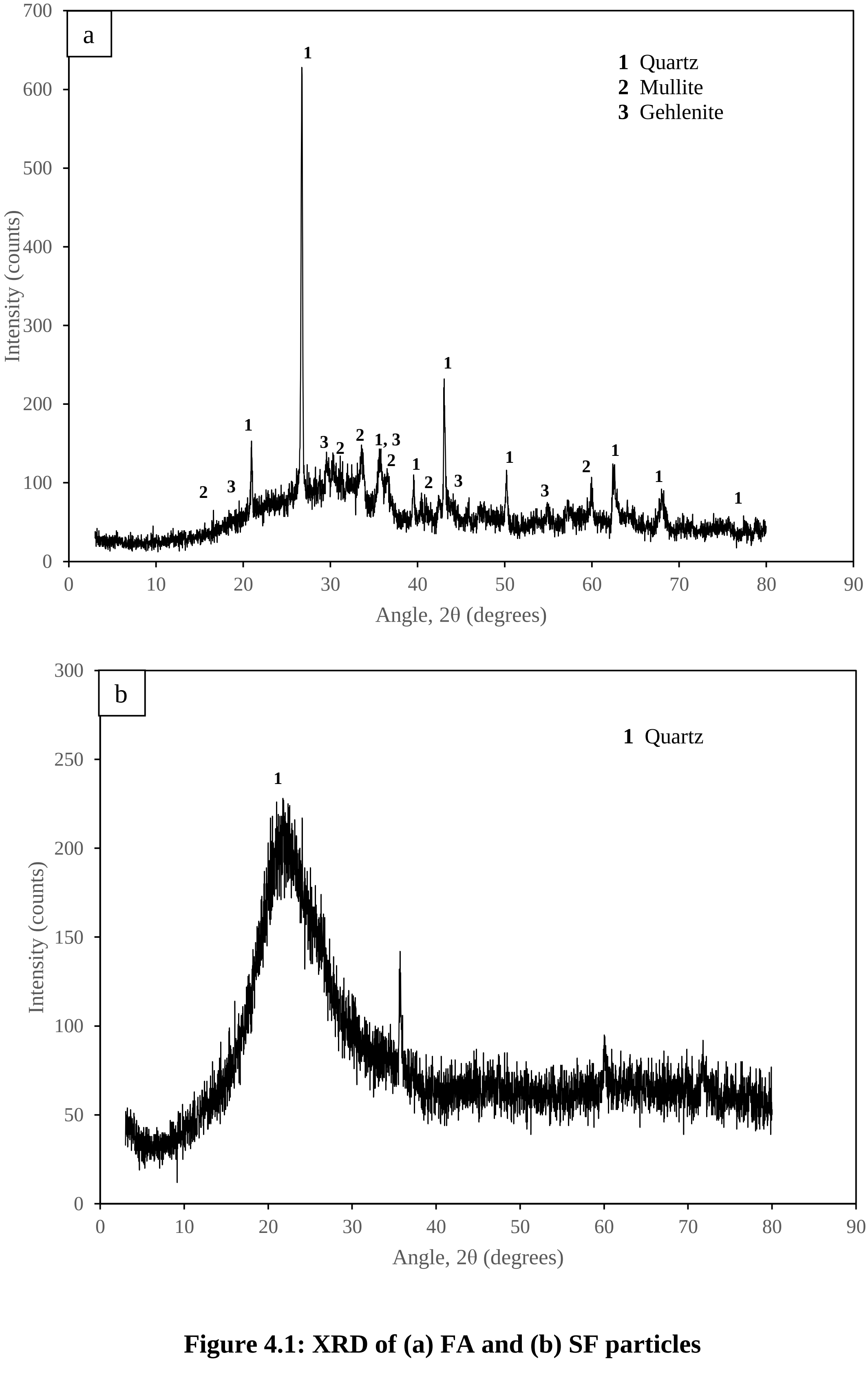

Figure 4.1: XRD of (a) FA and (b) SF particles

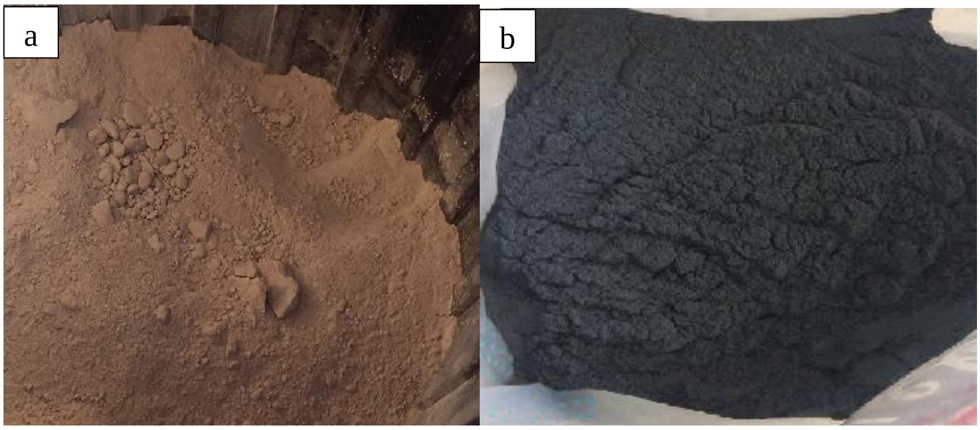

Figure 4.2: (a) FA sample and (b) SF sample

Table 4.1: Chemical composition of OPC, FA and SF

Chemical composition	OPC (%)	FA (%)	SF (%)
Calcium oxide (CaO)	68.97	18.86	0.06
Silicon dioxide (SiO_2)	16.29	38.91	96.21
Aluminium oxide (Al_2O_3)	4.17	13.4	0.04
Ferric oxide (Fe_2O_3)	3.51	15.68	0.15
Magnesium oxide (MgO)	1.73	3.99	0.46
Sulfur trioxide (SO_3)	-	1.84	-
Potassium oxide (K_2O)	0.99	2.5	0.28
Sodium oxide (Na_2O)	0.1	2.11	0.09
Loss on ignition (LOI)	-	1.66	1.71

4.2.1.4. Aggregate, Mixing Water and Chemical Admixture

In order to investigate the effect of FA and SF as a partial replacement of binder, the same concrete components of Mix 6 (B2/C2/D2) from Chapter 3 were used. In this regard, SiMn slag was used as coarse aggregate, marine sand sampled at Tanjung Lobang Beach and mixed with 30% of quarry dust by volume was used as fine aggregate, and seawater was used as mixing water. Limestone was also used as coarse aggregate for comparison purpose. The seawater was slightly alkaline and had a pH value of 8.1. This suggested that the seawater could potentially react with silica and alumina content of FA and SF to cause geo-polymerization (Lv et al., 2020). In addition, sodium naphthalene sulphonate formaldehyde, which was categorized as a Type A chemical admixture in accordance with the ASTM C494 (2019) standard, was used as superplasticizer. More detailed material characterization was provided in

Section 3.2.1.2 for the coarse aggregate, Section 3.2.1.3 for the fine aggregate, Section 3.2.1.4 for the mixing water and Section 3.2.1.5 for the superplasticizer.

4.2.2. Response Surface Method

RSM is a statistical technique used to develop a mathematical model that describes one or more responses over a range of input variables (Whitcomb and Anderson, 2004). The RSM establishes a polynomial relationship between the responses and the variables, including their influence and significance to the model. The model can be used to predict and optimize the response. The development of the statistical model begins with the collection of experimental data, followed by the selection of an appropriate model to fit the data. The model is then evaluated for adequacy. A statistical software, Design Expert v11, has been used for the design of experiment, mathematical formulation, statistical analysis and response optimization (Design-Expert, 2018). This software uses analysis of variance (ANOVA) to investigate the interaction among variables as well as their influence on the response.

The responses studied in this investigation are compressive strength (y_1), splitting tensile strength (y_2), sorptivity (y_3), chloride permeability (y_4) and slump value (y_5). The variables that control these responses are FA/B (x_1) and SF/B (x_2), which represent the ratio of fly ash and silica fume contents to the total binder, respectively. The variable ranges are 0–0.4 for FA/B and 0–0.3 for SF/B. Ponikiewski and Gołaszewski (2014) recommended the use of FA up to 30%, while Kwan and Chen (2013) suggested an addition not exceeding 40%. This study therefore chooses the upper limit of 40% to avoid excessive loss of concrete strength due to the FA replacement (Sumer, 2012). As for SF, Aldahdooh et al. (2013) and Tripathi et al. (2020) found an optimum replacement level of 23% and 20% respectively. The SF replacement level used in this study is limited to 30% because further addition will increase concrete cohesiveness and affect the mixture homogeneity (Ahmad, 2017).

The mathematical formulation developed using RSM can be expressed as a quadratic or higher-order polynomial equation as shown in Eq. 4.1.

$$y = \beta_o + \sum_{i=1}^{k} \beta_i x_i + \sum_{i=1}^{k} \beta_j x_i{}^2 + \sum_{i}^{k} \sum_{j}^{k} \beta_{ij} x_i x_j + \cdots + \sum_{i}^{k} \beta_h x_h{}^h + \varepsilon \qquad \text{Eq. 4.1}$$

In the equation, y denotes the response, x indicates the coded value of variable, β is the coefficient of regression, k is the number of variable, i, j as well as h are the polynomial degrees of the model representing linear, quadratic and higher-order polynomials respectively, and ε is a random error in the system (DeRousseau et al., 2018; Rezaifar et al., 2016).

4.2.3. Design of Concrete Mixture

Table 4.2 shows twenty-one concrete mixtures used to assess the strength and durability of SF and FA based concrete. The Central Composite Design (CCD) method, an effective approach to design experiments, was used to develop these combinations of concrete mixtures. Two variables, FA/B and SF/B, were inputs for the design of experiment. Figure 4.3 illustrates all the design points of the CCD, where each point represents one type of concrete mixture. The variables at the boundary in CCD are coded as α. The face-centered CCD was used, which limited the coded values of +α and -α to +1 and -1 respectively. These coded values refer to the area bound by the regression model that is effective in predicting the response. This method initially recommended thirteen concrete mixtures, which were mix no. 1–4 as factorial points, 5–8 as axial points and 9–13 as center points as shown in Figure 4.3. Five center points were used to compute the error within concrete mixture and to determine the repeatability. However, the recommended concrete mixtures had a large gap between the design points, which was not sufficient to produce a more precise trend in experimental results. As such, eight additional concrete mixtures (mix no. 14–21) distributed at the boundary of variables were included, as shown in Figure 4.3.

Control concrete mix design denoted as “Control” was obtained from Mix 6 (B2/C2/D2) in Chapter 3. FA and SF were incorporated to partially replace the OPC of Control mix in accordance with the outcome of CCD. The incorporation of FA and SF was based on the absolute volume concept as described in Section 3.3.1. Mix description was used to denote the detail of binder replacement level of each mixture. For example, mix no. 4 was referred to as “FA40SF30”, which indicated a ternary blend of 40% FA and 30% SF. The w/c ratio of all mixtures remained constant at 0.32. The dosage of SP was 1% of the total binder content. In order to study the effect of FA and SF on concrete workability, the SP dosage remained constant. The compaction time of fresh concrete would be increased if the workability was found to be unsatisfactory in accordance with ASTM C192 (2012) standard. This was to ensure the homogeneity of the concrete produced. Compressive strength, splitting tensile strength, sorptivity, chloride permeability and slump value of all mixtures were determined. Mix no. 0 referred to as “Limestone” was included for comparison purpose. Limestone mix was the Mix 5 (B1/C2/D2) in Chapter 3, which had the same mixture proportions as Control mix, except that SiMn slag was completely replaced by limestone as coarse aggregate.

Table 4.2: Mix proportion for fly ash and silica fume based concrete

Mix no.	Mix description	FA/B	SF/B	OPC (kg/m^3)	SiMn slag (kg/m^3)	Marine sand (kg/m^3)	Quarry dust (kg/m^3)	Seawater (kg/m^3)	SP (kg/m^3)
0	Limestone	0	0	550	965*	515	173	176	5.5
1	Control	0	0	550	1115	515	173	176	5.5
2	SF30	0	0.3	385	1115	488	164	176	5.5
3	FA40	0.4	0	330	1115	508	171	176	5.5
4	FA40SF30	0.4	0.3	165	1115	481	161	176	5.5
5	FA20	0.2	0	440	1115	512	172	176	5.5
6	FA20SF30	0.2	0.3	275	1115	484	162	176	5.5
7	SF15	0	0.15	468	1115	501	168	176	5.5
8	FA40SF15	0.4	0.15	248	1115	494	166	176	5.5
9	FA20SF15	0.2	0.15	358	1115	498	167	176	5.5
10	FA20SF15	0.2	0.15	358	1115	498	167	176	5.5
11	FA20SF15	0.2	0.15	358	1115	498	167	176	5.5
12	FA20SF15	0.2	0.15	358	1115	498	167	176	5.5
13	FA20SF15	0.2	0.15	358	1115	498	167	176	5.5
14	SF7.5	0	0.075	509	1115	508	171	176	5.5
15	SF22.5	0	0.225	426	1115	495	166	176	5.5
16	FA10	0.1	0	495	1115	514	172	176	5.5
17	FA30	0.3	0	385	1115	510	171	176	5.5
18	FA10SF30	0.1	0.3	330	1115	486	163	176	5.5
19	FA30SF30	0.3	0.3	220	1115	482	162	176	5.5
20	FA40SF7.5	0.4	0.075	289	1115	501	168	176	5.5
21	FA40SF22.5	0.4	0.225	206	1115	488	164	176	5.5

Note:
FA/B is the ratio of FA content to the total binder content.
SF/B is the ratio of SF content to the total binder content.
*Limestone was used to fully replace the SiMn slag as coarse aggregate in this mixture.

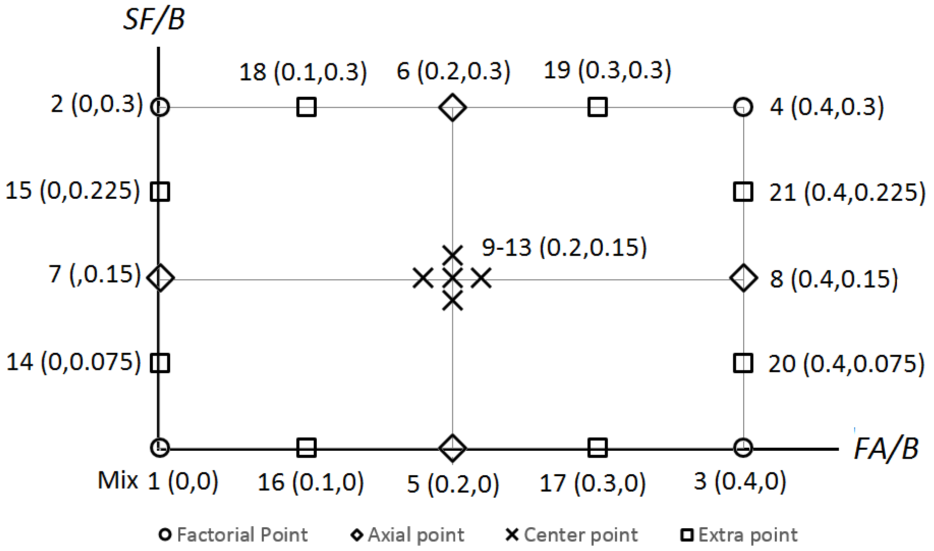

Figure 4.3: Design of experiment using CCD

4.2.4. Experimental Method

4.2.4.1. Preparation of Concrete Specimen

The same concrete mixing method described in Section 3.2.2 was used for the preparation of concrete specimen. In this investigation, FA and SF were first blended with OPC for 30 seconds before mixing with coarse and fine aggregates in order to ensure uniform distribution of the binder.

4.2.4.2. Compressive Strength Test

The test setup presented in Section 3.2.3.2 was used for the compressive strength test. The compression test was performed on cube specimen with dimension of 100 x 100 x 100 mm. Concrete specimen for all mixes was tested after 7, 28 and 90 days of curing except for the Control and Limestone mixes, which were tested for 1, 7, 14, 28, 56 and 90 days.

4.2.4.3. Splitting Tensile Strength Test

The test setup presented in Section 3.2.3.3 was used for the splitting tensile strength test. Cylindrical specimen of 100 mm diameter and 200 mm length was prepared and tested at 7, 28 and 90 days for all mixes.

4.2.4.4. Sorptivity Test

The same testing procedure presented in Section 3.2.3.5 was used for the sorptivity test. The test was conducted on concrete specimen for all mixes after 28, 90 and 180 days of curing except for the Control and Limestone mixes, which were tested for 14, 28, 56, 90 and 180 days.

4.2.4.5. Rapid Chloride Ion Penetration Test

The same testing procedure presented in Section 3.2.3.6 was used for the RCPT. The test was conducted on concrete specimen for all mixes after 28, 90 and 180 days of curing.

4.2.4.6. Scanning Electron Microscope Analysis

Concrete specimen was prepared using the method described in Section 3.2.3.8. The SEM analysis was carried out on concrete specimen for the Control and optimized mixes at 315 days of age. The purpose of SEM analysis was to assess the long-term performance of the concrete.

4.3. Experimental Result and Discussion

Table 4.3 presents test results for concrete mixes no. 9–13 (center points in CCD). These mixes are the SiMn slag concrete incorporated with 20% FA and 15% SF. Based on the results, the repeatability of experiment is examined. The discrepancy of all concrete properties was small. The highest standard deviation was 5.27 mm for concrete slump, 1.53 MPa for compressive strength, 0.11 MPa for splitting tensile strength, $0.13\text{x}10^{-3}$ mm/sec$^{1/2}$ for sorptivity and 16.7 C for chloride permeability. The coefficient of variance ranged from 1.64% to 6.21%, indicating a small degree of dispersion over the mean. The analysis showed that the deviation of results was within the acceptable range and that the error of repeated tests was unlikely to result in imprecision.

Table 4.3: Repeatability of concrete property in experiment

Concrete property	Test result of FA20SF15					Mean (n=5)	SD	COV (%)
	Mix no. 9	Mix no. 10	Mix no. 11	Mix no. 12	Mix no. 13			
Slump value (mm)	89	77	88	80	90	84.8	5.27	6.21
7-day compressive strength (MPa)	52.87	55.81	53.19	52.02	55.12	53.8	1.43	2.65
28-day compressive strength (MPa)	74.89	78.39	76.24	75.93	78.34	76.76	1.39	1.81
90-day compressive strength (MPa)	90.63	94.76	93.47	91.89	94.23	93	1.53	1.64
7-day splitting tensile strength (MPa)	3.44	3.69	3.71	3.59	3.62	3.61	0.09	2.63
28-day splitting tensile strength (MPa)	5.35	5.56	5.54	5.29	5.46	5.44	0.11	1.95
90-day splitting tensile strength (MPa)	6.03	6.28	6.23	6.01	6.17	6.14	0.11	1.77
28-day sorptivity (mm/sec$^{1/2}$x10^{-3})	3.12	2.96	2.91	2.99	2.71	2.94	0.13	4.55
90-day sorptivity (mm/sec$^{1/2}$x10^{-3})	2.9	2.8	271	2.82	2.6	2.77	0.1	1.77
180-day sorptivity (mm/sec$^{1/2}$x10^{-3})	2.54	2.49	2.42	2.49	2.42	2.47	0.05	1.92
28-day chloride permeability (C)	997.3	996.35	995.5	973.95	951.1	967.6	16.7	1.73
90-day chloride permeability (C)	702	681.9	670.5	701.6	660.1	683.2	16.66	2.44
180-day chloride permeability (C)	502	481.85	471.3	493	465	482.6	13.58	2.84
SD – Standard deviation; COV – Coefficient of variance								

4.3.1. Comparison of Compressive Strength between SiMn Slag and Limestone Concrete

Figure 4.4 shows the development of compressive strength of the limestone concrete and control concrete, also referred to as SiMn slag concrete. Both types of concrete increased in strength with curing time, but the strength gain slowly decreased. Concrete compressive strength at 1, 7 and 28 days was approximately 40%, 70% and 80% of 90-day strength respectively. This showed that the hydration became more complete as the concrete aged. The strength of limestone concrete was slightly higher than that of control concrete. The percentage difference was 11.7%, 10.6%, 8.5%, 4.1%, 4.7% and 5.2% at 1, 7, 14, 28, 56 and 90 days respectively. This was due to the angular shape and smooth surface of SiMn slag aggregate, which weakened the bonding with cementitious paste. The strength reduction was also ascribed to stronger aggregate characteristics of limestone than SiMn slag. The limestone aggregate had a higher abrasion resistance than SiMn slag as shown in Table 3.1, which produced a higher strength concrete. The findings were consistent with the study of Kilic et al. (2008), in which the concrete compressive strength improved when a stronger aggregate was used.

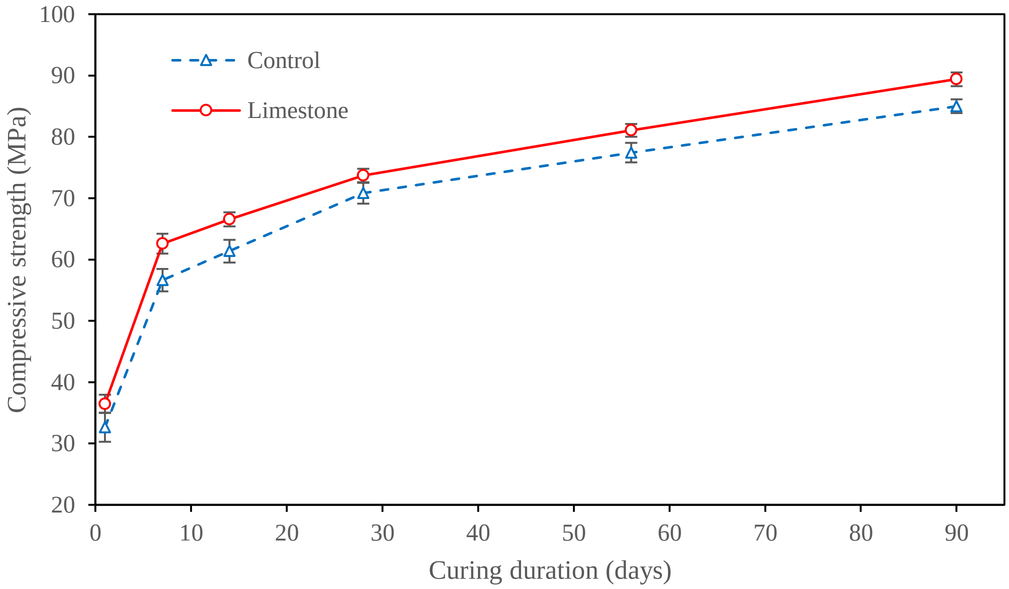

Figure 4.4: Control and limestone concrete compressive strength

The strength difference between the two concrete types was constant at various ages. The average strength difference was 4.33 MPa and the standard deviation was 1.03 MPa, indicating a fairly linear strength relationship between limestone and control concrete. In this context, the correlation between the compressive strength of the two concrete types was established by means of a regression analysis as shown in Figure 4.5. The two compressive strengths were presented as a linear equation in Eq. 4.2.

$$\mathrm{f_{c,LS}} = 0.991\mathrm{f_{c,SM}} + 4.9027 \qquad \text{Eq. 4.2}$$

In Eq. 4.2, $\mathrm{f_{c,LS}}$ represents the compressive strength of limestone concrete and $\mathrm{f_{c,SM}}$ refers to the compressive strength of control concrete. The established correlation has an R^2 value of 0.9963, indicating a high fitness for the regression model. The equation can be used to estimate the compressive strength of limestone concrete based on that of SiMn slag concrete and vice versa.

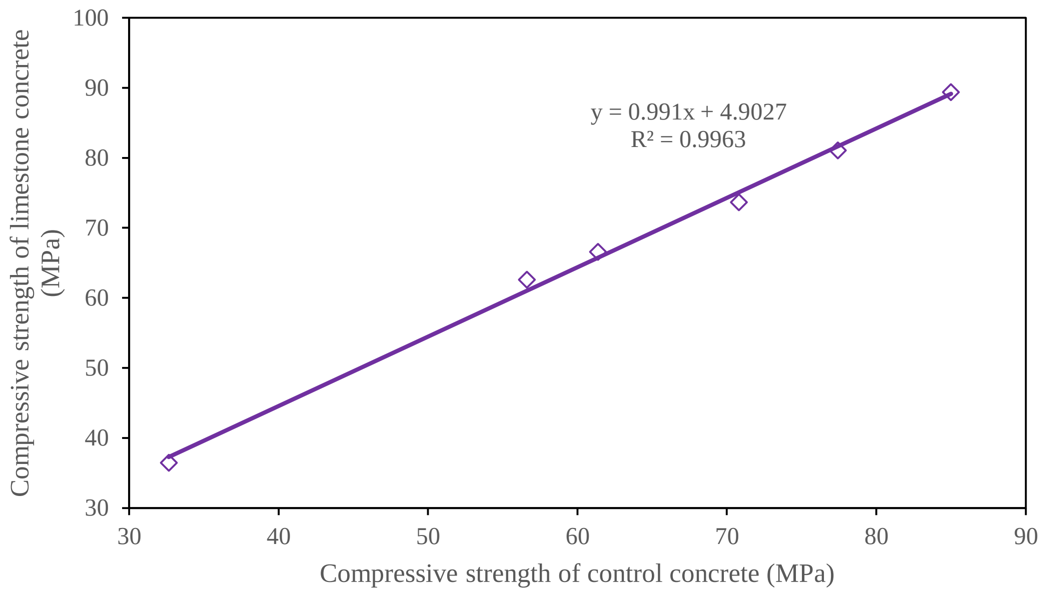

Figure 4.5: Correlation of compressive strength between control and limestone concrete

4.3.2. Comparison of Sorptivity between SiMn Slag and Limestone Concrete

Figure 4.6 shows the variation of sorptivity with curing duration for limestone and control concrete. The sorptivity of both types of concrete decreased over time, showing an improved in concrete durability. This was due to more complete hydration of concrete at a later age. The sorptivity of limestone concrete was lower than that of control concrete. The percentage difference was 27.3%, 32.2%, 35.8%, 39.3% and 44.19% at 14, 28, 56, 90 and 180 days respectively. SiMn slag aggregate was more angular than the limestone aggregate, resulting in a weaker bonding with cement paste and higher permeability.

The difference of sorptivity between the limestone and SiMn slag concrete was also constant over the age. The average difference was $1.436\text{x}10^{-3}$ mm/sec$^{0.5}$ and the standard deviation was $0.075\text{x}10^{-3}$ mm/sec$^{0.5}$. This also showed a linear relationship for sorptivity between limestone and SiMn slag concrete. Hence, the correlation between the sorptivity of the two concrete types was established using the regression analysis as shown in Figure 4.7. The linear relationship of sorptivity between two concrete was expressed Eq. 4.3.

$$S_{c,LS} = 0.9258S_{c,SM} - 1.1288 \qquad \text{Eq. 4.3}$$

In Eq. 4.3, $S_{c,LS}$ represents the sorptivity of limestone concrete and $S_{c,SM}$ refers to the sorptivity of SiMn slag concrete. The established correlation has an R^2 value of 0.9976, showing a high fitness for the regression model. The equation can be used to estimate the sorptivity of limestone concrete based on that of SiMn slag concrete and vice versa.

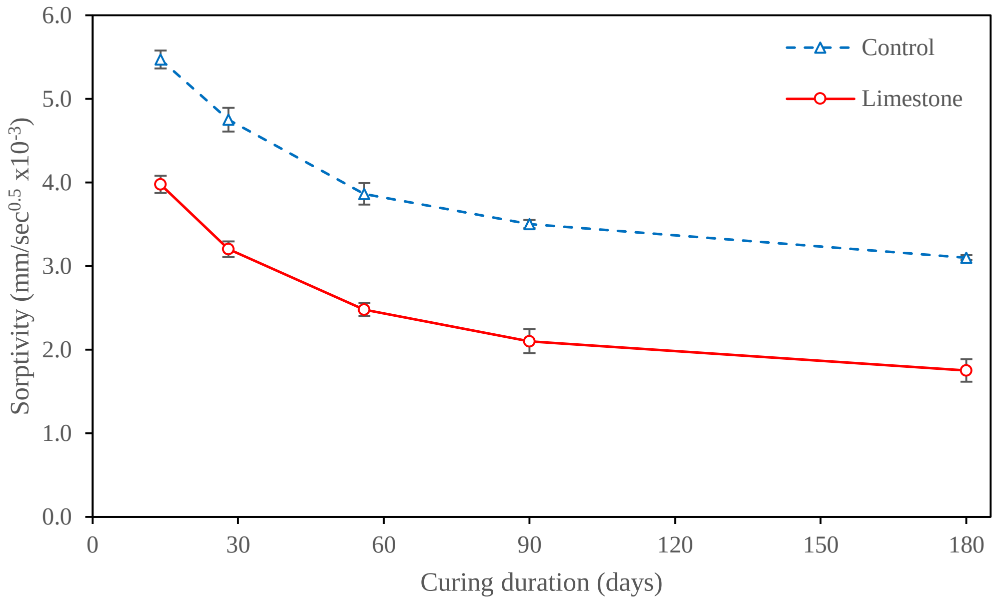

Figure 4.6: Sorptivity of control and limestone concrete

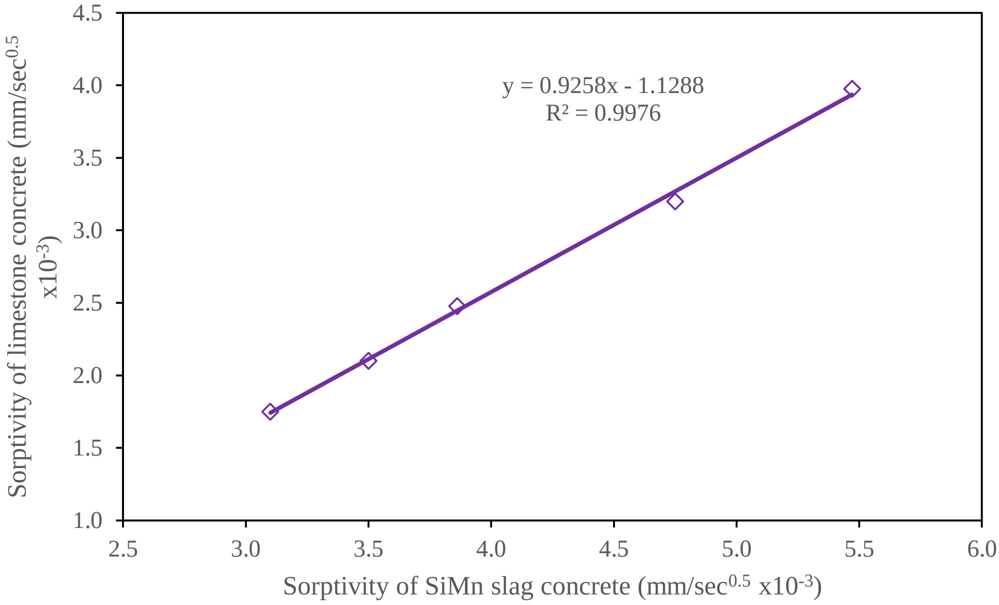

Figure 4.7: Correlation of sorptivity between control and limestone concrete

4.3.3. Workability of SiMn Slag Concrete Incorporated with FA and SF

Figure 4.8 presents the workability of concrete assessed by the slump test. The slump value ranged from 30 mm to 247 mm, showing a significant impact of FA and SF on concrete workability.

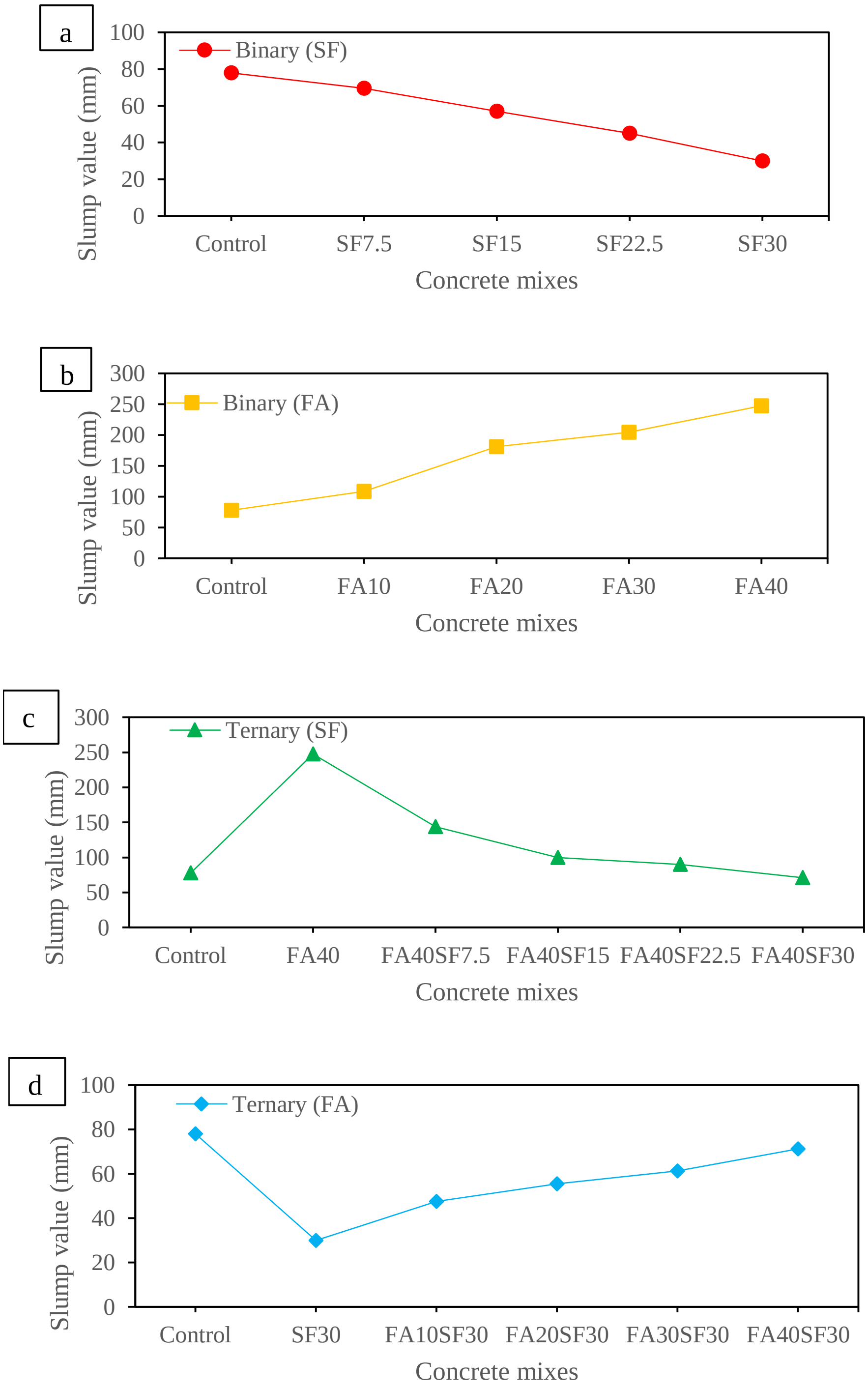

Figure 4.8: Effect of workability of (a) SF in binary, (b) FA in binary, (c) SF in ternary, and (d) FA in ternary blended concrete

The slump value decreased with an increase in the replacement level of SF in binary blended concrete as shown in Figure 4.8(a). Binary blended concrete containing 30% SF had the lowest slump value, which reduced the slump by 62% compared to the control mix. The reduction was caused by the large specific surface area of fine SF, which increased the water demand of concrete. The incorporation of SF also caused the concrete to become more cohesive and sticky, leading to a lower workability. The findings were in line with previous studies by Bagheri et al. (2013) and Mazloom et al. (2004). Based on the result, it is not recommended to use an SF replacement level of more than 15% as this would cause the slump value to be below the minimum value of 50 mm suggested by the ACI standard for concrete pumping (ACI Committee 304, 1996) .

In contrast, the concrete slump value increased with the FA replacement level in binary blended concrete as shown in Figure 4.8(b). For example, the binary blended concrete containing 40% FA achieved the highest slump value of 247 mm. This was due to the ball bearing effect provided by the round and smooth FA that reduced inter-particle friction in fresh concrete. Similar conclusion was also reached by Kwan and Chen (2013), who observed a significant increase in the flow of cement paste that contained FA up to 40%.

For the combined effect, the workability of FA concrete decreased with an increase of SF content as shown in Figure 4.8(c). The workability of FA40SF7.5, FA40SF15, FA40SF22.5 and FA40SF30 concrete was 41.8%, 59.6%, 63.6% and 71.2% respectively, below that of FA40 concrete. The use of SF increased the cohesiveness of concrete resulting in a loss of workability (Bagheri et al., 2013). The decrease in workability might also be ascribed to the use of seawater as mixing water. As shown in Table 3.3, seawater had a pH of 8.1 and was alkaline, which could react with alumino-silicate content in FA and SF to form early cementation and reduce workability (Lv et al., 2020). Nevertheless, the disadvantage of SF on workability could be overcome by increasing the content of FA as shown in Figure 4.8(d). The slump value of FA10SF30, FA20SF30, FA30SF30 and FA40SF30 concrete was 17.5 mm, 25.5 mm, 31.25 mm and 41.25 mm higher than that of SF30 concrete respectively. The spherical FA particles acted as ball bearings between the concrete mixtures to provide a lubricant effect (Kwan and Chen, 2013).

4.3.4. Compressive Strength of SiMn Slag Concrete Incorporated with FA and SF

The compressive strength of concrete determined after 7, 28 and 90 days of curing is shown in Figure 4.9. The strength of all the concrete mixes increased orderly with the curing time or age.

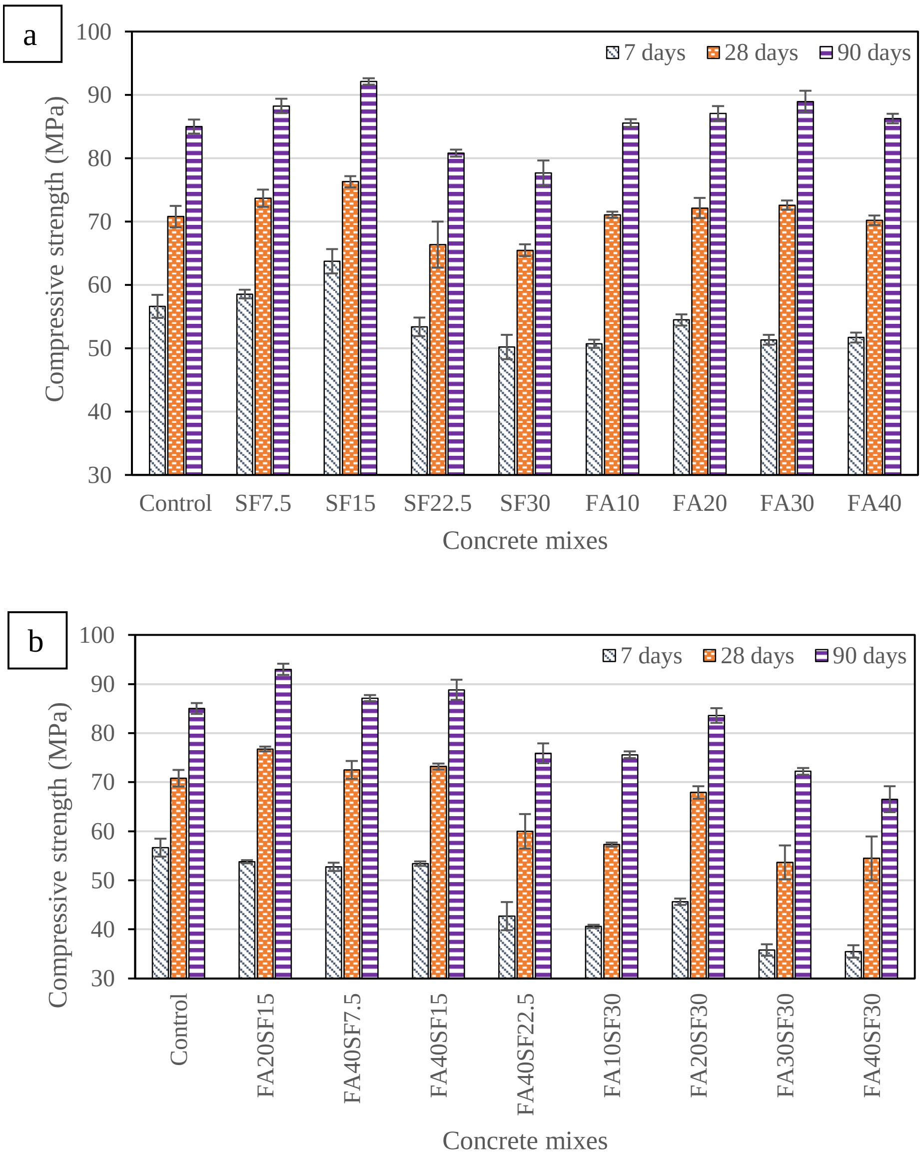

Figure 4.9: Effect of FA and SF on compressive strength of (a) binary and (b) ternary concrete

As shown in Figure 4.8(a), binary concrete blended with SF up to 15% of replacement level achieved higher compressive strength than the control mix regardless of age. But the further addition of SF led to a lower concrete strength than the control mix. The strength increase at 7 days was 3.4% and 12.6% for SF7.5 and SF15 concrete respectively. This was attributed to the pozzolanic reaction of fine SF, which reacted rapidly with $Ca(OH)_2$ from cement hydration to form C-S-H. However, the strength of the SF22.5 and SF30 concrete mixes decreased by 5.7% and 11.3% respectively. The result showed that the optimum SF content was between 15% and 22.5%, above which there would be a shortage of $CaOH_2$ for pozzolanic reaction (Bhanja and Sengupta, 2005). The reduction of strength was also due to the increased concrete cohesiveness resulting in a less homogeneous mixture. The results tied well with the studies of Tripathi et al. (2020) and Mazloom et al. (2004) which showed an optimum dose of SF between 15% and 25% in terms of compressive strength.

As for the effect of FA on binary blended concrete, the 7-day compressive strength decreased by 10.4%, 3.8%, 9.3% and 8.7% respectively for FA10, FA20, FA30 and FA40 mixes. Although seawater was used as mixing water, the expected high early strength caused by alkaline activation or geo-polymerization was not evident in these mixes due to low alkalinity of seawater. In order to achieve geo-polymerization, Do et al. (2019) showed that seawater had to be used in combination with other alkaline activators, such as sodium silicate and sodium hydroxide. The study also limited seawater content to 17% of total alkaline activator solution. Besides, chloride from seawater could react and cause dissolution of hydrated aluminate structure from cementitious matrix to form a distorted brucite-like structure, reducing the concrete strength (Balonis et al., 2010; Torres-Luque et al., 2015). Nevertheless, the compressive strength improved with the curing time. At 90 days, these FA mixes had a higher strength than the control mix with a percentage of 0.7%, 2.4%, 4.7% and 1.5% respectively. FA had a particle size bigger than SF. As a result, the total surface area of FA particles was lower, which reduced the rate of pozzolanic reaction to gain strength. FA contained aluminium oxide and silicon dioxide in amorphous state, which reacted gradually with $Ca(OH)_2$ to form C-S-H. The result was consistent with the work of Sumer (2012), Kondraivendhan and Bhattacharjee (2015) and Alaka and Oyedele (2016). The reaction between chloride from seawater and aluminate from FA also produced Friedel's slat and Kuzel's salt, which could fill up concrete pores and improve concrete strength (Balonis et al., 2010).

The results in Figure 4.9(b) showed the synergistic effect of FA and SF on ternary blended concrete, which compensated for their individual limitations. SF improved compressive strength which offset the lower strength gain caused by FA at early age.

The incorporation of 7.5% of SF as in FA40SF7.5 and 15% as in FA40SF15 improved the 7-day compressive strength of FA40 concrete by 2.0% and 3.3% respectively. In both cases, the SF incorporation also improved the 28-day strength by 3.3% and 4.3% as well as the 90-day strength by 1.0% and 3.0%. In addition to inducing pozzolanic reaction, the fine SF also acted as a filler to increase the nucleation of C-S-H which improved the strength gain (Bagheri et al., 2013). The FA20SF15 concrete had the highest strength improvement of 8.4% at 28 days and 9.4% at 90 days compared to the control, though its 7-day compressive strength was 5.0% lower. This was due to the mutual interaction between the pozzolanic reaction of FA and the filler effect provided by SF. In addition, the effect of high-volume cement replacement was studied through the FA40SF15, FA20SF30, FA30SF30 and FA40SF30 mixes. The 90-day compressive strength of these concrete compared to the control mix was 4.5%, -1.7%, -15.04% and -21.8% respectively. Although the compressive strength was reduced due to the use of high-volume FA and SF, the substitution was justified from a sustainability point of view.

4.3.5. Splitting Tensile Strength of SiMn Slag Concrete Incorporated with FA and SF

Figure 4.10 shows the splitting tensile strength of binary and ternary blended concrete at 7, 28 and 90 days. The tensile strength increased with the curing time and it showed a similar result trend to that of the compressive strength.

As shown in Figure 4.10(a), SF improved the tensile strength of binary blended concrete at both early and late ages, when the replacement level was 15% or less. The strength of SF15 concrete was 9.4%, 16.5% and 14.8% higher than the control mix at 7, 28 and 90 days respectively. This was in line with the work of Bhanja and Sengupta (2005) who noticed an increase in splitting tensile strength if the SF replacement level was between 5% and 20%. The increase in early strength was attributed to the fine SF, which provided a filler effect on the concrete pore. The strength gain was increased at a later age due to a more complete pozzolanic reaction of SF.

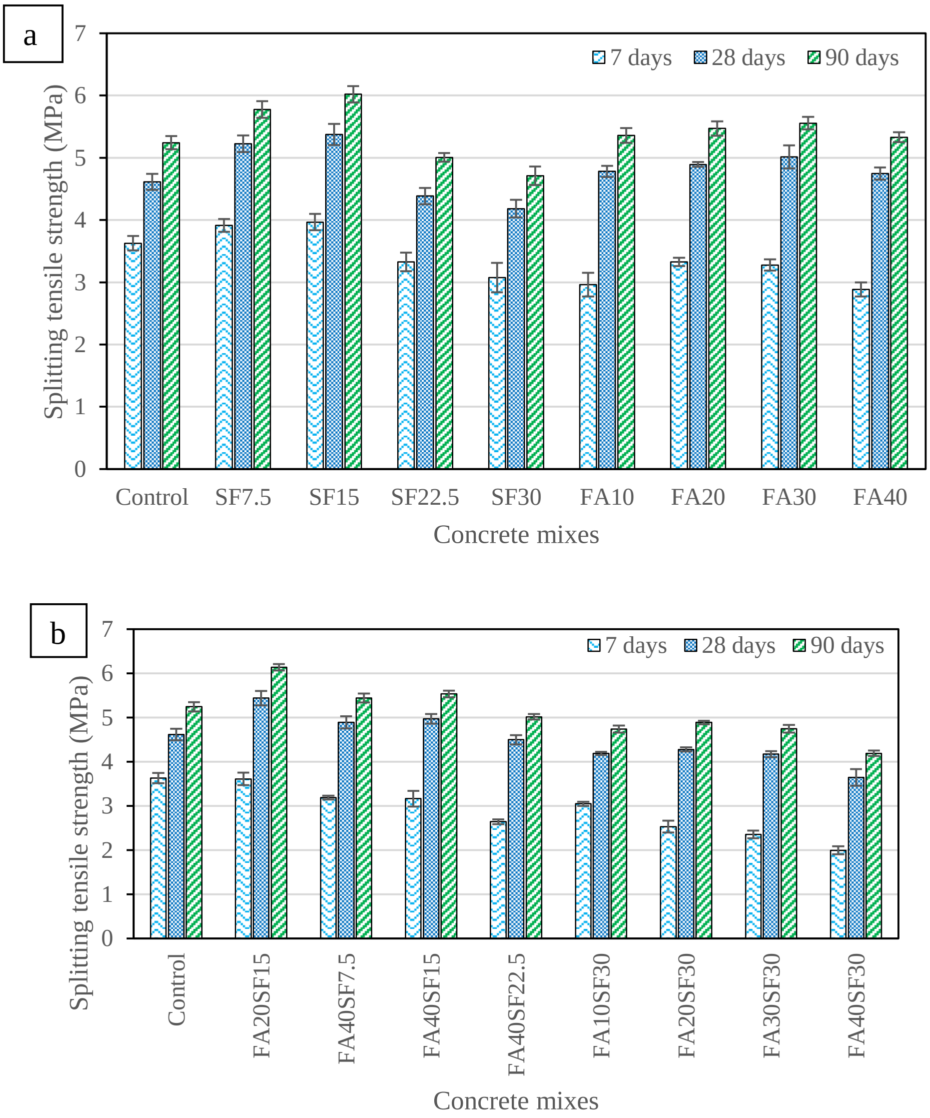

Figure 4.10: Effect of FA and SF on splitting tensile strength of (a) binary and (b) ternary concrete

All replacement levels of FA lowered the 7-day tensile strength of binary blended concrete, but increased the strength at 28 and 90 days. The FA30 concrete achieved the highest 28-day and 90-day tensile strengths with an improvement of 8.7% and 6.0% respectively, though the 7-day strength was 9.6% lower than the control mix. The lower early strength was due to the slow pozzolanic reaction of FA, but the reaction gradually became more complete, resulting in more C-S-H formation and higher strength at the later age (Yazici and Arel, 2012). Thereafter, the result showed a declining trend of strength increase for the addition of FA above 30%. Further substitution of cement by FA resulted in a reduction of $Ca(OH)_2$ from hydration for use in pozzolanic reaction. Both the splitting tensile and compressive strengths indicated that the optimum dosage of FA in binary blended concrete was 30%.

The synergy of FA and SF in ternary blended concrete had a stronger effect on tensile strength as depicted in Figure 4.10(b). FA20SF15 concrete reached the highest strength improvement of 17.9% and 17.2% at 28 and 90 days, respectively, and had a comparable 7-day strength of control concrete. The filler effect of SF compensated for the lower early strength caused by FA and the pozzolanic reaction of FA further increased strength at a later age (Bagheri et al., 2013). The incorporation of FA improved the tensile strength of SF concrete at a later age by 0.6%, 3.8% and 0.9%, respectively, in the FA10SF30, FA20SF30 and FA30SF30 mixes, compared to the SF30 mix. The results also showed an increase in the tensile strength of FA concrete due to the addition of SF. For example, the 7-day tensile strength of FA40SF7.5 and FA40SF15 concrete was 10.4% and 9.3%, respectively, higher than FA40 concrete. However, a further substitution of FA and SF above 60% in ternary blended concrete resulted in a severe reduction of strength. Dave et al. (2017) found that the substitution of quaternary binder above 50% was not effective in improving concrete tensile strength. This was due to the lack of $Ca(OH)_2$ content for pozzolanic reaction to provide bonding strength.

4.3.6. Sorptivity of SiMn Slag Concrete Incorporated with FA and SF

The rate of water absorption of concrete was studied using the sorptivity test. Figure 4.11 presents the sorptivity of concrete determined after 28, 90 and 180 days of curing. The sorptivity of all concrete mixes decreased with the curing time, indicating an improved durability over time. More complete hydration of concrete was achieved at a later age which densified concrete pore due to the formation of C-S-H.

Figure 4.11(a) showed that the incorporation of SF with a percentage of up to 15% improved the sorptivity of binary blended concrete. The extent of improvement in sorptivity decreased with an increase in the SF replacement level. The SF22.5 concrete had a similar sorptivity to the control concrete. Further incorporation of SF up to 30% increased sorptivity by 15.6%, 36.6% and 47.1% at 28, 90 and 180 days respectively, indicating reduced durability. The decrease in sorptivity at a lower SF content was due to the filling of concrete pore by fine SF, which improved the microstructural fineness. Bagheri et al. (2013) demonstrated that SF reduced pore connectivity of concrete. The pore structure of concrete was also enhanced by the pozzolanic reaction of SF. Meanwhile, higher sorptivity at a higher SF content was due to more pores caused by the high cohesiveness of concrete.

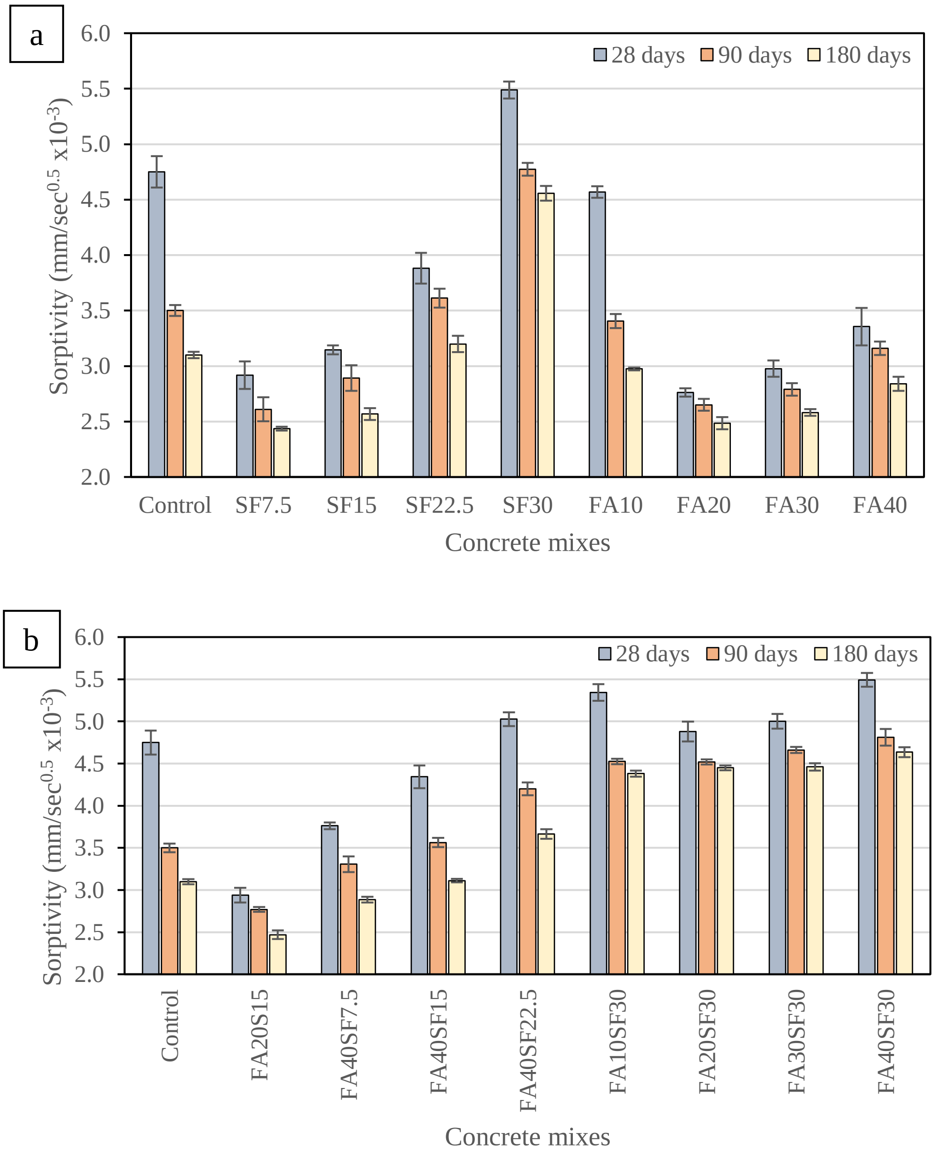

Figure 4.11: Effect of FA and SF on sorptivity of (a) binary and (b) ternary concrete

The sorptivity of all binary concrete blended with FA was below that of control concrete at all ages. For example, the improvement in sorptivity was 4.1%, 19.9%, 16.7% and 8.4% for FA10, FA20, FA30 and FA40 concrete respectively at 180 days. This was due to the pozzolanic reaction of FA, which densified the concrete pore with more C-S-H formation. Ponikiewski and Gołaszewski (2014) also demonstrated that the addition of FA reduced water absorption of concrete by creating a more compact pore structure through the pozzolanic reaction. In addition, the Friedel's salt, which was formed by the reaction between chloride from seawater and aluminate from FA, provided a pore sealing effect that minimized concrete sorptivity (Balonis et al., 2010).

As for ternary blended concrete in Figure 4.11(b), the results mostly showed higher sorptivity than control concrete, with the exception of FA20SF15, FA40SF7.5 and FA40SF7.5 mixes. This was due to the high level of OPC replacement by SF and FA, where the resulting concrete was deficient in $Ca(OH)_2$ for pozzolanic reaction. The geo-polymerization effect caused by seawater was not evident in sorptivity due to low alkalinity of seawater. Belviso et al. (2010) found that the use of seawater had no effect on the geo-polymerization of FA and the effect was comparable to the use of distilled water. Nonetheless, FA20SF15 and FA40SF7.5 concrete improved the 180-day sorptivity by 20.3% and 6.8% respectively, while FA40SF15 concrete had comparable sorptivity to the control mix. The findings tied well with the study by Radlinski and Olek (2012) which showed a substantial improvement in sorptivity when 20% FA and 15% SF were incorporated. Besides, the incorporation of FA also reduced the sorptivity of SF concrete. For example, FA10SF30, FA20SF30 and FA30SF30 concrete reduced the 90-day sorptivity of SF30 concrete by 5.2%, 5.4% and 2.5% respectively. The pozzolanic reaction of FA filled up the concrete pores. In terms of durability, it is not recommended to substitute OPC with FA and SF in high volume.

4.3.7. Chloride Permeability of SiMn Slag Concrete Incorporated with FA and SF

The chloride permeability expressed as the charge passed through concrete is determined by the RCPT. Figure 4.12 presents the chloride permeability of binary and ternary concrete blended with FA and SF at 28, 90 and 180 days. The chloride permeability of concrete decreased over time due to more complete hydration.

The result in Figure 4.12(a) showed that the chloride permeability of binary concrete blended with SF decreased with an increase in the replacement level. SF30 concrete had the largest reduction in chloride permeability, which was 67.3%, 59.9% and 59.0% lower than control concrete at 28, 90 and 180 days respectively. As for FA in binary blended concrete, chloride permeability also decreased with an increase in FA content. FA concrete showed a slightly lower reduction than SF concrete. FA40 concrete had the largest reduction in chloride permeability, which was 59.9%, 51.1% and 49.0% lower than control concrete at 28, 90 and 180 days respectively.

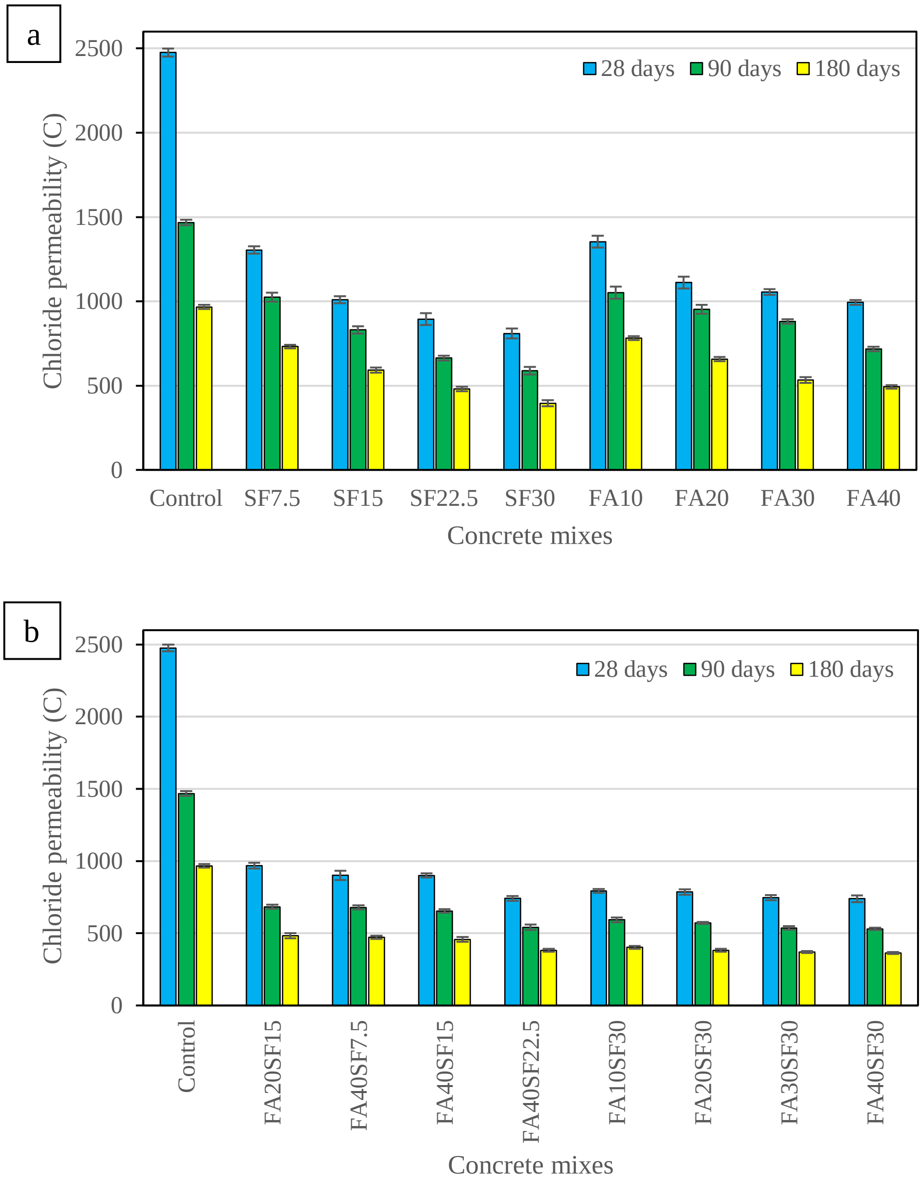

Figure 4.12: Effect of FA and SF on chloride permeability of (a) binary and (b) ternary concrete

Figure 4.12(b) showed that ternary blended concrete had a combined effect of FA and SF on minimizing chloride permeability. Chloride permeability decreased with the total replacement level of FA and SF. In this regard, FA40SF30 concrete achieved the lowest chloride permeability with a reduction of 70.1%, 63.9% and 62.5% at 28, 90 and 180 days respectively compared to control concrete. Dave et al. (2017) and Radlinski and Olek (2012) found that the reduction in chloride permeability was due to the pozzolanic reactions of FA and SF, which reduced capillary pores and compacted the concrete pore structure. This result was slightly different from the findings of sorptivity test described in Section 4.3.6. This was attributed to the modification of chemical composition in concrete as a result of the incorporation of FA and SF. FA and SF diluted concrete pore solution and reduced hydroxide (OH^-) concentration of concrete. In this case, RCPT, which measured electric current based on hydroxide (OH^-) and chloride (Cl^-) ions, was influenced by pore solution chemistry. Neithalath and Jain (2010) found that when supplementary cementitious material such as SF was used in RCPT, 70% of permeability improvement was attributed to pore refinement, while another 30% was due to a reduction in concrete alkalinity. Nevertheless, the result still showed that the chloride permeability of FA20SF15 concrete decreased by 60.9%, 53.5% and 50.1% at 28, 90 and 180 days respectively compared to the control. It is necessary to perform other tests, such as the sorptivity test, to supplement the RCPT in assessing concrete durability.

4.4. Development of Prediction Model using Response Surface Method

4.4.1. Mathematical Prediction Model for Concrete Property

Concrete properties in terms of compressive strength, splitting tensile strength, sorptivity, chloride permeability and workability of concrete presented previously were inputs to the development of prediction model. The RSM was used to perform statistical analysis and to establish the relationship between these concrete properties and the FA and SF contents. The resulting prediction models are summarized in Table 4.4. These models were expressed as polynomial functions of x_1 as FA/B and x_2 as SF/B, which were the ratios of FA and SF content to total binder content.

Prediction models for compressive strength and splitting tensile strength at 7, 28 and 90 days were all expressed as quadratic polynomial functions of FA/B and SF/B. The models showed that SF/B contributed significantly to the strength of both early and later ages. In contrast, FA/B had a less significant effect on 7-day strength, but its effect was more prominent on 28-day and 90-day strengths. As such, the polynomial coefficients of FA/B increased with concrete age, indicating that the parameter had a higher influence. The result was consistent with the statistical models of Aldahdooh et al. (2013), Nehdi and Summer (2002) and Bayramov et al. (2004), which showed that quadratic functions were suitable for describing the relationship between concrete strength and supplementary cementitious material content.

Sorptivity at 28, 90 and 180 days was formulated as cubic equations. The models showed a decrease in sorptivity as FA/B and SF/B increased until the optimum point was reached. SF/B had a steeper curve slope than FA/B, indicating its greater effect on the sorptivity. The degree of polynomial equations for sorptivity was higher than that of Guneyisi et al. (2014) and Rezaifar et al. (2016), who developed linear and quadratic models respectively in their studies. This was due to a wider range of variables being investigated in this study.

As for chloride permeability, the 28-day and 90-day prediction models were quartic equations, and the 180-day model was cubic. The use of quartic models was due to the sudden reduction of chloride permeability of concrete with only slight incorporation of FA and SF at 28 and 90 days. This confirmed that the decrease in chloride permeability was caused by modification of pore chemistry rather than pore refining contributed by FA and SF. Nonetheless, the 180-day chloride permeability equation was more similar to the sorptivity equation since the pore refining effect caused by pozzolanic reaction of FA and SF was more pronounced.

Concrete slump value was formulated as a cubic equation with a non-linear relationship to FA and SF. The equation indicated that the increased use of SF greatly decreased the slump value, but the use of FA improved the slump value. Sonebi (2004) showed that fresh properties of concrete could be expressed as cubic functions of FA content, OPC content, superplasticizer dosage and w/b ratio. Lotfy et al. (2014) used quadratic equations to model the relationship between fresh properties and concrete variables.

Table 4.4: Prediction model for concrete property

Parameter	**Compressive strength (MPa)**			**Splitting tensile strength (MPa)**		
	7 days	**28 days**	**90 days**	**7 days**	**28 days**	**90 days**
Polynomial degree	Quadratic	Quadratic	Quadratic	Quadratic	Quadratic	Quadratic
Constant	55.63	69.2	82.78	3.43	4.62	5.19
x_1	-24.19	39.56	60.37	-0.29	3.79	4.39
x_2	79.55	97.42	107.07	7.32	8.77	9.67
x_1x_2	-83.34	86.39	-98.58	-4.69	-3.19	-2.94
x_1^2	36.51	-93.09	-135.85	-2.34	-9.32	-11.18
x_2^2	-340.67	-404.45	-425.9	-28.65	-35.57	-38.91

Parameter	**Sorptivity (mm/sec$^{1/2}$ x10^{-3})**			**Chloride permeability (C x10^{3})**			**Slump value (mm)**
	28 days	**90 days**	**90 days**	**28 days**	**90 days**	**90 days**	
Polynomial degree	Cubic	Cubic	Cubic	Quartic	Quartic	Cubic	Cubic
Constant	4.82	3.56	3.14	2.47	1.47	0.96	77.51
x_1	-3.97	-4.13	-3.36	-17.99	-6.74	-1.77	455.76
x_2	-34.49	-18.12	-12.70	-26.39	-9.50	-3.12	-381.08
x_1x_2	92.55	43.01	32.60	138.86	35.04	10.06	-3147.72
x_1^2	-41.102	-3.61	-1.02	85.34	32.67	0.69	27.87
x_2^2	172.81	101.11	54.58	185.39	65.29	4.61	2589.18
$x_1x_2^2$	-227.56	-102.70	-75.11	-418.03	-81.54	-12.15	6857.14
$x_1^2x_2$	-30.50	-20.81	-17.05	-312.37	-92.01	-7.31	172.62
x_1^3	105.87	29.06	19.20	-174.47	-68.48	2.08	-311.91
x_2^3	-168.69	-91.35	11.24	-606.22	-258.27	-1.36	-6195.41
$x_1x_2^3$	-	-	-	450.27	120.54	-	-
$x_1^2x_2^2$	-	-	-	353.79	5.08	-	-
$x_1^3x_2$	-	-	-	251.72	128.28	-	-
x_2^4	-	-	-	733.30	379.13	-	-

x_1 denotes independent variable FA/B.
x_2 denotes independent variable SF/B.

4.4.2. Evaluation of Model Fitness based on Analysis of Variance

The fitness of mathematical prediction models was evaluated using a two-way analysis of variance (ANOVA). The ANOVA determined the significance of model and variables on the responses through the F-test. The p-value at the significance level of 0.05 was used to determine the validity of null hypothesis. The null hypotheses were established if the variable had no effect on the response and if the interaction between variables had no effect on the response. When the p-value from F-test was not zero and less than 0.05, the null hypothesis was rejected and the variables were regarded as statistically significant.

Table 4.5, Table 4.6 and Table 4.7 summarize the outcomes of ANOVA for concrete strength, durability and workability prediction models respectively. The result showed that the variable SF/B for all models had a p-value of less than 0.05 and was statistically significant. Thus, SF/B was included in the prediction models. On the contrary, FA/B was tested as an insignificant variable except for the 7-day strengths, 28-day chloride permeability and 180-day chloride permeability models. Exclusion of insignificant variables might improve the prediction model. However, in this study, it reduced the overall accuracy of model prediction and as such the variables were not excluded. Lotfy et al. (2014) had used all the variables, including those not significant, in the models to enhance their accuracy. Higher degree polynomial variables and interactions between them were similarly assessed and the results were shown in Appendix C to avoid lengthy content. Furthermore, the ANOVA showed that the lack of fit of all models had p-value of more than 0.05, indicating that it was not significant. The lack of model fitness did not cause residual errors. The mean square of pure error was less than that of model and also, in general, that of lack of fit, indicating that the error between the replicate runs was minimal.

Table 4.8 shows the goodness-of-fit statistics for prediction models. The coefficient of determination (R^2) of all models ranged from 0.853 to 0.999. These R^2 values were close to 1, indicating that the regression models fit the data points. The 7-day, 28-day and 90-day compressive strength models had marginally lower R^2 values of 0.896, 0.853 and 0.895 respectively. This was ascribed to a higher sensitivity of high strength concrete to the material variations and testing environment. The adjusted R^2 and predicted R^2 were used to justify the inclusion of insignificant variables in the model. When insignificant variables were included, the adjusted R^2 plateaued. The predicted R^2 decreased if too many insignificant terms were included. The difference between adjusted and predicted R^2 should be less than 0.2 in order to limit the number of insignificant terms and to ensure the reliability of prediction (Design-Expert, 2018). The 28-day compressive strength model had the largest difference between two R^2s of 0.106. The difference for all models was below this value, indicating that the addition of insignificant terms had no negative influence on the prediction. Besides, the adequate precision of all models was well above 4, showing that the models had a low prediction error and were therefore sufficiently fit for optimization (Noordin et al., 2004).

In summary, the ANOVA showed that null hypotheses were rejected for all models and that the models were statistically significant. The models contained all important terms required by ANOVA and were therefore adequate to describe the relationship between variables and responses.

Table 4.5: ANOVA of prediction model for concrete strength

Response	Source	Sum of square	Mean square	F-value	p-value	Significance
7-day compressive strength	Model	902.76	180.55	25.86	0.0001	Yes
	FA/B	214.70	214.70	30.75	0.0001	Yes
	SF/B	382.63	382.63	54.81	0.0001	Yes
	Lack of fit	94.53	8.59	3.37	0.1257	No
	Pure Error	10.19	2.55	-	-	-
28-day compressive strength	Model	959.97	191.99	17.38	0.0001	Yes
	FA/B	49.78	49.78	4.51	0.0508	No
	SF/B	419.87	419.87	38.01	0.0001	Yes
	Lack of fit	156.10	14.19	5.91	0.0504	No
	Pure Error	9.61	2.40	-	-	-
90-day compressive strength	Model	1060.03	212.01	25.58	0.0001	Yes
	FA/B	33.78	33.78	4.08	0.0618	No
	SF/B	404.32	404.32	48.78	0.0001	Yes
	Lack of fit	112.64	10.24	3.51	0.1185	No
	Pure Error	11.68	2.92	-	-	-
7-day splitting tensile strength	Model	4.90	0.98	32.85	0.0001	Yes
	FA/B	1.63	1.63	54.78	0.0001	Yes
	SF/B	1.21	1.21	40.70	0.0001	Yes
	Lack of fit	0.40	0.04	3.19	0.1369	No
	Pure Error	0.05	0.01	-	-	-
28-day splitting tensile strength	Model	5.38	1.08	39.50	0.0001	Yes
	FA/B	0.08	0.08	2.86	0.1117	No
	SF/B	1.60	1.60	58.89	0.0001	Yes
	Lack of fit	0.35	0.03	2.32	0.2168	No
	Pure Error	0.06	0.01	-	-	-
90-day splitting tensile strength	Model	6.35	1.27	44.18	0.0001	Yes
	FA/B	0.12	0.12	4.14	0.0598	No
	SF/B	1.66	1.66	57.78	0.0001	Yes
	Lack of fit	0.37	0.03	2.36	0.2111	No
	Pure Error	0.06	0.01	-	-	-

Table 4.6: ANOVA of prediction model for concrete durability

Response	Source	Sum of square	Mean square	F-value	p-value	Significance
28-day sorptivity	Model	199.38 x10^{-7}	22.15 x10^{-7}	34.15	0.0001	Yes
	FA/B	0.01 x10^{-7}	0.01 x10^{-7}	0.14	0.7109	No
	SF/B	8.08 x10^{-7}	8.08 x10^{-7}	12.46	0.0047	Yes
	Lack of fit	6.24 x10^{-7}	0.89 x10^{-7}	4.00	0.0993	No
	Pure Error	0.89 x10^{-7}	0.22 x10^{-7}	-	-	-
90-day sorptivity	Model	23.20 x10^{-7}	13.69 x10^{-7}	63.42	0.0001	Yes
	FA/B	0.10 x10^{-7}	0.10 x10^{-7}	0.49	0.5003	No
	SF/B	5.15 x10^{-7}	5.15 x10^{-7}	23.85	0.0005	Yes
	Lack of fit	1.87 x10^{-7}	0.27 x10^{-7}	2.11	0.2450	No
	Pure Error	0.51 x10^{-7}	0.13 x10^{-7}	-	-	-
	Model	134.21 x10^{-7}	14.91 x10^{-7}	208.91	0.0001	Yes

180-day sorptivity	FA/B	0.01 x10^{-7}	0.01 x10^{-7}	1.13	0.3115	No
	SF/B	2.91 x10^{-7}	2.91 x10^{-7}	40.73	0.0001	Yes
	Lack of fit	0.67 x10^{-7}	0.01 x10^{-7}	3.40	0.1271	No
	Pure Error	0.11 x10^{-7}	0.03 x10^{-7}	-	-	-
28-day chloride permeability	Model	2.76 x10^{6}	1.97 x10^{5}	468.51	0.0001	Yes
	FA/B	20955.03	20955.03	49.80	0.0004	Yes
	SF/B	4808.75	4808.75	11.43	0.0148	Yes
	Lack of fit	1130.85	565.42	1.62	0.3048	No
	Pure Error	1393.63	348.41	-	-	-
90-day chloride permeability	Model	1.01 x10^{6}	72242.33	283.09	0.0001	Yes
	FA/B	351.70	351.70	1.38	0.2849	No
	SF/B	10236.72	10236.72	40.11	0.0007	Yes
	Lack of fit	142.55	71.27	0.21	0.8225	No
	Pure Error	1388.59	347.15	-	-	-
180-day chloride permeability	Model	4.66 x10^{5}	51760.64	226.18	0.0001	Yes
	FA/B	3125.99	3125.99	13.66	0.0035	Yes
	SF/B	6135.65	6135.65	26.81	0.0003	Yes
	Lack of fit	1594.74	227.82	0.99	0.5380	No
	Pure Error	922.53	230.63	-	-	-

Table 4.7: ANOVA of prediction model for concrete workability

Response	Source	Sum of square	Mean square	F-value	p-value	Significance
Slump value	Model	59691.43	6632.38	84.26	0.0001	Yes
	FA/B	231.80	231.80	2.94	0.1142	No
	SF/B	478.86	478.86	6.08	0.0313	Yes
	Lack of fit	727.09	103.87	2.99	0.1531	No
	Pure Error	138.80	34.70	-	-	-

Table 4.8: Analysis of prediction model fitness

Response	R^2	Adjusted R^2	Predicted R^2	Adequate precision	Estimated error (95% CI)
7-day compressive strength	0.896	0.861	0.806	17.63	±2.28 MPa
28-day compressive strength	0.853	0.804	0.698	13.35	±2.87 MPa
90-day compressive strength	0.895	0.860	0.797	16.76	±2.48 MPa
7-day splitting tensile strength	0.916	0.888	0.830	20.46	±0.15 MPa
28-day splitting tensile strength	0.929	0.906	0.862	19.67	±0.14 MPa
90-day splitting tensile strength	0.936	0.915	0.872	21.01	±0.15 MPa
28-day sorptivity	0.965	0.937	0.861	15.61	±0.23 x10^{-3} mm/sec$^{0.5}$
90-day sorptivity	0.981	0.966	0.917	21.01	±0.13 x10^{-3} mm/sec$^{0.5}$
180-day sorptivity	0.994	0.989	0.973	37.35	±0.08 x10^{-3} mm/sec$^{0.5}$
28-day chloride permeability	0.999	0.997	0.924	100.21	±22.45 C
90-day chloride permeability	0.999	0.995	0.972	69.34	±17.48 C
180-day chloride permeability	0.995	0.990	0.975	57.78	±13.47 C
Slump value	0.986	0.974	0.940	35.18	±7.90 mm

4.5. Optimization, Validation and Application of Prediction Model

4.5.1. Optimization of Concrete Property with Experimental Validation

The optimization of concrete properties was carried out using the prediction models in Table 4.4 developed from RSM. Table 4.9 presents the criteria of optimization for variables and responses. The main objective of optimization was to maximize compressive and splitting tensile strengths, and to minimize sorptivity and chloride permeability of concrete. The optimization was carried out over the feasible ranges of FA/B and SF/B as 0 to 0.4 and 0 to 0.3 respectively. The slump value was targeted to fall between 80 mm and 210 mm, with the lower limit being set for concrete pumping and the upper limit being recommended by BS EN 12350-2 (2009).

Table 4.9: Optimization criteria for variable and response

Variable and response	Optimization target	Lower limit	Upper limit
FA/B	Within range	0	0.4
SF/B	Within range	0	0.3
7-day compressive strength (MPa)	Maximize	35.46	63.73
28-day compressive strength (MPa)	Maximize	53.66	78.39
90-day compressive strength (MPa)	Maximize	66.50	94.76
7-day splitting tensile strength (MPa)	Maximize	1.99	3.97
28-day splitting tensile strength (MPa)	Maximize	3.64	5.56
90-day splitting tensile strength (MPa)	Maximize	4.19	6.28
28-day sorptivity (mm/sec$^{0.5}$ x10^{-3})	Minimize	2.713	5.493
90-day sorptivity (mm/sec$^{0.5}$ x10^{-3})	Minimize	2.604	4.812
180-day sorptivity (mm/sec$^{0.5}$ x10^{-3})	Minimize	2.415	4.636
28-day chloride permeability (C)	Minimize	739.30	2475.45
90-day chloride permeability (C)	Minimize	529.85	1467.90
180-day chloride permeability (C)	Minimize	362.40	966.50
Slump value (mm)	Within range	80	210

In the optimization process, FA/B and SF/B were varied simultaneously in order to compute the combination of variables that achieved the optimization objective. The optimization process also considered the interaction of the responses. These responses were expressed as a composite desirability function determined from the geometric mean desirability of individual responses (Myers et al., 2016). The desirability function could range from 0 to 1, with 0 indicated an outside-of-range prediction and 1 denoted an ideal prediction. The optimization was therefore performed by maximizing the desirability.

Optimum values of FA/B as 0.163 and SF/B as 0.115 were obtained from the optimization process. Figure 4.13 shows a graphical illustration of the desirability function. The desirability of optimization was 0.896. The region bounded by FA/B of 0.1–0.3 and SF/B of 0.06–0.18 generally had a high desirability of more than 0.8. FA/B had a more significant effect to achieve a higher optimization desirability. It was found that when SF/B was zero, the use of FA/B between 0.1 and 0.4 could still result in a desirability between 0.61 and 0.75. In contrast, the desirability function illustrated that when FA/B was zero, the use of SF/B at all levels resulted in zero desirability.

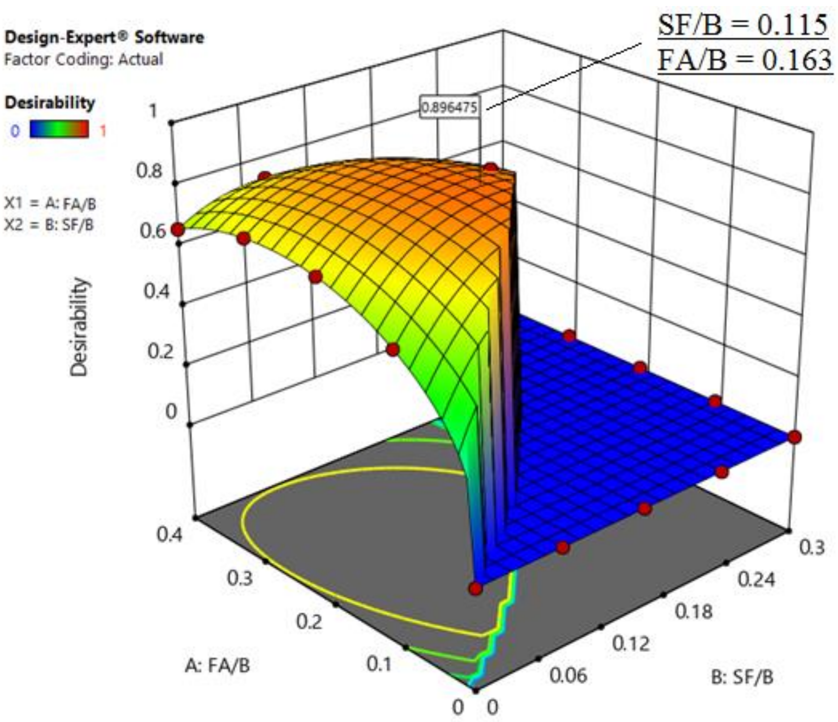

Figure 4.13: Desirability function of optimization

Experiments were again conducted to validate the optimization outcomes. All concrete properties predicted by the models were tested in the validation experiment. Materials from the same source were used. Concrete mix proportions were adjusted using FA/B as 0.163 and SF/B as 0.115. In all experiments, the same procedures and conditions described in Section 4.2.4 were used.

Figure 4.14 shows the results of validation tests using the optimum FA and SF contents, as well as the comparison with the predicted results and limestone concrete determined as Mix 5 (B1/C2/D2) in Chapter 3. In terms of strength, concrete generally achieved a higher experimental value than the predicted outcome. The 7-day compressive strength had the highest error of 3.4%. The experimental sorptivity was close to the predicted value. The 90-day sorptivity had the highest error of 4.9%. As for chloride permeability, the 28-day results showed a higher error of 18.0%. This was attributed to the limited design points to consider the sensitivity of the model to OH^- and Cl^- ions related chemistry in concrete caused by FA and SF. The drawback of CCD method was that the effect of variables within the box of CCD (Figure 4.3) on response was not covered by the model development. The optimum FA and SF contents that fell within this region caused less accurate prediction of chloride permeability. Nonetheless, the error decreased at an older age to 9.1% and 10.3% respectively for 90-day and 180-day chloride permeability.

The validation study proves that the optimum FA and SF contents of 16.3% and 11.5% respectively are compatible with the optimization outcome. The optimization of FA and SF improves the hardened state properties of SiMn slag concrete. In this regard, the 90-day compressive strength, 90-day tensile strength, 180-day sorptivity and 180-day chloride permeability are improved by 10.4%, 18.9%, 24.9% and 44.6% respectively.

As report in Chapter 3, SiMn slag concrete without the inclusion of FA and SF had a lower strength and durability than limestone concrete. For example, its 90-day compressive strength and 28-day chloride permeability were 4.9% and 19.2% lower than that of limestone concrete. In this study, however, the use of FA and SF at the optimum replacement level overcomes the limitation of SiMn slag concrete. The 90-day compressive strength, 90-day tensile strength, 180-day sorptivity and 180-day chloride permeability have been improved by 4.2%, 1.6%, 27.3% and 24.0% respectively, compared to limestone concrete.

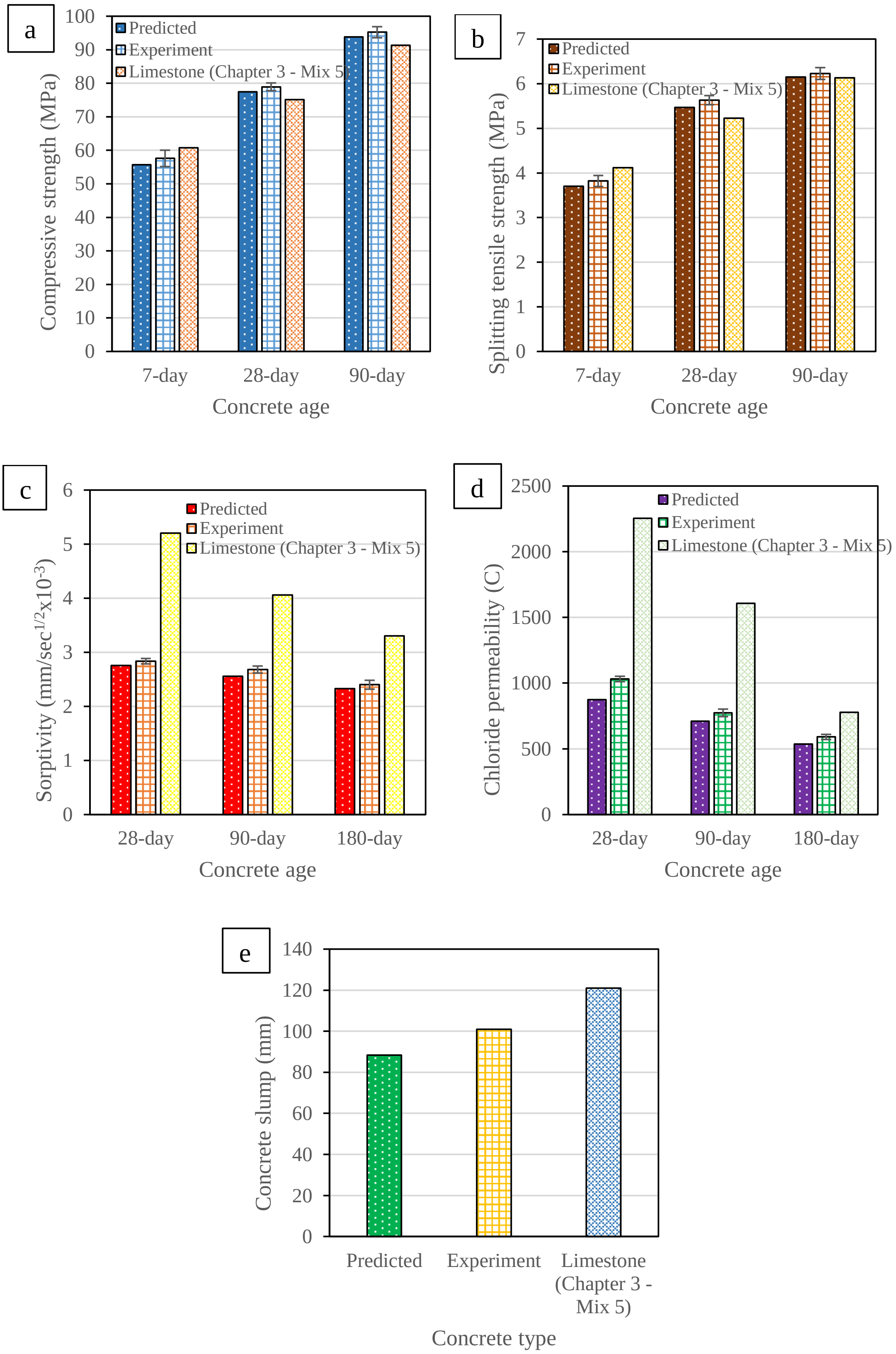

Figure 4.14: Predicted and experiment results and comparison with limestone concrete in terms of a) compressive strength, b) tensile strength, c) sorptivity, d) chloride permeability and e) concrete slump

4.5.2. Microstructure of SiMn Slag Concrete with Optimum FA and SF

SEM analysis was conducted to examine the microstructure of control and optimized concrete (16.3% FA and 11.5% SF) at 315 days. The SEM images showing the ITZ of control concrete and optimized concrete are presented in Figure 4.15(a) and Figure 4.15(b) respectively. The cloud-like morphology is referred to as C-S-H. The hexagonal plate-like crystals are referred to as $Ca(OH)_2$. As shown in Figure 4.15(a), a few groups of $Ca(OH)_2$ were found abundantly in the cement paste of control concrete. Conversely, a lower amount of $Ca(OH)_2$ was found and more C-S-H was observed in the optimized concrete as shown in Figure 4.15(b). This was attributed to the pozzolanic reaction of SF and FA, which consumed the $Ca(OH)_2$ to form the C-S-H strength gel.

Besides, more noticeable pores could be found on the ITZ of control concrete as shown in Figure 4.15(a). In contrast, the distribution of cement paste on the ITZ of optimized concrete as in Figure 4.15(b) was more uniform, indicating a stronger interlocking bond between the paste and the SiMn slag aggregate. The trace of cement paste filling up the pore on the surface of aggregate was also observed in the optimized concrete. The SEM analysis has shown that the optimized concrete has a more compact microstructure than the control concrete. The findings have confirmed the improved strength and durability of the optimized concrete.

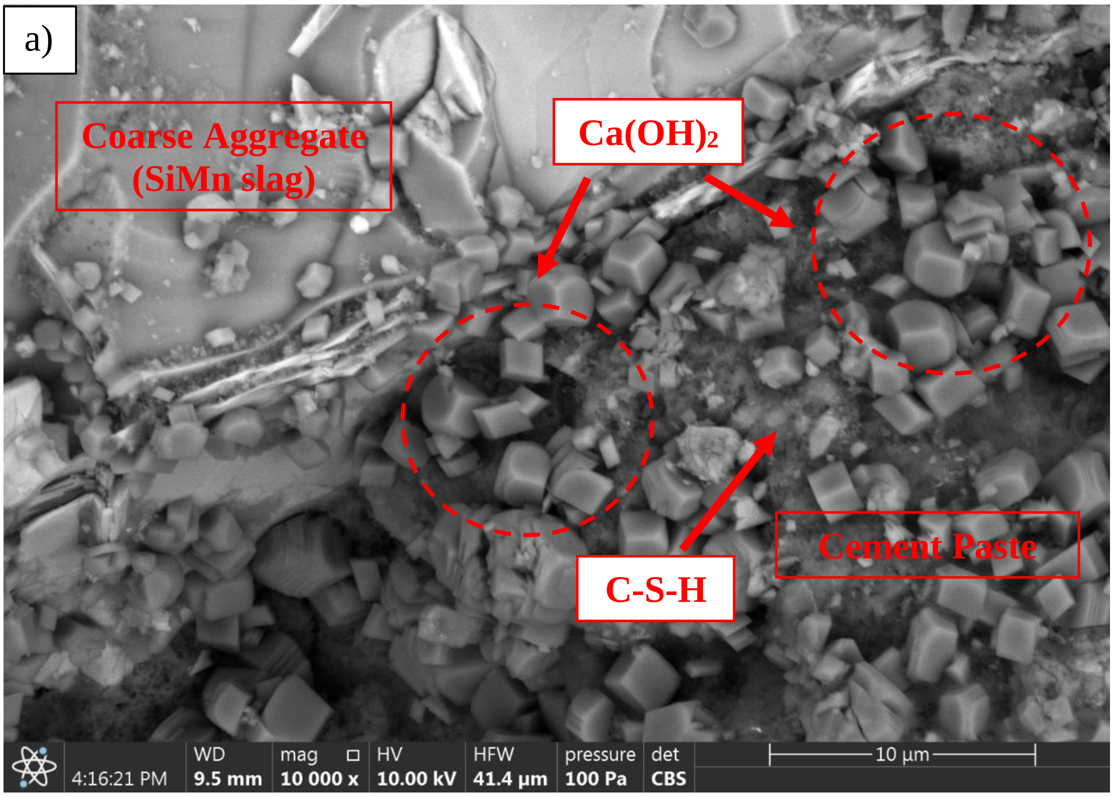

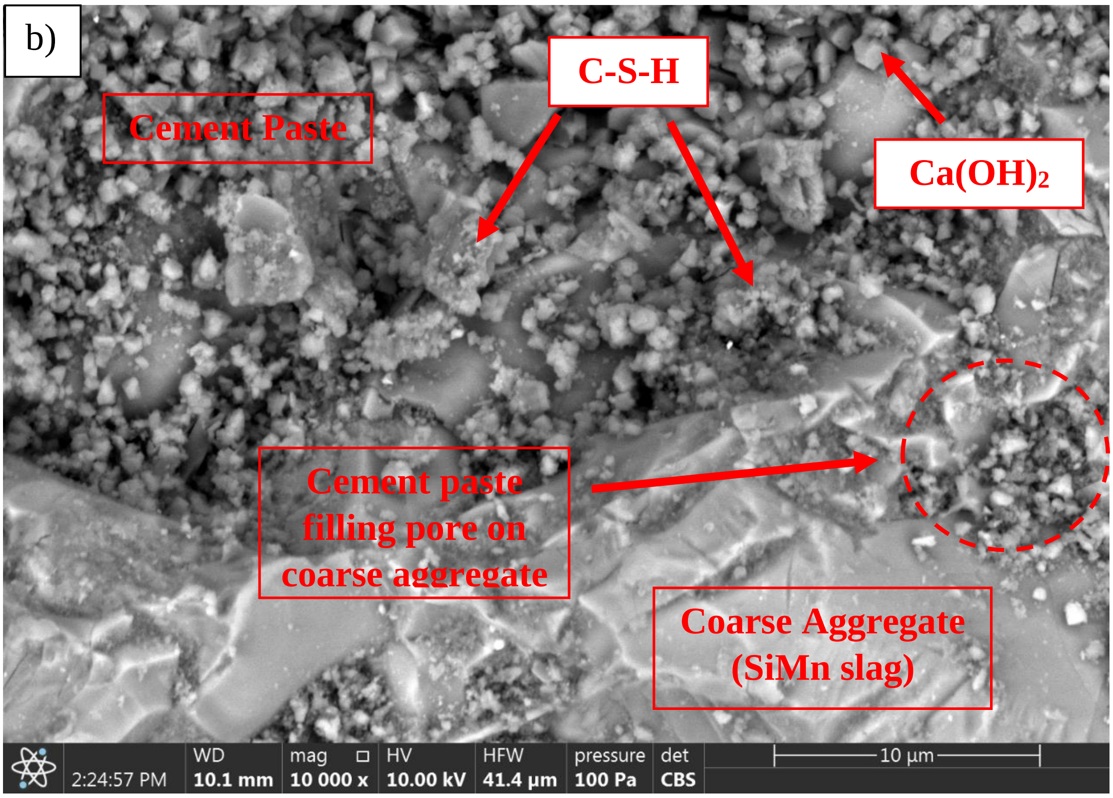

Figure 4.15: SEM images on interfacial transition zone of (a) control concrete and (b) optimized concrete at 315 days

4.5.3. Application of Prediction Model on Limestone Concrete

The application of the prediction models to concrete produced from the limestone aggregate is presented in this section. Three sets of prediction were made for the 28-day compressive strength targeting 65 MPa, 70 MPa and 75 MPa. The model proposed various predicted outcomes using various combinations of FA/B and SF/B. Selection of the predicted outcomes was based on the use of high FA and SF replacement levels that improved sustainability of concrete. The selected values are shown in Table 4.10, which are 39% FA and 21.9% SF for test A, 36.6% FA and 17.9% SF for test B, as well as 25.9% FA and 15.7% SF for test C. The 7-day, 28-day and 90-day compressive strengths of SiMn concrete were predicted using the prediction models in Table 4.4. The 28-day, 90-day and 180-day sorptivity of SiMn slag were also predicted. Using the predicted value of SiMn slag concrete, the compressive strength and sorptivity of limestone concrete were obtained from Eq. 4.2 and Eq. 4.3 respectively.

Table 4.10: Predicted FA and SF contents at targeted compressive strength

Test	Targeted 28-day compressive strength	Predicted outcome		
		FA/B	SF/B	Desirability
A	65 MPa	0.39	0.219	1.0
B	70 MPa	0.366	0.179	1.0
C	75 MPa	0.259	0.157	1.0
Slump value was set within 80 mm to 210 mm for test set A, B and C				

Experiments were carried out to validate the predicted compressive strength of SiMn slag and limestone concrete for 7, 28 and 90 days. Concrete specimens were prepared and tested using similar procedures and conditions. Figure 4.16 presents the test results as well as the comparison with the predicted results in terms of concrete strength. For SiMn slag concrete, the experimental 28-day compressive strength generally achieved the target value for test A, B and C, with an error of 4.6%, 2.6% and 4.6% respectively. Test A concrete had a slightly lower strength than predicted due to its high SF content, which decreased concrete homogeneity. Nonetheless, the issue did not arise in test B and test C. The results further confirmed the accuracy of model in concrete strength prediction. Figure 4.17 presents the test results and comparison with the predicted values in terms of sorptivity of concrete. In test A, B and C, SiMn slag concrete achieved lower durability than the target, with error ranged between 0.3% and 8.2%. This was also ascribed to high SF content which increased the cohesiveness of concrete.

The compressive strength of limestone concrete is higher than that of SiMn slag concrete. But with increasing FA and SF contents, the strength difference was reduced. The improvement in the strength of SiMn slag concrete by FA and SF was more significant than that of limestone concrete. The finding was similar to that of Tang et al. (2019), who found a better strength improvement of recycled aggregate concrete made with blast furnace slag as a mineral admixture. Besides, the percentage error for all tests ranged from 0.9% to 5.4%, indicating satisfactory accuracy of Eq. 4.2 for the conversion of strength between the SiMn slag and limestone concrete. The sorptivity of limestone concrete is lower than that of SiMn slag concrete. Despite the substitution levels of FA and SF, the sorptivity difference between two concrete types was similar. The percentage error ranged from 5.3% to 11.4%, showing satisfactory accuracy of Eq. 4.3. In summary, the use of the RSM models to predict the concrete strength manufactured from limestone aggregate is valid. It is essential that the correlation between the two types of concrete is appropriately established.

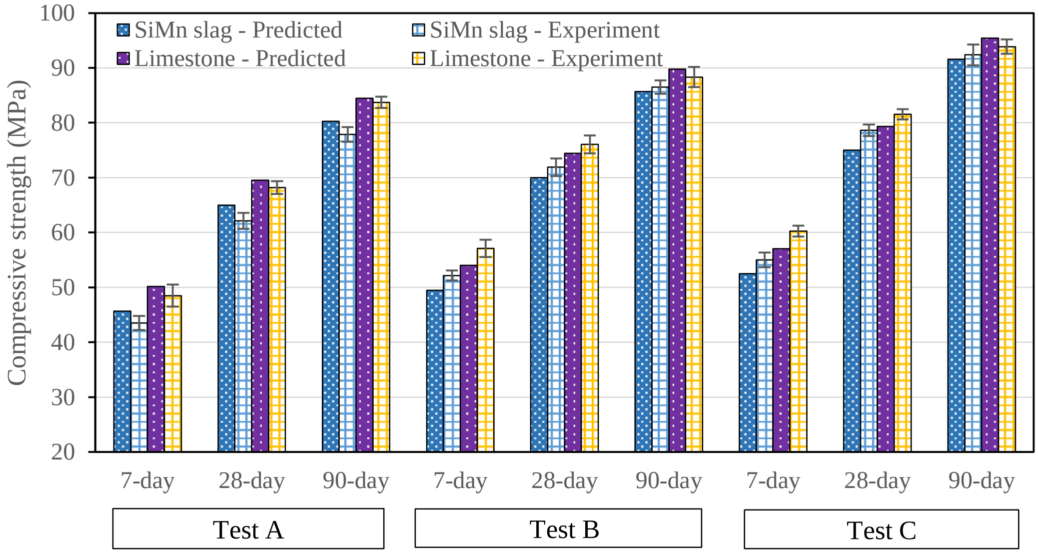

Figure 4.16: Comparison of predicted and experiment compressive strength for SiMn slag and limestone concrete

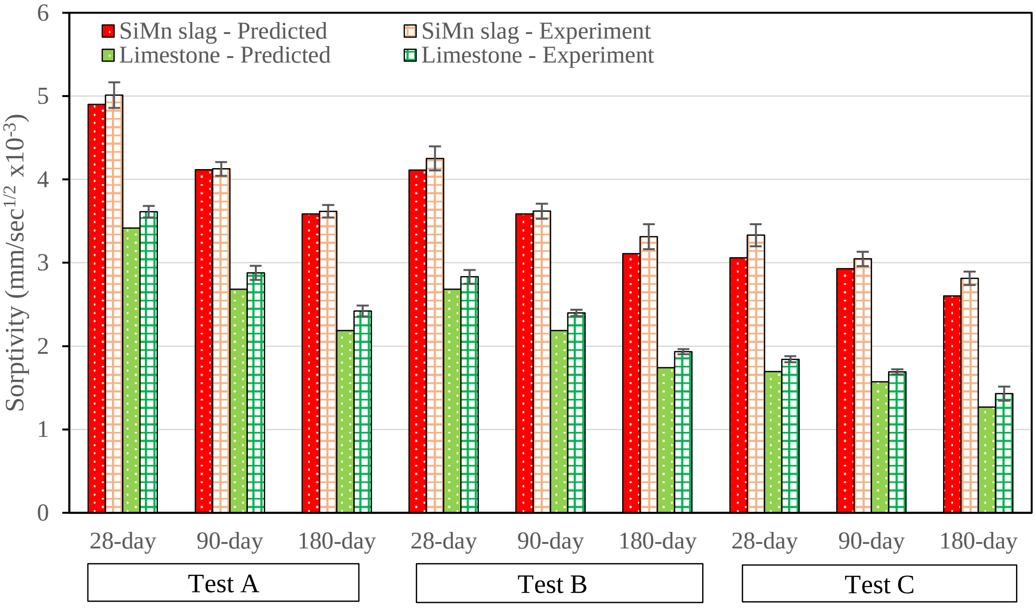

Figure 4.17: Comparison of predicted and experiment sorptivity for SiMn slag and limestone concrete

4.5.4. Further Opportunity for Optimized FA and SF Concrete

The previous section examined and discussed the fundamental properties of concrete. Nonetheless, concrete optimized with FA and SF also has improved advantages in other properties, especially with regard to its practical application. The following further elaborates on the opportunities for the application of optimized FA and SF concrete.

4.5.4.1. Fracture Toughness

The failure of concrete in all states of stress is closely associated with defect due to cracking. Fracture toughness is an important parameter used to describe the mechanism of crack initiation and propagation, especially in the case of brittle materials such as concrete (Golewski, 2018). There are three modes of concrete fracture relating to the three-dimensional failure, namely mode I (K_{Ic}), mode II (K_{IIc}) and mode III (K_{IIIc}). K_{Ic} represents pure tensile loading, K_{IIc} represents in-plane shearing and K_{IIIc} represents anti-plane shearing.

Mechanical properties, such as compressive and splitting tensile strength, can directly influence the fracture toughness of concrete. Past research has shown that the use of blends such as FA and SF can increase the strength of concrete and hence its fracture toughness. Golewski (2018) found that FA concrete had a lower early-age but higher late-age mode III stress intensity factor (K_{IIIc}), which showed a similar pattern to compressive strength. In addition, Liu et al. (2020b) showed that the incorporation of 30% SF could increase K_{Ic} by up to 64% because SF improved cement bonding and reduced stress relaxation. Therefore, as the strength of optimized FA and SF concrete has been improved in this study, optimization can also contribute to the improvement of concrete fracture toughness. Nevertheless, further investigation is still required to acquire data to confirm this hypothesis.

4.5.4.2. Resistance to Dynamic Load

Dynamic resistance is a key factor in the assessment of material structural performance and safety, especially for concrete, which is brittle and strain-rate sensitive (Nili and Afroughsabet, 2010). The behavior of concrete under transient dynamic loads, such as earthquake impacts, machine operation and explosion, is different from that of concrete under static loads. Resistance of concrete to dynamic load can be determined using both destructive and non-destructive tests. Destructive tests include drop-weight test, explosive test, projectile impact test and split-Hopskinson bar test (Song et al., 2005), whereas the damping test is non-destructive test (Noushini et al., 2013).

As most researches focus on static or quasi-static loading, there are fewer investigations documenting dynamic behaviors of concrete, particularly those optimized with SF and FA. Optimized concrete, which possesses high strength and high durability, is perceived to also exhibit better resistance to dynamic loading. Zhao and Zhang (2019) have found that the dynamic tensile strength has increased with SF content due to improved concrete pore structure. The finer property of SF filled the particle gap in cement, reducing the porosity. In contrast, Nili and Afroughsabet (2010) found that the improvement of impact resistance by SF was not proportional to the increased compressive strength as concrete became more brittle. Nonetheless, FA can be used to increase the ductility of concrete, which may improve its dynamic resistance, but this requires further investigation (Ali et al., 2020).

4.5.4.3. Synergy with Other Additive

The current study focuses on the optimization of ternary cement using FA and SF to maximize the mechanical and durability properties of concrete. Research can be expanded by the introduction of other additives such as ground granulated blast furnace slag (GGBS), metakaolin (MK) and marble waste powder (MWP) to further boost concrete performance. Gesoglu et al. (2009) showed that the addition of GGBS as quaternary cement could reduce the sorptivity and chloride permeability of FA and SF concrete. Slag, such as GGBS, typically contains chemical compositions that are more stable and can thus facilitate better pozzolanic reaction. Dave et al. (2018) have demonstrated that MK is a better additive than GGBS in terms of strength due to its higher content of silica and alumina for pozzolanic reaction. In addition, Choudhary et al. (2020) found that the use of quaternary cement containing FA, SF and MWP at a replacement level of up to 50% could produce concrete with lower permeability than control concrete due to pore refining. In line with the latest research trend towards environmental sustainability, the use of high-volume cement replacement without comprising strength and durability is of best interest. Future study is recommended to consider the synergy of FA and SF concrete with other additives in optimization so as to produce more sustainable concrete.

4.6. Concluding Remark

This study uses binary and ternary cement blends of SF and FA to enhance the strength and durability of SiMn slag concrete using the RSM. Based on the outcomes of the experiment and also the optimization, the following conclusion can be drawn.

1. The concrete compressive and splitting tensile strength showed a similar pattern of results. Incorporation of SF up to 15% increased strength at all ages, but a further addition reduced strength. FA incorporation of up to 40% increased 28-day and 90-day strength, but decreased 7-day strength due to slow pozzolanic reaction. For ternary blended concrete, SF compensated for reduced 7-day strength caused by FA and their combined effect further increased strength at 28 and 90 days.
2. For durability, the use of 0–15% SF reduced concrete sorptivity. But, when the SF content was above 15%, the sorptivity increased. Concrete containing 0–40% FA exhibited lower sorptivity than the control. Ternary blended concrete further

reduced sorptivity, with FA20SF15 concrete having the largest reduction of 38.1%, 20.9% and 20.3% at 28, 90 and 180 days respectively.

3. Chloride permeability of binary and ternary blended concrete decreased with increasing FA and SF contents. FA40SF30 concrete had the lowest chloride permeability at 28, 90 and 180 days, with a reduction of 70.1%, 63.9% and 62.5% respectively.
4. Using the RSM, prediction models for compressive and splitting tensile strengths at 7, 28 and 90 days were presented as quadratic models. Cubic models were developed for sorptivity at 28, 90 and 180 days, chloride permeability at 180 days and concrete slump. Quartic models were developed for chloride permeability at 28 and 90 days.
5. The prediction models were evaluated as statistically significant based on the two-way ANOVA with significance level below 0.05. Residual errors from lack of fit and pure errors were minimal. The adjusted and predicted R^2 showed that the prediction models were adequate to describe the relationship between variables and responses and were fit for optimization.
6. From optimization, the FA and SF contents with maximum strength and minimum permeability were 16.3% and 11.5% respectively. The 90-day compressive strength, 90-day tensile strength, 180-day sorptivity, 180-day chloride permeability were improved by 10.4%, 18.9%, 24.9% and 44.6% respectively. These properties were also improved by 4.2%, 1.6%, 27.3% and 24% respectively, compared to normal limestone concrete.
7. The SEM analysis confirmed that the optimized concrete exhibited a more compact ITZ and better bonding of cement paste with aggregate than the control.
8. Linear equations were established to correlate the compressive strength and sorptivity between SiMn slag and limestone concrete. The validation experiment showed that the equations used in conjunction with the RSM models predicted the compressive strength and sorptivity of limestone concrete with good accuracy.

Chapter 5. Durability and Cyclic Behavior of Concrete Exposed to Sulphate Attack and Wetting-Drying Action

5.1. Introduction

Concrete is prone to deterioration due to sulphate attack and wetting-drying action (WDA) when exposed to hostile marine climate. The concrete surface can be physically damaged, resulting in cracking that adversely affects the durability of concrete. In marine applications, concrete is also susceptible to cyclic loading such as wave and wind actions. In this context, the degradation of mechanical properties of concrete can jeopardize its resistance to cyclic loading. This chapter presents the effect of sulphate attack and WDA on the durability and compressive cyclic behavior of concrete through experimental investigation.

Experiment was conducted to assess the concrete performance by simulating the marine wetting-drying environment. Six types of concrete mixture were studied in the investigation. The first three mixtures examined the effect of SiMn slag aggregate, with Mix 6 (B2/C2/D2) from Chapter 3 serving as the control mix, Mix 6 (B2/C2/D2) optimized with SF, and Mix 6 (B2/C2/D2) optimized with FA and SF using RSM from Chapter 4. For comparison, three other similar concrete mixtures containing limestone aggregate were included. In this case, Mix 5 (B1/C2/D2) was used as the control mix with FA and SF contents identical to the SiMn slag concrete.

The effects of WDA, sulphate concentration (5%, 12.5% and 20%) and period of exposure (30, 60, 90, 120 and 150 days) were studied in the experiment. The assessed concrete properties were physical appearance, sulphate penetration profile, mass and volume changes, compressive strength and splitting tensile strength. In addition, scanning electron microscope (SEM) analysis was used to investigate the microstructure of concrete, including interfacial transition zone (ITZ). Furthermore, cyclic compression test was carried out to determine the fatigue behavior of concrete degraded by sulphate attack and WDA. The effects of sulphate attack and WDA, upper stress loading level and loading frequency on fatigue life, residual strain, variation of elastic modulus and post-cyclic compressive strength were studied in the cyclic loading test.

5.2. Experimental Programme

5.2.1. Concrete Mix Design

Concrete mix design used for the experiment in this chapter is shown in Table 5.1. Six types of mix proportion were included to assess the performance of concrete subjected to sulphate attack and WDA. The first three concrete mixes were based on the Mix 6 (B2/C2/D2) of Chapter 3, which used SiMn slag as coarse aggregate and was abbreviated as SiMn(X). The notation "X" included C, SF and SF-FA, which respectively represented Mix 6 (B2/C2/D2) as control mix, Mix 6 (B2/C2/D2) optimized with SF and Mix 6 (B2/C2/D2) optimized with FA and SF. The optimization of FA and SF in these mixtures was performed using the Response Surface Method (RSM) model presented in Chapter 4. The detail of the optimization is presented in Appendix D. Furthermore, three types of limestone concrete with similar FA and SF contents to the SiMn slag concrete were included for comparison. The limestone concrete was abbreviated as LS(X). The properties of all the materials used were similar to those presented in Section 3.2.1 and Section 4.2.1. For all the mixes, the w/c ratio was kept constant at 0.32. The SP dosage was 1% of the total binder content. The workability of each concrete mix has been determined by slump test and the results are shown in Table 5.1.

Table 5.1: Concrete mix proportion for durability and cyclic loading tests

Material	**Mix proportion (kg/m^3)**					
	SiMn (C)	SiMn (SF)	SiMn (SF-FA)	LS (C)	LS (SF)	LS (SF-FA)
Cement	550	472	406	550	472	406
SF	0	78	54	0	78	54
FA	0	0	90	0	0	90
SiMn slag	1115	1115	1115	0	0	0
Limestone	0	0	0	965	965	965
Marine sand	515	501	501	515	501	501
Quarry dust	173	168	168	173	168	168
Seawater	176	176	176	176	176	176
Superplasticizer	5.5	5.5	5.5	5.5	5.5	5.5
Slump value (mm)	75	52	106	90	76	125

5.2.2. Test Method

5.2.2.1. Preparation of Concrete Specimen

The concrete specimen was prepared based on the mixing method described in Section 3.2.2 for control concrete and Section 4.2.4.1 for concrete containing FA and SF. Previous test results indicated that concrete with an age of 90 days was able to achieve the targeted strength. Beyond the 90-day age, the concrete exhibited more constant properties including strength and permeability due to more complete hydration. Therefore, all concrete specimens were fully submerged in water for 165 days prior to the WDA and sulphate immersion test to minimize the effect of hydration on the result.

5.2.2.2. Wetting-Drying of Concrete Specimen

The 165-day-old concrete specimens were transferred to plastic containers of the dimension shown in Figure 5.1 for cyclic wetting-drying and sulphate immersion test. A 20 mm diameter tap was mounted at the bottom of the container that was used to drain the salt solution. The specimens were elevated with a 50 mm thick layer of gravel to prevent direct contact with the trapped water during the drying process. The wetting-drying process consisted of immersing the specimen in salt solution for 12 hours and drying them in the air at 27±1 ^{o}C for 11 hours. The test procedure took 45 minutes to drain the salt solution and 15 minutes to fill the container. Therefore, the duration of one complete wetting-drying cycle was 24 hours. During the wetting period, the container was covered with a lid to prevent loss of moisture. The drained salt solution has been stored in a separate tightly covered container. The salt solution used in the wetting stage was prepared by dissolving the chemical grade sodium sulphate (Na_2SO_4) powder in water. Na_2SO_4 solutions with three different concentrations were used, namely 5wt% (Exposure I), 12.5wt% (Exposure II) and 20wt% (Exposure III). The solution was freshly replaced every 30 days. The wetting-drying periods for the respective specimens were 30, 60, 90, 120 and 150 days.

In addition, specimens were also treated by fully immersing them in salt solution for comparison. Two types of solution, 20wt% Na_2SO_4 solution (Exposure IV) and tap water (Exposure C), were used. Furthermore, concrete specimens were also placed at the breakwater (Exposure A) of Tanjung Lobang Beach in Miri, Malaysia. Table 5.4 presents a summary of exposure conditions in this investigation.

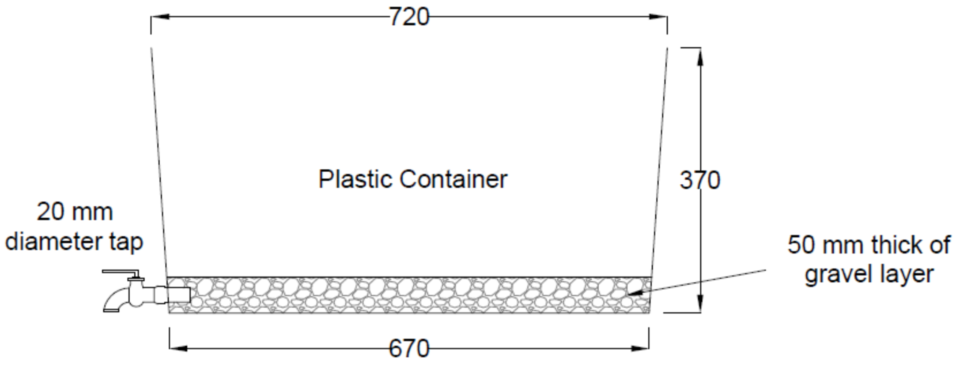

Side View

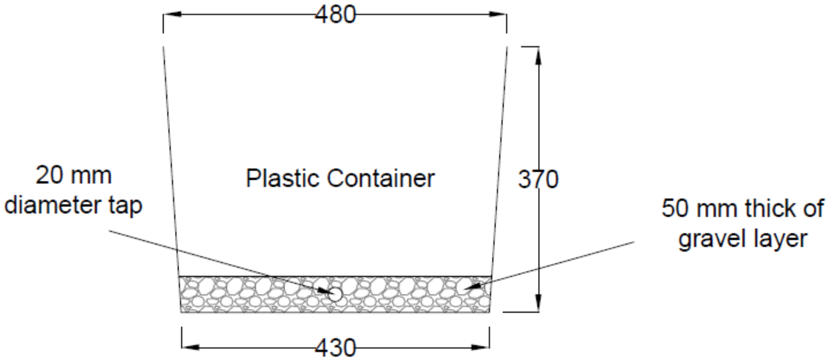

Front View

Figure 5.1: Setup of container for wetting and drying of specimen

5.2.2.3. Sulphate Penetration Profile Test

Concrete prism with a dimension of 75 x 75 x 300 mm was used in the sulphate profile test. With the exception of one of the square surfaces, other sides of the prism were coated with epoxy paint. In this scenario, the sulphate (SO_4^{2-}) ion diffused into the concrete in unidimensional flow, causing deterioration and damage. The sulphate intrusion profile was determined by measuring the distribution of SO_4^{2-} ions from the surface to the interior of the concrete. After 90 days and 150 days of wetting-drying exposure, powder samples were collected from the concrete specimen by drilling at several points along the ingress path. The samples were obtained from four penetration depths, which ranged from 0 to 5 mm, 5 to 10 mm, 10 to 15 mm and 15 to 20 mm, with the average depths of 2.5, 7.5, 12.5 and 17.5 mm respectively. The SO_4^{2-} ion content of the powder sample was determined using the barium sulphate gravimetric method in accordance with ASTM C114 (2018) standard. Table 5.2 shows the initial SO_4^{2-} ion contents of concrete for each mix which were determined prior to sulphate attack and WDA.

Table 5.2: Initial SO_4^{2-} ion content of concrete

Concrete mix	Initial SO_4^{2-} content (%)
LS(C)	0.41
LS(SF)	0.32
LS(SF-FA)	0.28
SiMn(C)	0.48
SiMn(SF)	0.35
SiMn(SF-FA)	0.31

5.2.2.4. Mass and Volume Change

Concrete experienced changes in mass and volume due to the deterioration caused by sulphate attack and WDA. Concrete prisms 75 x 75 x 300 mm were used for the measurement of changes in mass and volume. The change in mass and volume was determined using Eq. 5.1 and Eq. 5.2. Both mass and volume changes were determined after 30, 60, 90, 120 and 150 days of exposure.

$$\Delta M_d = \frac{M_o - M_d}{M_o} \times 100 \qquad \text{Eq. 5.1}$$

$$\Delta V_d = \frac{V_o - V_d}{V_o} \times 100 \qquad \text{Eq. 5.2}$$

where ΔM_d and ΔV_d are the mass and volume change of concrete at the respective exposure time, M_o and V_o are the mass and volume of concrete before the exposure, and M_d and V_d are mass and volume of concrete at the respective exposure period.

5.2.2.5. Compressive Strength Test

The test method described in Section 3.2.3.2 was used to assess the compressive strength of concrete. The compression test was performed on cube specimen with dimensions of 100 x 100 x 100 mm. Concrete compressive strength was determined after 0, 30, 60, 90, 120 and 150 days of exposure to sulphate attack and WDA.

5.2.2.6. Splitting Tensile Strength Test

The test method described in Section 3.2.3.3 was used for determining the splitting tensile strength. The test was performed on cylindrical specimen with 100 mm in diameter and 200 mm in height. Splitting tensile strength of concrete was determined after 0, 30, 60, 90, 120 and 150 days of exposure to sulphate attack and WDA.

5.2.2.7. Scanning Electron Microscope Analysis

Concrete specimen was prepared in accordance with the method presented in Section 3.2.3.8. SEM analysis was performed on SiMn(C), SiMn(SF-FA) and LS(SF-FA) after 150 days of exposure to WDA in 20% Na_2SO_4 solution. The concrete specimens immersed in tap water for the same period were also tested for comparison.

5.2.2.8. Cyclic Loading Test

The cyclic compressive loading test for concrete was performed on 50 mm cube specimens using a 100 kN Instron Universal Testing Machine 5982 as shown in Figure 5.2. Compressive strength of specimen under static loading was determined based on the test method described in Section 5.2.2.5. Table 5.3 shows the details of all test specimens. In cyclic loading, the lower stress level (S_{min}) was set constant at 1% of the static compressive strength of concrete. The upper stress levels (S_{max}) studied in the investigation were 30%, 40%, 45%, 80%, 85% and 90% of compressive strength. The loading frequencies investigated were 0.6, 0.8 and 1 Hz. The specimens were labelled as Tx-Sy-Fz, with “T” referring to the type of concrete mix exposed to particular condition, “S” referring to the upper stress level and “F” referring to the loading frequency, as shown in Table 5.3. For example, T2-S0.9-F0.8 indicated SiMn(SF-FA) concrete exposed to 150 days of WDA in 20% Na_2SO_4 solution, and was tested using 90% compressive strength as S_{max} at a loading frequency of 0.8 Hz. Three specimens from each type of concrete were tested.

The average static compressive strength of concrete specimens was first determined and this value was used as input for the cyclic loading test. Before the cyclic loading test, concrete specimen was pre-loaded at 5 kN for 2 minutes to flatten the loading surface. The force and displacement of the specimen in vertical direction were recorded using the loading cell and extensometer respectively. The test was terminated after 10,000 loading cycles if the specimen did not fail. The compressive strength of the intact specimen was then tested.

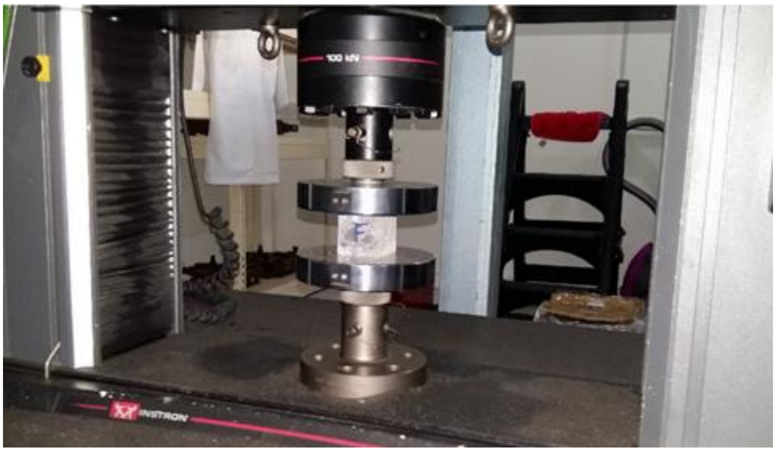

Figure 5.2: Cyclic compressive loading test set-up

Table 5.3: Detail of test specimens

Series	Notation	S_{max}	S_{min}	Loading frequency (Hz)	Number of specimen	Concrete Mix	Exposure condition
1	T1	1	-	-	3	SiMn(SF-FA)	150 days full immersion + tap water
	T1-S0.3-F0.8	0.3	0.01	0.8	3		
	T1-S0.4-F0.8	0.4	0.01	0.8	3		
	T1-S0.45-F0.8	0.45	0.01	0.8	3		
	T1-S0.45-F0.6	0.45	0.01	0.6	3		
	T1-S0.45-F1.0	0.45	0.01	1.0	3		
2	T2	1	-	-	3	SiMn(SF-FA)	150 days WDA + 20% Na_2SO_4
	T2-S0.45-F0.8	0.45	0.01	0.8	3		
	T2-S0.8-F0.8	0.8	0.01	0.8	3		
	T2-S0.85-F0.8	0.85	0.01	0.8	3		
	T2-S0.9-F0.8	0.9	0.01	0.8	3		
3	T3	1	-	-	3	LS(SF-FA)	150 days WDA + 20% Na_2SO_4
	T3-S0.9-F0.8	0.9	0.01	0.8	3		
	T3-S0.85-F0.8	0.85	0.01	0.8	3		
	T3-S0.8-F0.8	0.8	0.01	0.8	3		

5.2.3. Summary of Test Programme

Table 5.4 shows the test programme for the study. Three concrete specimens were prepared for each test period and the average value was used in the analysis. The changes in mass and volume of concrete were measured on the sulphate penetration profile test specimens.

Table 5.4: Summary of test programme for concrete exposed to sulphate attack and WDA

Test	**Exposure condition**	**Test duration (days)**					
		SiMn(C)	SiMn(SF)	SiMn(SF-FA)	LS(C)	LS(SF)	LS(SF-FA)
Sulphate profile	Exposure I	-	-	-	90, 150	-	-
	Exposure III	150	150	150	90, 150	150	150
	Exposure IV	-	-	-	90, 150	-	-
Mass change	Exposure I	-	-	-	0, 30, 60, 90, 120, 150	-	-
	Exposure III	0, 30, 60, 90, 120, 150	0, 30, 60, 90, 120, 150	0, 30, 60, 90, 120, 150	0, 30, 60, 90, 120, 150	0, 30, 60, 90, 120, 150	0, 30, 60, 90, 120, 150
	Exposure IV	-	-	-	0, 30, 60, 90, 120, 150	-	-
Volume change	Exposure I	-	-	-	0, 30, 60, 90, 120, 150	-	-
	Exposure III	0, 30, 60, 90, 120, 150	0, 30, 60, 90, 120, 150	0, 30, 60, 90, 120, 150	0, 30, 60, 90, 120, 150	0, 30, 60, 90, 120, 150	0, 30, 60, 90, 120, 150
	Exposure IV	-	-	-	0, 30, 60, 90, 120, 150	-	-
Compressive strength	Exposure I	-	-	-	0, 30, 60, 90, 120, 150	-	-
	Exposure II	-	-	-	0, 30, 60, 90, 120, 150	-	-
	Exposure III	0, 30, 60, 90, 120, 150	0, 30, 60, 90, 120, 150	0, 30, 60, 90, 120, 150	0, 30, 60, 90, 120, 150	0, 30, 60, 90, 120, 150	0, 30, 60, 90, 120, 150
	Exposure IV	-	-	-	0, 30, 60, 90, 120, 150	-	-
	Exposure A	-	-	-	0, 30, 60, 90, 120, 150	-	-
Splitting tensile strength	Exposure I	-	-	-	0, 30, 60, 90, 120, 150	-	-
	Exposure II	-	-	-	0, 30, 60, 90, 120, 150	-	-
	Exposure III	0, 30, 60, 90, 120, 150	0, 30, 60, 90, 120, 150	0, 30, 60, 90, 120, 150	0, 30, 60, 90, 120, 150	0, 30, 60, 90, 120, 150	0, 30, 60, 90, 120, 150
	Exposure IV	-	-	-	0, 30, 60, 90, 120, 150	-	-
SEM analysis	Exposure III	150	-	150	-	-	150
	Exposure C	150	-	150	-	-	150
Cyclic Loading	Exposure III	-	-	150	-	-	150
	Exposure C	-	-	150	-	-	-

Exposure I – WDA + 5% Na_2SO_4 solution
Exposure II – WDA + 12.5% Na_2SO_4 solution
Exposure III – WDA + 20% Na_2SO_4 solution
Exposure IV – Immersion + 20% Na_2SO_4 solution
Exposure C – Immersion + water
Exposure A – Sample put on actual site

5.3. Durability of Concrete

5.3.1. Physical Appearance

The physical appearance of concrete specimen was visually inspected. For all the specimens, no change in color and general shape was observed. Figure 5.3 shows pictures of LS(C) concrete at 0 day and after 30 days and 150 days of exposure to WDA in 20% Na_2SO_4 solution (Exposure III). The 30-day specimens were slightly stained with white powdery efflorescence on their surface, while the surface of 150-day specimens was covered with more visible efflorescence. The efflorescence was caused by the precipitation of sulphate salt concrete during the drying stage of concrete. The result was consistent with the findings of Yu et al. (2018) and Zhongya et al. (2019), who also observed white efflorescence near the concrete surface after exposure to Na_2SO_4 solution. Long-term exposure to WDA trapped more salt in the concrete pore, resulting in more efflorescence. The efflorescence formation indicated salt crystallization, and hence some damage to the concrete might have occurred.

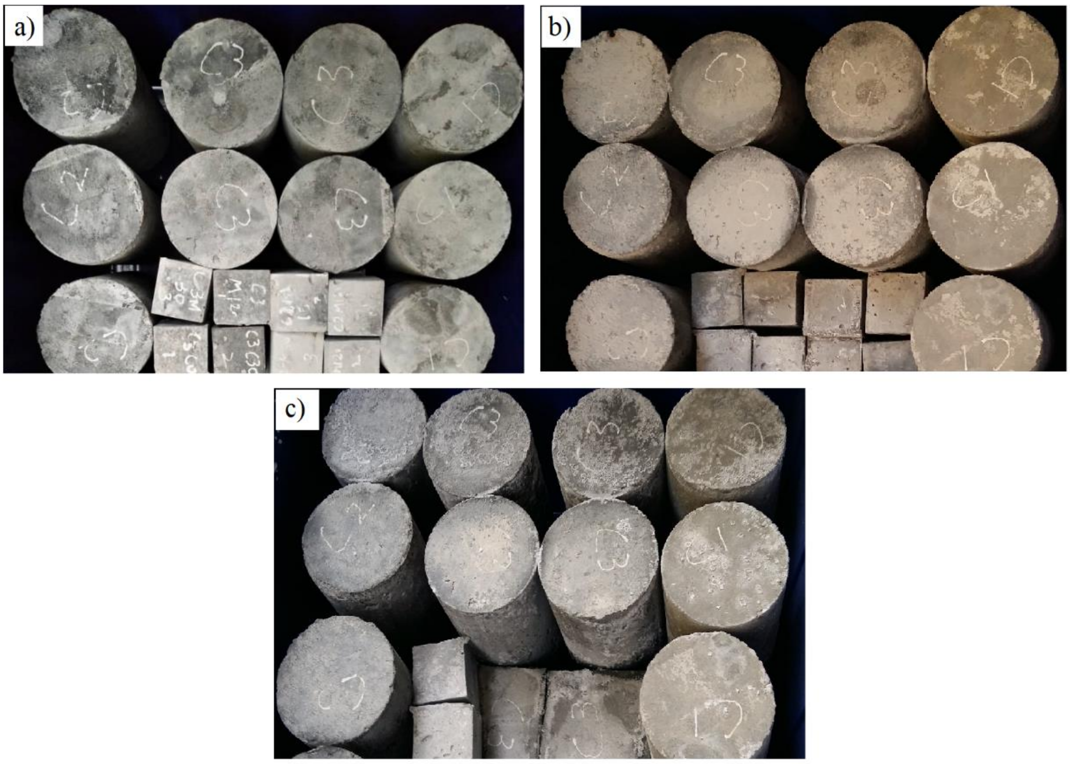

Figure 5.3: LS(C) exposed to WDA in 20% Na_2SO_4 solution (Exposure III) for (a) 0 day, (b) 30 days and (c) 150 days

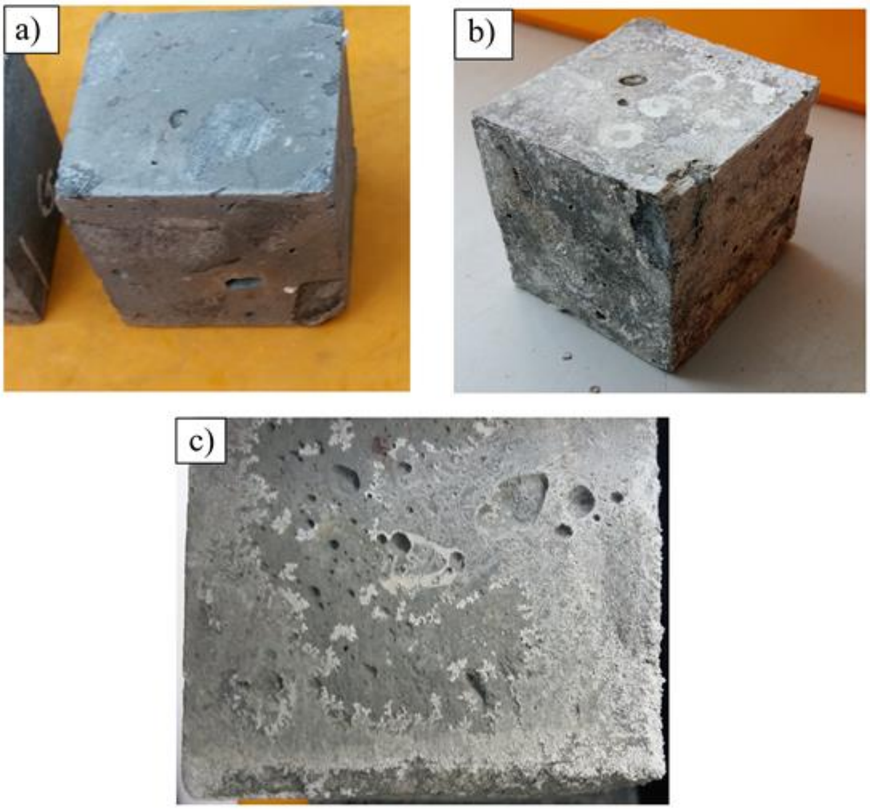

Figure 5.4: SiMn(SF-FA) after 150 days of (a) WDA + 5% Na_2SO_4 solution (Exposure I), (b) WDA + 20% Na_2SO_4 solution (Exposure III) and (c) Immersion + 20% Na_2SO_4 solution (Exposure IV)

Figure 5.4 compares the physical appearance of SiMn(C) concrete after 150 days of exposure to three types of conditions, namely WDA in 5% Na_2SO_4 solution (Exposure I), WDA in 20% Na_2SO_4 solution (Exposure III) and full immersion in 20% Na_2SO_4 solution (Exposure IV). Under Exposure I, the mortar layer of concrete, particularly on the edge, was slightly peeled off and some cracks formed on the surface. As comparatively less efflorescence was present, the damage might be caused by shrinkage during the drying of concrete (Chen et al., 2016). The damage of the specimens exposed to Exposure III was more severe, with more significant delamination of the mortar layer and cracking of the concrete. The damage was due to a larger scale of salt crystallization as the concrete surface was covered with more efflorescence compared to Exposure I. It was also attributed to the dissolution of hydrate components as a consequence of the sulphate attack (Jiang and Niu, 2016). Concrete specimens under Exposure IV had suffered relatively less physical damage than the other two exposure conditions. The surface was slightly swollen and stained with efflorescence. Concrete expansion was caused by the formation of ettringite and gypsum due to sulphate attack. By comparing the concrete in Exposure III and Exposure IV, WDA induced more severe physical degradation. Although the concrete was continuously re-wetted during each cycle, the long-term drying effect caused shrinkage and cracking of concrete.

5.3.2. Sulphate Penetration Profile

The initial sulphate (SO_4^{2-}) ion content of concrete for all mixes prior to the test has been determined and is shown in Table 5.2. All concrete contained a low amount of initial SO_4^{2-} ion, ranging from 0.28% to 0.48%. The initial SO_4^{2-} ion content in concrete was produced by the hydration of cement. The partial replacement of cement by FA and SF could slightly reduce the initial SO_4^{2-} ion content. In the following section, the initial SO_4^{2-} ion content was deducted from the measured SO_4^{2-} ion value in the sulphate penetration profile of concrete.

Figure 5.5 shows the sulphate penetration profile of all types of concrete after 150 days of exposure to WDA in 20% Na_2SO_4 solution (Exposure III). The SO_4^{2-} ion content decreased with an increase in depth towards the interior of concrete. The SO_4^{2-} ion content was 1.72%–2.58%, 0.73%–1.23% and 0.42%–0.57% at the average depth of 2.5 mm, 7.5 mm and 12.5 mm respectively. At an average depth of 17.5 mm, all concrete mixes had a SO_4^{2-} ion content of less than 0.5%. SiMn(C) had the highest SO_4^{2-} ion content along the depth of penetration. Nevertheless, the incorporation of FA and SF improved the concrete resistance to sulphate penetration. The effect of FA and SF was also shown in limestone concrete, where the SO_4^{2-} ion contents of LS(SF) and LS(SF-FA) reduced by 0.19% and 0.41% compared to LS(C) at 2.5 mm depth. The findings were in line with those of Qi et al. (2017) who found better sulphate resistance if the concrete was incorporated with GGBS and FA. The use of FA and SF enhanced the concrete pore structure and improved its resistance against sulphate intrusion.

Besides, the SO_4^{2-} ion content of limestone concrete was typically lower than that of SiMn slag concrete. The higher sulphate concentration of SiMn slag concrete was due to the weaker bonding of SiMn slag aggregate with cementitious matrix. The SiMn slag aggregate was angular and had a smoother surface than limestone aggregate. Zhang et al. (2019) also found that a weaker aggregate bonding of recycled aggregate concrete resulted in increased intrusion of sulphate. But, the difference in SO_4^{2-} ion content between the concrete mixes decreased with the increasing depth of concrete.

The sulphate profile of LS(C) exposed to 90 and 150 days of three exposure conditions, namely WDA in 5% Na_2SO_4 solution (Exposure I), WDA in 20% Na_2SO_4 solution (Exposure III) and full immersion in 20% Na_2SO_4 solution (Exposure IV), is shown in Figure 5.6. The SO_4^{2-} ion content along the concrete depth increased with time. For instance, SO_4^{2-} ion content of LS(C) was 1.35% at depth 0–5 mm after 90 days of exposure to Exposure III. After 150 days of exposure, the SO_4^{2-} ion content increased to 2.15% at the same depth. The increment was due to the diffusion of SO_4^{2-} ion caused by concentration gradient and the capillary absorption. Besides, the sulphate attack also damaged the concrete, causing cracks and leading to a more penetration of SO_4^{2-} ion (Maes and De Belie, 2014).

The SO_4^{2-} ion content of concrete in Exposure III was approximately two times higher than that in Exposure I. This was due to the higher concentration of Na_2SO_4 solution used in Exposure III, but the increment was not directly proportional to the increase in solution concentration. A higher solution concentration produced a greater amount of expansive components such as ettringite and gypsum, which filled up the concrete pore and had a slight effect on slowing sulphate penetration (Tang et al., 2018). By comparing the Exposure III and Exposure IV, the WDA increased the SO_4^{2-} ion content by approximately 1.3 times the SO_4^{2-} ion content in concrete exposed to full immersion. The cyclic behavior of WDA accumulated the SO_4^{2-} ion at the wetting front, which induced higher concentration gradient for diffusion (Qi et al., 2018).

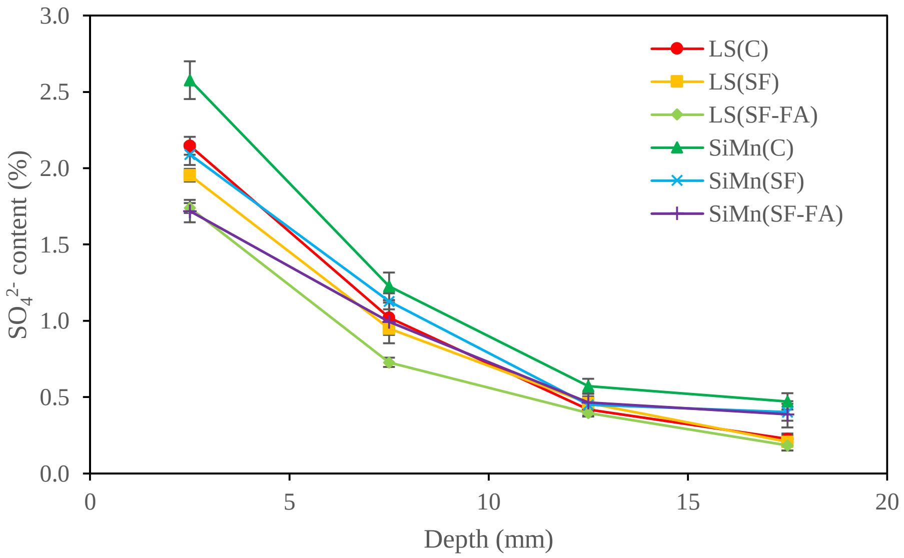

Figure 5.5: Sulphate penetration profile of concrete exposed to 150 days of WDA in 20% Na_2SO_4 solution (Exposure III)

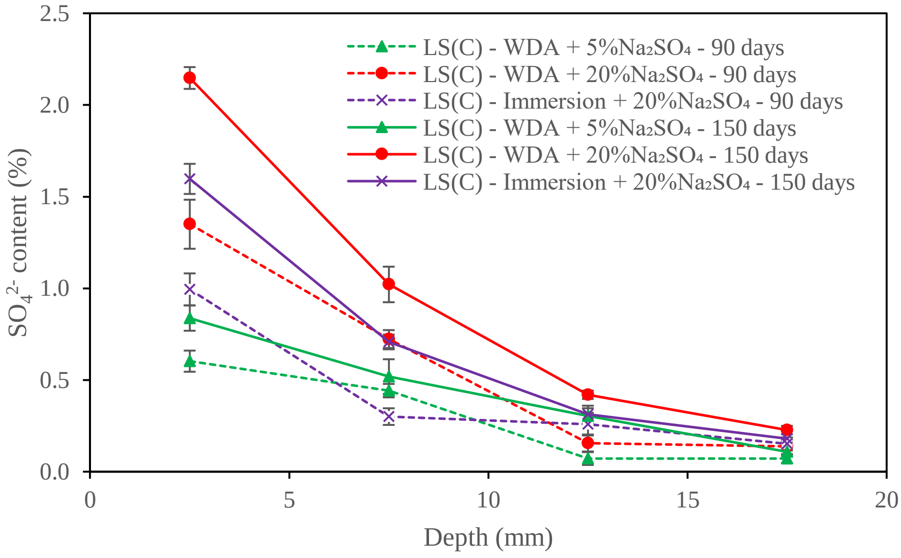

Figure 5.6: Sulphate penetration profile of LS(C) exposed to 90 days and 150 days of various conditions

5.3.3. Mass Change

The mass change of concrete with exposure time was also measured. Figure 5.7 shows the mass change of concrete for all mixes exposed to WDA in 20% Na_2SO_4 solution (Exposure III). The concrete experienced two stages of mass change, which were an increasing stage and a decreasing stage. Both SiMn(C) and LS(C) exhibited a similar trend of mass change. The mass of both concrete types increased by 0.43% and 0.42% at 60 days, but they decreased to -0.49% and -0.39% at 150 days. Jiang and Niu (2016) also observed a two-stage mass change for concrete exposed to WDA in various types of sulphate solution. The mass gain was due to the formation of ettringite and gypsum inside concrete pores. However, at the later stage, the accumulation of these expansive products exerted stress to damage the concrete, leading to a mass loss. The surface damage, such as spalling of mortar layer due to shrinkage during the drying period, also resulted in the mass loss (Tang et al., 2018).

The incorporation of SF, as in SiMn(SF) and LS(SF), delayed the onset of mass loss at 120 days. Furthermore, SiMn(SF-FA) and LS(SF-FA), which contained FA and SF, did not undergo a mass-decreasing stage of up to 150 days. The addition of FA and SF enhanced the pore structure of concrete and reduced the intrusion of sulphate. The pozzolanic reaction of FA and SF also improved the mechanical property of concrete and the resultant concrete had a higher resistance to sulphate attack and WDA. The results related well to the research of Qi et al. (2017) who found a constant mass gain in concrete containing FA and GGBS for up to 270 days.

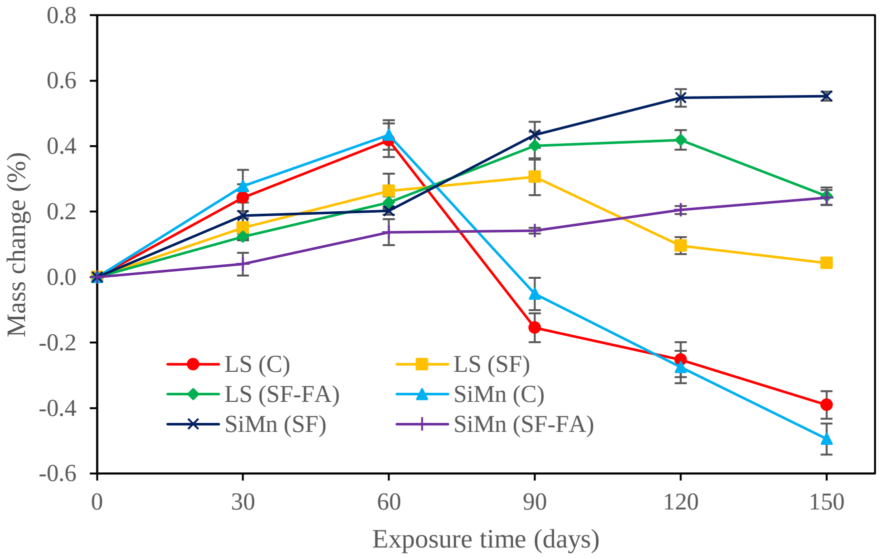

Figure 5.7: Mass change with exposure time for concrete exposed to WDA in 20% Na_2SO_4 solution (Exposure III)

Figure 5.8 compares the mass change of LS(C) exposed to three types of exposure environment, namely WDA in 5% Na_2SO_4 solution (Exposure I), WDA in 20% Na_2SO_4 solution (Exposure III) and full immersion in 20% Na_2SO_4 solution (Exposure IV). From 0 to 90 days, the mass of concrete in Exposure I gradually increased and then became constant, with no noticeable mass-decreasing stage. The maximum mass gain in Exposure I was 0.28% lower than that in Exposure III. The greater mass gain of concrete in Exposure III was attributed to a higher concentration of sulphate solution, which increased the formation of ettringite and gypsum. The deterioration process of concrete was accelerated by the use of higher sulphate solution concentration. On top of that, the mass change of concrete in Exposure IV had a similar result trend to that in Exposure III, but with at a lower rate. The difference was particularly evident at the mass-decreasing stage. At 150 days, the mass loss for Exposure IV was 0.32% less than that of Exposure III. This indicated that the WDA had a significant effect on the aggravation of sulphate attack. The wetting and drying cycle increased the penetration of sulphate and induced salt crystallization to exacerbate the deterioration.

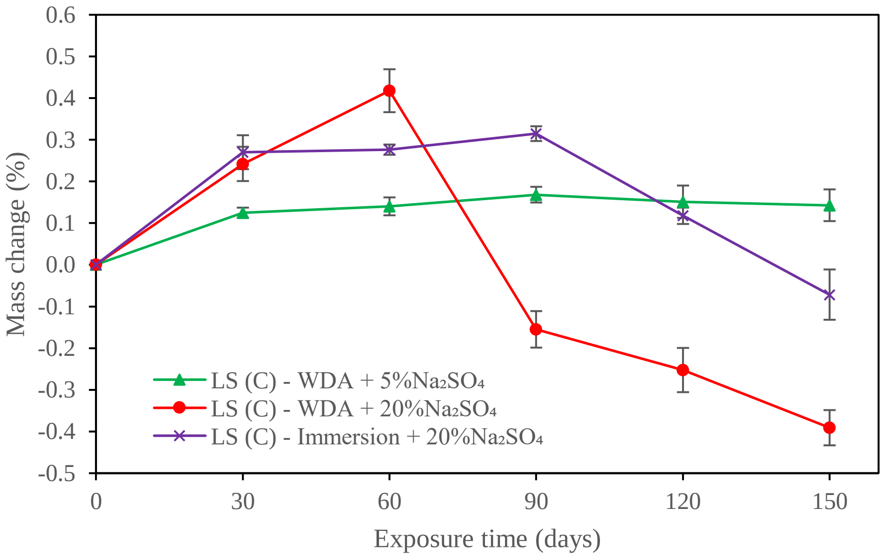

Figure 5.8: Mass change with exposure time for LS(C) exposed to various conditions

5.3.4. Volume Change

In addition to mass change, concrete experienced swelling and expansion as a result of the sulphate attack. Figure 5.9 shows the volume expansion of concrete for all mixes after 150 days of exposure to WDA in 20% Na_2SO_4 solution (Exposure III). The volume of concrete increased gradually over the exposure time. The expansion was minimal at the early exposure time, but was more evident at a later stage. For example, the concrete volume increased by 0.16% –0.4% at 60 days, and it increased by 0.73%–1.23% at 150 days. The expansion was due to the formation of expansive products such as ettringite and gypsum caused by sulphate attack (Maes and De Belie, 2014). The lower expansion rate during the early stage was due to the filling up of concrete pores by these products. But, a further accumulation of ettringite and gypsum caused the concrete to expand at the later stage.

Limestone concrete expanded more than SiMn slag concrete in the early stage, but less in the later stage. The expansion of LS(C), LS(SF) and LS(SF-FA) concrete was 0.15%, 0.11% and 0.13%, respectively, more than that of SiMn(C), SiMn(SF) and SiMn(SF-FA) concrete at 30 days. At 150 days, however, the expansion of limestone concrete was 0.14%, 0.06% and 0.07%, respectively, less than that of SiMn slag concrete. This was attributed to the lower compressive and tensile strengths of SiMn slag concrete in resisting expansion. But, at the early stage, the weaker bonding of SiMn slag aggregate with cement paste resulted in more concrete pores, providing space for the accumulation of expansive products. Qi et al. (2017) also found that recycled aggregate concrete was more porous than normal concrete, which experienced more expansion. Besides, the addition of FA and SF reduced concrete expansion. FA and SF strengthened the mechanical property of concrete to resist the expansion. The refinement of pore structure by FA and SF also reduced the permeability of concrete, minimizing the penetration of sulphate ion. Zhongya et al. (2019) demonstrated that the expansion of FA concrete and SF concrete was 1.3% and 1.2%, respectively, lower than that of control concrete.

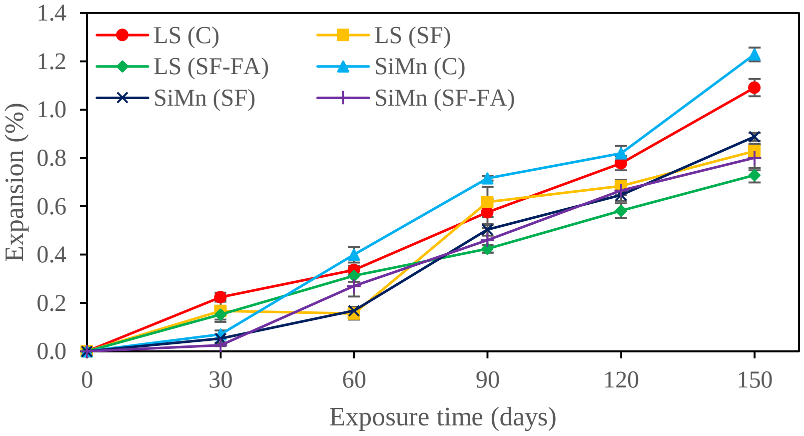

Figure 5.9: Expansion of concrete exposed to WDA in 20% Na_2SO_4 solution (Exposure III)

Figure 5.10 shows the volume expansion of LS(C) concrete exposed to different exposure conditions, including WDA in 5% Na_2SO_4 solution (Exposure I), WDA in 20% Na_2SO_4 solution (Exposure III) and immersion in 20% Na_2SO_4 solution (Exposure IV). The volume expansion of concrete in Exposure I was approximately 2 to 3 times less than that of concrete in Exposure III. The use of salt solution with a higher sulphate concentration accelerated the damage process. The expansion of concrete in Exposure IV was less than that in Exposure III, but higher than that in Exposure I. The expansion of concrete exposed to WDA was approximately 1.5 times higher than that of concrete subjected to full immersion in sulphate solution with the same concentration. The result was consistent with that reported by Yu et al. (2018), who showed that WDA caused a two-fold volume expansion relative to concrete that was completely submerged in salt solution. Apart from the increased sulphate penetration rate, the WDA also induced salt crystallization, which caused expansion.

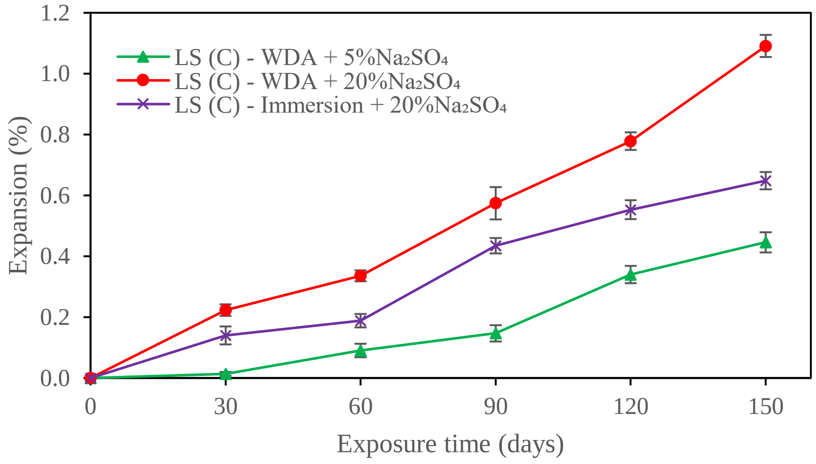

Figure 5.10: Expansion of LS(C) exposed to various conditions

5.3.5. Compressive Strength

The change in compressive strength for all concrete exposed to 150 days of WDA in 20% Na_2SO_4 solution (Exposure III) is shown in Figure 5.11. The compressive strength of concrete decreased over the period of exposure. This was due to the degradation damage caused by the formation of ettringite and gypsum within the concrete pore. The sulphate attack also used up cement hydrate which induced dissolution of $Ca(OH)_2$ and C-A-H, resulting in strength loss (Roziere et al., 2009). Furthermore, the WDA caused the occurrence of salt crystallization, resulting in the degradation of concrete mechanical property. The drying stage of WDA also caused concrete damage due to shrinkage (Tang et al., 2018).

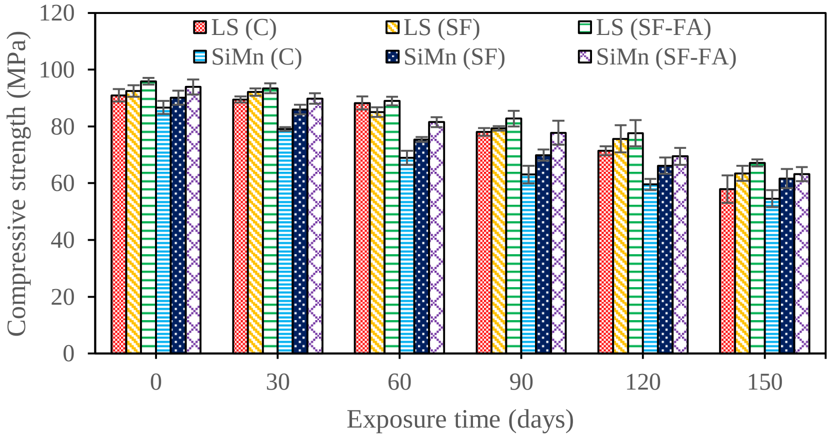

Figure 5.11: Compressive strength of concrete exposed to WDA in 20% Na_2SO_4 solution (Exposure III)

The compressive strength in Figure 5.11 has been normalized with the respective concrete strength at 0 day of exposure in order to better illustrate the deterioration as shown in Figure 5.12. The SiMn slag concrete displayed a greater reduction in strength than the limestone concrete. For example, at 150 days, the strength reduction of SiMn(C), SiMn(SF) and SiMn(SF-FA) was 0.72%, 0.19% and 2.64% more than that of LS(C), LS(SF) and LS(SF-FA), respectively. This was because the limestone aggregate was stronger than the SiMn slag aggregate, which produced concrete with better mechanical property to resist the sulphate attack and WDA. Nonetheless, the use of FA and SF improved the concrete resistance and compensated for the drawback of SiMn slag concrete. For instance, at 150 days, the normalized strength of SiMn(SF) and SiMn(SF-FA) was 4% and 3% respectively higher than LS(C). Zhongya et al. (2019) also noted an improved resistance to sulphate attack for concrete containing FA and SF.

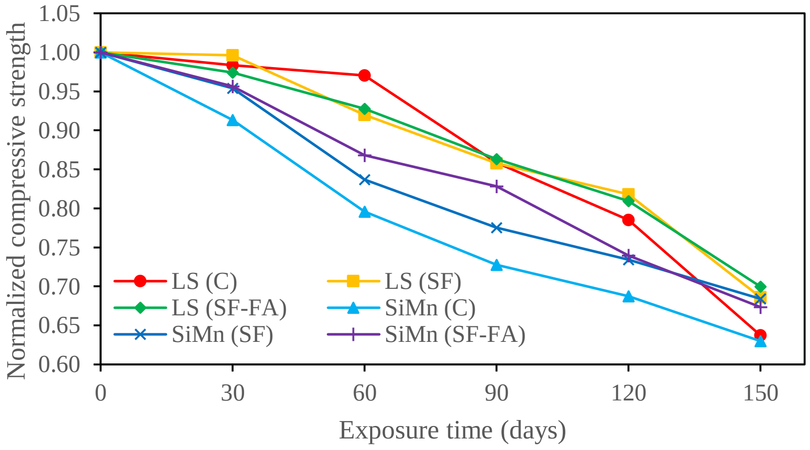

Figure 5.12: Normalized compressive strength of concrete exposed to WDA in 20% Na_2SO_4 solution (Exposure III)

Figure 5.13 and Figure 5.14 present, respectively, the compressive strength and normalized strength of LS(C) concrete exposed to five exposure conditions. These exposure conditions are WDA in 5% Na_2SO_4 solution (Exposure I), WDA in 12.5% Na_2SO_4 solution (Exposure II), WDA in 20% Na_2SO_4 solution (Exposure III), full immersion in 20% Na_2SO_4 solution (Exposure IV) and actual environment (Exposure A). When comparing Exposure I with Exposure III, an increase in sulphate concentration from 5% to 20% resulted in an additional 23% strength reduction for LS(C) concrete at 150 days. The strength loss at 150 days for Exposure I was equal to the strength loss at 90 days for Exposure III. The use of higher sulphate concentration accelerated the damage process.

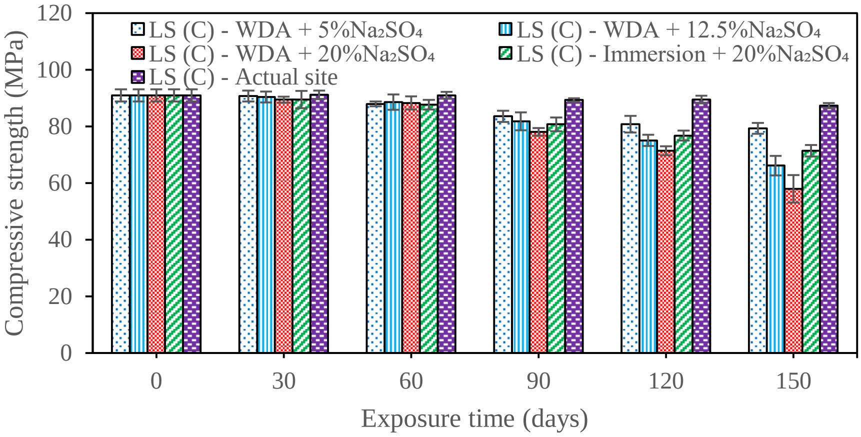

Figure 5.13: Compressive strength of LS(C) exposed to various conditions

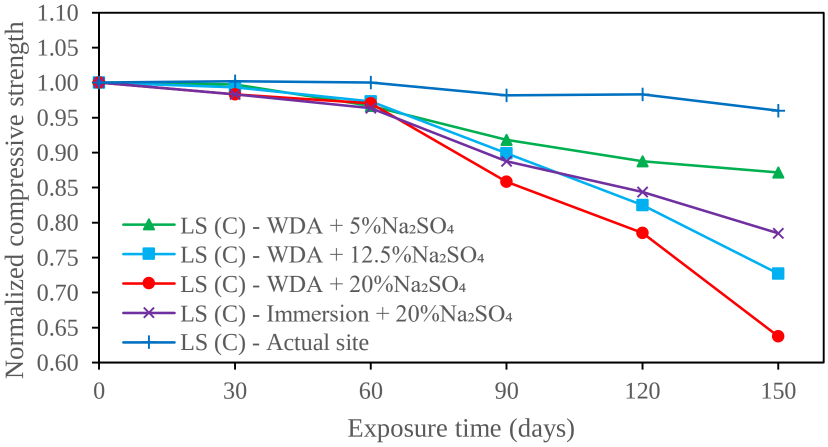

Figure 5.14: Normalized compressive strength of LS(C) exposed to various conditions

The WDA increased the concrete strength loss as seen in Exposure III and Exposure IV. At 150 days, the strength loss of concrete in Exposure III was 15% greater than that in Exposure IV. Yu et al. (2018) also demonstrated that the strength of concrete exposed to WDA was 10% lower than that of concrete fully immersed in sulphate solution. The WDA also caused salt crystallization, which weakened the concrete strength. On top of that, the strength loss of concrete exposed to actual environment was minimal, as shown in Exposure A. The concrete strength decreased by 4% at 150 days. This was attributed to a lower concentration of sulphate in seawater at the coast. As shown in Table 3.3, the seawater at the actual site contained approximately 0.17%

of SO_4^{2-} and 1.98% Cl^- ions. Furthermore, the existence of chloride in seawater reduced the sulphate penetration since the formation of Friedel's salt from chloride filled up the concrete pores and delayed the sulphate attack (Jiang and Niu, 2016). The concrete damage in Exposure A was most probably due to salt crystallization and drying shrinkage caused by the WDA. The finding was consistent with that reported by Zhongya et al. (2019) who showed that the strength loss of concrete exposed to actual environment was two times slower than that exposed to WDA in a 5% Na_2SO_4 solution.

5.3.6. Splitting Tensile Strength

The degradation of splitting tensile strength of concrete caused by sulphate attack and WDA was also studied. Figure 5.15 presents the splitting tensile strength of all types of concrete exposed to WDA in 20% Na_2SO_4 solution (Exposure III). Similar to the compressive strength, the tensile strength decreased over the exposure duration. The splitting tensile strength of all concrete ranged from 5.3 MPa to 6.57 MPa, 4.71 MPa to 6.25 MPa, 4.41 MPa to 5.83 MPa and 4 MPa to 5.36 MPa at 0, 90, 120 and 150 days respectively. The tensile strength was normalized with respect to the tensile strength at day 0 as depicted in Figure 5.16. Reduction of splitting tensile strength was generally less than that of compressive strength. At 150 days, SiMn(C) had the highest tensile strength reduction of 25% compared to 37% for compressive strength. This was because the concrete encountered less internal stress from the expansive products of ettringite, gypsum and salt crystal when it was subjected to tensile force. The result was slightly different from the findings of Tang et al. (2018), which showed that the tensile strength loss was greater than the compressive strength loss. This was because higher strength concrete, which experienced less degradation, had been used in this study.

As shown in Figure 5.16, all SiMn slag concrete had a slightly higher tensile strength loss than the limestone concrete. The difference in the strength loss between two concrete types was between 0.62% and 2.53%. The SiMn slag aggregate had a lower crushing value and abrasion resistance than the limestone aggregate. The mechanical property of concrete, including splitting tensile strength, produced by the weaker aggregate was therefore lower (Alsayed and Amjad, 1996). The addition of FA and SF reduced the strength loss caused by sulphate attack and WDA. As in LS(SF) and

SiMn(SF), the incorporation of SF reduced the strength loss by 2.38% for limestone concrete and 3.88% for SiMn slag concrete. In addition, the use of both FA and SF further reduced the strength loss of LS(SF-FA) and SiMn(SF-FA) by 3.58% and 5.49% respectively. The pozzolanic reaction of FA and SF refined the concrete pore and hence increased its resistance to sulphate attack and WDA (Zhongya et al., 2019).

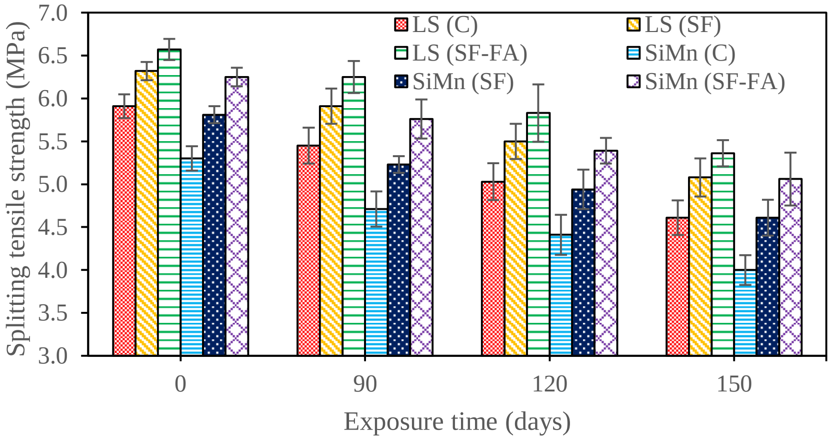

Figure 5.15: Splitting tensile strength of concrete exposed to WDA in 20% Na_2SO_4 solution (Exposure III)

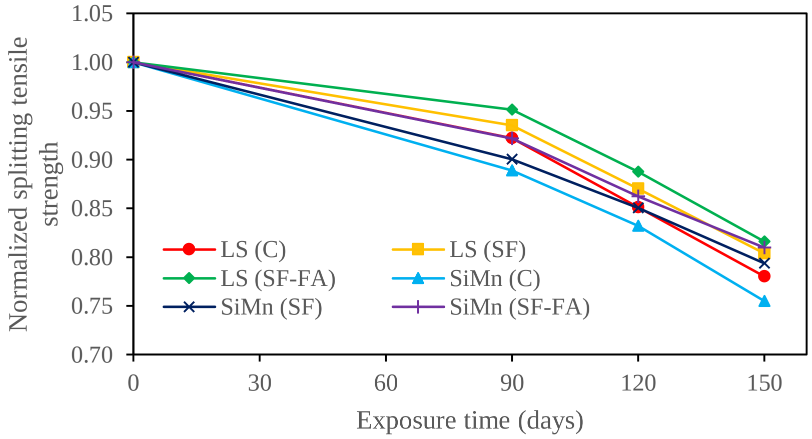

Figure 5.16: Normalized splitting tensile strength of concrete exposed to WDA in 20% Na_2SO_4 solution (Exposure III)

Figure 5.17 depicts the splitting tensile strength and Figure 5.18 shows the normalized strength of LS(C) concrete exposed to four exposure conditions, which are WDA in 5% Na_2SO_4 solution (Exposure I), WDA in 12.5% Na_2SO_4 solution (Exposure II), WDA in 20% Na_2SO_4 solution (Exposure III) and full immersion in 20% Na_2SO_4 solution (Exposure IV). The rise in concentration of Na_2SO_4 solution from 5% to 20%

increased the loss of tensile strength by approximately 2 times. Tang et al. (2018) also showed that the tensile strength of concrete decreased by an additional 33% when the sulphate concentration increased from 5% to 10%. Furthermore, the loss of tensile strength for concrete exposed to full immersion was 7% less than that of the concrete exposed to WDA. The drying stage in WDA caused shrinkage and salt crystallization, exacerbating the tensile strength loss.

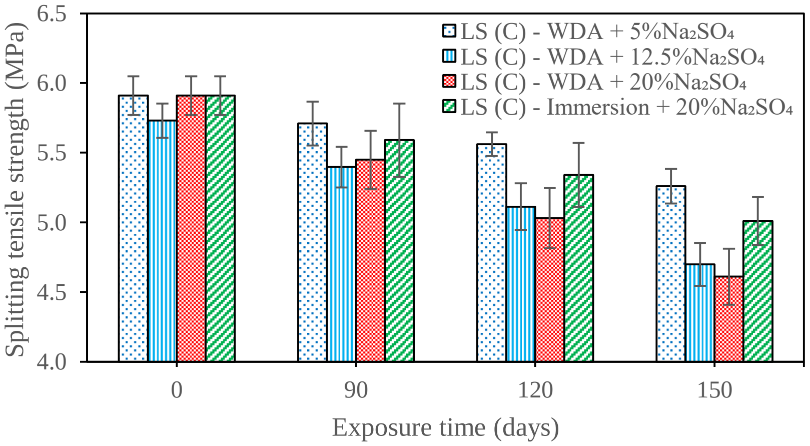

Figure 5.17: Splitting tensile strength of LS(C) exposed to various conditions

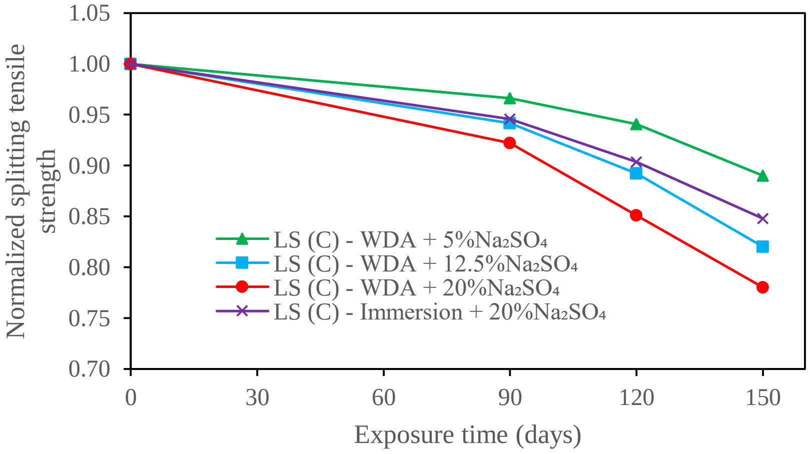

Figure 5.18: Normalized splitting tensile strength of LS(C) exposed to various conditions

5.3.7. SEM Analysis

The microstructure of SiMn(C), SiMn(SF-FA) and LS(SF-FA) exposed to full immersion in tap water for 150 days (Exposure C) is shown in Figure 5.19 (a), (b) and (c) respectively. Clusters of cloud-like C-S-H crystals and hexagonal $Ca(OH)_2$ morphology were observed in Figure 5.19. The presence of these elements, in close proximity, indicated a compact microstructure of concrete. All concrete had a good and strong bonding between cement paste and aggregate, as the transition between them was not apparent. A trace of cement paste was also detected on the aggregate surface of all concrete types, suggesting a dense microstructure. Besides, SiMn(C) contained more hexagonal morphology than SiMn(SF-FA) and LS(SF-FA), indicating a higher content of $Ca(OH)_2$. This was attributed to the pozzolanic reaction of FA and SF, which consumed $Ca(OH)_2$ to produce C-S-H gel in SiMn(SF-FA) and LS(SF-FA). The result was in line with the finding of Nochaiya et al. (2010), who observed a lesser amount of $Ca(OH)_2$ in FA concrete and SF concrete.

Figure 5.20(a), (b) and (c) respectively show the SEM images of SiMn(C), SiMn(SF-FA) and LS(SF-FA) after 150 days of WDA in 20% Na_2SO_4 solution (Exposure III). As shown in the images, a bundle of needle-like crystals was found randomly on the surface of cement paste. The needle-like crystal was the product of sulphate attack known as ettringite. Jiang and Niu (2016) and Qi et al. (2017) also found that the ITZ of concrete, particularly in the pore, had been filled with ettringite. The accumulation of needle-like ettringite was responsible for the expansion of concrete described in Section 5.3.4. Although the FA and SF in SiMn(SF-FA) and LS(SF-FA) reduced the $Ca(OH)_2$ amount through pozzolanic reaction, sulphate could still react with C-A-H to form ettringite. As a result of sulphate attack, the growth of ettringite and the dissolution of $Ca(OH)_2$ and C-A-H resulted in a loose concrete microstructure, which gradually contributed to the degradation of concrete mechanical property. In addition, cracks were also found in concrete exposed to WDA as shown in Figure 5.20. This was attributed to the cyclic WDA, which led to the development of micro-cracks. Yu et al. (2018) showed that the loss of moisture during the drying stage had caused concrete shrinkage. Furthermore, salt crystallization also caused the formation of micro-cracks in concrete.

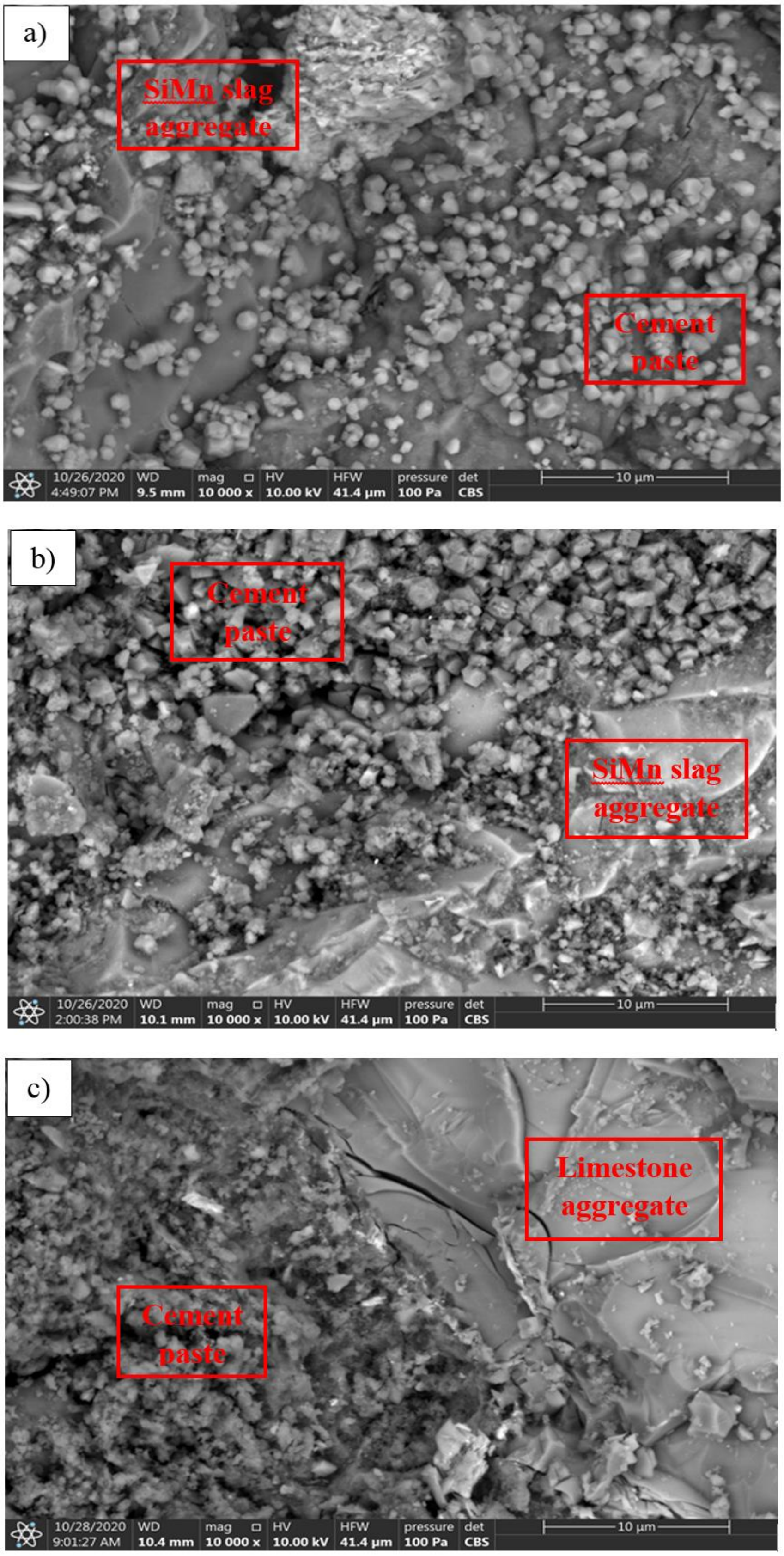

Figure 5.19: SEM image of (a) SiMn(C), (b) SiMn(SF-FA) and (c) LS(SF-FA) after 150 days of full immersion in water (Exposure C)

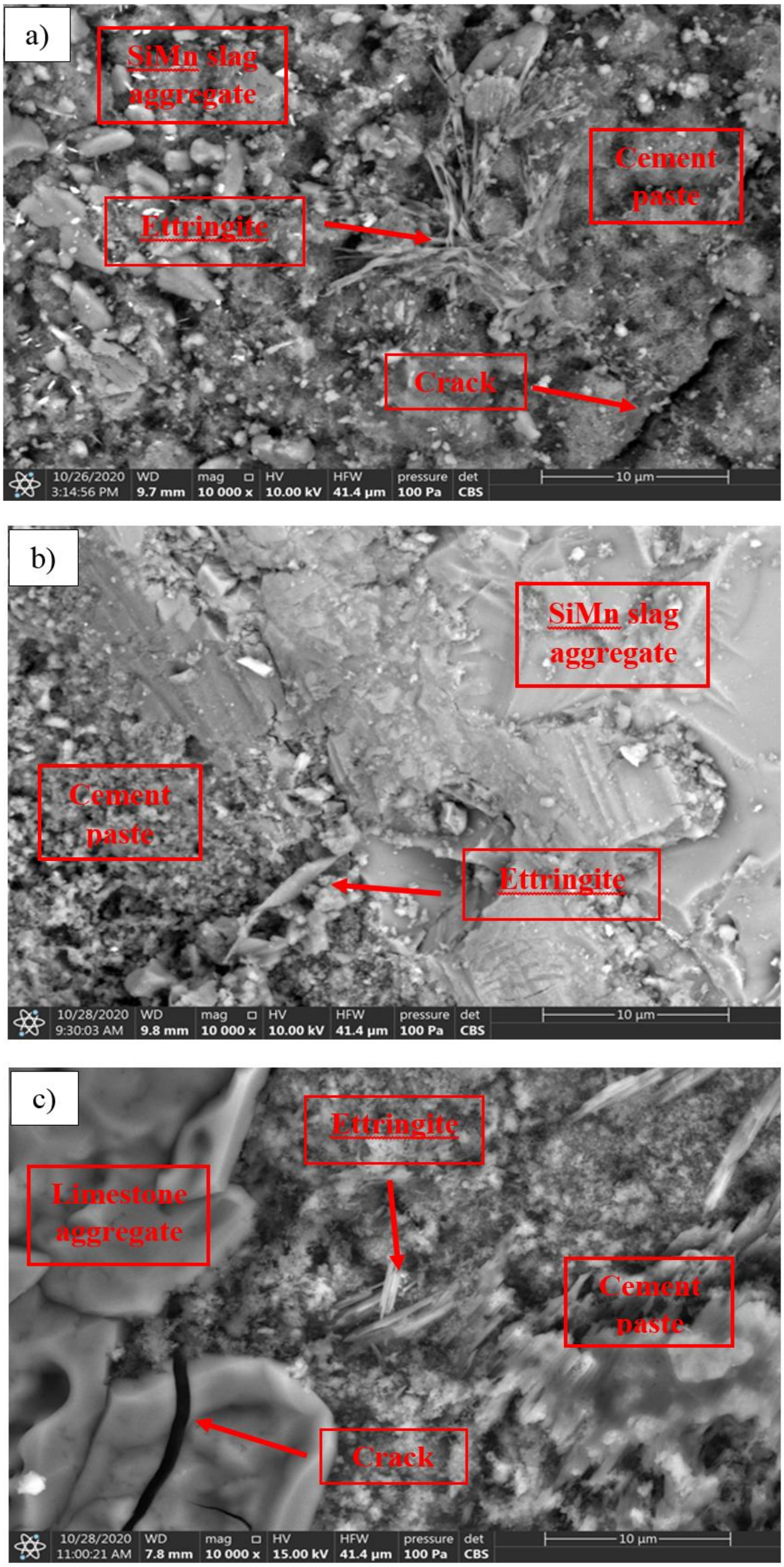

Figure 5.20: SEM image of (a) SiMn(C), (b) SiMn(SF-FA) and (c) LS(SF-FA) after 150 days of WDA in 20% Na_2SO_4 solution (Exposure III)

5.4. Behavior of Concrete Subjected to Cyclic Loading

5.4.1. Compressive Strength under Static Loading

The compressive strength of concrete under static loading has been studied using 50 mm cubic specimens and the results are shown in Table 5.5. T1 was SiMn(SF-FA) specimen that had been fully submerged in tap water (Exposure C) for 150 days. T2 and T3 were respectively SiMn(SF-FA) and LS(SF-FA) specimens exposed to WDA in 20% of Na_2SO_4 solution (Exposure III) for 150 days. The average compressive strength of T1, T2 and T3 was measured as 91.37 MPa, 40.98 MPa and 45.86 MPa, with a standard deviation of 1.02 MPa, 2.16 MPa and 2.21 MPa respectively. The standard deviation of T2 and T3 was higher than that of T1. This was attributed to the inconsistent deteriorating effect of the sulphate attack and WDA and inhomogeneous property of concrete (Tang et al., 2018). The irregular defects in concrete specimen had resulted in the higher variance in compressive strength.

Table 5.5: Concrete compressive strength of 50 mm cube under static loading

Series	Specimen	Compressive strength (MPa)			Strength relative to 100 mm cube
		Measured	Mean	Standard deviation	
1	T1-1	92.52	91.37	1.02	0.97
	T1-2	91.54			
	T1-3	90.05			
2	T2-1	38.21	40.64	2.16	0.64
	T2-2	40.26			
	T2-3	43.46			
3	T3-1	42.96	45.86	2.21	0.68
	T3-2	46.31			
	T3-3	48.32			

The specimen size effect was also studied by comparing the compressive strength of 50 mm cube to 100 mm cube as shown in Table 5.5. According to Del Viso et al. (2008), the compressive strength of concrete generally decreased with an increase in cube size due to the presence of more flaws in larger cube. However, T1 had a compressive strength slightly lower than that of 100 mm cube, with a ratio of 0.97. This was due to the relatively larger coarse aggregate used in the manufacture of 50 mm cube, which had a negative effect on the homogeneity of concrete. Fladr and Bily (2018) also found that the minimum relative strength between a 100 mm cube and a

50 mm cube was 0.9. Following the sulphate attack and WDA, the relative strength of T2 and T3 was further reduced to 0.64 and 0.68 respectively, indicating a more severe deterioration of the smaller specimen. Based on the sulphate penetration profile in Section 5.3.2, the depth of concrete that was affected by the sulphate attack was up to 20 mm. Under a three-dimensional intrusion of sulphate, the 50 mm cube was almost completely deteriorated by the sulphate attack and WDA.

5.4.2. Fatigue Life of Concrete

The fatigue life (N_f) of all concrete specimens has been determined and presented in Table 5.6. At the low upper stress level (S_{max}), such as 30%, 40% and 45% of compressive strength (f_c), the specimens did not fail after 10,000 cycles of loading. Further cyclic loading was required in order for the concrete to fail, but it was not carried out due to time and cost constraints. Nevertheless, the behavior of these specimens with respect to deformation and elasticity of concrete is elaborated in Section 5.4.3 and Section 5.4.4. The failure of the specimen occurred when the upper stress level was greater than 80% of compressive strength. As shown in Table 5.6, the fatigue life pattern of these specimens was inconsistent and widely distributed due to their inhomogeneous properties and high sensitivity to experimental set-up and loading conditions. The analysis of this type of result can be carried out using the S-N curves (Wu and Jin, 2019). The S-N curves for T2 and T3 specimens are depicted in Figure 5.21. The fatigue life of concrete decreased with the increase in the upper stress level. This was ascribed to more rapid development of crack at a stress level which was close to the compressive strength of concrete. The finding was consistent with that of Humme et al. (2016) who found that the fatigue life of specimen using S_{max} of 0.7 was greater than that of specimen using S_{max} of 0.8. The equation showing the relationship between S_{max} and N_f has been developed as Eq. 5.3 for T2 and Eq. 5.4 for T3. The coefficient of determination (R^2) for Eq. 5.3 and Eq. 5.4 is 0.9428 and 0.8789 respectively.

$$S_{max} = -0.0568 \log N_f + 1.0221; \quad R^2 = 0.9428 \qquad \text{Eq. 5.3}$$

$$S_{max} = -0.0529 \log N_f + 1.0172; \quad R^2 = 0.8789 \qquad \text{Eq. 5.4}$$

The regression equation for T2 was slightly lower than that for T3, indicating a lower fatigue life of T2 under constant stress level. The descending slope of T2 equation was also steeper than that of T3. In this regard, the fatigue strength corresponding to a fatigue life of 1 million loading cycles was $0.681f_c$ for T2 and $0.700f_c$ for T3, indicating a weaker resistance of T2 against fatigue loading. This was due to the weaker and more brittle properties of SiMn slag aggregate in T2 concrete. As shown in Table 3.1, the SiMn slag aggregate had lower abrasion resistance than the limestone aggregate of T3 concrete. Furthermore, SiMn slag aggregate was flakier and had a higher slenderness ratio than limestone aggregate, resulting in concrete with lower dynamic resistance. Wu and Jin (2019) found that the concrete incorporated with demolished concrete lump (DCL) as coarse aggregate had a slightly lower fatigue strength than normal concrete. Since the DCL aggregate had a lower mechanical property, the resulting concrete had a lower fatigue resistance.

Table 5.6: Fatigue life (N_f) of cube specimen

Series	Specimen	Fatigue life, N_f (cycles)	Series	Specimen	Fatigue life, N_f (cycles)
1	T1-S0.3-F0.8-1	10,000 (Not failed)	2	T2-S0.8-F0.8-1	5708
	T1-S0.3-F0.8-2	10,000 (Not failed)		T2-S0.8-F0.8-2	6324
	T1-S0.3-F0.8-3	10,000 (Not failed)		T2-S0.8-F0.8-3	7407
	T1-S0.4-F0.8-1	10,000 (Not failed)		T2-S0.85-F0.8-1	1039
	T1-S0.4-F0.8-2	10,000 (Not failed)		T2-S0.85-F0.8-2	1123
	T1-S0.4-F0.8-3	10,000 (Not failed)		T2-S0.85-F0.8-3	2110
	T1-S0.45-F0.8-1	10,000 (Not failed)		T2-S0.9-F0.8-1	73
	T1-S0.45-F0.8-2	10,000 (Not failed)		T2-S0.9-F0.8-2	157
	T1-S0.45-F0.8-3	10,000 (Not failed)		T2-S0.9-F0.8-3	245
	T1-S0.45-F0.6-1	10,000 (Not failed)	3	T3-S0.8-F0.8-1	7713
	T1-S0.45-F0.6-2	10,000 (Not failed)		T3-S0.8-F0.8-2	8481
	T1-S0.45-F0.6-3	10,000 (Not failed)		T3-S0.8-F0.8-3	9346
	T1-S0.45-F1.0-1	10,000 (Not failed)		T3-S0.85-F0.8-1	1538
	T1-S0.45-F1.0-2	10,000 (Not failed)		T3-S0.85-F0.8-2	1870
	T1-S0.45-F1.0-3	10,000 (Not failed)		T3-S0.85-F0.8-3	2415
2	T2-S0.45-F0.8-1	10,000 (Not failed)		T3-S0.9-F0.8-1	52
	T2-S0.45-F0.8-2	10,000 (Not failed)		T3-S0.9-F0.8-2	273
	T2-S0.45-F0.8-3	10,000 (Not failed)		T3-S0.9-F0.8-3	449

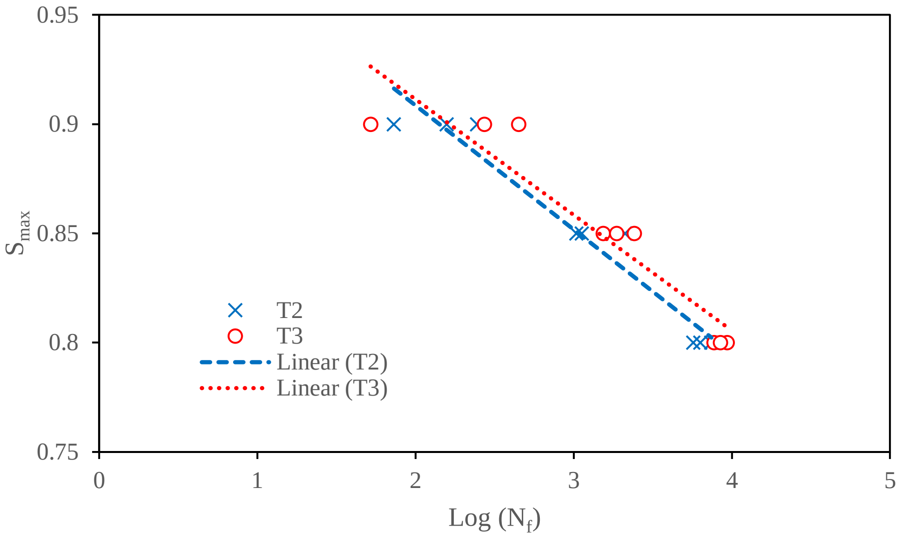

Figure 5.21: S-N curve of T2 and T3 specimen

5.4.3. Deformation of Concrete

Concrete undergoes permanent deformation in terms of residual strain as a result of cyclic loading. The residual strain over the fatigue life of T2 and T3 loaded at upper stress level of 80% and loading frequency of 0.8 Hz is shown in Figure 5.22. In the graph, the strain was normalized with respect to the strain of the last cycle, and the loading cycle is normalized to fatigue life. The residual strain is divided into three stages, namely initial creeping stage, quasi-linear stage and fatigue stage (Choi et al., 2016; Medeiros et al., 2015). The initial creeping stage occurred during 0 to 10% of fatigue life, when the deformation of concrete increased rapidly. This was due to the collapse of void and crack of concrete. In the quasi-linear stage that lasted up to 90% of fatigue life, concrete experienced a low rate of strain increase due to the gradual degradation of inherent defects and the formation of new cracks. The fatigue stage corresponded to a rapid increase in deformation whereby the defects exacerbated and transformed into unstable macro-cracks, leading concrete failure.

As shown in Figure 5.22, T2 specimen generally had a higher residual strain than T3 specimen at the initial stage. For example, at the normalized fatigue life of 0.2, the residual strain of T2 was almost two times that of T3. This indicated that T2 had more inherent defects and was weaker than T3. The SiMn slag aggregate used in T2 concrete was flaky and had a relatively smooth surface compared with the limestone aggregate in T3 concrete. As a result, the bonding between SiMn slag aggregate and cement paste was weaker (Kazjonovs et al., 2010). Furthermore, the SiMn slag aggregate had a lower abrasion resistance than limestone aggregate. Under the dynamic effect of cyclic loading, the development of crack in SiMn slag aggregate was faster than that in the limestone aggregate, contributing to larger deformation. Wu and Jin (2019) also found that the concrete containing demolished concrete lump (DCL) aggregate had a higher residual strain due to its weaker mechanical property.

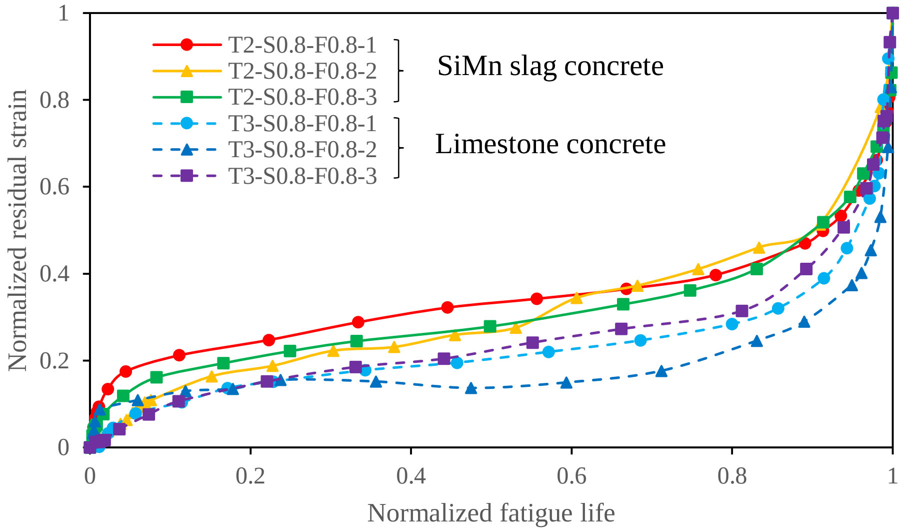

Figure 5.22: Normalized residual strain over fatigue life

Figure 5.23 presents the average residual displacement of intact specimens after 10,000 loading cycles. The residual displacement increased as the upper stress level increased. The residual displacement of T1-S0.4-F0.8 and T1-S0.45-F0.8 was respectively 24.8% and 54.4% higher than that of T1-S0.3-F0.8. The increase in displacement with respect to the upper stress level was not linear. According to Yang et al. (2014), the stress-strain relationship of concrete became non-linear when the stress level exceeded 40% of the compressive strength. By comparing T1-S0.45-F0.6, T1-S0.45-F0.8 and T1-S0.45-F1.0, the residual displacement increased with the decrease in loading frequency. At a lower loading frequency, the loading on concrete had to be sustained for a longer period time, resulting in a greater creeping effect of concrete. Wu and Jin (2019) reported a rate-dependent property of concrete when the loading frequency was below 1.17 Hz. As for the effects of sulphate attack and WDA, the residual displacement of T2-S0.45-F0.8 was 49.7% higher than that of T1-S0.45-F0.8. T2-S0.45-F0.8 was exposed to 150 days of WDA in 20% Na_2SO_4 solution

(Exposure III) and T1-S0.45-F0.8 was fully immersed in tap water for the same period (Exposure C). The sulphate attack and WDA weakened the concrete due to the formation of expansive products and the dissolution of cement hydrate, which softened the concrete. As such, the deteriorated concrete experienced a more significant deformation.

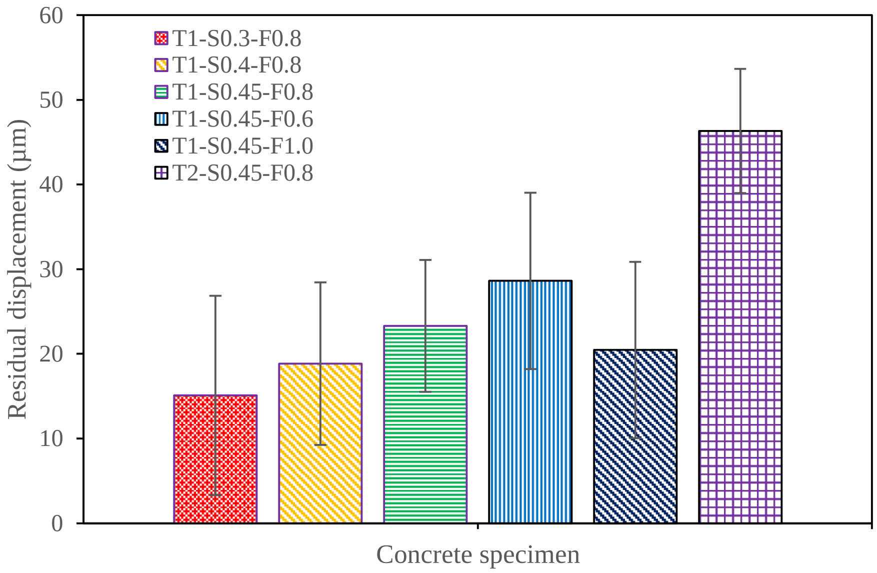

Figure 5.23: Residual displacement of specimen after 10,000 loading cycles

5.4.4. Modulus of Elasticity

The modulus of elasticity of T2 and T3 is also plotted against the fatigue life and is shown in Figure 5.24. The elasticity was normalized to its initial elasticity (E_o) and the loading cycle was normalized to its fatigue life. The change in elasticity of all concrete specimens was divided into three stages. All the specimens experienced a rapid-stiffening stage, followed by a constant-stiffening stage and, eventually, a rapid-softening stage, and similarly to the residual strain, the three-stage evolution of elasticity occurred at 0%–10%, 10%–90% and 90–100% of fatigue life, respectively. During the rapid-stiffening stage, concrete experienced an increase in modulus of elasticity by up to 9% of its initial value. The finding was slightly different from that presented in a previous study, in which concrete did not experience a noticeable increase in elasticity (Cachim et al., 2002; Wu and Jin, 2019). The increased modulus of elasticity was due to the closure of pores, which made the concrete denser and more compact. The elasticity of concrete improved further but at a lower rate during the constant-stiffening stage. The defect developed at this stage, such as micro-crack, had negligible effect on the robustness of concrete. In the rapid-softening stage, the modulus of elasticity decreased rapidly by at most 17.4% as in T2-S0.8-F0.8-3. The degradation of stiffness was attributed to the development of macro-cracks, which ultimately led to concrete failure.

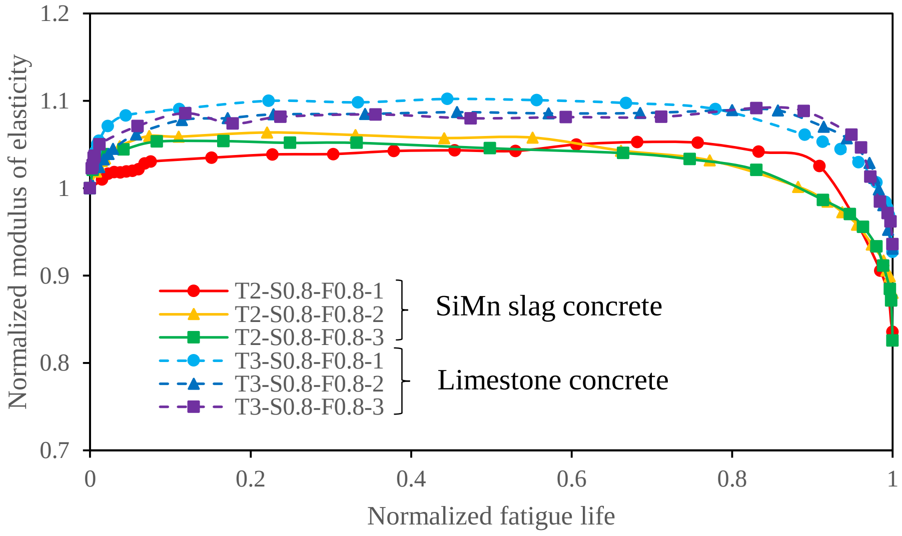

Figure 5.24: Normalized modulus of elasticity over fatigue life

As shown in Figure 5.24, T3 experienced a greater increase in elasticity at the initial stage and a smaller decrease in elasticity at the later stage compared to T2. At 10% of fatigue life, T3 had the highest E/E_o of 1.09 compared to 1.06 exhibited by T2. At a normalized fatigue life of 1, the lowest E/E_o value was 0.826 for T2 and 0.936 for T3. The higher stiffness of T3 was due to its higher resistance to cyclic loading than T2 concrete. T3 concrete was made of stronger limestone aggregate that had a higher abrasion resistance than the SiMn slag aggregate in T2. Besides, the SiMn slag aggregate had a smoother surface than the limestone aggregate, which affected its bonding with cement paste. Consequently, T2 concrete suffered a greater decrease in elasticity during failure.

The normalized modulus of elasticity for all intact specimens after 10,000 cycles of loading was determined and the result was shown in Figure 5.25. The elasticity of all the specimens was higher than their respective initial elasticity (E_o), indicating that concrete failure was not imminent. The increase in the upper stress level caused a greater stiffening effect on concrete. Compared to T1-S0.3-F0.8, the increase in elasticity of T1-S0.4-F0.8 and T1-S0.45-F0.8 was 0.9% and 1.8% higher respectively. This was because more concrete pores were closed at a higher stress level. The results also showed that the loading frequency did not have significant effect on the elasticity of concrete. T1-S0.45-F0.6, T1-S0.45-F0.8 and T1-S0.45-F1.0 had similar normalized elasticity values of 1.051, 1.055 and 1.053 respectively. After 150 days of exposure to WDA in 20% Na_2SO_4 solution (Exposure III), T2-S0.45-F0.8 had normalized elasticity of 1.040. This value was slightly lower than the normalized elasticity of 1.055 for T1-S0.45-F0.8 that was fully immersed in tap water (Exposure C). The sulphate attack and WDA deteriorated the mechanical property, resulting in concrete softening and loss of elastic modulus (Li et al., 2020; Yu et al., 2018).

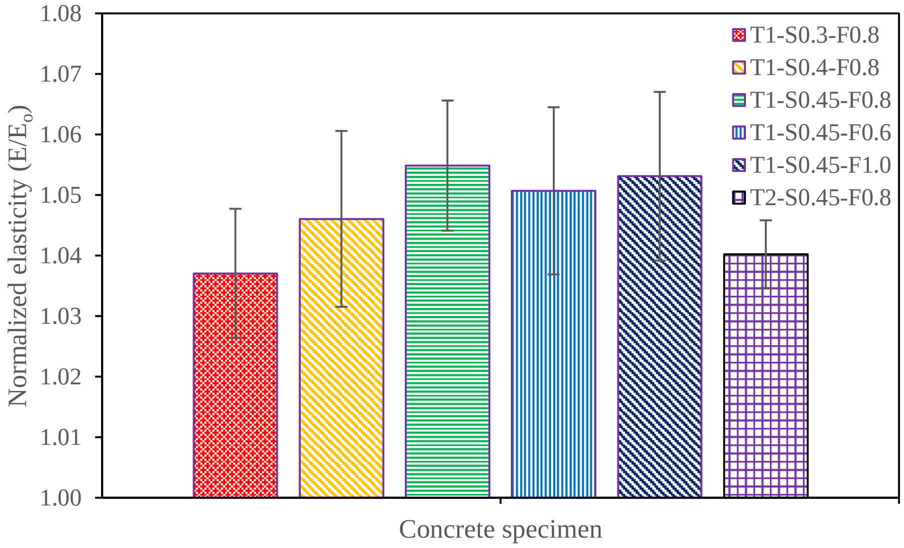

Figure 5.25: Normalized elasticity of specimen after 10,000 loading cycles

5.4.5. Compressive Strength after Cyclic Loading

After 10,000 loading cycles, six sets of intact specimens were statically loaded to determine their compressive strength using the standard test method presented in Section 5.2.2.5. The compressive strength of these specimens is shown in Table 5.7. The compressive strength of concrete after cyclic loading ($f_{c,after}$) was between 0.98 and 1.05 times their respective original strength (f_c). The $f_{c,after}$ of concrete was higher than f_c except for T1-S0.3-F0.8. The increase in strength was attributed to the improved stiffness caused by the closure of concrete pores after cyclic loading. This finding was consistent with that of Wu and Jin (2019), who discovered the compressive strength of concrete increased by 6% to 16% after 1.5 million loading cycles. As for the reduced compressive strength of T1-S0.3-F0.8, this could be ascribed to the inherent defects of the concrete that caused the variance of result. Furthermore, cyclic loading at S_{max} of 0.3 might not result in permanent pore closure, as the concrete was still within elastic range (Yang et al., 2014).

Table 5.7: Compressive strength of intact specimens after cyclic loading

Specimen	**f_c (MPa)**	**$f_{c,after}$ (MPa)**	**Standard deviation of $f_{c,after}$ (MPa)**	**$f_{c,after}/f_c$**
T1-S0.3-F0.8	91.37	89.48	0.94	0.98
T1-S0.4-F0.8		92.73	1.01	1.01
T1-S0.45-F0.8		93.65	0.85	1.02
T1-S0.45-F0.6		93.11	0.48	1.02
T1-S0.45-F1.0		92.16	0.97	1.01
T2-S0.45-F0.8	40.64	42.52	2.13	1.05

5.5. Concluding Remark

This research studied the durability of concrete exposed to combined sulphate attack and WDA. The concrete was subjected to mainly four types of condition, namely WDA in 5% (Exposure I), 12.5% (Exposure II) and 20% (Exposure III) Na_2SO_4 solution and full immersion in 20% (Exposure IV) Na_2SO_4 solution. The behavior of concrete subjected to cyclic loading, before and after the deterioration caused by sulphate attack and WDA, has also been investigated. Based on the experimental results, the following conclusions can be drawn.

1. In each exposure condition, concrete specimens were stained with white powdery efflorescence due to salt crystallization. The concrete was physically damaged with stripping of mortar layer at the specimen edge and concrete surface cracking. The WDA and an increase in sulphate solution concentrations caused more severe concrete damage.
2. The SO_4^{2-} ion penetrated into concrete up to a depth of 20 mm and the maximum SO_4^{2-} ion content of 1.72%–2.58% was found on the surface.
3. Concrete exhibited a mass change in two stages, increasing initially and decreasing later. The highest mass gain of concrete was 0.24%–0.55% and the maximum mass

loss was 0.39%–0.49%. The formation of expansive products such as ettringite and gypsum and the salt crystallization was responsible for the mass gain. The mass loss was caused by spalling and shrinkage of concrete during drying stage.

4. The volume of concrete increased with the exposure duration due to the accumulation of ettringite and gypsum. The maximum expansion of concrete was 0.45% for Exposure I, 0.73%–1.23% for Exposure III and 0.65% for Exposure IV.
5. Both compressive and splitting tensile strengths decreased over the exposure duration due to concrete damage caused by cracking. The degradation of compressive strength was approximately 12% higher than the splitting tensile strength.
6. Ettringite and cracks were found on the microstructure of concrete that had been exposed to sulphate attack and WDA.
7. Based on cyclic loading tests, the replacement of limestone with SiMn slag as a coarse aggregate in concrete slightly shifted the S–N curve downwards. The SiMn slag concrete had a shorter fatigue life than limestone concrete under a similar loading condition.
8. SiMn slag concrete exhibited a higher residual strain increase than limestone concrete. The degradation of elastic modulus of SiMn slag concrete was also higher than that of limestone concrete.
9. After 10,000 cycles of loading, the intact specimens exhibited a residual displacement, improved modulus of elasticity and higher compressive strength.
10. The sulphate attack and WDA caused a softening of concrete, resulting in a lower concrete resistance to cyclic loading. The cumulative combined deterioration of sulphate attack and WDA increased the residual displacement of concrete and reduced its modulus of elasticity.

Chapter 6. Numerical Modelling of Cyclic Loading on Concrete Deteriorated by Sulphate Attack and Wetting-Drying Action

6.1. Introduction

This chapter elaborates the numerical modelling and analysis of cyclic loading on concrete. Finite element analysis software, ABAQUS, has been used to model the cyclic loading. The Concrete Damaged Plasticity (CDP) of ABAQUS was used for the constitutive modelling of concrete material. The degradation of material property caused by sulphate attack and wetting-drying action (WDA) was considered in the material model by modifying the mechanical properties of concrete. Based on the result of static loading test, the CDP parameters of model were calibrated and a mesh sensitivity study was carried out. The model was then validated against the cyclic loading test results of objective three from Chapter 5. In addition, parametric studies were carried out to investigate the effects of compressive strength, lower stress level and specimen size. Lastly, the developed numerical model was used to predict the fatigue life of concrete exposed to long-term deterioration caused by sulphate attack and WDA.

6.2. Constitutive Model of Concrete

6.2.1. Compressive Strength

The sulphate attack and WDA degrade the mechanical properties of concrete, affecting its stress-strain behavior. The stress-strain curve of concrete is divided into two portions, which are ascending branch and descending branch. The combined effects of sulphate attack and WDA were considered in the ascending branch of stress-strain curve since this portion represented the load-deformation characteristics prior to concrete failure (Liu et al., 2020a). The compressive strength is the main property affecting the stress-strain curve. As discussed in Section 5.3.5, the compressive strength of concrete degraded over time as a result of sulphate attack and WDA. The degraded strength of concrete can be expressed as Eq. 6.1.

$$f_d = D_{WDA} f_o \qquad \text{Eq. 6.1}$$

where f_d is the degraded strength, f_o is the undamaged strength and D_{WDA} is the factor considering damage caused by sulphate attack and WDA.

Table 6.1 presents the compressive strength damage factor ($D_{WDA,C}$) of concrete determined in Section 5.3.5. The relationship of $D_{WDA,C}$ with exposure time (T) is shown in Figure 6.1(a). The relationship is established after 90 days of degradation because the damage is more apparent at that point. Figure 6.1(b) depicts the power and coefficient of the established relationship as a function of Na_2SO_4 solution concentration (C). Using regression analysis, the $D_{WDA,C}$ is expressed in terms of exposure time and sulphate concentration as shown in Eq. 6.2. A power function is used as it better describes the loss of concrete strength, with the rate of degradation gradually decreases over the exposure time. The declining strength degradation is related to the limit of sulphate penetration into concrete, as evidenced by the findings in Section 5.3.2. Figure 6.2(a) presents the compressive strength damage relationship between limestone concrete and SiMn slag concrete. Figure 6.2(b) shows the relationship between concrete with and without the incorporation of FA and SF. Based on Figure 6.2, the constant "A" is specified to account for the use of SiMn slag, FA and SF as described in Eq. 6.3.

$$D_{WDA,C} = A(0.1332C^{1.4876})T^{-(0.3372\ln(C)-0.4403)} \qquad \text{Eq. 6.2}$$

$$\begin{aligned} A &= 1 \text{ for limestone concrete} \\ &= 0.9216 \text{ for SiMn slag concrete} \\ &= 1.0376 \text{ for concrete containing FA and SF} \end{aligned} \qquad \text{Eq. 6.3}$$

where A is the constant considering the type of concrete for compressive strength, C is the concentration of Na_2SO_4 solution and T is the exposure duration.

The above equations are derived based on the compressive strength of a cube specimen. But, cylinder compressive strength is required for input in ABAQUS. Therefore, Eq. 3.17 is used for the conversion between cylinder and cube strength. By substituting Eq. 6.2, Eq. 6.3 and Eq. 3.17 into Eq. 6.1, the degraded compressive strength for cylinder specimen ($f_{cy,d}$) is determined from Eq. 6.4.

$$f_{cy,d} = D_{WDA,C}(0.6945f_{cu,o} + 0.12) \qquad \text{Eq. 6.4}$$

where $f_{cy,d}$ is the degraded cylinder compressive strength and $f_{cu,o}$ is the undamaged cube compressive strength.

Table 6.1: Compressive strength degradation caused by sulphate attack and WDA (obtained from Section 5.3.5)

Mix	**Compressive strength degradation by sulphate attack and WDA ($D_{WDA,C}$)**				
	20% Na_2SO_4 solution				
	30 days	**60 days**	**90 days**	**120 days**	**150 days**
LS(C)	0.9834	0.9703	0.8586	0.7851	0.6373
LS(SF)	0.9960	0.9197	0.8580	0.8179	0.6861
LS(SF-FA)	0.9741	0.9278	0.8633	0.8093	0.6997
SiMn(C)	0.9131	0.7957	0.7277	0.6875	0.6301
SiMn(SF)	0.9539	0.8368	0.7754	0.7343	0.6843
SiMn(SF-FA)	0.9566	0.8679	0.8284	0.7397	0.6734
Mix	**12.5% Na_2SO_4 solution**				
	30 days	**60 days**	**90 days**	**120 days**	**150 days**
LS(C)	0.9933	0.9732	0.8989	0.8251	0.7272
Mix	**5% Na_2SO_4 solution**				
	30 days	**60 days**	**90 days**	**120 days**	**150 days**
LS(C)	0.9975	0.9668	0.9185	0.8875	0.8718

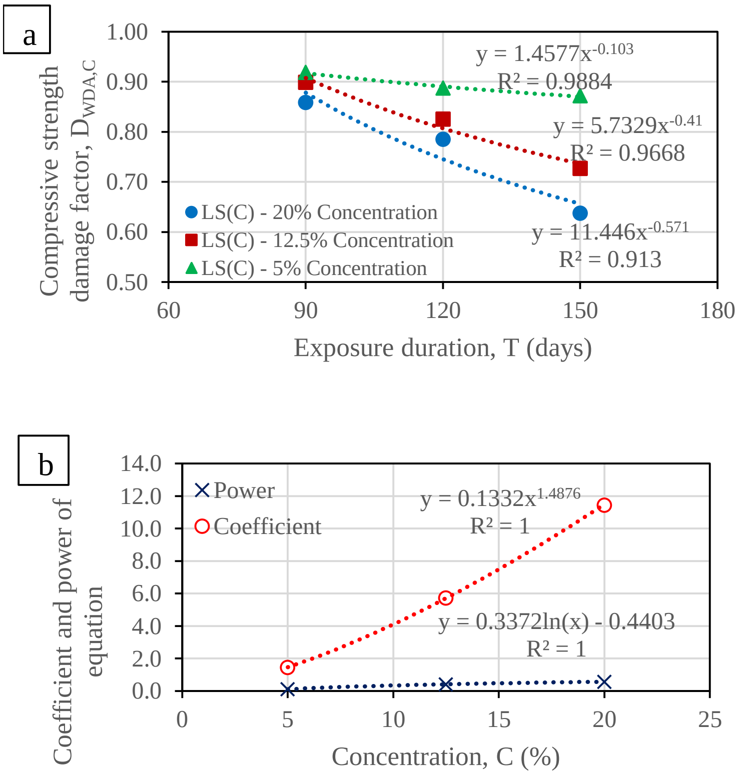

Figure 6.1: Correlation of (a) compressive strength damage factor with exposure duration; (b) power and coefficient with concentration

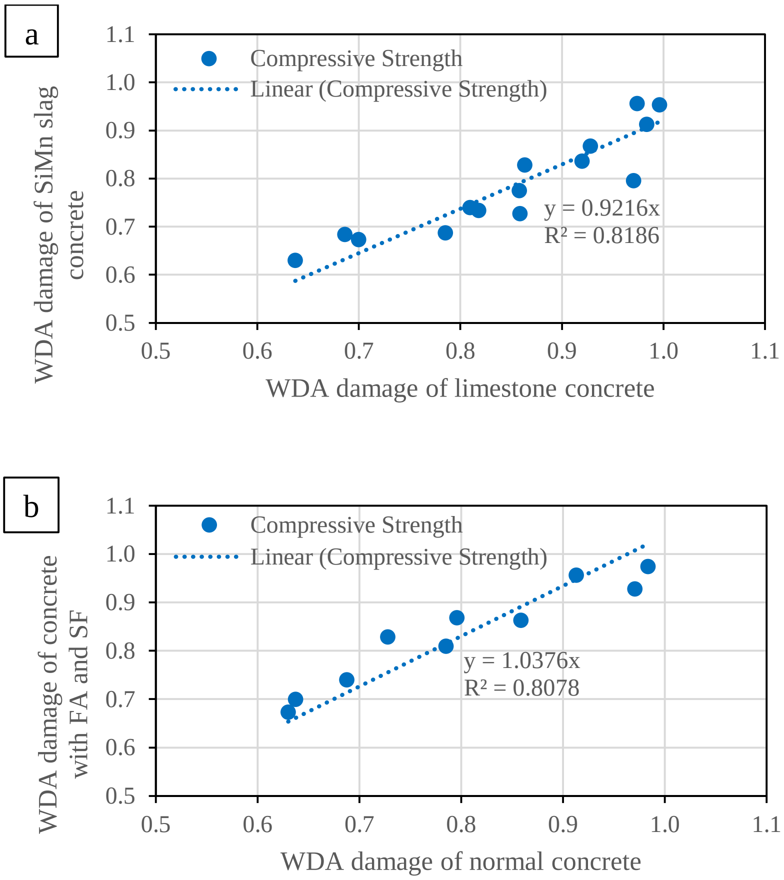

Figure 6.2: Correlation for compressive strength damage factor between (a) limestone and SiMn slag concrete; (b) normal and SF-FA concrete

6.2.2. Tensile Strength

The sulphate attack and WDA also deteriorates the splitting tensile strength as discussed in Section 5.3.6. Using the experimental data in Table 6.2, the relationship of splitting tensile strength damage factor ($D_{WDA,T}$) with exposure time (T) and solution concentration (C) is similarly determined as shown in Figure 6.3(a) and (b). Based on the regression analysis, $D_{WDA,T}$ is determined as Eq. 6.5. Figure 6.4(a) shows the splitting tensile strength damage relationship between limestone concrete and SiMn slag concrete. Figure 6.4(b) presents the relationship between normal concrete and concrete incorporated with FA and SF. Based on the above relationship, the constant “B” is determined as Eq. 6.6.

$$D_{WDA,T} = B(0.8683C^{0.5105})T^{-(0.121\ln(C)-0.038)} \qquad \text{Eq. 6.5}$$

$$\begin{aligned} \mathrm{B} &= 1 \text{ for limestone concrete} \\ &= 0.9735 \text{ for SiMn slag concrete} \\ &= 1.0334 \text{ for concrete containing FA and SF} \end{aligned} \qquad \text{Eq. 6.6}$$

where B is the constant considering the type of concrete for splitting tensile strength.

The numerical modelling in ABAQUS requires the material property input in terms of uniaxial tensile strength. The splitting tensile strength (f_{st}) is therefore converted to uniaxial tensile strength (f_{ct}) using Eq. 6.7 which is obtained from AS3600 (2018) standard. The degraded splitting tensile strength is formulated as Eq. 6.8. The undamaged splitting tensile strength ($f_{st,o}$) is converted from the undamaged cubic compressive strength ($f_{cu,o}$) using Eq. 6.9. The Eq. 6.9 is obtained by substituting Eq. 3.17 into Eq. 3.18.

$$f_{ct,o} = 0.9 f_{st,o} \qquad \text{Eq. 6.7}$$

$$f_{ct,d} = 0.9 D_{WDA,T} f_{st,o} \qquad \text{Eq. 6.8}$$

$$f_{st,o} = 0.2153(0.6945 f_{cu,o} + 0.12)^{0.7978} \qquad \text{Eq. 6.9}$$

where $f_{ct,o}$ and $f_{ct,d}$ are undamaged and damaged uniaxial tensile strength and $f_{st,o}$ and $f_{st,d}$ are undamaged and damaged splitting tensile strength.

Table 6.2: Splitting tensile strength degradation caused by sulphate attack and WDA (obtained from Section 5.3.6)

Mix	**Splitting tensile strength degradation by sulphate attack and WDA ($D_{WDA,T}$)**		
	20% Na_2SO_4 solution		
	90 days	**120 days**	**150 days**
LS(C)	0.9222	0.8511	0.7800
LS(SF)	0.9351	0.8703	0.8038
LS(SF-FA)	0.9513	0.8874	0.8158
SiMn(C)	0.8887	0.8321	0.7547
SiMn(SF)	0.9002	0.8503	0.7935
SiMn(SF-FA)	0.9216	0.8624	0.8096
Mix	**12.5% Na_2SO_4 solution**		
	90 days	**120 days**	**150 days**
LS(C)	0.9418	0.8921	0.8200
Mix	**5% Na_2SO_4 solution**		
	90 days	**120 days**	**150 days**
LS(C)	0.9662	0.9408	0.8900

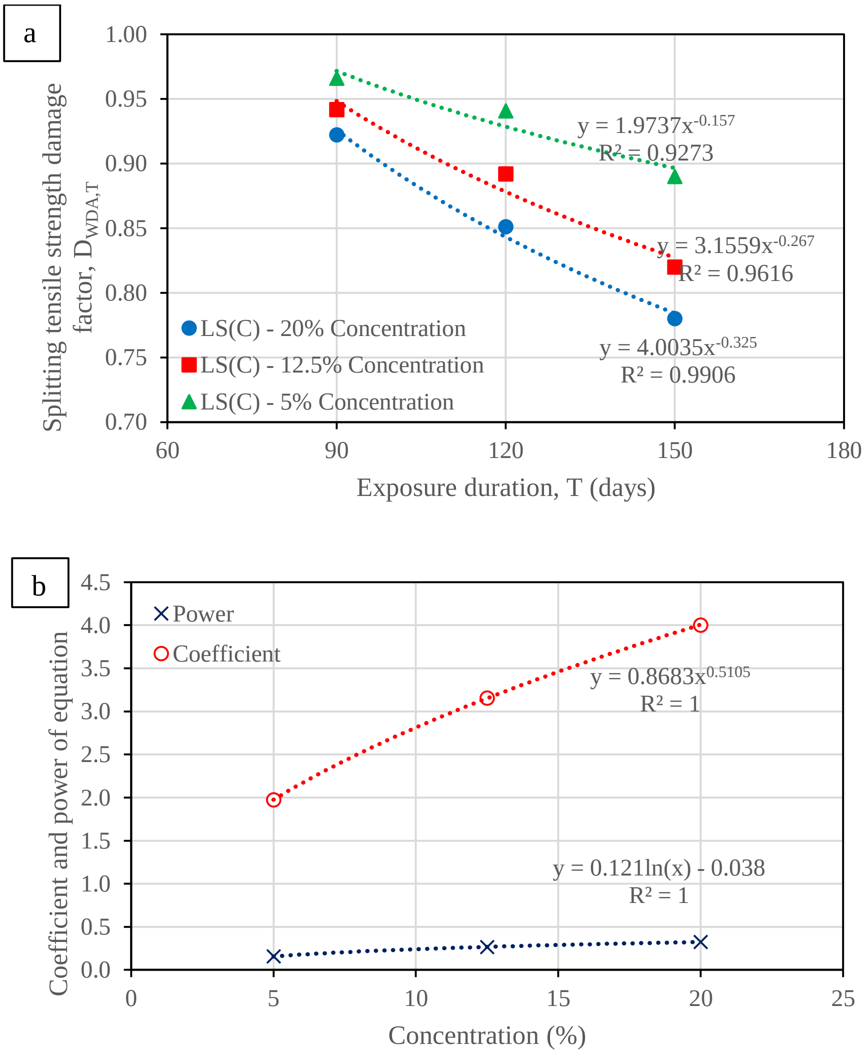

Figure 6.3: Correlation of (a) splitting tensile strength damage factor with exposure duration; (b) power and coefficient with concentration

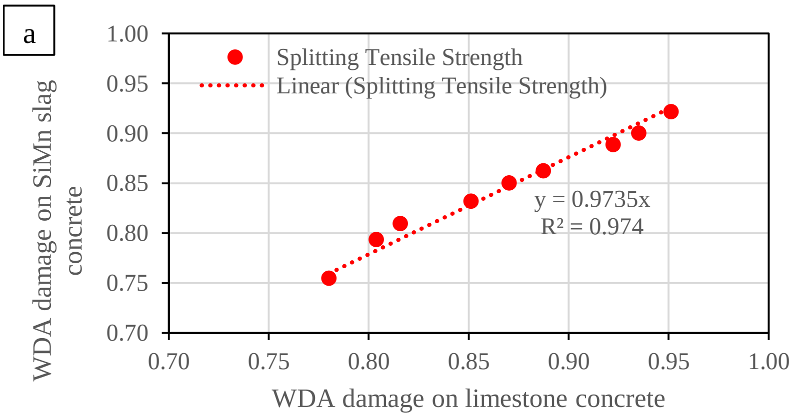

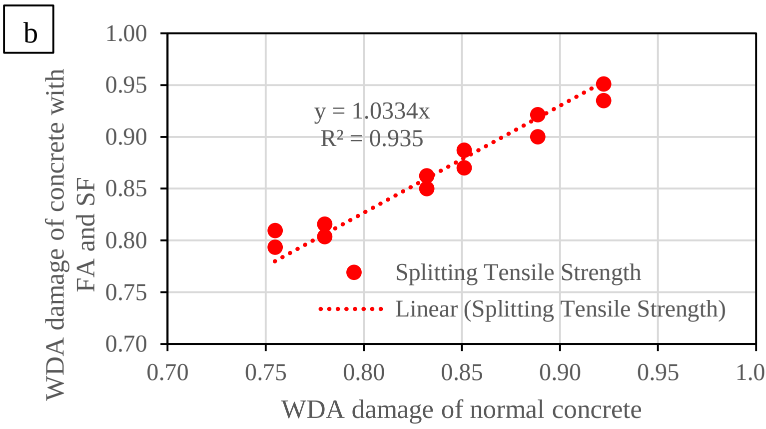

Figure 6.4: Correlation for splitting tensile strength damage factor between (a) limestone and SiMn slag concrete; (b) normal and SF-FA concrete

6.2.3. Modulus of Elasticity

According to AS3600 (2018) and ACI 318M (2008) standards, the elastic modulus of concrete can be described as a function of compressive strength and density. Table 6.3 summarizes the cylinder compressive strength, density, and elastic modulus of limestone concrete and SiMn slag concrete determined in Section 4.3.1. Both types of concrete use marine sand as fine aggregate and seawater as mixing water. Figure 6.5 presents the relationship of elastic modulus with compressive strength for both concrete types using the experimental data in Table 6.3. This relationship is also benchmarked against the standards and published literature. The relationship for elastic modulus of limestone concrete is more similar to that of ACI 318M (2008) as shown in Figure 6.5(a). As for the SiMn slag concrete, the elastic modulus is less than that of limestone concrete. This is ascribed to the lower abrasion resistance of SiMn slag aggregate compared to that of limestone aggregate as seen in Table 3.1. As shown in Figure 6.5(b), the relationship between elastic modulus and compressive strength for SiMn slag concrete is more similar to the empirical model developed by Yang et al. (2014).

Based on the relationship presented in Figure 6.5, the elastic modulus is determined as Eq. 6.10 for limestone concrete and Eq. 6.11 for SiMn slag concrete. Both elastic modulus equations have a high R^2 value of 0.9976 and 0.9948 respectively.

$$E_{C,LS} = 6007.2 {f_{cy}}^{0.4426} \quad \text{Eq. 6.10}$$

$$E_{C,SM} = 7075.6 {f_{cy}}^{0.3931} \quad \text{Eq. 6.11}$$

where $E_{C,LS}$ and $E_{C,SM}$ are the elastic modulus for limestone concrete and SiMn slag concrete respectively, and f_{cy} is cylinder compressive strength of concrete.

Table 6.3: Compressive strength, density and modulus of elasticity of limestone concrete and SiMn slag concrete

Day	Limestone concrete		
	Density (kg/m³)	**Cylinder compressive strength (MPa)**	**Modulus of elasticity (MPa)**
1	-	25.44	25167
7	-	43.6	32638
14	-	46.36	33934
28	2359.15	51.3	35591
56	2358.48	56.43	37751
90	2361.17	62.22	39311
Day	**SiMn slag concrete**		
	Density (kg/m³)	**Cylindrical compressive strength (MPa)**	**Modulus of elasticity (MPa)**
1	-	22.8	23373
7	-	39.44	29106
14	-	42.74	30528
28	2415.72	49.3	32549
56	2417.78	53.89	34004
90	2436.18	59.15	35691

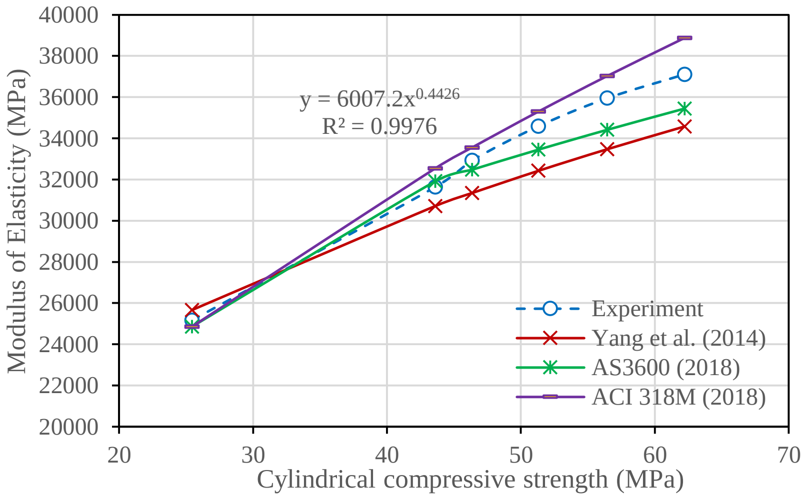

(a) Limestone concrete

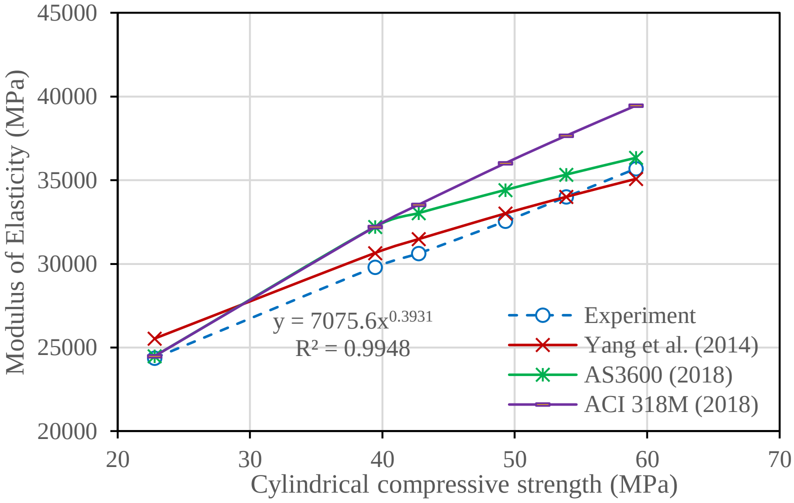

(b) SiMn slag concrete

Figure 6.5: Relationship of modulus of elasticity with compressive strength

6.2.4. Stress-strain Model in Compression

Stress-strain behavior of concrete is an important material property for modelling the cyclic loading on concrete. The empirical model for uniaxial compression developed by Yang et al. (2014) that requires only the compressive strength to generate the stress-strain curve, is used. Concrete, which possesses a non-linear stress-strain behavior, is then represented as a parabola as shown in Figure 6.6.

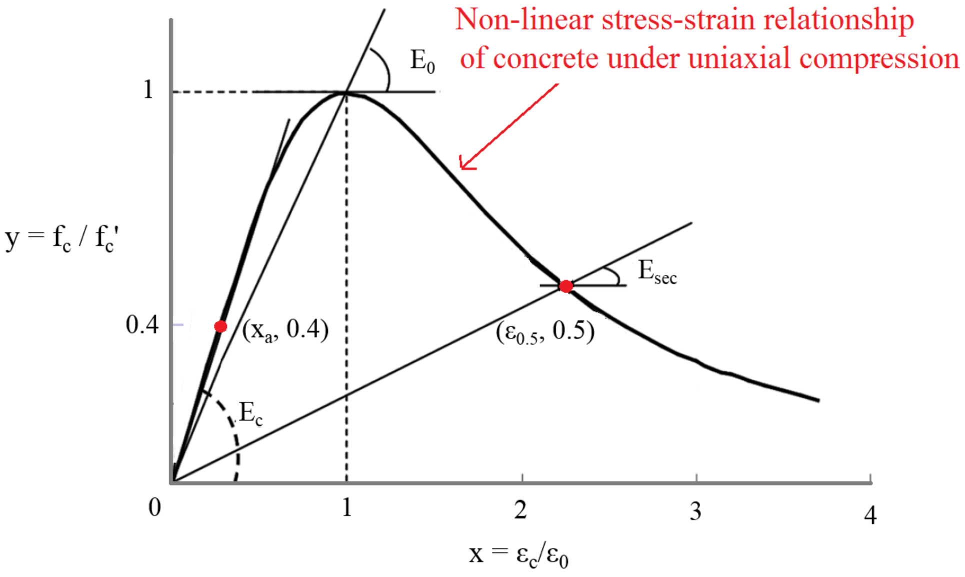

Figure 6.6: Empirical stress-strain model of concrete in compression (Yang et al., 2014)

The stress-strain curve is expressed as Eq. 6.12 with a distinct β_1 parameter specified for ascending and descending branches. The β_1 parameter for ascending and descending branches is given by Eq. 6.13 and Eq. 6.14 respectively.

$$f_c = \frac{(\beta_1 + 1)\frac{\varepsilon_c}{\varepsilon_o}}{\left(\frac{\varepsilon_c}{\varepsilon_o}\right)^{\beta_1} + \beta_1} f'_c \qquad \text{Eq. 6.12}$$

$$\beta_1 = 0.2e^{0.73\xi} \text{ for } \varepsilon_c \leq \varepsilon_o \qquad \text{Eq. 6.13}$$

$$\beta_1 = 0.41e^{0.77\xi} \text{ for } \varepsilon_c \geq \varepsilon_o \qquad \text{Eq. 6.14}$$

where f_c is compressive stress, ε_c is compressive strain, f_c' is peak stress, ε_o is strain that corresponds to peak stress and ξ is equal to $(f_c'/10)^{0.67}(2300/\rho_c)^{1.17}$ and ρ_c is concrete density.

Yang et al. (2014) also developed an equation using regression analysis to determine the strain which corresponded to peak stress (ε_o) and the strain at 50% of peak stress of descending branch ($\varepsilon_{0.5}$), as shown in Eq. 6.15 and Eq. 6.16 respectively.

$$\varepsilon_o = 0.0016e^{240\left(\frac{f'_c}{E_c}\right)} \qquad \text{Eq. 6.15}$$

$$\varepsilon_{0.5} = 0.0035e^{1.2\left(\frac{10}{f'_c}\times\frac{\rho_c}{2300}\right)^{1.75}} \qquad \text{Eq. 6.16}$$

Figure 6.7 compares the stress-strain curve obtained from experiment to that determined by the empirical model. It is shown that the empirical model can reasonably represent define the ascending and descending branches of the curve for both limestone and SiMn slag concrete.

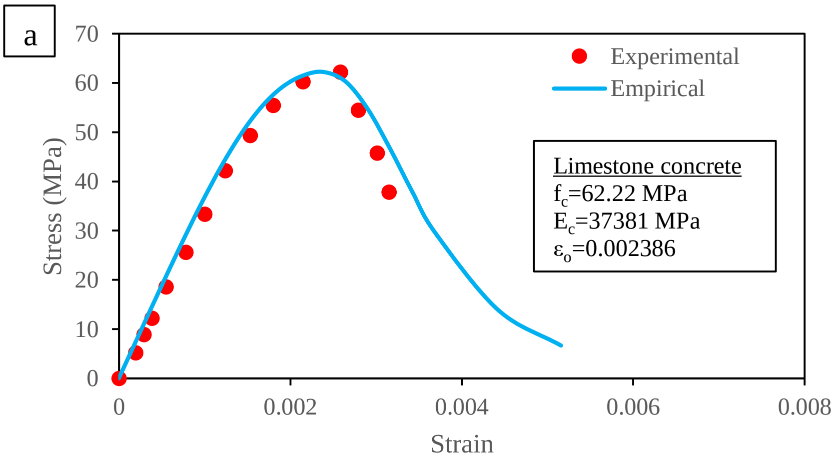

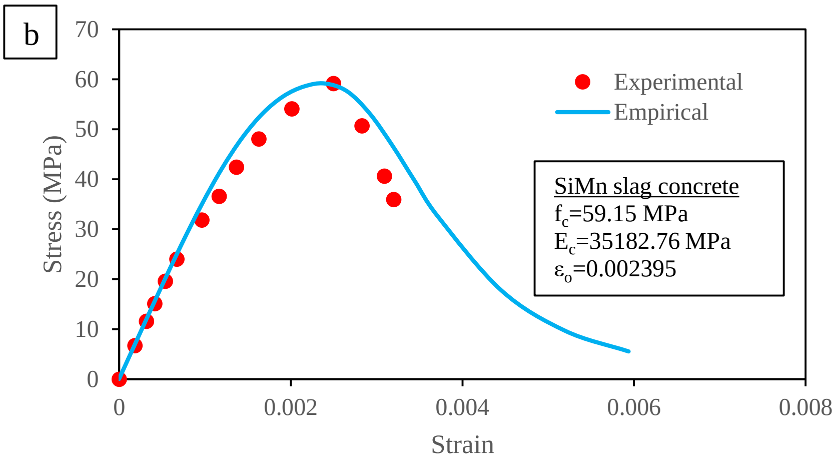

Figure 6.7: Comparison between experimental and empirical stress-strain curve for (a) limestone concrete and (b) SiMn slag concrete

6.2.5. Stress-strain Model in Tension

The stress-strain curve of concrete in tension is another fundamental property in the modelling of the cyclic behavior since it governs the cracking of concrete. It is relatively difficult to determine uniaxial tensile strength of concrete through experiment due to the sophisticated test set-up required (Nayal and Rasheed, 2006). The uniaxial tensile test of concrete is also sensitive to test set-up, with a slight misalignment significantly altering the stress distribution and hence affecting the test results. Nayal and Rasheed (2006) developed a tension stiffening model as shown in Figure 6.8(a). In this model, there is a sudden drop of stress at the critical tensile strain (ε_{cr}) from σ_{t0} to $0.8\sigma_{t0}$. The use of such model could result in infinity gradient and cause runtime errors in ABAQUS CDP model. The tensile stiffening model has been modified by Wahalathantri et al. (2011) as shown in Figure 6.8(b). In the model, the sudden drop was slanted from (ε_{cr}, σ_{t0}) to ($1.25\varepsilon_{cr}$, $0.77\sigma_{t0}$) and the run time errors in ABAQUS could be minimized. Therefore, Wahalathantri et al. (2011) tensile stiffening model is used in this study to generate the tensile stress-strain curve. The ascending curve is linear up to the peak stress as shown in Figure 6.8(b). The descending curve begins with a drop in peak stress which is caused by the initiation of concrete cracking. The descending branch consists of two segments that reflect primary and secondary cracking. The tensile strain at peak stress (ε_{cr}) can be determined from Eq. 6.17.

$$\varepsilon_{cr} = \frac{f_{ct}}{E_c} \qquad \text{Eq. 6.17}$$

where ε_{cr} is tensile strain at peak stress and f_{ct} is the uniaxial tensile strength of concrete.

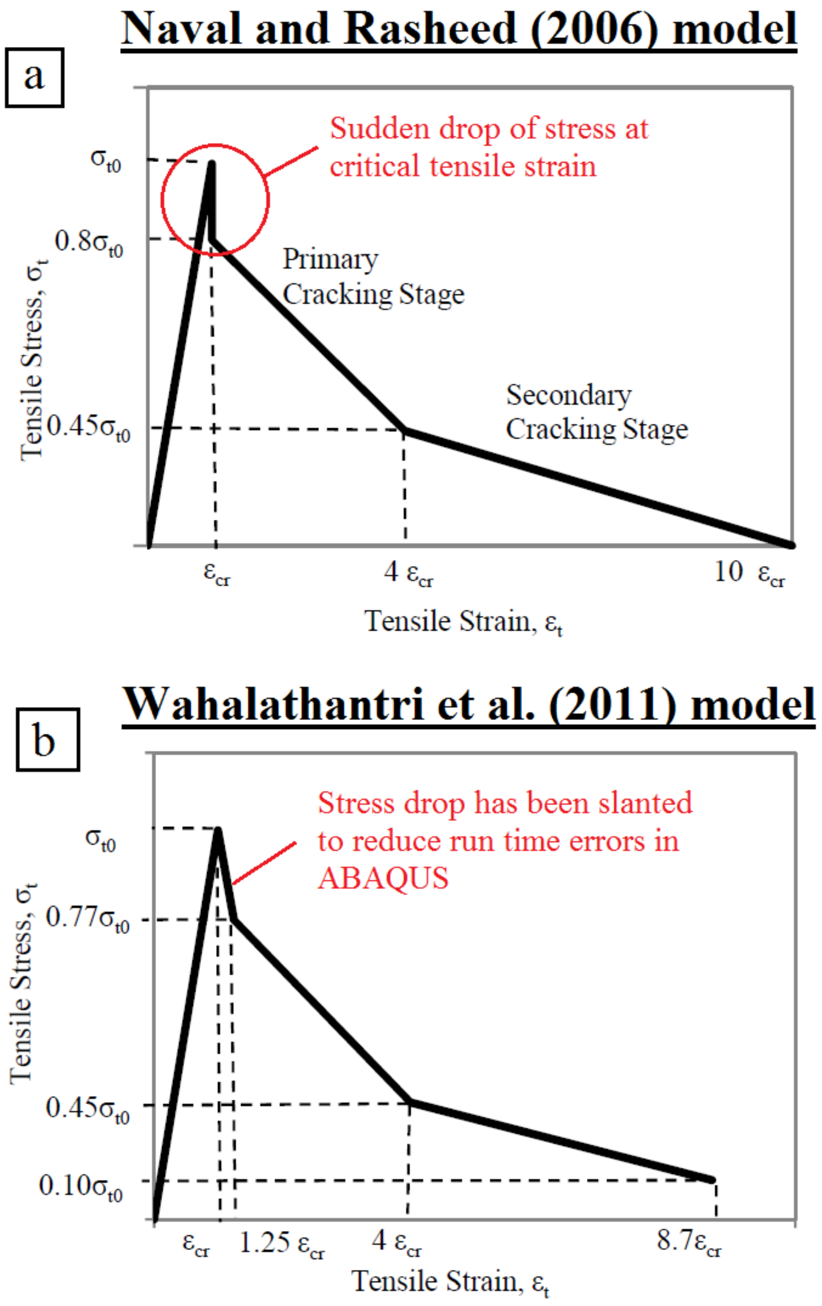

Figure 6.8: Empirical stress-strain model for concrete in uniaxial tension developed by (a) Nayal and Rasheed (2006) and (b) Wahalathantri et al. (2011)

6.2.6. Concrete Damaged Plasticity in ABAQUS

The Concrete Damaged Plasticity (CDP) model is adopted in this study to simulate the non-linearity of concrete subjected to cyclic loading. The CDP model in ABAQUS is based on the plastic damage model which was first developed by Lubliner et al. (1989) and later modified by Lee and Fenves (1998). It provides capability to model the quasi-brittle characteristics of concrete in terms of beam, truss, shell and solid elements. In the CDP model, the inelastic behavior of concrete is reflected by the damaged elasticity and isotropic plasticity. The stress tensor is given in the Eq. 6.18. The damage parameter d is defined in Eq. 6.19, where s_c and s_t correspond to the compressive and tensile stiffness recovery respectively.

$$\sigma = (1 - d)\bar{\sigma} = (1 - d)E_o(\varepsilon - \varepsilon^{pl}) \qquad \text{Eq. 6.18}$$

$$(1 - d) = (1 - s_t d_c)(1 - s_c d_t) \qquad \text{Eq. 6.19}$$

where d corresponds to the damage parameter ranging from 0 to 1, $\bar{\sigma}$ refers to the effective stress, E_o is the initial modulus of elasticity, ε and ε^{pl} are the total strain and plastic strain, respectively.

6.2.6.1. Yield Function

The yield function in terms of effective stress is given in Eq. 6.20, which accounts for the evolution of strength under compression and tension. In the equation, $\bar{q}$ is the Mises stress, $\bar{p}$ is the hydrostatic stress and $\bar{\sigma}_{max}$ is the maximum principal stress. The parameter α is determined from Eq. 6.21, where σ_{c0} and σ_{b0} are the initial uniaxial and initial biaxial compressive strengths respectively. A default value of 1.16 for σ_{b0}/σ_{c0} is used in the ABAQUS (Abaqus, 2012). The parameter β is calculated from Eq. 6.22, where $\bar{\sigma}_c\varepsilon_c^{pl}$ and $\bar{\sigma}_t\varepsilon_t^{pl}$ are the effective compressive and effective tensile cohesion stresses respectively. The parameter γ is expressed as a function of the tensile-to-compressive meridian ratio (K_c), as shown in Eq. 6.23, which defines the shape of yield surface.

$$F = \frac{1}{1 - \alpha}\left(\bar{q} - 3\alpha\bar{p} + \beta\varepsilon^{pl}\langle\bar{\sigma}_{max}\rangle - \gamma\langle-\bar{\sigma}_{max}\rangle\right) - \bar{\sigma}_c\varepsilon_c^{pl} \qquad \text{Eq. 6.20}$$

$$\alpha = \frac{(\sigma_{b0}/\sigma_{c0}) - 1}{2(\sigma_{b0}/\sigma_{c0}) - 1} \qquad \text{Eq. 6.21}$$

$$\beta = \frac{\bar{\sigma}_c \varepsilon_c^{pl}}{\bar{\sigma}_t \varepsilon_t^{pl}}(1 - \alpha) - (1 + \alpha) \qquad \text{Eq. 6.22}$$

$$\gamma = \frac{3(1 - K_c)}{2K_c - 1} \qquad \text{Eq. 6.23}$$

6.2.6.2. Plastic Flow

In the CDP model, the plastic flow of concrete is determined from the Drucker-Prager hyperbolic function. The flow potential function (G) is given in Eq. 6.24, where ε is the eccentricity defining the rate of function approaching asymptote, σ_{t0} is the uniaxial tensile strength and ψ is the dilation angle of the p-q plane. The dilation angle indicates the direction of plastic strain increment.

$$G = \sqrt{(\varepsilon \sigma_{t0} \tan \psi)^2 + \bar{q}^2} - \bar{p} \tan \psi \qquad \text{Eq. 6.24}$$

The ABAQUS uses 0.1 as the default value for eccentricity, meaning that concrete has approximately the same dilation angle for all confining stresses (Abaqus, 2012). The use of lower eccentricity can result in a convergence problem, particularly under low confining pressure, due to the tight curvature of flow potential that intersects the p-axis.

6.2.6.3. Viscoplastic Regularization

The softening behavior and stiffness degradation of concrete can lead to convergence problem, especially in the implicit analysis. Viscoplastic regularization is therefore used in the constitutive equation in order to improve the convergence. The CDP model in ABAQUS adopts the Duvaut-Lions regularization method, which allows for stress outside the yield surface. Eq. 6.25 presents the viscoplastic strain rate tensor.

$$\dot{\varepsilon}_v^{pl} = \frac{1}{\mu}\left(\varepsilon^{pl} - \varepsilon_v^{pl}\right) \qquad \text{Eq. 6.25}$$

where μ is the viscous parameter defining the relaxation of plastic strain and ε^{pl} is the determined plastic strain.

The viscous parameter μ can similarly be introduced in the stiffness degradation variable as in Eq. 6.26, so that the damage can be determined with additional relaxation time. The viscoplastic model for the stress-strain relationship is thus given in Eq. 6.27.

$$\dot{\mathrm{d}}_{\mathrm{v}} = \frac{1}{\mu}(\mathrm{d} - \mathrm{d}_{\mathrm{v}}) \qquad \text{Eq. 6.26}$$

$$\sigma = (\mathrm{d} - \mathrm{d}_{\mathrm{v}})\mathrm{D}_{\mathrm{o}}^{\mathrm{el}} : (\varepsilon - \varepsilon_{\mathrm{v}}^{\mathrm{pl}}) \qquad \text{Eq. 6.27}$$

where d refers to the degradation parameter determined in the inviscid model.

6.3. Numerical Modelling of Cyclic Loading – Development and Calibration of Model

6.3.1. Specimen Detail and Geometry Modelling

Concrete cube specimens tested under cyclic loading in Chapter 5 are modelled in this section. The detail of the test specimens is shown in Table 6.4. The specimen was cyclically loaded to failure when the upper stress levels 80%, 85% and 90% had been used. For specimens tested using the upper stress levels of 30%, 40% and 45%, the cyclic loading was modelled up to 10,000 cycles, which was similar to the experiment. The number of cycle to failure, stress-strain curve and deformation determined from the model were then validated against the experimental results. The cyclic loading model was restricted to a loading frequency of 0.8 Hz, which corresponded to experimental condition. Additional data will be required to conduct further frequency analysis if another frequency is used in the cyclic model. All of the test specimens were 50 mm cubes and were made up of plain concrete. In the ABAQUS, the concrete cube was modelled as a 3D deformable solid as shown in Figure 6.9.

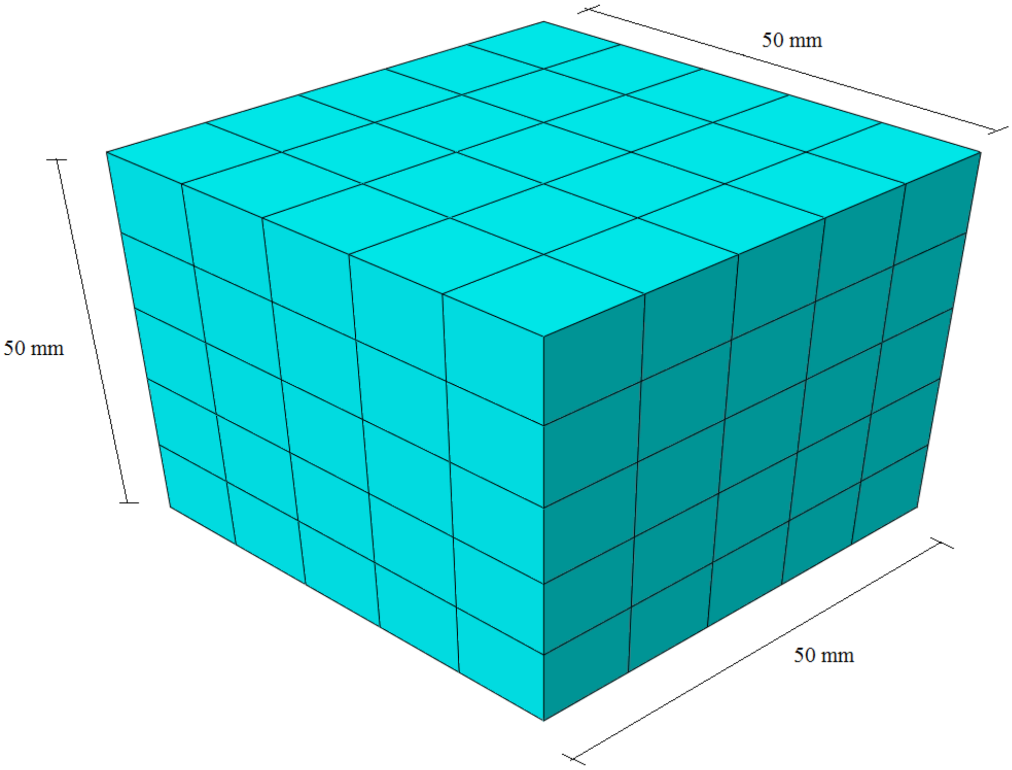

Figure 6.9: Concrete cube specimen for modelling in ABAQUS

Table 6.4: Detail of test specimens

Specimen	Upper stress level, S_{max}	Loading Cycle	Compressive strength (MPa) – Cube / Cylinder	Coarse aggregate type
T1-S0.4-F0.8	0.4	10,000	91.37 / 63.58	SiMn slag
T1-S0.45-F0.8	0.45	10,000		
T2-S0.45-F0.8	0.45	10,000	40.64 / 28.34	SiMn slag
T2-S0.8-F0.8	0.8	Up to failure		
T2-S0.85-F0.8	0.85	Up to failure		
T2-S0.9-F0.8	0.9	Up to failure		
T3-S0.8-F0.8	0.8	Up to failure	45.86 / 31.97	Limestone
T3-S0.85-F0.8	0.85	Up to failure		
T3-S0.9-F0.8	0.9	Up to failure		

6.3.2. Material Property

6.3.2.1. Concrete Density

Concrete density was determined from the average density of 28-day, 56-day and 90-day test results shown in Table 6.5. The concrete incorporated with SiMn slag aggregate had an average density of 2423.22 kg/m^3, while the density of limestone concrete was 2359.6 kg/m^3. The SiMn slag concrete had a higher density due to the heavier property of SiMn slag aggregate than the limestone aggregate as shown in Table 3.1. The concrete density was assumed to be constant in the modelling of the respective types of concrete.

Table 6.5: Concrete density determined from experiment

Day	**Density (kg/m^3)**	
	SiMn slag concrete	**Limestone concrete**
28	2415.72	2359.15
56	2417.78	2358.48
90	2436.18	2361.17
Average	2423.22	2359.6
Specimen	T1, T2	T3

6.3.2.2. Modulus of Elasticity

Table 6.6 presents the modulus of elasticity for concrete specimens T1, T2 and T3. The modulus of elasticity was determined from experiment and compared with that determined from Eq. 6.10 and Eq. 6.11. The calculated values were similar to the experimental values, indicating that the equation was fairly accurate. Nevertheless, the modulus of elasticity measured from the experiment was used in the numerical study to ensure more representative and realistic scenario. Eq. 6.10 and Eq. 6.11 were used if the experimental value was not available.

Table 6.6: Modulus of elasticity for specimen T1, T2 and T3

Specimens	T1	T2	T3
Modulus of elasticity (from experiment)	35671 MPa	26117 MPa	27138 MPa
Modulus of elasticity (from Eq. 6.10 and Eq. 6.11)	36194 MPa	26347 MPa	27840 MPa

6.3.2.3. Concrete Property in Compression

The stress-strain curve of concrete under compression was determined using the empirical relationship provided in Eq. 6.12. The compressive behavior of concrete in terms of damaged parameter (d_c) and inelastic strain (ε_{in}) is required for material property input in CDP model. The inelastic strain corresponding to the compressive strength is given in Eq. 6.28. The damaged parameter for concrete strength is determined from Eq. 6.29. In order to check the validity of the calculated inelastic strain, the plastic strain (ε_{pl}) is also determined using Eq. 6.30, whereby the plastic strain should increase with the inelastic strain. The input of compressive behavior for specimen T1, T2 and T3 is presented in Table 6.7.

$$\varepsilon_{in} = \varepsilon_c - \frac{\sigma_c}{E_c} \qquad \text{Eq. 6.28}$$

$$d_c = 1 - \frac{\sigma_c}{\sigma_{max}} \qquad \text{Eq. 6.29}$$

$$\varepsilon_{pl} = \varepsilon_{in} - \frac{d_c}{1 - d_c}\varepsilon_o \qquad \text{Eq. 6.30}$$

Table 6.7: Compressive behavior of concrete specimen for CDP model

Specimen T1			
Compressive stress, σ_c (MPa)	**Compressive damage, d_c**	**Inelastic strain, ε_{in}**	**Plastic strain, ε_{pl}**
45.02	0	0	0
51.15	0	0.00005	0.00005
56.65	0	0.00014	0.00014
60.58	0	0.00028	0.00027
62.86	0	0.00046	0.00046
63.58	0	0.00068	0.00068
61.89	0.03	0.00098	0.00093
57.05	0.10	0.00136	0.00118
49.95	0.21	0.00181	0.00143
41.91	0.34	0.00228	0.00168
34.08	0.46	0.00274	0.00193
17.05	0.73	0.00395	0.00267
8.52	0.87	0.00492	0.00340
4.50	0.93	0.00577	0.00414
Specimen T2			
Compressive stress, σ_c (MPa)	**Compressive damage, d_c**	**Inelastic strain, ε_{in}**	**Plastic strain, ε_{pl}**
18.02	0	0	0
20.60	0	0.00005	0.00005
23.49	0	0.00014	0.00014
26.94	0	0.00043	0.00043
27.78	0	0.00060	0.00060
28.34	0	0.00010	0.00010
25.11	0.11	0.00202	0.00190
22.44	0.21	0.00257	0.00235
17.39	0.39	0.00367	0.00325
13.63	0.52	0.00468	0.00412
10.86	0.62	0.00565	0.00498
8.81	0.69	0.00659	0.00585
7.28	0.74	0.00751	0.00672
5.21	0.82	0.00932	0.00845
Specimen T3			

Compressive stress, σ_c (MPa)	**Compressive damage, d_c**	**Inelastic strain, ε_{in}**	**Plastic strain, ε_{pl}**
20.61	0	0	0
22.64	0	0.00003	0.00003
26.04	0	0.00012	0.00012
30.22	0	0.00039	0.00039
31.27	0	0.00056	0.00056
31.97	0	0.00096	0.00096
30.93	0.03	0.00141	0.00137
28.49	0.11	0.00190	0.00178
25.49	0.20	0.00242	0.00219
22.45	0.30	0.00294	0.00260
14.97	0.53	0.00445	0.00384
9.15	0.71	0.00632	0.00550
7.37	0.77	0.00722	0.00633
5.05	0.84	0.00896	0.00800

6.3.2.4. Concrete Property in Tension

Uniaxial stress-strain curve was calculated using the empirical model proposed by Wahalathantri et al. (2011) as shown in Section 6.2.5. The uniaxial tensile strength was determined from the experimental splitting tensile strength using Eq. 6.7. Similar to compressive behavior, the tensile behavior of concrete in terms of inelastic strain, damaged parameter and plastic strain is determined from Eq. 6.31, Eq. 6.32 and Eq. 6.33 respectively. Table 6.8 summarizes the input of tensile behavior of specimen T1, T2 and T3 for CDP model.

$$\varepsilon_{\mathrm{in}} = \varepsilon_{\mathrm{t}} - \frac{\sigma_{\mathrm{t}}}{\mathrm{E_c}} \qquad \text{Eq. 6.31}$$

$$\mathrm{d_t} = 1 - \frac{\sigma_{\mathrm{t}}}{\sigma_{\mathrm{max}}} \qquad \text{Eq. 6.32}$$

$$\varepsilon_{\mathrm{pl}} = \varepsilon_{\mathrm{in}} - \frac{\mathrm{d_t}}{1-\mathrm{d_t}}\varepsilon_{\mathrm{cr}} \qquad \text{Eq. 6.33}$$

Table 6.8: Tensile behavior of concrete specimen for CDP model

<table>
<tr><th>Specimen</th><th colspan="2">Splitting tensile strength (MPa) (from experiment)</th><th>Uniaxial tensile strength (MPa) (from Eq. 6.7)</th></tr>
<tr><td>T1</td><td colspan="2">5.86</td><td>5.27</td></tr>
<tr><td>T2</td><td colspan="2">3.21</td><td>2.89</td></tr>
<tr><td>T3</td><td colspan="2">3.52</td><td>3.17</td></tr>
<tr><th colspan="4">Specimen T1</th></tr>
<tr><th>Tensile stress, σ_t (MPa)</th><th>Tensile damage, d_c</th><th>Inelastic strain, ε_{in}</th><th>Plastic strain, ε_{pl}</th></tr>
<tr><td>5.27</td><td>0</td><td>0</td><td>0</td></tr>
<tr><td>4.06</td><td>0.23</td><td>0.00006</td><td>0.00003</td></tr>
<tr><td>3.05</td><td>0.42</td><td>0.00029</td><td>0.00024</td></tr>
<tr><td>2.37</td><td>0.55</td><td>0.00045</td><td>0.00038</td></tr>
<tr><td>2.00</td><td>0.62</td><td>0.00058</td><td>0.00050</td></tr>
<tr><td>1.26</td><td>0.76</td><td>0.00083</td><td>0.00073</td></tr>
<tr><td>0.53</td><td>0.90</td><td>0.00109</td><td>0.00097</td></tr>
<tr><th colspan="4">Specimen T2</th></tr>
<tr><th>Tensile stress, σ_t (MPa)</th><th>Tensile damage, d_c</th><th>Inelastic strain, ε_{in}</th><th>Plastic strain, ε_{pl}</th></tr>
<tr><td>2.89</td><td>0</td><td>0</td><td>0</td></tr>
<tr><td>2.23</td><td>0.23</td><td>0.00005</td><td>0.00002</td></tr>
<tr><td>1.67</td><td>0.42</td><td>0.00022</td><td>0.00018</td></tr>
<tr><td>1.30</td><td>0.55</td><td>0.00034</td><td>0.00029</td></tr>
<tr><td>1.10</td><td>0.62</td><td>0.00043</td><td>0.00038</td></tr>
<tr><td>0.69</td><td>0.76</td><td>0.00063</td><td>0.00055</td></tr>
<tr><td>0.29</td><td>0.90</td><td>0.00082</td><td>0.00073</td></tr>
<tr><th colspan="4">Specimen T3</th></tr>
<tr><th>Tensile stress, σ_t (MPa)</th><th>Tensile damage, d_c</th><th>Inelastic strain, ε_{in}</th><th>Plastic strain, ε_{pl}</th></tr>
<tr><td>3.17</td><td>0</td><td>0</td><td>0</td></tr>
<tr><td>2.44</td><td>0.23</td><td>0.00005</td><td>0.00002</td></tr>
<tr><td>1.83</td><td>0.42</td><td>0.00023</td><td>0.00019</td></tr>
<tr><td>1.43</td><td>0.55</td><td>0.00035</td><td>0.00030</td></tr>
<tr><td>1.20</td><td>0.62</td><td>0.00045</td><td>0.00039</td></tr>
<tr><td>0.76</td><td>0.76</td><td>0.00066</td><td>0.00058</td></tr>
<tr><td>0.32</td><td>0.90</td><td>0.00086</td><td>0.00077</td></tr>
</table>

6.3.3. Boundary Condition

The loading and boundary conditions of the cube specimen were modelled in accordance with the experimental conditions. Figure 6.10 shows the diagram of specimen applied with boundary and loading conditions in ABAQUS model. As shown in Figure 6.11, the bottom surface of the specimen was pinned by restraining the motion in x, y and z directions. With the restraint on top surface, only movement in z direction was allowed. This was because the movement in x and y directions of top surface was restrained by the loading plate in the experiment. The cyclic loading on cube specimen was applied in steps. As shown in Figure 6.12, the lower stress level of cyclic loading was applied as pre-loading, which was 1% of the cube compressive strength. Subsequently, a triangular cyclic loading was applied to the specimen up to the upper stress level by defining the loading cycle in tabular amplitude. Each cyclic loading step was applied with 500 loading cycles on the specimen. As such, 20 steps were created in order to apply 10,000 loading cycles.

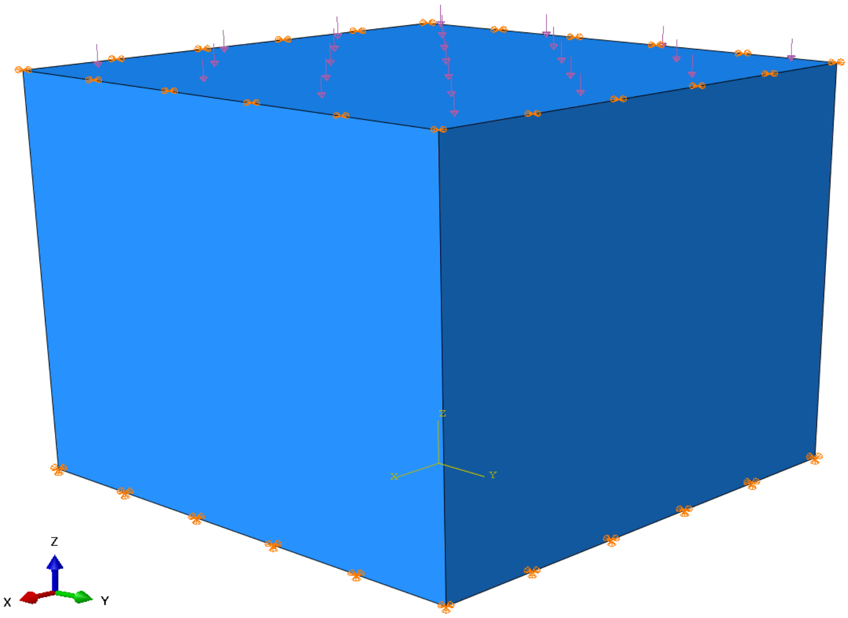

Figure 6.10: Cube specimen with applied loading and boundary conditions

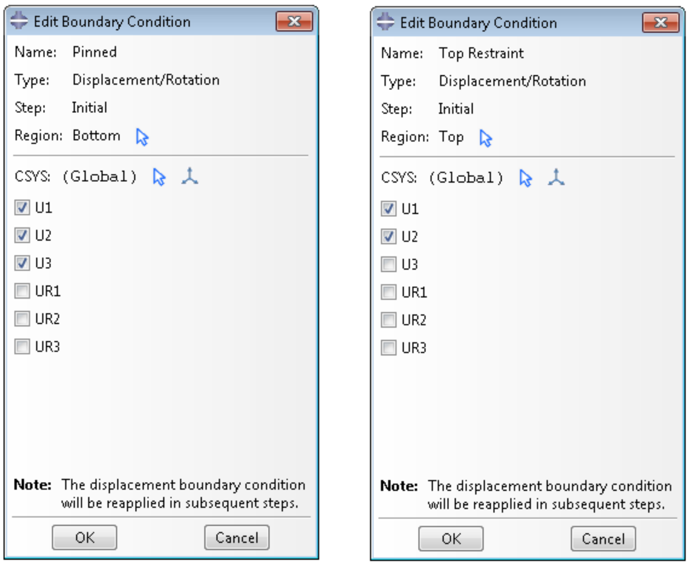

Edit Boundary Condition

Name: Pinned
Type: Displacement/Rotation
Step: Initial
Region: Bottom
CSYS: (Global)
☑ U1
☑ U2
☑ U3
☐ UR1
☐ UR2
☐ UR3

Note: The displacement boundary condition will be reapplied in subsequent steps.

Edit Boundary Condition

Name: Top Restraint
Type: Displacement/Rotation
Step: Initial
Region: Top
CSYS: (Global)
☑ U1
☑ U2
☐ U3
☐ UR1
☐ UR2
☐ UR3

Note: The displacement boundary condition will be reapplied in subsequent steps.

Figure 6.11: Boundary condition of cube specimen

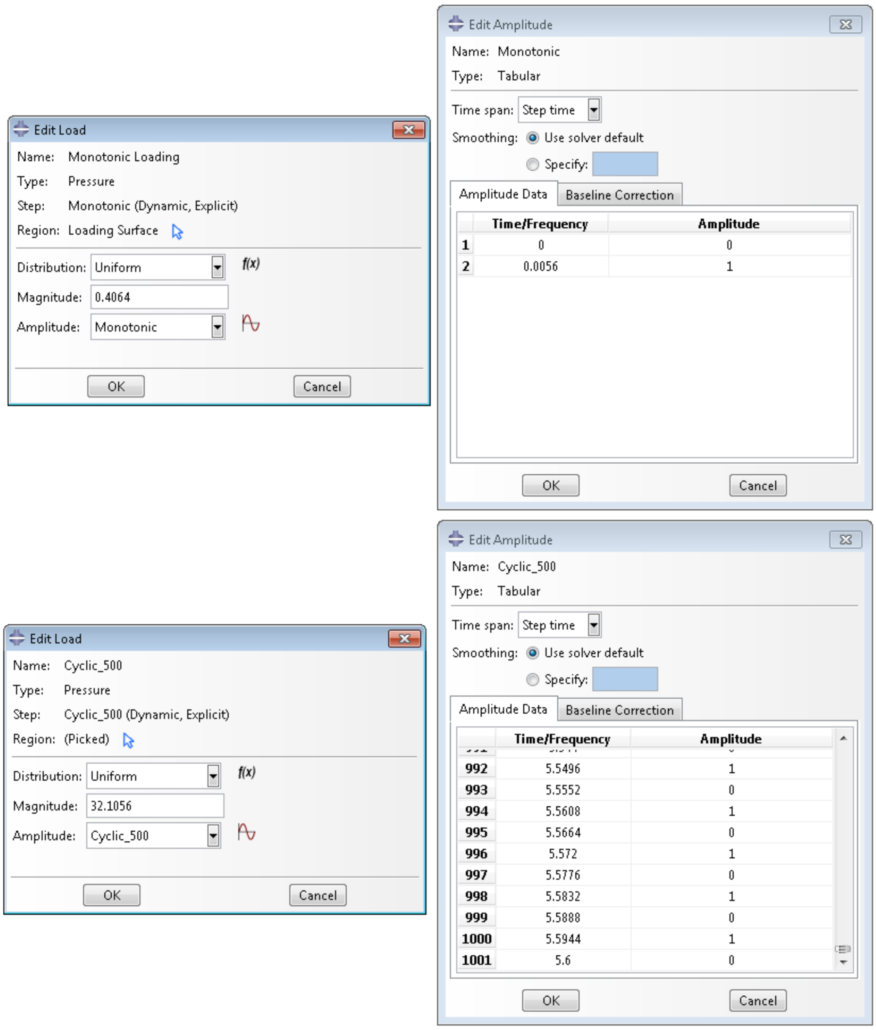

Edit Load

Name: Monotonic Loading
Type: Pressure
Step: Monotonic (Dynamic, Explicit)
Region: Loading Surface

Distribution: Uniform
Magnitude: 0.4064
Amplitude: Monotonic

Edit Amplitude

Name: Monotonic
Type: Tabular

Time span: Step time
Smoothing: ● Use solver default
○ Specify:

	Time/Frequency	Amplitude
1	0	0
2	0.0056	1

Edit Load

Name: Cyclic_500
Type: Pressure
Step: Cyclic_500 (Dynamic, Explicit)
Region: (Picked)

Distribution: Uniform
Magnitude: 32.1056
Amplitude: Cyclic_500

Edit Amplitude

Name: Cyclic_500
Type: Tabular

Time span: Step time
Smoothing: ● Use solver default
○ Specify:

	Time/Frequency	Amplitude
992	5.5496	1
993	5.5552	0
994	5.5608	1
995	5.5664	0
996	5.572	1
997	5.5776	0
998	5.5832	1
999	5.5888	0
1000	5.5944	1
1001	5.6	0

(a) Pre-loading and cyclic loading amplitude

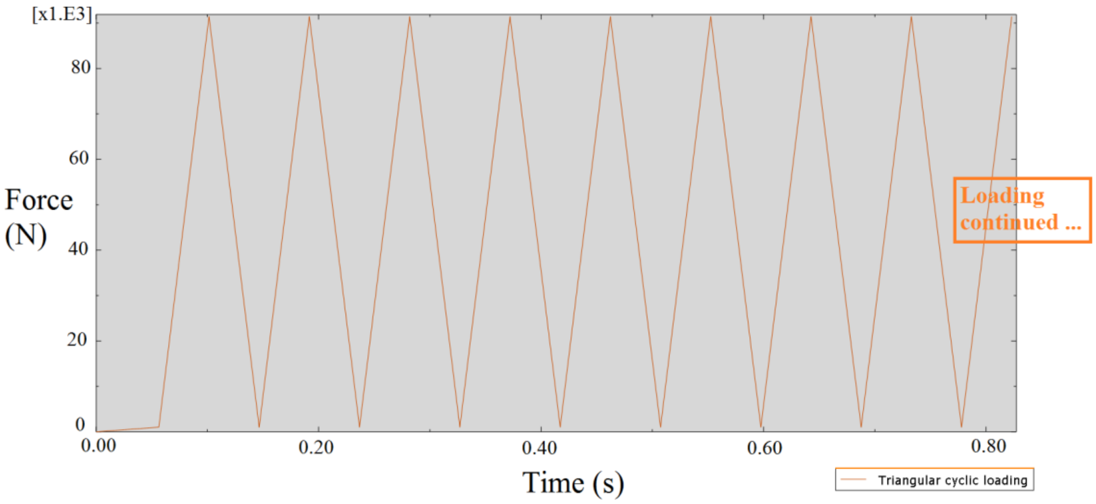

(b) Triangular cyclic loading

Figure 6.12: Loading on cube specimen

6.3.4. Configuration of Time Step

The solution procedure used in modelling the cyclic loading was the dynamic explicit solver. Explicit formulation was used because this solver did not require the formation of global stiffness matrix and the equations were solved element by element (Genikomsou and Polak, 2015). The explicit solver had less convergence problems as only the current stress tensor was evaluated in the transient solution. However, the explicit solver usually requires a small time step and is not stable if the time step is greater than Courant-Friedrichs-Lewy (CFL) time step (Abaqus, 2012). Therefore, frequency analysis has to be performed to assess the time step of explicit solver. Figure 6.13 depicts the failed cube specimen in frequency analysis due to compressive crushing. The natural frequency for this failure mode was found to be 18617 Hz and the hence time period was 5.37x10^{-5} s. However, the time was too short for dynamic explicit solver and caused a spike in the kinetic energy. According to Coelho et al. (2015), the acceptable ratio of kinetic energy to internal energy should be less than 0.05. The time step was therefore multiplied by a factor of 200 in such a way that the kinetic energy caused by compressive loading was much lower than the internal energy as depicted in Figure 6.14. In this regard, a time step of 0.0112 s was used for one complete cycle of loading and unloading.

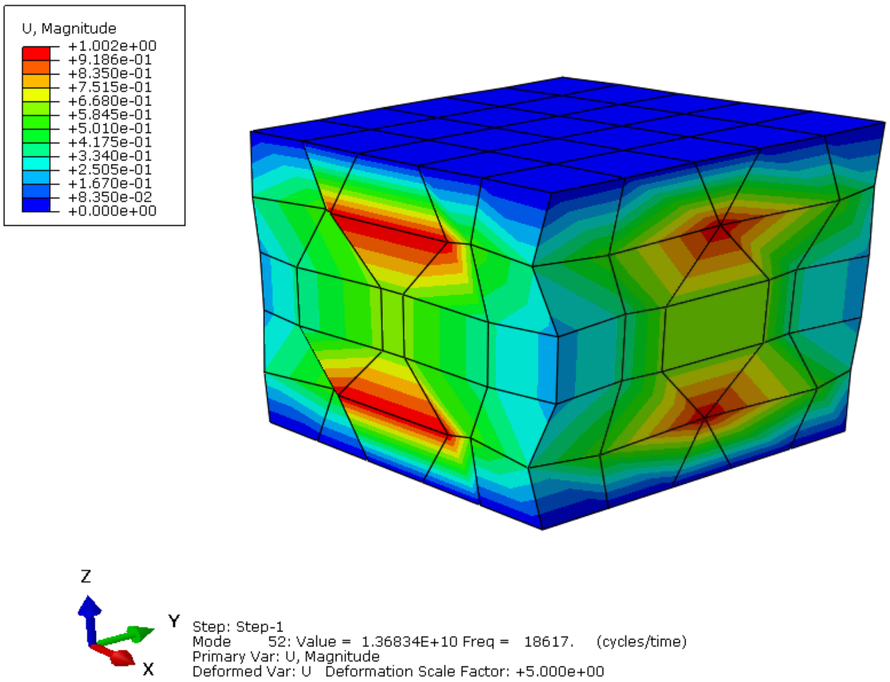

Figure 6.13: Frequency analysis of cube specimen

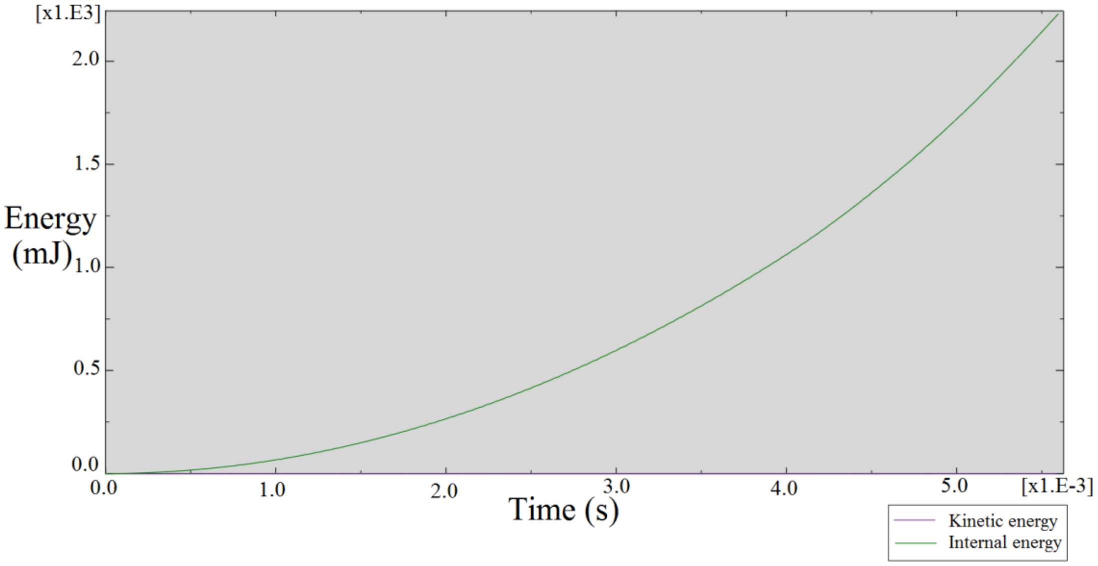

Figure 6.14: Plot of kinetic energy and internal energy against time step for specimen under compression

6.3.5. Type and Meshing of Element

An 8-noded hexahedral element with reduced integration, C3D8R, has been used for modelling the non-linear characteristic of concrete. The C3D8R is a general purpose linear continuum element that is suitable to model three dimensional solid material with large deformation. In ABAQUS, the C3D8R is used by default with the hourglass control scheme, which prevents large distortion caused by zero energy modes (Abaqus, 2012). The integration point located in the middle of C3D8R element can provide an accurate estimate of stress and strain as shown in Figure 6.15. Therefore, smaller-sized elements of a smaller size are usually needed to evaluate the stress particularly close to the boundary of structure.

A mesh sensitivity study was performed using the T2 specimen in order to determine the appropriate mesh size. The mesh sizes used in the study were 6 mm, 8 mm, 10 mm, 12.5 mm and 16 mm, which divided the cube specimens into 512, 216, 125, 64 and 27 elements respectively. Stress-strain response of T2 specimen under static compressive loading was plotted and compared to experimental result as shown in Figure 6.16. It was shown that the peak compressive stress of cube specimen decreased with the mesh size. The mesh sizes of 16 mm and 12.5 mm were too coarse, leading to an overestimation of the cube compressive strength. The cube specimen with a mesh of

10 mm had a peak stress comparable to the experimental value, though with a negligible 2.1% difference. A further decrease in mesh size to 8 mm and 6 mm had a minimal effect on the stress, with only a difference of 1.2% and 3.6% respectively, when compared to the experimental value. Therefore, the mesh size of 10 mm, which was not too fine and hence more optimal in terms of computational time, was chosen for the subsequent analysis.

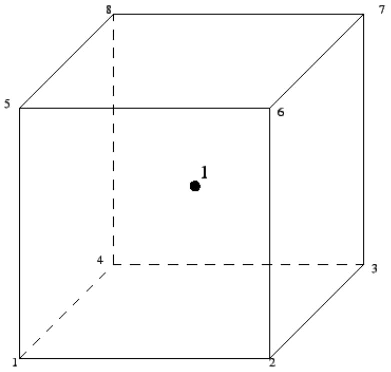

Figure 6.15: 8-noded hexahedral element

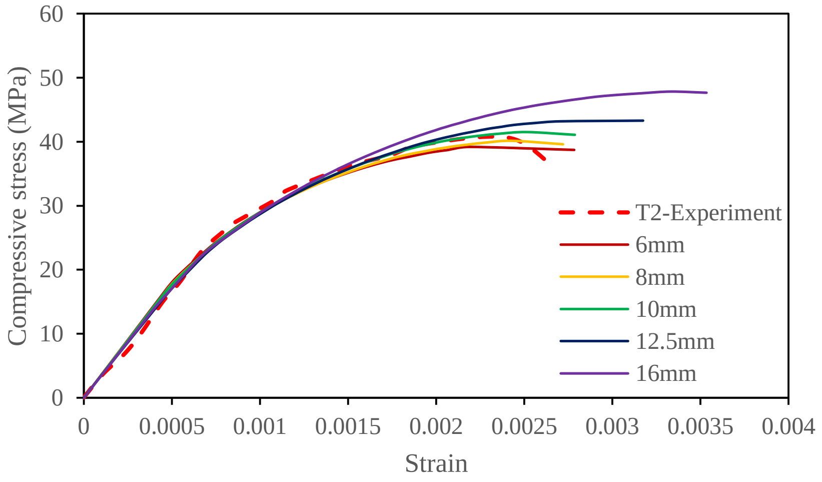

Figure 6.16: Stress-strain response of T2 specimen using different mesh sizes

6.3.6. Calibration of CDP Parameter

The input of CDP parameters in the ABAQUS includes dilation angle, eccentricity, ratio of biaxial to uniaxial strength (σ_{b0}/σ_{c0}), ratio of tensile to compressive meridian (K_c) and viscosity parameter. Although some default values were given in ABAQUS, a sensitivity study was still performed to calibrate these parameters. According to

Abaqus (2012) user manual, the viscosity parameter did not have effect on the regularization of viscoplasticity if the dynamic explicit solver was used in the analysis. Therefore, a viscosity parameter of 0 was used. Other CDP parameters were calibrated against T2 specimen test result under static compressive loading. The stress-strain response of T2 specimen was compared in the sensitivity study.

6.3.6.1. Dilation Angle

The angle of dilation defines the behavior of plastic strain growth when the shear stress in concrete approaches the critical value. Brittle material such as concrete typically has a dilation angle between 31° and 42° (Genikomsou and Polak, 2015). Figure 6.17 presents the influence of dilation angle on the stress-strain curve of T2 specimen under compression. The peak compressive stress and the corresponding strain gradually increased as the dilation angle increased from 20° to 40°. A higher value of dilation angle corresponded to more ductile material behavior. The stress-strain response of specimen with a dilation angle of 40° more closely matched the experimental result and was therefore used in this study.

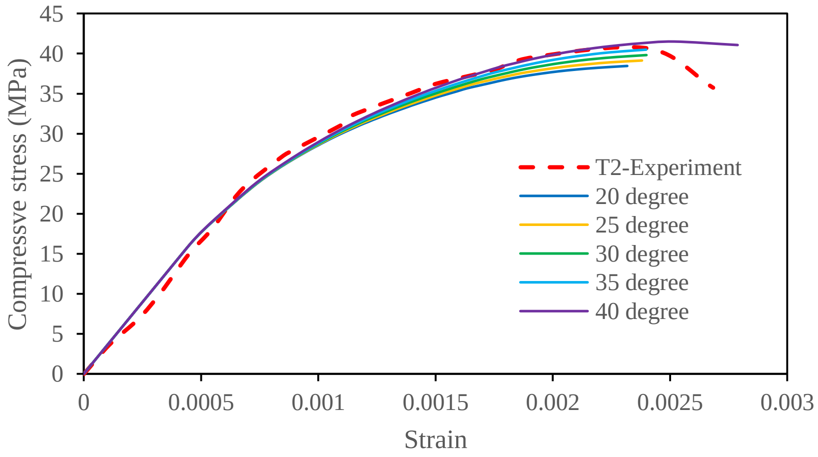

Figure 6.17: Stress-strain response of T2 specimen using different dilation angles

6.3.6.2. Eccentricity

The eccentricity determines the rate of hyperbolic flow potential approaching the asymptote. The eccentricity of CDP model is always a small positive number (Abaqus, 2012). Figure 6.18 compares the stress-strain curve of T2 specimen when different eccentricity values have been used in the model. The results showed that the eccentricity value had no effect on the stress-strain response of concrete subjected to compressive loading. As such, in the model, eccentricity with a default value of 0.1 was chosen.

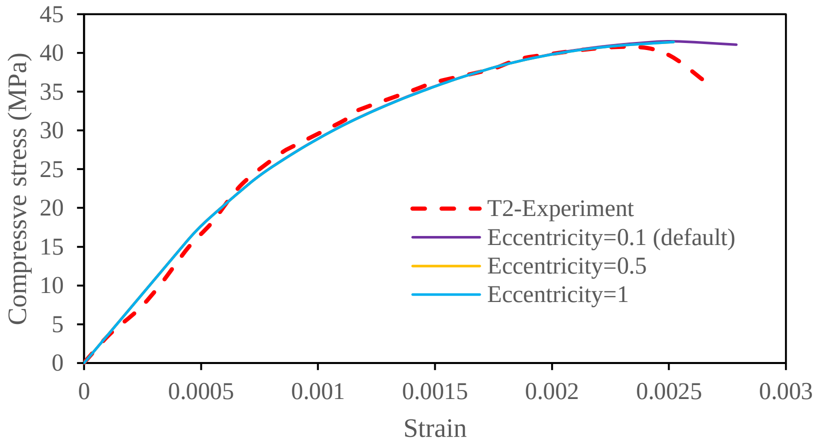

Figure 6.18: Stress-strain response of T2 specimen using different values of eccentricity

6.3.6.3. Ratio of Tensile to Compressive Meridian (K_c)

The parameter K_c is the ratio of tensile meridian to compressive meridian in the deviatory plane. Based on the Drucker-Prager yield criterion, the K_c value can range from 0.667 to 1, where the value of 1 represents the circular deviatory plane of failure surface. Figure 6.19 compares the stress-strain curve of T2 specimen with the use of various K_c values. Peak stress and strain significantly decreased with an increase in K_c value. Based on the sensitivity study, the default K_c value of 0.667 was selected as it matched the experimental result reasonably well.

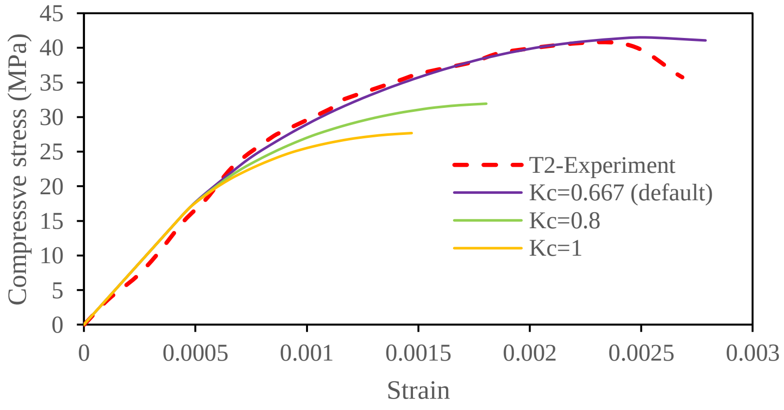

Figure 6.19: Stress-strain response of T2 specimen using different K_c values

6.3.6.4. Ratio of Biaxial to Uniaxial Strength (σ_{b0}/σ_{c0})

The ratio of biaxial to uniaxial strength (σ_{b0}/σ_{c0}) specifies the point of concrete failure under biaxial compression. Figure 6.20 shows the influence of σ_{b0}/σ_{c0} on the stress-strain response. The peak stress and the corresponding strain increased with the σ_{b0}/σ_{c0} ratio. The stress-strain curve of concrete with a default value of 1.16 was best fit to the experimental result and was selected in this study.

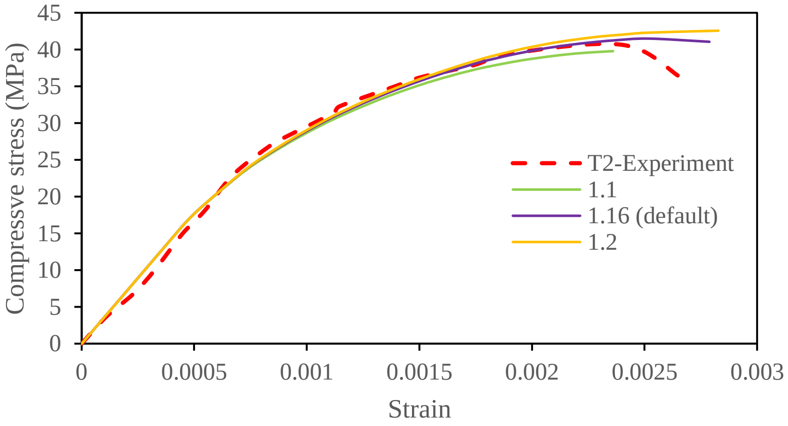

Figure 6.20: Stress-strain response of T2 specimen using different σ_{b0}/σ_{c0} ratios

6.3.6.5. Summary of CDP Parameter

The CDP parameters calibrated based on T2 specimen are shown in Table 6.9. These values were used in the modelling of concrete cyclic loading. The calibrated model also reasonably well predicted the stress-strain response of T1 and T3 specimens as shown in Figure 6.21. When compared to experimental results, the difference in peak stress was 6.8% for T1 and 3.9% for T3.

Table 6.9: Input of CDP parameters

CDP parameter	Calibrated value
Dilation angle	40^o
Eccentricity	0.1
Ratio of Tensile to Compressive Meridian (K_c)	0.667
Ratio of Biaxial to Uniaxial Strength (σ_{b0}/σ_{c0})	1.16
Viscosity parameter	0

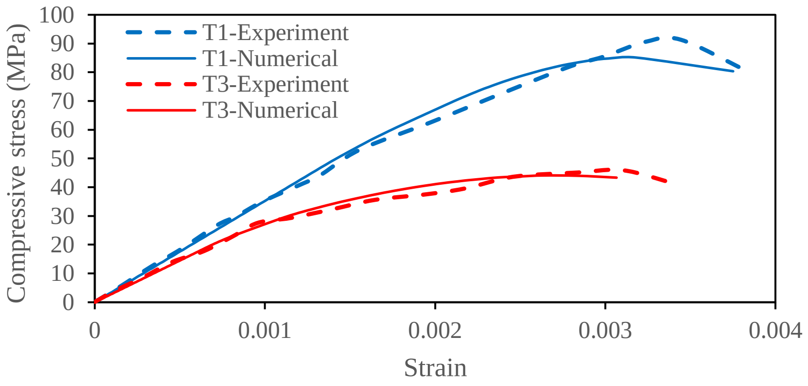

Figure 6.21: Stress-strain responses of T1 and T3 using calibrated model

6.4. Numerical Analyses – Results and Discussions

6.4.1. Validation of Model with Experimental Results

The calibrated model was used to simulate the cyclic loading on the test specimens as detailed in Table 6.4. In the following sections, the numerical results for fatigue life, stress-strain behavior and residual deformation are compared to the experimental results. The cyclic loading test failure mode of specimen is compared between experiment and numerical analysis. The comparison for T2 specimen is shown in Figure 6.22. In the numerical model, the maximum plastic strain is used to depict the crack pattern of concrete. Both experimental and numerical results indicated that the cracks developed close to the edge of specimen. The plastic strain was also concentrated along the center of the specimen, indicating a crushing failure.

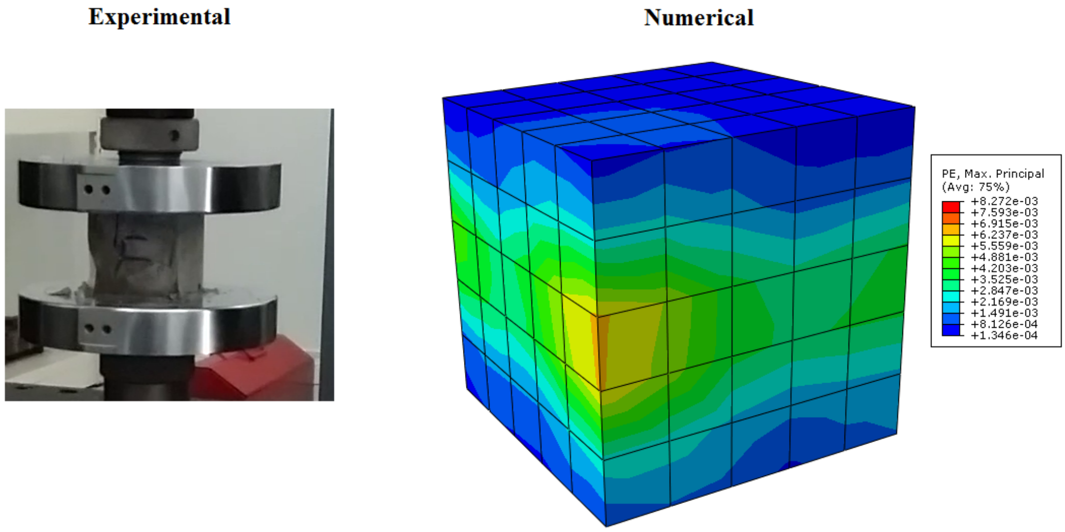

Figure 6.22: Experimental and numerical failure mode of T2 specimen under cyclic loading

6.4.1.1. Comparison of Fatigue Life

The fatigue life of T2 and T3 specimens obtained from numerical analysis is summarized in Table 6.10. The failure cycle of specimen from the model was within the range that had been determined in experiment. At the upper stress levels (S_{max}) of 80% and 85%, the concrete lasted for more loading cycles and failed at the value close to the highest experimental fatigue life. The concrete failed relatively early at a higher S_{max} of 90% due to its brittle behavior and non-linear property. Figure 6.23 depicts a comparison of numerical and experimental S-N curves. The numerical S-N curve was slightly higher than the experimental curve, indicating that the concrete had a longer fatigue life for a given stress level. This was due to the limitation of the actual test, in which the concrete had an inhomogeneous property, resulting in considerable strength variation. The material constitutive model reasonably represented the lower fatigue life of T2 than that of T3, by considering their properties in terms of compressive strength, tensile strength and elastic modulus. The analysis showed that the fatigue life predicted by the numerical model agreed fairly well with the experimental results.

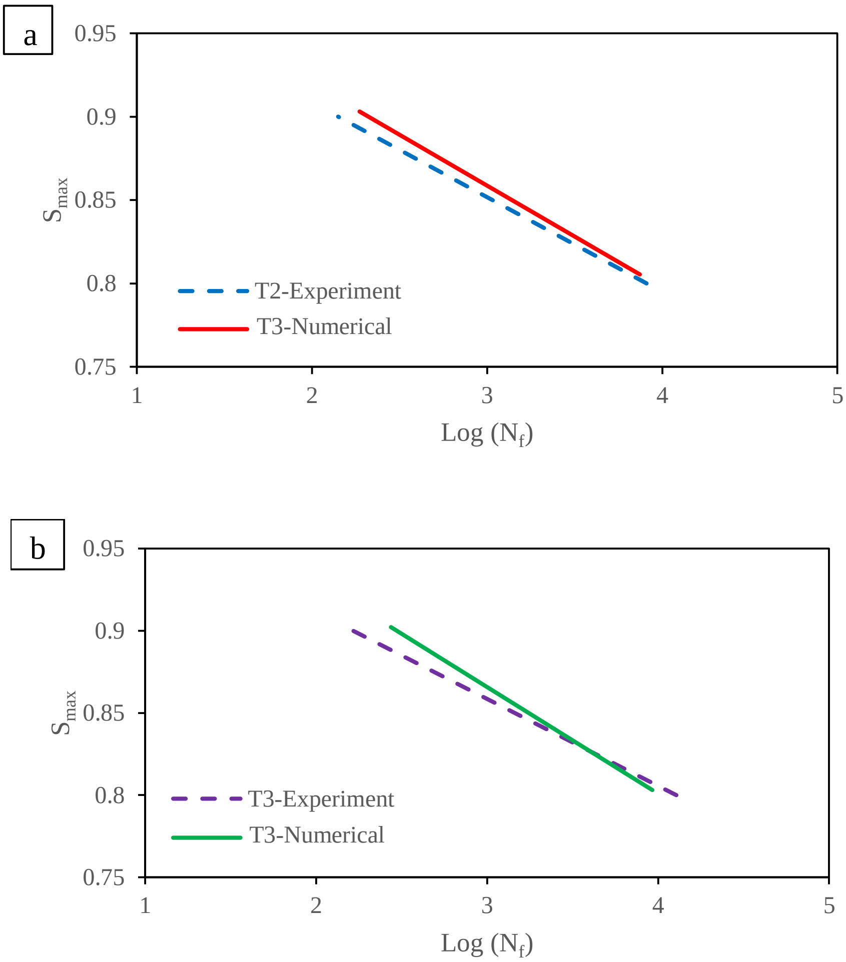

Figure 6.23: Comparison of S-N curves for (a) T2 and (b) T3 specimens

Table 6.10: Comparison of fatigue life

Specimen	**Fatigue life, N_f (cycle)**	
	Numerical model	**Experiment**
T2-S0.8-F0.8	7443	5708, 6324, 7407
T2-S0.85-F0.8	1930	1039, 1123, 2110
T2-S0.9-F0.8	187	73, 157, 245
T3-S0.8-F0.8	9251	7713, 8481, 9346
T3-S0.85-F0.8	2130	1538, 1870, 2415
T3-S0.9-F0.8	274	52, 273, 449

6.4.1.2. Comparison of Stress-strain Curve in Cyclic Loading

The stress-strain curves obtained from numerical analysis of T2-S0.8-F0.8 and T3-S0.8-F0.8 under cyclic loading are shown in Figure 6.24(a) and (b). The stress-strain curves of T2-S0.8-F0.8 were plotted after 1, 4000 and 7000 loading cycles, and the curves of T3-S0.8-F0.8 were plotted after 1, 5000 and 9000 loading cycles. These intervals of loading cycle were selected due to their distinct curve lines. The curves were compared to those determined from the experiment having a similar failure cycle. As the number of cycles increased, the curves progressively shifted to the right, showing a rise in residual strain. The gradient of the stress-strain curve also decreased as the number of cycles increased, which indicated a degraded elastic modulus of concrete.

In addition, it was shown that the displacement of both types of specimens measured in the experiment was greater than that calculated from numerical analysis. The difference in displacement was approximately 9.1%–14.8% for T2-S0.8-F0.8 and 10.5%–30.1% for T3-S0.8-F0.8. The discrepancy of results became more obvious when the concrete approached the failure point. Both T2-S0.8-F0.8 and T3-S0.8-F0.8 specimens were subjected to sulphate attack and WDA prior to the cyclic loading test. Thus, the sulphate attack and WDA softened the concrete and increased its deformation during the cyclic loading (Roziere et al., 2009). The effect on the descending branch of stress-strain curve was not considered in the numerical model, resulting in greater discrepancy towards the specimen failure point. It is recommended that further investigation be conducted to collect more data in order to improve the accuracy of the cyclic loading model. Nonetheless, the disparity in stress-strain curves arisen from this limitation had minimal impact on the prediction of concrete fatigue life, though the strain at failure was greater.

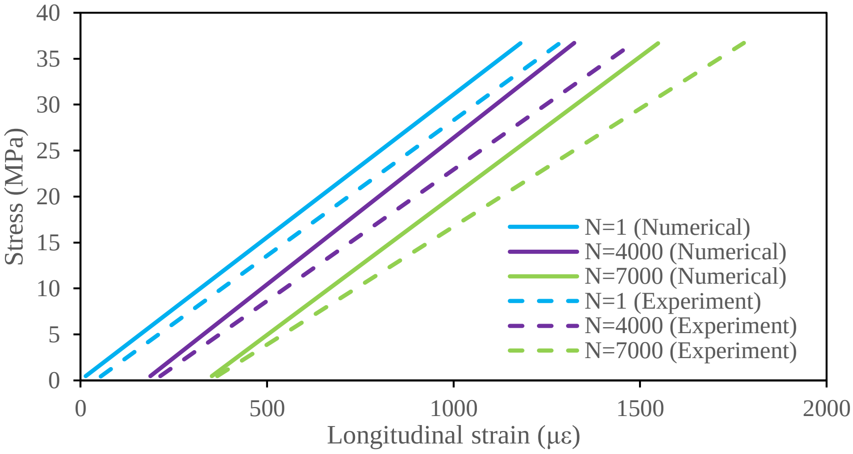

(a) T2-S0.8-F0.8 [N_f=7443 (Num.) vs 7407 (Exp.)]

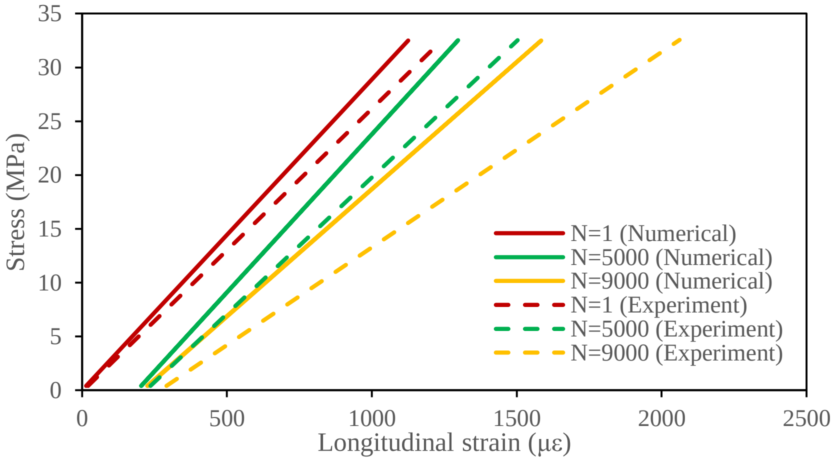

(b) T3-S0.8-F0.8 [N_f=9251 (Num.) vs 9346 (Exp.)]

Figure 6.24: Stress-strain curves of (a) T2-S0.8-F0.8 and (b) T3-S0.8-F0.8 under cyclic loading

6.4.1.3. Comparison of Residual Displacement

Figure 6.25 compares the residual displacement of intact specimens T1-S0.4-F0.8, T1-S0.45-F0.8 and T2-S0.45-F0.8 after 10,000 loading cycles. The numerical analysis showed that the residual displacement of T1 specimens loaded at 40% and 45% upper stress levels was slightly lower than the experimental values. The disparity between numerical and experimental displacements was 22.6% for T1-S0.4-F0.8 and T1-S0.45-F0.8 for 18.1%. This could be due to the limitation of CDP material model in simulating the opening and closing of concrete cracks caused by cyclic loading, as they are represented in terms of stiffness recovery. The CDP model also overestimated the energy dissipating capability of specimen, resulting in a lower residual displacement predicted by the model compared to the experimental value (Xiao et al., 2016).

As for the T2-S0.45-F0.8, the displacement discrepancy between numerical and experimental values was comparatively greater. The numerical residual displacement of T2-S0.45-F0.8 was 41.9% less than that determined by the experiment. This was because the softening effect caused by sulphate attack and WDA on the descending branch of stress-strain curve at the post failure was not accounted for in the numerical model. Further research into the effect of sulphate attack and WDA on the descending branch of stress-strain curve is therefore recommended in order to obtain more data for model calibration.

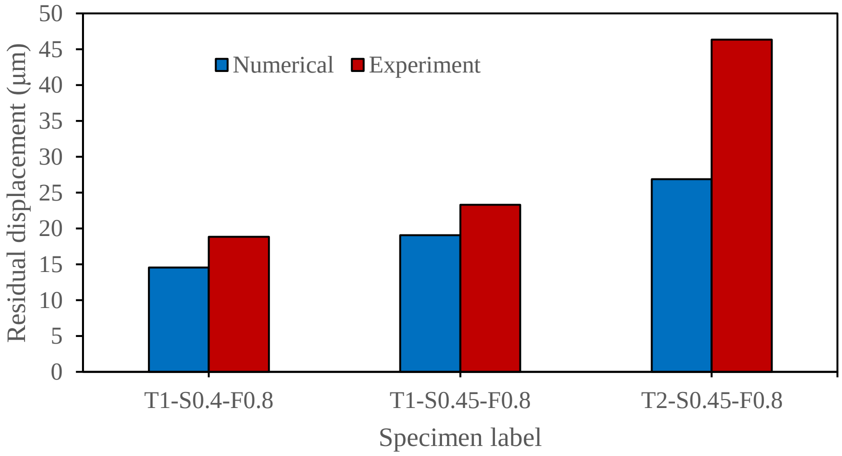

Figure 6.25: Comparison of residual displacement for intact specimen after 10,000 loading cycles

6.4.2. Parametric Study

The validation study has shown that the numerical analysis agrees fairly well with the experimental results and that the model can reasonably predict the fatigue life of concrete. Due to time and cost savings of using the numerical model, a number of parametric studies were performed to further investigate the cyclic behavior of concrete. The effect of concrete compressive strength (f_c'), lower stress level (S_{min}) and cube specimen size on the fatigue life was studied. Table 6.11 shows the range of each parameter in the study. In the numerical analysis, the upper stress level (S_{max}) was kept constant at 90% and the material property of SiMn slag concrete was used.

Table 6.11: Specimen detail for parametric study

Specimen	f_c' (MPa)	S_{min}	Cube specimen size (mm)
P1	20	0.05	50
P2	50	0.05	50
P3	80	0.05	50
P4	80	0.1	50
P5	80	0.2	50
P6	80	0.05	100
P7	80	0.05	150

6.4.2.1. Effect of Compressive Strength

The fatigue life of concrete with compressive strengths of 20 MPa, 50 MPa and 80 MPa has been determined using the numerical model and the results are shown in Figure 6.26. When the compressive strength was increased from 20 MPa to 50 MPa and 80 MPa, the fatigue life of concrete decreased from 309 cycles to 231 cycles and 176 cycles, respectively. This was because the failure mode of high strength concrete was more brittle than that of low strength concrete. As a result, the strain of concrete at failure load decreased, resulting in lower cyclic loading resistance of concrete. Kim and Kim (1996) also demonstrated that the fatigue life of concrete decreased when the strength increased from 26 MPa to 103 MPa. The S-N curve for high strength concrete was also steeper and had a lower fatigue life. Furthermore, the rate of fatigue strain increment in high strength concrete was higher than that in low strength concrete (Lantsoght et al., 2016).

The fatigue stress-strain curves for P1, P2 and P3 obtained from the numerical model are depicted in Figure 6.27. The monotonic stress-strain curves of these specimens are also plotted for comparison. The fatigue strain at the lower and upper stress levels gradually increased with the loading cycles. As the fatigue strain approached the descending branch of the monotonic stress-strain curve, the failure occurred for all concrete specimens. As shown in Figure 6.27, high strength concrete failed more rapidly and experienced less degradation of elastic modulus. This was due to brittle behavior of high strength concrete and its lower capacity to remain intact as the inelastic strain developed.

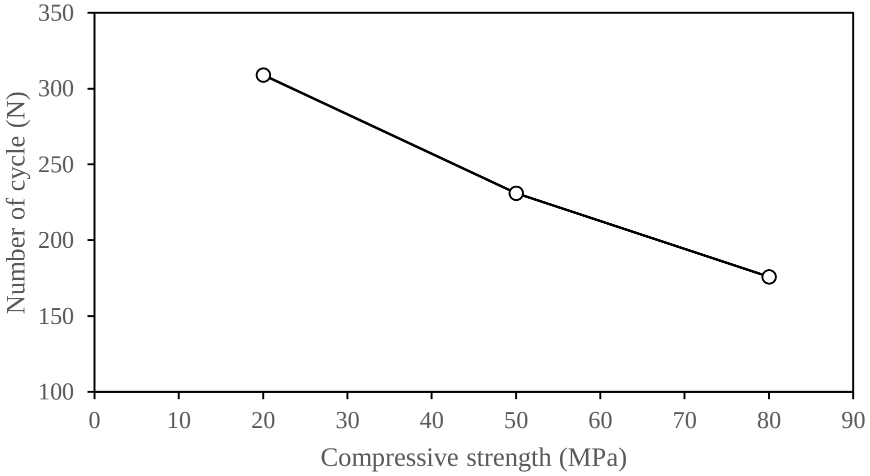

Figure 6.26: Effect of compressive strength on fatigue life

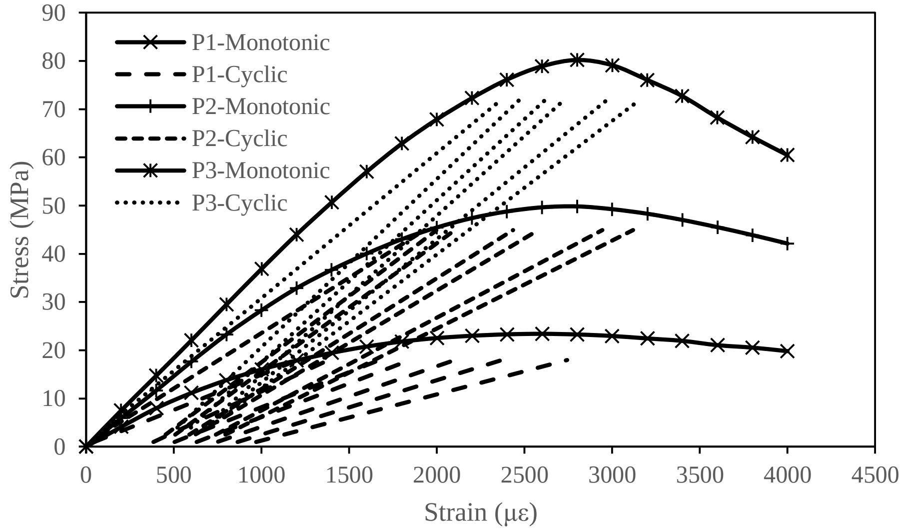

Figure 6.27: Effect of compressive strength on fatigue stress-strain curve

6.4.2.2. Effect of Lower Stress Level

The numerical model was used to evaluate the fatigue life of concrete at the lower stress level (S_{min}) of 5%, 10% and 20%. The upper stress level (S_{max}) was kept constant at 90%. Figure 6.28 depicts the number of cycles to failure for P3, P4 and P5 specimens. Based on the numerical analysis, raising the lower stress level from 5% to 10% increased the fatigue life of concrete from 176 cycles to 306 cycles. A further increase in the lower stress level to 20% significantly increased the fatigue life to 1042 cycles. This was attributed to the reduced dynamic impact when the lower stress level was greater. As the stress range between S_{max} and S_{min} decreased, the concrete experienced less deformation in one loading cycle and hence less damage. Humme et al. (2016) demonstrated that raising the lower stress level from 20% to 30% prolonged the fatigue life of concrete by 4 times. A further increase in the lower stress level to 40% resulted in an intact specimen at 1,000,000 loading cycles. The S-N curve also moved upwards when the lower stress level increased. Figure 6.29 compares the fatigue stress-strain curves of P4 and P5 specimens. It was shown that the P5 specimen had a greater fatigue strain at failure than the P4 specimen. Due to the greater value of lower stress level, P5 experienced a lower stiffness degradation per loading cycle and was capable of withstanding more loading cycles that caused greater deformation. Nevertheless, both P4 and P5 experienced a similar stiffness degradation near the point of failure.

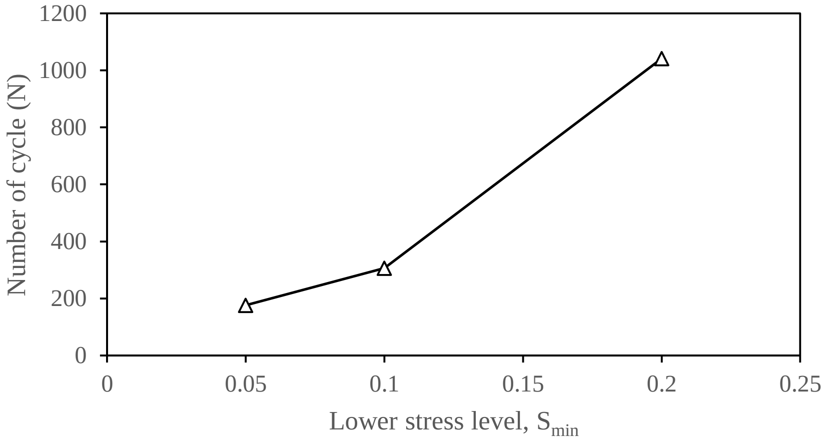

Figure 6.28: Effect of lower stress level on fatigue life

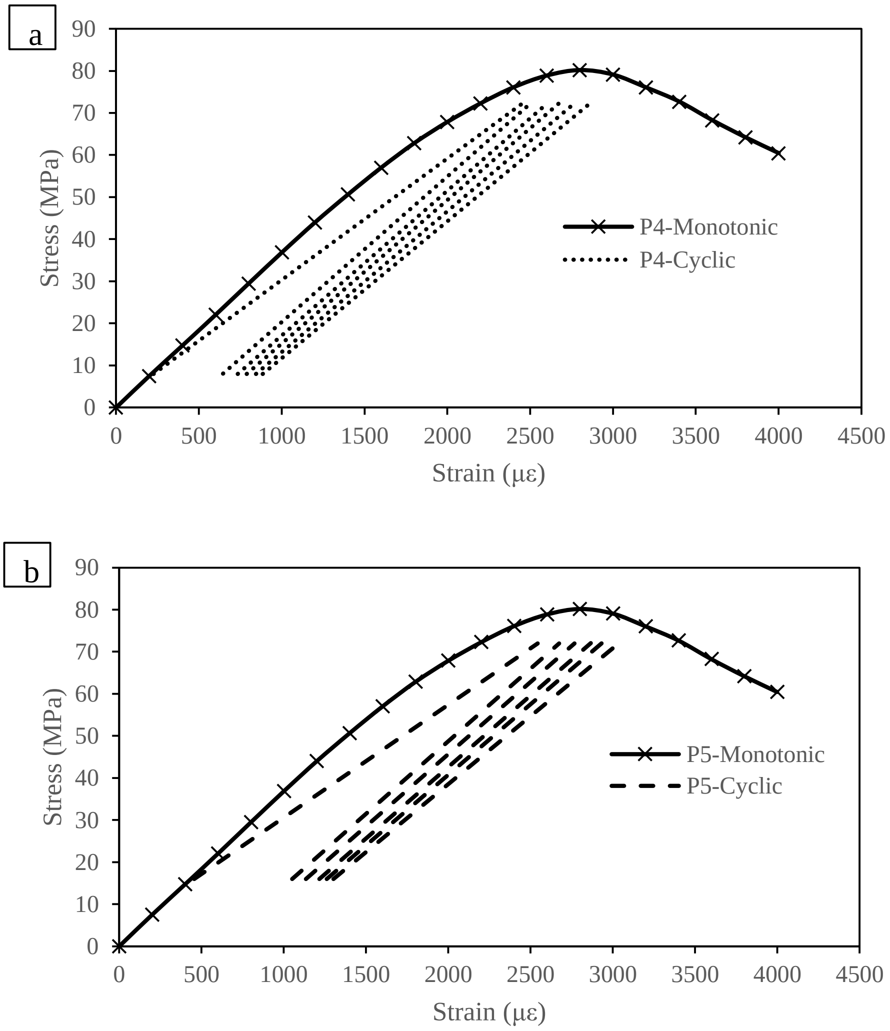

Figure 6.29: Fatigue stress-strain curve of (a) P4 and (b) P5 specimens

6.4.2.3. Effect of Specimen Size

The effect of specimen size on the fatigue life of concrete is also investigated using the numerical model. Figure 6.30 presents the fatigue life of 50 mm, 100 mm and 150 mm cube specimens. The fatigue life of 50 mm cube was 176 cycles, 100 mm cube was 189 cycles and 150 mm cube was 203 cycles. The fatigue life slightly increased as the specimen size increased. This was due to the influence of higher number of elements in the numerical analysis. For a similar mesh size, the larger specimen had a higher number of elements meshed, resulting in a slight over-estimation of stiffness. However, according to Fladr and Bily (2018), a larger specimen contained more defects such as cracks and pores, increasing the probability of failure and hence having a lower fatigue life. This effect was not considered in the numerical model due to the difficulty in quantifying the defects in concrete, which varied between specimens. Nonetheless, the results showed that the largest difference in fatigue life of the specimens studied was 27 cycles, which was minimal. Genikomsou and Polak (2015) showed that the same mesh size could be used to model concrete specimens of varying size and dimension.

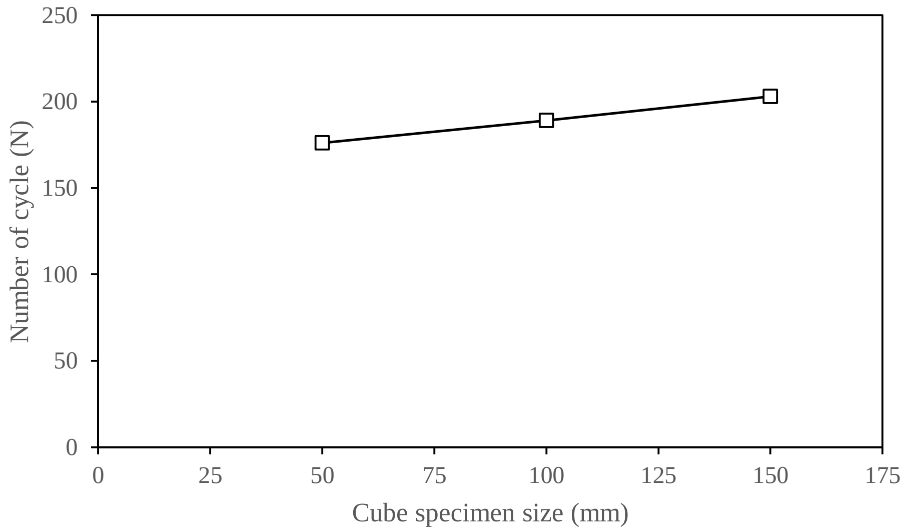

Figure 6.30: Effect of specimen size on fatigue life

6.4.3. Fatigue Life Prediction of Concrete Exposed to Long-term Sulphate Attack and WDA

The aim of this section is to use the developed numerical model to predict the fatigue life of concrete after long-term deterioration caused by sulphate attack and WDA. In this study, three types of concrete were used, SiMn (Plain), SiMn (FA+SF) and LS (Plain). SiMn (Plain) denoted normal SiMn slag concrete composed of SiMn slag as coarse aggregate, marine sand as fine aggregate and seawater. SiMn (FA+SF) was SiMn slag concrete that had been optimized with FA and SF as partial replacement for cement. LS (Plain) denoted limestone concrete incorporated with limestone as coarse aggregate, marine sand as fine aggregate and seawater.

For comparison purposes, all types of concrete were given a compressive strength of 60 MPa. The concrete was assumed to be exposed to a wetting-drying environment with a sulphate concentration of 4.5% for 20, 35 and 50 years. According to ACI 215R-74 (1997), the fatigue strength of concrete after ten million loading cycles was 55% of its initial compressive strength. This study therefore assessed the fatigue life of SiMn (Plain), SiMn (FA+SF) and LS (Plain) after 20, 35 and 50 years of deterioration, with a loading of 55% of original compressive strength as the upper stress level in cyclic loading. In this case, the loading was 33 MPa. The detail of the concrete is summarized in Table 6.12. The material constitutive model outlined in Sections 6.2.1 to 6.2.6 was used to determine the degraded concrete properties for the respective exposure periods. The fatigue life of concrete was evaluated using the developed ABAQUS numerical model.

Figure 6.31 presents the fatigue life of SiMn (Plain), SiMn (FA+SF) and LS (Plain) in relation to the exposure time. After 20 years of deterioration, which was also equivalent to 7305 WDA cycles, the fatigue life decreased significantly from ten million cycles to 831 cycles for SiMn (Plain), 2549 cycles for SiMn (FA+SF) and 9798 cycles for LS(Plain). This was because the compressive strength significantly decreased to 63% of original strength for SiMn (Plain), 66% for SiMn (FA+SF) and 69% for LS (Plain). This resulted in a high upper stress level that decreased the fatigue life substantially. After being subjected to degradation for 35 years (12784 WDA cycles) and 50 years (18263 WDA cycles), the fatigue life of SiMn (Plain) was reduced to 160 cycles and 59 cycles, respectively. At 35 years and 50 years, SiMn (FA+SF) had a fatigue life of 1556 cycles and 334 cycles, respectively, and LS (Plain) had a fatigue life of 6101 cycles and 4362 cycles, respectively. The limestone concrete had a higher fatigue life due to its higher resistance to the deterioration caused by sulphate attack and WDA. Besides, the results showed that the use of FA and SF in concrete significantly prolonged the fatigue life. For example, the fatigue life of SiMn (Plain) at 20 years was equivalent to that of SiMn (FA+SF) at 45 years. Based on these findings, it can be concluded that the concrete optimized with FA and SF as partial replacement for cement has a longer service life in hostile marine environment.

Table 6.12: Concrete exposed to long-term sulphate attack and WDA

Concrete type	SiMn (Plain), SiMn (FA+SF), LS (Plain)
Compressive strength	60 MPa
Sulphate concentration	4.5%
WDA exposure duration	20, 35, 50 years
Fatigue strength for 10,000,000 loading cycles defined by ACI 215R-74 (1997)	55% of original compressive strength (equivalent to 33 MPa, which was used as upper stress level in cyclic loading)

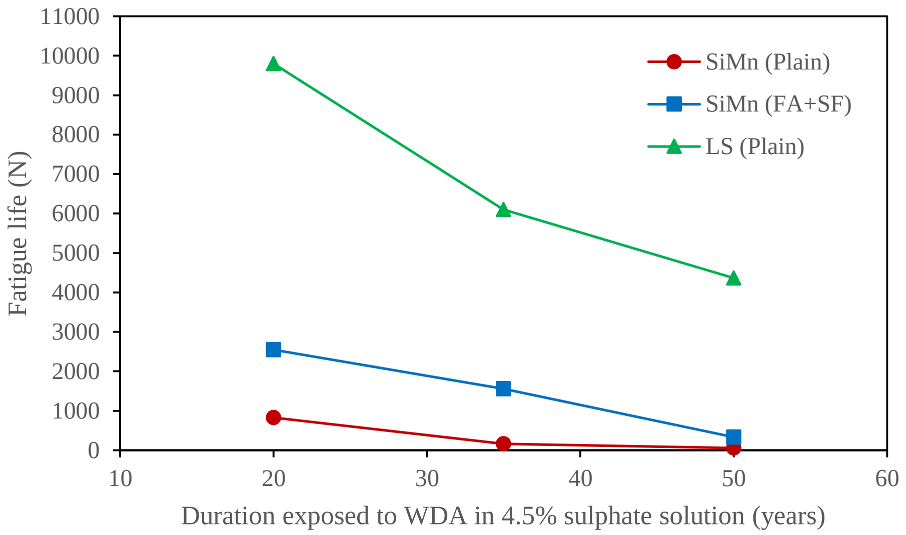

Figure 6.31: Fatigue life of concrete after deterioration

6.5. Concluding Remark

This chapter presents the numerical modelling and analysis of concrete subjected to cyclic loading using ABAQUS. The Concrete Damaged Plasticity (CDP) was used to model the concrete property. The material properties of concrete deteriorated by sulphate attack and wetting-drying action (WDA) were also considered in the constitutive model. The developed numerical model was first validated by the experimental results and then used to study the effect of compressive strength, lower stress level and specimen on concrete fatigue life. The fatigue life of concrete exposed to long-term sulphate attack and WDA was also predicted using the model. Based on the numerical analysis, the following conclusions are drawn.

1. The stress-strain curve determined from numerical model for concrete specimen under static loading matched reasonably well with that determined experimentally. The peak stress and strain of T2 specimen were 2.1% and 4.6% higher, respectively, when compared to the experimental results.
2. The validation study showed that the numerical model predicted fairly well the fatigue life of concrete. The numerical S-N curves for SiMn slag concrete and limestone concrete were quite similar to the experimental curves.

3. By comparing the fatigue stress-strain curves, the strain determined by the model was 9.1%–14.8% and 10.5%–30.1% lower than the experimental values for limestone concrete and SiMn slag concrete respectively.
4. The residual displacement determined from the model was lower than the displacement found in the experiment, with a difference of 18.1%–41.9%.
5. The parametric study showed that the fatigue life of concrete decreased by 25% and 43%, respectively, as the concrete strength increased from 20 MPa to 50 MPa and 20 MPa to 80 MPa.
6. Raising the lower stress level from 5% to 10% and 5% to 20% of compressive strength significantly increased the fatigue life of concrete from 176 cycles to 306 cycles and 1042 cycles respectively.
7. The size of specimen had negligible effect on the fatigue life of concrete.
8. After 20, 35 and 50 years of degradation by sulphate attack and WDA, the fatigue life of concrete using a loading of 55% design compressive strength as upper stress level was reduced to 831 cycles, 160 cycles and 59 cycles respectively for normal SiMn slag concrete. The SiMn slag concrete optimized with FA and SF as partial replacement to cement had a significantly higher fatigue life of 2549 cycles, 1556 cycles and 334 cycles at these exposure times respectively.

Chapter 7. Conclusion and Recommendation

7.1. Introduction

Concrete production using locally available materials such as marine sand and seawater will lower manufacturing costs in coastal areas as it reduces the need to import and transport material from inland. Construction cost can be further reduced with the incorporation of industrial wastes such as silicomanganese (SiMn) slag, fly ash (FA) and silica fume (SF) in concrete. The use of such wastes better promotes sustainability because it is an effective waste management and can conserve conventional resources. Concrete structures in marine region are often degraded by the hostile environment. The deterioration mechanisms, such as sulphate attack, wetting-drying action (WDA) and cyclic loading, have jeopardized the long-term durability of concrete.

Against this backdrop, this study investigates, the effect of alternative materials on the strength and durability of concrete. In objective one, experiments have been carried out to study the use of SiMn slag as coarse aggregate, marine sand as fine aggregate and seawater in concrete. In objective two, FA and SF were substituted as binary and ternary blended cements to enhance SiMn slag concrete. The effects of FA and SF on concrete strength, durability and workability were assessed through experiment. The results were statistically evaluated and optimized using the Response Surface Method (RSM). In objective three, the effect of sulphate attack and WDA on concrete degradation was investigated. Experiment was conducted to assess the durability and cyclic behavior of concrete exposed to sulphate attack and WDA. To resolve time and cost constraints of experiment, a numerical model was developed in objective four to predict the fatigue life of concrete.

Accordingly, this chapter concludes the outcomes of this research project based on the findings in the respective objectives. A discussion on the extension of current research to future work is also given in this chapter.

7.2. Conclusion

7.2.1. Effect of Marine Sand, Seawater and Silicomanganese Slag on Strength and Durability

Objective one: To investigate the effect of the use of marine sand, seawater and SiMn slag on the strength and durability of concrete.

This study has developed six types of concrete mixture to examine the effect of incorporation of silicomanganese (SiMn) slag as coarse aggregate, marine sand as fine aggregate and seawater as mixing water on the concrete strength and durability. The experimental results show that a sustainable concrete with comparable strength and durability to conventional concrete can be produced by incorporating the SiMn slag, marine sand and seawater. The concrete can also be used for various application such as marine structures, residential houses and industrial buildings. The following are the conclusions for objective one:

1. In terms of workability, the use of SiMn slag as coarse aggregate reduced the concrete slump by 36% due to poor aggregate size grading, when compared to normal limestone concrete. The use of marine sand and seawater have reduced concrete slump by 26% and 32% respectively.
2. The compressive and tensile strengths of SiMn slag concrete have reduced by as much as 9.2% and 17.5% respectively due to flaky characteristic of the aggregate. The concrete incorporated with marine sand and seawater achieved a higher strength at early age, but a lower late-age strength when compared to the control concrete.
3. SiMn slag concrete had lower water absorption of 4.1%, 3.9% and 3.8%, at 28, 90 and 180 days respectively, compared to control concrete with water absorption of 5.3%, 4.8% and 4.6%. At the corresponding ages, the water absorption of concrete reduced to 3.9%, 3.7% and 3.5% with the incorporation of marine sand and seawater.
4. The sorptivity and chloride permeability of SiMn slag concrete were higher at 28 days, but comparable to control concrete at 90 and 180 days. The results showed that marine sand reduced the sorptivity and chloride permeability of concrete and was able to offset the drawback caused by the use of SiMn slag in terms of durability.

5. The sulphate resistance of concrete in terms of compressive strength loss was marginal at an early age, ranging from 0.28% to 3.53% during the 7-day and 28-day test periods. The strength loss was higher after 90 days of the sulphate immersion testing, with the maximum loss value of 9.9%.
6. SiMn slag concrete had a similar interfacial transition zone (ITZ) to the control concrete. In both types of concrete, the cement paste was properly bonded with coarse aggregate. The concrete containing marine sand possessed a more compact ITZ with less voids present in cement paste.

7.2.2. Effect of Fly Ash and Silica Fume on Workability, Strength and Workability

Objective two: To optimize FA and SF as ternary binder with cement in concrete containing marine sand, seawater and SiMn slag, based on workability, strength and durability.

The experiment was designed using Central Composite Design (CCD) method to determine the effect of FA and SF on strength and durability of concrete containing marine sand, seawater and SiMn slag. The interaction of FA and SF on strength, durability and workability of the concrete was statistically evaluated using analysis of variance (ANOVA). The optimization of FA and SF was performed using Response Surface Method (RSM). Based on the outcomes of the experiment and also the optimization, the following conclusions are drawn.

1. The incorporation of 0–15% SF increased compressive and tensile strengths at all ages, but further SF addition reduced the strength. The incorporation of 0–40% FA increased the strength at 28 and 90 days, but decreased the 7-day strength due to slow pozzolanic reaction. In ternary blended concrete, SF compensated for the reduced 7-day strength caused by FA and their combined effect further increased strength at 28 and 90 days.
2. The use of 0–15% SF decreased concrete sorptivity, but further addition of SF increased the sorptivity. Concrete containing 0–40% FA exhibited lower sorptivity than the control. The combined use of FA and SF in ternary blended concrete reduced the sorptivity further. FA20SF15 concrete, which was made up of 20%

FA and 15% SF, had the lowest sorptivity, with a reduction of 38.1%, 20.9% and 20.3% at 28, 90 and 180 days respectively, compared to the control concrete.

3. In binary and ternary blended concrete, the chloride permeability decreased with an increase in FA and SF contents. FA40SF30 concrete, which contained 40% FA and 30% SF, had the lowest chloride permeability at 28, 90 and 180 days, with reductions of 70.1%, 63.9% and 62.5% respectively.
4. Using the RSM, prediction models for compressive and splitting tensile strengths at 7, 28 and 90 days were presented as quadratic models. Cubic models were developed for sorptivity at 28, 90 and 180 days, chloride permeability at 180 days, and concrete slump. Quartic models were developed for chloride permeability at 28 and 90 days.
5. The prediction models were evaluated as statistically significant based on the two-way ANOVA, with significance level below 0.05. The residual errors from lack of fit and pure errors were minimal. The adjusted and predicted R^2 showed that the prediction models were adequate to describe the relationship between variables and responses and were fit for optimization.
6. Optimization and experimental validation showed that the combination of 16.3% FA and 11.5% SF had the highest strength and lowest permeability. For example, the 90-day compressive strength, 90-day tensile strength, 180-day sorptivity, 180-day chloride permeability improved by 10.4%, 18.9%, 24.9% and 44.6% respectively when compared to the control. These properties were 4.2%, 1.6%, 27.3% and 24% respectively better than the normal concrete made up of limestone aggregate.
7. Microstructural analysis using scanning electron microscope (SEM) showed that the optimized concrete had a more compact ITZ and stronger bonding of cement paste with aggregate compared to the control concrete.
8. Linear equations between SiMn slag and limestone were established for the compressive strength and sorptivity. The equations used in conjunction with the RSM models predicted the compressive strength and sorptivity of limestone concrete with good accuracy. The prediction error was 0.8%–5.4% for compressive strength and 5.3%–11.4% for sorptivity.

7.2.3. Durability and Cyclic Behavior of Concrte

Objective three: To assess the durability and compressive cyclic behavior of the optimized concrete subjected to sulphate attack and WDA.

The experiment was conducted to simulate the wetting-drying environment by using different concentrations (5%, 12.5% and 20%) of Na_2SO_4 solution for 150 days. The durability of normal concrete and concrete optimized with FA and SF was assessed. In the study, comparison has been made between the performance of SiMn slag and limestone concrete. Also, the cyclic loading test was conducted to investigate the compressive fatigue behavior of concrete before and after the deterioration. Based on the experimental results, the following conclusions are made.

1. After 150 days of exposure, the concrete specimen surface was covered with white powdery efflorescence. The surface was also damaged with cracking and peeling of mortar layer near the specimen edge. The WDA, as well as the use of higher sulphate concentrations, caused more severe damage.
2. At a penetration depth of 0–5 mm, the sulphate (SO_4^{2-}) ion content ranged from 0.6% to 2.58%, depending on concrete type and exposure condition. The SO_4^{2-} ion content decreased to a range of 0.07% and 0.4% at the depth range of 15–20 mm. Sulphate penetration was greater in concrete exposed to WDA than the concrete exposed to full immersion.
3. Concrete experienced a mass gain of 0.04%–0.55% during the period 0–90 days and a mass loss of 0.07%–0.49% during the period 90–150 days. Nevertheless, the concrete incorporated with FA and SF gained mass throughout the exposure period due to its higher strength and lower permeability.
4. Concrete expanded over time due to the gradual formation of ettringite and gypsum within concrete pores. The maximum expansion of all concrete types ranged between 0.45% and 1.23%.
5. The compressive and splitting tensile strengths of all types of concrete decreased over exposure duration, with a maximum reduction of 13%–37%. The reduction in compressive strength was approximately 12% higher than the reduction in splitting tensile strength.
6. Morphology of ettringite and crack was observed on the microstructure of concrete exposed to sulphate attack and WDA.

7. Based on the cyclic loading test, the S-N curve of SiMn slag concrete was slightly lower than that of limestone concrete, indicating that SiMn slag concrete had a lower fatigue life.
8. The residual strain of SiMn slag concrete was higher than that of limestone concrete due to the lower abrasion resistance of SiMn slag aggregate.
9. The degradation of elastic modulus of SiMn slag concrete under cyclic loading was greater than that of limestone concrete.
10. After 10,000 cycles of loading, the intact specimens exhibited a residual displacement of 15.1–46.3 μm. The elastic modulus improved by 1.037–1.055 times. The compressive strength increased by 1.01–1.05 times.
11. The sulphate attack and WDA, combined with cyclic loading, softened the concrete, causing an increase in residual displacement and a decrease in modulus of elasticity.

7.2.4. Concrete Behavior under Cyclic Loading and Wetting-Drying Action

Objective four: To develop a numerical model to predict the fatigue life of concrete subjected to sulphate attack and WDA.

The numerical model for cyclic loading of concrete was developed using ABAQUS. The constitutive relationship on the degradation of concrete properties induced by sulphate attack and WDA was developed and used in conjunction with Concrete Damaged Plasticity (CDP) model in the numerical analysis. The model was then validated by comparing numerical and experimental results. By using the validated model, parametric study on the effect of compressive strength, lower stress level and specimen size on the fatigue life was performed. The model is used to predict the fatigue life of concrete exposed to long-term sulphate attack and WDA. Based on the numerical analysis, the conclusions of this study are presented below.

1. The numerical model simulated the stress-strain behavior of concrete under monotonic loading fairly accurately. The peak stress and strain were 2.1% and 4.6% higher, respectively, when compared to the experimental results.
2. In cyclic loading, the numerical model predicted the fatigue life of concrete reasonably well. The maximum difference between numerical and experimental

results was 30 cycles, 285 cycles and 95 cycles for the loading at upper stress levels of 90%, 85% and 80% respectively. The S-N curves obtained from numerical analysis were close to the experimental curves for both SiMn slag and limestone concrete.

3. By comparing the fatigue stress-strain curves, the strain determined by the model was 9.1%–14.8% and 10.5%–30.1% less than the experimental values for limestone concrete and SiMn slag concrete respectively. For the intact specimens, the residual displacement from the model was 18.1%–22.6% less than the displacement determined through experiment.
4. According to the parametric study, at a constant upper stress level of 90%, raising the compressive strength from 20 MPa to 50 MPa and from 20 MPa to 80 MPa decreased the fatigue life of concrete by 25% and 43%, respectively.
5. The use of greater value of lower stress level substantially increased the fatigue life of concrete. The fatigue life increased from 176 cycles to 306 cycles and 1042 cycles, when the lower stress level was increased from 5% to 10% and 5% to 20% of compressive strength, respectively.
6. The size of specimen had negligible effect on the fatigue life of concrete.
7. The long-term exposure to sulphate attack and WDA significantly reduced the fatigue life of concrete. For SiMn slag concrete, the fatigue life of concrete loaded at 55% of design compressive strength was reduced to 831 cycles, 160 cycles and 59 cycles after 20, 35 and 50 years, respectively. The SiMn slag concrete optimized with FA and SF as partial replacements had a higher fatigue life of 2549 cycles, 1556 cycles and 334 cycles, respectively, at these exposure times.

7.3. Recommendation for Future Research

This project has provided a better insight into the concrete incorporated with marine sand, seawater, SiMn slag, FA and SF. The study sheds more light on the concrete deterioration mechanism caused by sulphate attack coupled with WDA. The impact of the deterioration on the behavior of concrete under cyclic loading was investigated. Based on the outcomes of this research, the following recommendations are proposed for further study.

1. In the investigation of the effect of using the above mentioned materials, it is recommended that the performance of concrete related to the practical application is to be studied. The investigation can include the concrete properties such as fracture toughness and long-term shrinkage.
2. The effect of FA and SF as binary and ternary binder was investigated in this research. The study can be extended to determine the synergetic effect of FA and SF with other types of supplementary cementitious materials such as blast furnace slag, palm oil fuel ash (POFA) and metakaolin.
3. This study demonstrated that the RSM prediction model developed based on SiMn slag concrete can be used to predict properties of limestone concrete through the additional established relationship. In this connection, it is recommended to develop a holistic guideline so that the existing RSM model can be applied to other types of concrete mixture.
4. This study focused on producing concrete with optimum strength and durability mainly for marine application. Hence, the ratio of FA and SF was selected to maximize these two parameters. For practical use, other aspects such as cost, environmental factor and logistic consideration have to be taken into account and can be recommended in future study.
5. In this study, a constant stress level was used in the cyclic loading test to consider wave action in the worst-case scenario. Future study can be extended to investigate the effect of variable stress amplitude for cyclic loading since it better reflects the actual loading.

References

Abaqus. 2012. Abaqus Analysis User's Manual (V6.14 ed.).

ACI Committee 211. 1998. *Guide for Selecting Proportions for High-Strength Concrete with Portland Cement and Fly Ash* (ACI 211.4R-93). Farmington Hills, MI: American Concrete Institute.

ACI Committee 215. 1997. *Considerations for Design of Concrete Structures Subjected to Fatigue Loading* (ACI 215R-74). Farmington Hills, MI: American Concrete Institute.

ACI Committee 304. 2007. *Placing concrete by pumping methods* (ACI 304.2R-96). Farmington Hills, MI: American Concrete Institute.

ACI Committee 318. 2008. *Building code requirements for structural concrete* (ACI 318M-08). Farmington Hills, MI: American Concrete Institute.

ACI Committee 357. 1997. *Guide for the Design and Construction of Fixed Offshore Concrete Structure* (ACI 357R-84). Farmington Hills, MI: American Concrete Institute.

ACI Committee 365. 2017. *Rerport on Service-Life Prediction* (ACI 365.1R-17). Farmington Hills, MI: American Concrete Institute.

Ahmad, O. A. 2017. Production of High-Performance Silica Fume Concrete. *American journal of applied sciences, 14*(11), 1031.1038.

Ahmad, S. 2007. Optimum concrete mixture design using locally available ingredients. *Arabian Journal for Science and Engineering, 32*(1), 27-34.

Alaka, H. A., & Oyedele, L. O. 2016. High volume fly ash concrete: The practical impact of using superabundant dose of high range water reducer. *Journal of Building Engineering, 8,* 81-90.

Aldahdooh, M., Bunnori, N. M., & Johari, M. M. 2013. Evaluation of ultra-high-performance-fiber reinforced concrete binder content using the response surface method. *Materials & Design (1980-2015), 52,* 957-965.

Alexander, M., & Nganga, G. 2016. Introduction: Importance of marine concrete structures and durability design. *Marine Concrete Structures,* 1-13.

Alhozaimy, A., Hussain, R. R., Al-Zaid, R., & Al-Negheimish, A. 2012. Coupled effect of ambient high relative humidity and varying temperature marine environment on corrosion of reinforced concrete. *Construction and Building Materials, 28*(1), 670-679.

Ali, B., Qureshi, L. A., Shah, S. H. A., Rehman, S. U., Hussain, I., & Iqbal, M. 2020. A step towards durable, ductile and sustainable concrete: Simultaneous incorporation of recycled aggregates, glass fiber and fly ash. *Construction and Building Materials, 251,* 118980.

Allahverdi, A., & Ahmadnezhad, S. 2014. Mechanical activation of silicomanganese slag and its influence on the properties of Portland slag cement. *Powder technology, 251,* 41-51.

Alsayed, S. H., & Amjad, M. A. 1996. Strength, water absorption and porosity of concrete incorporating natural and crushed aggregate. *Journal of King Saud University-Engineering Sciences, 8*(1), 109-119.

Andrews-Phaedonos, F. 1996. *Establishing the durability performance of structural concrete*. Vic Roads.

Anudeep, R., Ramesh, K. V., & SowjanyaVani, V. 2015. Study on Mechanical Properties of Concrete With Various Slags as Replacement to Fine Aggregate. *Masterbuilder, 7*, 86.

Apostolopoulos, C. A., Koulouris, K. F., & Apostolopoulos, A. C. 2019. Correlation of Surface Cracks of Concrete due to Corrosion and Bond Strength (between Steel Bar and Concrete). *Advances in Civil Engineering, 2019*, 343-354.

Architectural Institute of Japan. 2015. *Japanese Architectureal Standard Specification for Reinforced Concrete Work* (JASS 5).

Arns, A., Dangendorf, S., Jensen, J., Talke, S., Bender, J., & Pattiaratchi, C. 2017. Sea-level rise induced amplification of coastal protection design heights. *Scientific reports*, *7*, 40171.

Arsham, H. (2011). Deterministic modeling: linear optimization with applications. *University of Baltimore*. Retrieved from http://home.ubalt.edu/ntsbarsh/opre640a/partIII.htm

ASTM C29, *Standard test method for bulk density and voids in aggregate*. 2017. West Conshohocken, PA: American Society for Testing and Materials.

ASTM C33, *Standard specification for concrete aggregates*. 2012. West Conshohocken, PA: American Society for Testing and Materials.

ASTM C39, *Standard test method for compressive strength of cylinderical concrete specimens*. 2012. West Conshohocken, PA: American Society for Testing and Materials.

ASTM C114, *Standard test methods for chemical analysis of hydraulic cement*. 2018. West Conshohocken, PA: American Society for Testing and Materials.

ASTM C143, *Standard test method for slump of hydraulic-cement concrete*. 2015. West Conshohocken, PA: American Society for Testing and Materials.

ASTM C150, *Standard specification of Portland cement*. 2012. West Conshohocken, PA: American Society for Testing and Materials.

ASTM C192, *Standard practice for making and curing concrete test specimens in the laboratory*. 2012. West Conshohocken, PA: American Society for Testing and Materials.

ASTM C494, *Standard specification for chemical admixtures for concrete*. 2019. West Conshohocken, PA: American Society for Testing and Materials.

ASTM C496, *Standard test method for splitting tensile strength of cylindrical concrete specimens*. 2012. West Conshohocken, PA: American Society for Testing and Materials.

ASTM C618, *Standard specification for coal fly ash and raw or calcined natural pozzolan for use in concrete*. 2019. West Conshohocken, PA: American Society for Testing and Materials.

ASTM C642, *Standard test method for density, absorption and voids in hardened concrete*. 2012. West Conshohocken, PA: American Society for Testing and Materials.

ASTM C1012, *Standard test method for length change of hydraulic-cement mortars exposed to a sulfate solution*. 2018. West Conshohocken, PA: American Society for Testing and Materials.

ASTM C1202, *Standard test method for elecrical indication of concrete's ability to resist chloride ion penetration*. 2012. West Conshohocken, PA: American Society for Testing and Materials.

ASTM C1585, *Standard test method for measurement of rate of absorption of water by hydraulic-cement concrete*. 2012. West Conshohocken, PA: American Society for Testing and Materials.

Backus, J., McPolin, D., Basheer, M., Long, A., & Holmes, N. 2013. Exposure of mortars to cyclic chloride ingress and carbonation. *Advances in Cement Research, 25*(1), 3-11.

Bagheri, A., Zanganeh, H., Alizadeh, H., Shakerinia, M., & Marian, M. A. S. 2013. Comparing the performance of fine fly ash and silica fume in enhancing the properties of concretes containing fly ash. *Construction and Building Materials, 47*, 1402-1408.

Balonis, M., Lothenbach, B., Le Saout, G., & Glasser, F. P. 2010. Impact of chloride on the mineralogy of hydrated Portland cement systems. *Cement and Concrete Research, 40*(7), 1009-1022.

Bayramov, F., Taşdemir, C., & Taşdemir, M. 2004. Optimisation of steel fibre reinforced concretes by means of statistical response surface method. *Cement and Concrete Composites, 26*(6), 665-675.

Belviso, C., Cavalcante, F., & Fiore, S. 2010. Synthesis of zeolite from Italian coal fly ash: differences in crystallization temperature using seawater instead of distilled water. *Waste Management, 30*(5), 839-847.

Bhanja, S., & Sengupta, B. 2005. Influence of silica fume on the tensile strength of concrete. *Cement and Concrete Research, 35*(4), 743-747.

Blankendaal, T., Schuur, P., & Voordijk, H. 2014. Reducing the environmental impact of concrete and asphalt: a scenario approach. *Journal of cleaner production, 66*, 27-36.

Bortoluzzi, E. A., Broon, N. J., Bramante, C. M., Felippe, W. T., Tanomaru Filho, M., & Esberard, R. M. 2009. The influence of calcium chloride on the setting time, solubility, disintegration, and pH of mineral trioxide aggregate and white Portland cement with a radiopacifier. *Journal of endodontics, 35*(4), 550-554.

Boulekbache, B., Hamrat, M., Chemrouk, M., & Amziane, S. 2016. Flexural behaviour of steel fibre-reinforced concrete under cyclic loading. *Construction and Building Materials, 126*, 253-262.

British Standard Institution. 2000. *Concrete specification, performance, production and conformity* (BS EN 206-1). Retrieved from BSI Publication.

British Standards Instituition. 2013. *Aggregates for Concrete* (BS EN 12620). Retrieved from BSI Publication.

British Standards Institution. 2009. *Testing fresh concrete - Part 2: Slump test* (BS EN 12350-2). Retrieved from BSI Publication.

British Standards Institution. 2013. *Maritime works - Part 1-4: General - Code of practice for materials* (BS 6349-1-4). Retrieved from BSI Publication.

British Standards Institution. 2015. *Concrete. Complementary British Standard to BS EN 206. Specification for constituent materials and concrete* (BS 8500-2). Retrieved from BSI Publication.

Cachim, P. B., Figueiras, J. A., & Pereira, P. A. 2002. Fatigue behavior of fiber-reinforced concrete in compression. *Cement and Concrete Composites, 24*(2), 211-217.

Cai, H., & Liu, X. 1998. Freeze-thaw durability of concrete: ice formation process in pores. *Cement and Concrete Research, 28*(9), 1281-1287.

Cai, X., He, Z., Tang, S., & Chen, X. 2016. Abrasion erosion characteristics of concrete made with moderate heat Portland cement, fly ash and silica fume using sandblasting test. *Construction and Building Materials, 127*, 804-814.

Cai, X., Zhang, Y., Gao, L., Wang, J., & Peng, H. 2019. Deterioration of cement asphalt pastes with polymer latexes and expansive agent under sulfate attack and wetting-drying cycles. *Engineering Failure Analysis*, 104252.

Chand, V. S., Rao, B. K., & Rao, C. H. 2020. Investigation on chloride penetration in concrete mixes of different cement replacement percentages with fly ash and silica fume. *Materials Today: Proceedings, 33,* 820-827.

Chang, C. F., & Chen, J. W. 2006. The experimental investigation of concrete carbonation depth. *Cement and Concrete Research, 36*(9), 1760-1767.

Chang, H. 2017. Chloride binding capacity of pastes influenced by carbonation under three conditions. *Cement and Concrete Composites, 84*, 1-9.

Chang, H., Mu, S., & Feng, P. 2018. Influence of carbonation on "maximum phenomenon" in surface layer of specimens subjected to cyclic drying-wetting condition. *Cement and Concrete Research, 103*, 95-109.

Cheah, C. B., Tiong, L. L., Ng, E. P., & Oo, C. W. 2019. The engineering performance of concrete containing high volume of ground granulated blast furnace slag and pulverized fly ash with polycarboxylate-based superplasticizer. *Construction and Building Materials, 202,* 909-921.

Chen, F., Gao, J., Qi, B., Shen, D., & Li, L. 2017. Degradation progress of concrete subject to combined sulfate-chloride attack under drying-wetting cycles and flexural loading. *Construction and Building Materials, 151*, 164-171.

Chen, X., Wang, G., Dong, Q., Zhao, X., & Wang, Y. 2020. Microscopic characterizations of pervious concrete using recycled Steel Slag Aggregate. *Journal of cleaner production, 254*, 120149.

Chen, Y., Gao, J., Tang, L., & Li, X. 2016. Resistance of concrete against combined attack of chloride and sulfate under drying–wetting cycles. *Construction and Building Materials, 106*, 650-658.

Cheng, S., Shui, Z., Gao, X., Lu, J., Sun, T., & Yu, R. 2020a. Degradation progress of Portland cement mortar under the coupled effects of multiple corrosive ions and drying-wetting cycles. *Cement and Concrete Composites*, 103629.

Cheng, S., Shui, Z., Gao, X., Yu, R., Sun, T., Guo, C., & Huang, Y. 2020b. Degradation mechanisms of Portland cement mortar under seawater attack and drying-wetting cycles. *Construction and Building Materials, 230*, 116934.

Cheng, S., Shui, Z., Sun, T., Yu, R., & Zhang, G. 2018. Durability and microstructure of coral sand concrete incorporating supplementary cementitious materials. *Construction and Building Materials, 171*, 44-53.

Chidiac, S., & Mahmoodzadeh, F. 2009. Plastic viscosity of fresh concrete–A critical review of predictions methods. *Cement and Concrete Composites, 31*(8), 535-544.

Chilana, L., Bhatt, A. H., Najafi, M., & Sattler, M. 2016. Comparison of carbon footprints of steel versus concrete pipelines for water transmission. *Journal of the Air & Waste Management Association, 66*(5), 518-527.

China Architecture & Building Press. 2010. *Technical Code for Application of Sea Sand Concrete* (JGJ206-2010).

Choi, H. B., & Kim, J. M. 2020. Properties of silicon manganese slag as an aggregate for concrete depending on cooling conditions. *Journal of Material Cycles and Waste Management, 22*(4), 1-14.

Choi, S. J., Mun, J. S., Yang, K. H., & Kim, S. J. 2016. Compressive fatigue performance of fiber-reinforced lightweight concrete with high-volume supplementary cementitious materials. *Cement and Concrete Composites, 73*, 89-97.

Choudhary, R., Gupta, R., Nagar, R., & Jain, A. 2020. Sorptivity characteristics of high strength self-consolidating concrete produced by marble waste powder, fly ash, and micro silica. *Materials Today: Proceedings, 32*, 531-535.

Chrisp, T., McCarter, W., Starrs, G., Basheer, P., & Blewett, J. 2002. Depth-related variation in conductivity to study cover-zone concrete during wetting and drying. *Cement and Concrete Composites, 24*(5), 415-426.

Coelho, A. M. G., Mottram, J. T., & Harries, K. A. 2015. Finite element guidelines for simulation of fibre-tension dominated failures in composite materials validated by case studies. *Composite Structures, 126*, 299-313.

Dandapat, R., & Deb, A. 2016. A probability based model for the erosive wear of concrete by sediment bearing water. *Wear, 350*, 166-181.

Dave, N., Misra, A. K., Srivastava, A., Sharma, A. K., & Kaushik, S. K. 2017. Study on quaternary concrete micro-structure, strength, durability considering the influence of multi-factors. *Construction and Building Materials*, *139*, 447-457.

Dave, N., Misra, A. K., Srivastava, A., Sharma, A. K., & Kaushik, S. K. 2018. Green quaternary concrete composites: Characterization and evaluation of the mechanical properties. *Structural Concrete, 19*(5), 1280-1289.

Del Viso, J., Carmona, J., & Ruiz, G. 2008. Shape and size effects on the compressive strength of high-strength concrete. *Cement and Concrete Research, 38*(3), 386-395.

DeRousseau, M., Kasprzyk, J., & Srubar III, W. 2018. Computational design optimization of concrete mixtures: A review. *Cement and Concrete Research, 109*, 42-53.

Design-Expert. 2018. Software for design of experiments. Minneapolis, USA: Stat-Ease Corporation.

Dias, W., Seneviratne, G., & Nanayakkara, S. 2008. Offshore sand for reinforced concrete. *Construction and Building Materials, 22*(7), 1377-1384.

Ding, W., & Olsen, S. E. 2000. Manganese and silicon distribution between slag and metal in silicomanganese production. *ISIJ international, 40*(9), 850-856.

Do, Q. M., Bui, T. H., & Thang, N. H. 2019. Effects of seawater content in alkaline activators to engineering properties of fly ash-based geopolymer concrete. *In Solid State Phenomena, 296*, 105-111.

Dong, Q., Wang, G., Chen, X., Tan, J., & Gu, X. 2020. Recycling of Steel Slag Aggregate in Portland Cement Concrete: An overview. *Journal of cleaner production, 282*, 124447.

Dong, Z., Wu, G., & Xu, Y. 2016. Experimental study on the bond durability between steel-FRP composite bars (SFCBs) and sea sand concrete in ocean environment. *Construction and Building Materials, 115*, 277-284.

Effler, S. W., Schimel, K., & Millero, F. J. 1986. Salinity, chloride, and density relationships in ion enriched Onondaga Lake, NY. *Water, Air, and Soil Pollution, 27*(1-2), 169-180.

Elwell, D., & Fu, G. 1995. Compression Testing of Concrete: Cylinders vs Cube. *New York State Department of Transportation, 22*, 1-28.

Erdal, H. I. 2013. Two-level and hybrid ensembles of decision trees for high performance concrete compressive strength prediction. *Engineering Applications of Artificial Intelligence, 26*(7), 1689-1697.

Erdem, T. K., & Kirca, O. 2008. Use of binary and ternary blends in high strength concrete. *Construction and Building Materials, 22*(7), 1477-1483.

Farahani, A., Taghaddos, H., & Shekarchi, M. 2015. Prediction of long-term chloride diffusion in silica fume concrete in a marine environment. *Cement and Concrete Composites, 59*, 10-17.

Fischer, G., & Li, V. C. 2002. Effect of matrix ductility on deformation behavior of steel-reinforced ECC flexural members under reversed cyclic loading conditions. *Structural Journal, 99*(6), 781-790.

Fladr, J., & Bily, P. 2018. Specimen size effect on compressive and flexural strength of high-strength fibre-reinforced concrete containing coarse aggregate. *Composites Part B: Engineering, 138*, 77-86.

Frias, M., de Rojas, M. I. S., & Rodríguez, C. 2009. The influence of SiMn slag on chemical resistance of blended cement pastes. *Construction and Building Materials, 23*(3), 1472-1475.

Frias, M., de Rojas, M. I. S., Santamaria, J., & Rodriguez, C. 2006. Recycling of silicomanganese slag as pozzolanic material in Portland cements: basic and engineering properties. *Cement and Concrete Research, 36*(3), 487-491.

Fu, C., Ye, H., Jin, X., Yan, D., Jin, N., & Peng, Z. 2016. Chloride penetration into concrete damaged by uniaxial tensile fatigue loading. *Construction and Building Materials, 125*, 714-723.

Gao, J., Yu, Z., Song, L., Wang, T., & Wei, S. 2013. Durability of concrete exposed to sulfate attack under flexural loading and drying–wetting cycles. *Construction and Building Materials, 39*, 33-38.

Garzon-Roca, J., Sena-Cruz, J. M., Fernandes, P., & Xavier, J. 2015. Effect of wet-dry cycles on the bond behaviour of concrete elements strengthened with NSM CFRP laminate strips. *Composite Structures, 132*, 331-340.

Genikomsou, A. S., & Polak, M. A. 2015. Finite element analysis of punching shear of concrete slabs using damaged plasticity model in ABAQUS. *Engineering Structures, 98*, 38-48.

Gentilini, C., Franzoni, E., Bandini, S., & Nobile, L. 2012. Effect of salt crystallisation on the shear behaviour of masonry walls: an experimental study. *Construction and Building Materials, 37*, 181-189.

Gesoglu, M., Guneyisi, E., & Ozbay, E. 2009. Properties of self-compacting concretes made with binary, ternary, and quaternary cementitious blends of fly ash, blast furnace slag, and silica fume. *Construction and Building Materials, 23*(5), 1847-1854.

Ghorab, H. Y., Hilal, M., & Antar, A. 1990. Effect of mixing and curing waters on the behaviour of cement pastes and concrete Part 2: Properties of cement paste and concrete. *Cement and Concrete Research, 20*(1), 69-72.

Giaccio, G., & Zerbino, R. 1998. Failure mechanism of concrete: combined effects of coarse aggregates and strength level. *Advanced Cement Based Materials, 7*(2), 41-48.

Giza, J. F., & Burke, D. F. 2013. Practical Implementation of Marine Concrete Specifications for Waterfront Structures *Ports 2013: Success through Diversification* (pp. 1127-1136).

Gokceoglu, C., Ulusay, R., & Sönmez, H. 2000. Factors affecting the durability of selected weak and clay-bearing rocks from Turkey, with particular emphasis on the influence of the number of drying and wetting cycles. *Engineering Geology, 57*(3-4), 215-237.

Golewski, G. L. 2018. Effect of curing time on the fracture toughness of fly ash concrete composites. *Composite Structures, 185*, 105-112.

Gonen, T., & Yazicioglu, S. 2007. The influence of mineral admixtures on the short and long-term performance of concrete. *Building and Environment, 42*(8), 3080-3085.

Guan, K. K. 2011. Surface and ambient air temperatures associated with different ground material: a case study at the University of California, Berkeley. *Environmental Science, 196*, 1-14.

Guneyisi, E., Gesoglu, M., Algın, Z., & Mermerdas, K. 2014. Optimization of concrete mixture with hybrid blends of metakaolin and fly ash using response surface method. *Composites Part B: Engineering, 60*, 707-715.

Gylltoft, K. 1984. A fracture mechanics model for fatigue in concrete. *Materiaux et construction, 17*(1), 55-58.

Hamze, Y. 2014. Concrete durability in harsh environmental conditions exposed to freeze thaw cycles. *Physics Procedia, 55*, 265-270.

Hasdemir, S., Tugrul, A., & Yılmaz, M. 2016. The effect of natural sand composition on concrete strength. *Construction and Building Materials, 112*, 940-948.

Haynes, H., O'Neill, R., Neff, M., & Kumar Mehta, P. 2010. Salt weathering of concrete by sodium carbonate and sodium chloride. *ACI Materials Journal, 107*(3), 258.

Haynes, H., O'Neill, R., Neff, M., & Mehta, P. K. 2008. Salt weathering distress on concrete exposed to sodium sulfate environment. *ACI Materials Journal, 105*(1), 35.

He, X., Zhou, J., Wang, Z., & Zhang, L. 2020. Study on mechanics and water transport characteristics of sea-sand concrete based on the volume analysis of each solid composition. *Construction and Building Materials, 257*, 119591.

Hemalatha, T., & Ramaswamy, A. 2017. A review on fly ash characteristics–Towards promoting high volume utilization in developing sustainable concrete. *Journal of cleaner production, 147*, 546-559.

Horszczaruk, E. 2005. Abrasion resistance of high-strength concrete in hydraulic structures. *Wear, 259*(1-6), 62-69.

Hoy, M., Rachan, R., Horpibulsuk, S., Arulrajah, A., & Mirzababaei, M. 2017. Effect of wetting–drying cycles on compressive strength and microstructure of recycled asphalt pavement–Fly ash geopolymer. *Construction and Building Materials, 144*, 624-634.

Hsu, T. T. 1984. Fatigue and microcracking of concrete. *Materiaux et construction, 17*(1), 51-54.

Huiguang, Y., Yan, L., Henglin, L., & Quan, G. 2011. Durability of sea-sand containing concrete: Effects of chloride ion penetration. *Mining Science and Technology (China), 21*(1), 123-127.

Humme, J., von der Haar, C., Lohaus, L., & Marx, S. 2016. Fatigue behaviour of a normal-strength concrete–number of cycles to failure and strain development. *Structural Concrete, 17*(4), 637-645.

Hussain, M. A. B., Abdullah, A. B., & Abdullah, R. B. 2018. Physical and Chemical Properties of Perak River Sand for Greensand Casting Molds. *Engineering Applications for New Materials and Technologies, 85*, 13-24.

Ibrion, M., Paltrinieri, N., & Nejad, A. R. 2020. Learning from failures: Accidents of marine structures on Norwegian continental shelf over 40 years time period. *Engineering Failure Analysis, 111*, 104487.

Indian Standards Bureau. 2008. *Specification for moulds for use in tests of cement and concrete* (IS: 10086-2008). Bahaduri Shah Zafar Marg, New Delhi: Bureau of Indian Standards.

IRC44. 2017. *Guidelines for cement concrete mix design for pavement*. Delhi: Indian Road Congress.

Islam, M. M., Islam, M. S., Al-Amin, M., & Islam, M. M. 2012. Suitability of sea water on curing and compressive strength of structural concrete. *J. Civil Eng, 40*, 37-45.

Itskos, G., Itskos, S., & Koukouzas, N. 2010. Size fraction characterization of highly-calcareous fly ash. *Fuel Processing Technology, 91*(11), 1558-1563.

Jerman, M., Scheinherrova, L., Medved, I., Krejsova, J., Dolezelova, M., Bezdicka, P., & Cerny, R. 2019. Effect of cyclic wetting and drying on microstructure, composition and length changes of lime-based plasters. *Cement and Concrete Composites, 104*, 103411.

Jiang, C., Gu, X., Huang, Q., & Zhang, W. 2017a. Deformation of concrete under high-cycle fatigue loads in uniaxial and eccentric compression. *Construction and Building Materials, 141*, 379-392.

Jiang, L., & Niu, D. 2016. Study of deterioration of concrete exposed to different types of sulfate solutions under drying-wetting cycles. *Construction and Building Materials, 117*, 88-98.

Jiang, L., Niu, D., Yuan, L., & Fei, Q. 2015. Durability of concrete under sulfate attack exposed to freeze–thaw cycles. *Cold Regions Science and Technology, 112*, 112-117.

Jiang, P., Jiang, L., Zha, J., & Song, Z. 2017b. Influence of temperature history on chloride diffusion in high volume fly ash concrete. *Construction and Building Materials, 144*, 677-685.

Karthikeyan, M., & Nagarajan, V. 2016. Feasibility study on utilization of marine sand in concrete for sustainable development. *Indian journal of Geo marine sciences, 45*(2), 313-318.

Katano, K., Takeda, N., Ishizeki, Y., & Iriya, K. 2013. Properties and application of concrete made with sea water and un-washed sea sand. *Proceedings of Third International conference on Sustainable Construction Materials and Technologies*, 1-10.

Kazjonovs, J., Bajare, D., & Korjakins, A. 2010. Designing of high density concrete by using steel treatment waste. *The 10th International Conference Modern building materials, structures and techniques*, 138-142.

Khan, M., & Ali, M. 2019. Improvement in concrete behavior with fly ash, silica-fume and coconut fibres. *Construction and Building Materials, 203*, 174-187.

Khan, M. U., Ahmad, S., & Al-Gahtani, H. J. 2017. Chloride-induced corrosion of steel in concrete: an overview on chloride diffusion and prediction of corrosion initiation time. *International Journal of Corrosion, 2017*, 581-590.

Kilic, A., Atis, C., Teymen, A., Karahan, O., Ozcan, F., Bilim, C., & Ozdemir, M. 2008. The influence of aggregate type on the strength and abrasion resistance of high strength concrete. *Cement and Concrete Composites, 30*(4), 290-296.

Kim, B. S., Jeong, S. B., Jeong, M. H., & Ryu, J. W. 2011. Upgrading of manganese from waste silicomanganese slag by a mechanical separation process. *Materials Transactions, 52*(8), 1705-1708.

Kim, J. K., & Kim, Y. Y. 1996. Experimental study of the fatigue behavior of high strength concrete. *Cement and Concrete Research, 26*(10), 1513-1523.

Kim, Y. Y., Lee, K. M., Bang, J. W., & Kwon, S. J. 2014. Effect of W/C ratio on durability and porosity in cement mortar with constant cement amount. *Advances in Materials Science and Engineering, 2014*, 1-12.

Kishar, E. A., Ahmed, D. A., Mohammed, M. R., & Noury, R. 2013. Effect of calcium chloride on the hydration characteristics of ground clay bricks cement pastes. *Beni-suef university journal of basic and applied sciences, 2*(1), 20-30.

Kockal, N. U., & Ozturan, T. 2011. Optimization of properties of fly ash aggregates for high-strength lightweight concrete production. *Materials & Design*, *32*(6), 3586-3593.

Kondraivendhan, B., & Bhattacharjee, B. 2015. Flow behavior and strength for fly ash blended cement paste and mortar. *International Journal of Sustainable Built Environment*, *4*(2), 270-277.

Kryzanowski, A., Mikos, M., Sustersic, J., & Planinc, I. 2009. Abrasion resistance of concrete in hydraulic structures. *ACI Materials Journal*, *106*(4), 349-356.

Kuhn, M., & Johnson, K. 2013. *Applied predictive modeling* (Vol. 26). New York: Springer.

Kuosa, H., Ferreira, R., Holt, E., Leivo, M., & Vesikari, E. 2014. Effect of coupled deterioration by freeze–thaw, carbonation and chlorides on concrete service life. *Cement and Concrete Composites, 47*, 32-40.

Kwan, A., & Chen, J. 2013. Adding fly ash microsphere to improve packing density, flowability and strength of cement paste. *Powder technology, 234*, 19-25.

Lantsoght, E. O., van der Veen, C., & de Boer, A. 2016. Proposal for the fatigue strength of concrete under cycles of compression. *Construction and Building Materials*, *107*, 138-156.

Lee, B. Y., & Kurtis, K. E. 2017. Effect of pore structure on salt crystallization damage of cement-based materials: Consideration of w/b and nanoparticle use. *Cement and Concrete Research, 98,* 61-70.

Lee, J., & Fenves, G. L. 1998. Plastic-damage model for cyclic loading of concrete structures. *Journal of engineering mechanics, 124*(8), 892-900.

Lee, M., & Barr, B. 2004. An overview of the fatigue behaviour of plain and fibre reinforced concrete. *Cement and Concrete Composites, 26*(4), 299-305.

Lehigh. (2011). Chloride and salinity. Retrieved from http://www.ei.lehigh.edu/envirosci/watershed/wq/wqbackground/chloridebg.html

Lenntech. (2018). Composition of Seawater in Various Locations. Retrieved from https://www.lenntech.com/composition-seawater.htm

Li, B., Mao, J., Nawa, T., & Liu, Z. 2016a. Mesoscopic chloride ion diffusion model of marine concrete subjected to freeze-thaw cycles. *Construction and Building Materials, 125*, 337-351.

Li, J., Xie, F., Zhao, G., & Li, L. 2020. Experimental and numerical investigation of cast-in-situ concrete under external sulfate attack and drying-wetting cycles. *Construction and Building Materials, 249*, 118789.

Li, L., Hou, B., Lu, Z., & Liu, F. 2018a. Fatigue behaviour of sea sand concrete beams reinforced with basalt fibre-reinforced polymer bars. *Construction and Building Materials, 179*, 160-171.

Li, Q., Geng, H., Huang, Y., & Shui, Z. 2015. Chloride resistance of concrete with metakaolin addition and seawater mixing: A comparative study. *Construction and Building Materials, 101*, 184-192.

Li, Y., Zhao, X., Singh, R. R., & Al-Saadi, S. 2016b. Tests on seawater and sea sand concrete-filled CFRP, BFRP and stainless steel tubular stub columns. *Thin-Walled Structures, 108,* 163-184.

Li, Y. L., Zhao, X. L., Raman, R. S., & Al-Saadi, S. 2018b. Thermal and mechanical properties of alkali-activated slag paste, mortar and concrete utilising seawater and sea sand. *Construction and Building Materials, 159,* 704-724.

Limeira, J., Agullo, L., & Etxeberria, M. 2010. Dredged marine sand in concrete: An experimental section of a harbor pavement. *Construction and Building Materials, 24*(6), 863-870.

Limeira, J., Agulló, L., & Etxeberria, M. 2012. Dredged marine sand as a new source for construction materials. *Materiales de Construcción, 62*(305), 7-24.

Limeira, J., Etxeberria, M., Agullo, L., & Molina, D. 2011. Mechanical and durability properties of concrete made with dredged marine sand. *Construction and Building Materials, 25*(11), 4165-4174.

Liu, F., You, Z., Yang, X., & Wang, H. 2018. Macro-micro degradation process of fly ash concrete under alternation of freeze-thaw cycles subjected to sulfate and carbonation. *Construction and Building Materials, 181*, 369-380.

Liu, J., Tang, K., Qiu, Q., Pan, D., Lei, Z., & Xing, F. 2014. Experimental investigation on pore structure characterization of concrete exposed to water and chlorides. *Materials, 7*(9), 6646-6659.

Liu, P., Chen, Y., Yu, Z., & Lu, Z. 2020a. Damage constitutive model and mechanical performance deterioration of concrete under sulfate environment. *Mathematical Problems in Engineering, 2020*, 1-16.

Liu, W., Cui, H., Dong, Z., Xing, F., Zhang, H., & Lo, T. Y. 2016. Carbonation of concrete made with dredged marine sand and its effect on chloride binding. *Construction and Building Materials, 120*, 1-9.

Liu, Y., Shi, C., Zhang, Z., Li, N., & Shi, D. 2020b. Mechanical and fracture properties of ultra-high performance geopolymer concrete: Effects of steel fiber and silica fume. *Cement and Concrete Composites, 112*, 103665.

Liu, Y. W., Yen, T., & Hsu, T. H. 2006. Abrasion erosion of concrete by water-borne sand. *Cement and Concrete Research, 36*(10), 1814-1820.

Lotfy, A., Hossain, K. M., & Lachemi, M. 2014. Application of statistical models in proportioning lightweight self-consolidating concrete with expanded clay aggregates. *Construction and Building Materials, 65*, 450-469.

Lubliner, J., Oliver, J., Oller, S., & Oñate, E. 1989. A plastic-damage model for concrete. *International Journal of Solids and Structures, 25*(3), 299-326.

Luping, T., & Gulikers, J. 2007. On the mathematics of time-dependent apparent chloride diffusion coefficient in concrete. *Cement and Concrete Research, 37*(4), 589-595.

Lv, W., Sun, Z., & Su, Z. 2020. Study of seawater mixed one-part alkali activated GGBFS-fly ash. *Cement and Concrete Composites, 106*, 103484.

Maes, M., & De Belie, N. 2014. Resistance of concrete and mortar against combined attack of chloride and sodium sulphate. *Cement and Concrete Composites, 53*, 59-72.

Malheiro, R. L. M. C., Camoes, A., Ferreira, R. M., Meira, G., & Amorim, M. 2014. Effect of carbonation on the chloride diffusion of mortar specimens exposed to cyclic wetting and drying. *XIII DBMC, International Conference on Durability of Building Materials and Components*, 482-489.

Marion, G., Millero, F. J., Camoes, M., Spitzer, P., Feistel, R., & Chen, C.-T. 2011. pH of seawater. *Marine Chemistry, 126*(1-4), 89-96.

Masateru, N., Masahiro, K., Takao, T., Kenji, N., & Yoshitaka, I. 2007. Pozzolanic Reactions between natural and Artificial Aggregate and the Concrete matrix. *2007 World of Coal Ash (WOCA)*, 7-10.

Mazloom, M., Ramezanianpour, A., & Brooks, J. 2004. Effect of silica fume on mechanical properties of high-strength concrete. *Cement and Concrete Composites, 26*(4), 347-357.

Medeiros, A., Zhang, X., Ruiz, G., Rena, C. Y., & Velasco, M. d. S. L. 2015. Effect of the loading frequency on the compressive fatigue behavior of plain and fiber reinforced concrete. *International Journal of Fatigue, 70,* 342-350.

Medeiros, M., Gobbi, A., Reus, G., & Helene, P. 2013. Reinforced concrete in marine environment: Effect of wetting and drying cycles, height and positioning in relation to the sea shore. *Construction and Building Materials, 44,* 452-457.

Medeiros, M. H., & Helene, P. 2009. Surface treatment of reinforced concrete in marine environment: Influence on chloride diffusion coefficient and capillary water absorption. *Construction and Building Materials, 23*(3), 1476-1484.

Mehta, P. K., & Monteiro, P. J. 2006. *Concrete microstructure, properties and materials*. New York: The McGraw-Hill Companies Inc.

Meira, G., Andrade, C., Padaratz, I., Alonso, C., & Borba Jr, J. 2007. Chloride penetration into concrete structures in the marine atmosphere zone–Relationship between deposition of chlorides on the wet candle and chlorides accumulated into concrete. *Cement and Concrete Composites, 29*(9), 667-676.

Miao, C., Mu, R., Tian, Q., & Sun, W. 2002. Effect of sulfate solution on the frost resistance of concrete with and without steel fiber reinforcement. *Cement and Concrete Research, 32*(1), 31-34.

Mohammadhosseini, H., Yatim, J. M., Sam, A. R. M., & Awal, A. A. 2017. Durability performance of green concrete composites containing waste carpet fibers and palm oil fuel ash. *Journal of cleaner production, 144,* 448-458.

Mohammed, T. U., Hamada, H., & Yamaji, T. 2004. Performance of seawater-mixed concrete in the tidal environment. *Cement and Concrete Research, 34*(4), 593-601.

Montanari, L., Suraneni, P., Tsui-Chang, M., Khatibmasjedi, M., Ebead, U., Weiss, J., & Nanni, A. 2019. Hydration, pore solution, and porosity of cementitious pastes made with seawater. *Journal of Materials in Civil engineering, 31*(8), 04019154.

Monteiro, P. J., Miller, S. A., & Horvath, A. 2017. Towards sustainable concrete. *Nature materials, 16*(7), 698-699.

Mosley, W. H., Hulse, R., & Bungey, J. H. 2012. *Reinforced concrete design: to Eurocode 2*. Brussels: Macmillan International Higher Education.

Mullauer, W., Beddoe, R. E., & Heinz, D. 2013. Sulfate attack expansion mechanisms. *Cement and Concrete Research, 52,* 208-215.

Mustapha, F., Sulaiman, A., Mohamed, R., & Umara, S. 2021. The effect of fly ash and silica fume on self-compacting high-performance concrete. *Materials Today: Proceedings, 39,* 965-969.

Muthukumar, M., Mohan, D., & Rajendran, M. 2003. Optimization of mix proportions of mineral aggregates using Box Behnken design of experiments. *Cement and Concrete Composites, 25*(7), 751-758.

Myers, R. H., Montgomery, D. C., & Anderson-Cook, C. M. 2016. *Response surface methodology: process and product optimization using designed experiments*. New Jersey: John Wiley & Sons.

Nadelman, E., & Kurtis, K. 2019. Durability of Portland-limestone cement-based materials to physical salt attack. *Cement and Concrete Research, 125,* 105859.

Nasir, M., Johari, M. A. M., Yusuf, M. O., Maslehuddin, M., Al-Harthi, M. A., & Dafalla, H. 2019. Impact of slag content and curing methods on the strength of alkaline-activated silico-manganese fume/blast furnace slag mortars. *Arabian Journal for Science and Engineering, 44*(10), 8325-8335.

Nath, S., & Kumar, S. 2016. Evaluation of the suitability of ground granulated silico-manganese slag in Portland slag cement. *Construction and Building Materials, 125*, 127-134.

Nath, S., & Kumar, S. 2017. Reaction kinetics, microstructure and strength behavior of alkali activated silico-manganese (SiMn) slag–Fly ash blends. *Construction and Building Materials, 147*, 371-379.

Nath, S., & Kumar, S. 2019. Influence of granulated silico-manganese slag on compressive strength and microstructure of ambient cured alkali-activated fly ash binder. *Waste and Biomass Valorization, 10*(7), 2045-2055.

Navarro, R., Zornoza, E., Garces, P., Sanchez, I., & Alcocel, E. 2017. Optimization of the alkali activation conditions of ground granulated SiMn slag. *Construction and Building Materials, 150*, 781-791.

Nayal, R., & Rasheed, H. A. 2006. Tension stiffening model for concrete beams reinforced with steel and FRP bars. *Journal of Materials in Civil engineering, 18*(6), 831-841.

Nehdi, M., & Summer, J. 2002. Optimization of ternary cementitious mortar blends using factorial experimental plans. *Materials and structures, 35*(8), 495-503.

Neithalath, N., & Jain, J. 2010. Relating rapid chloride transport parameters of concretes to microstructural features extracted from electrical impedance. *Cement and Concrete Research, 40*(7), 1041-1051.

Neville, A. M. 1966. A general relation for strengths of concrete specimens of different shapes and sizes. *Journal Proceedings, 63*(10), 1095-1110.

Neville, A. M. 1995. *Properties of concrete* (Vol. 4). London: Longman.

Nili, M., & Afroughsabet, V. 2010. Combined effect of silica fume and steel fibers on the impact resistance and mechanical properties of concrete. *International journal of impact engineering, 37*(8), 879-886.

Nishida, T., Otsuki, N., Ohara, H., Garba-Say, Z. M., & Nagata, T. 2013. Some considerations for applicability of seawater as mixing water in concrete. *Journal of Materials in Civil engineering, 27*(7), B4014004.

Niu, D. t., Ma, R., Wang, J. b., & Xu, S. h. 2015. Experiment study on the failure mechanism of dry-mix shotcrete under the combined actions of sulfate attack and drying–wetting cycles. *Construction and Building Materials, 81*, 74-80.

NOAA. (2018). How much water is in the ocean. Retrieved from https://oceanservice.noaa.gov/facts/oceanwater.html

NOAA. (2019). Tides and water level. Retrieved from https://oceanservice.noaa.gov/education/tutorial_tides/tides07_cycles.html

Nochaiya, T., Wongkeo, W., & Chaipanich, A. 2010. Utilization of fly ash with silica fume and properties of Portland cement–fly ash–silica fume concrete. *Fuel, 89*(3), 768-774.

Noordin, M. Y., Venkatesh, V., Sharif, S., Elting, S., & Abdullah, A. 2004. Application of response surface methodology in describing the performance of coated carbide tools when turning AISI 1045 steel. *Journal of Materials Processing Technology, 145*(1), 46-58.

Noushini, A., Samali, B., & Vessalas, K. 2013. Effect of polyvinyl alcohol (PVA) fibre on dynamic and material properties of fibre reinforced concrete. *Construction and Building Materials, 49*, 374-383.

Ogirigbo, O. R., & Ukpata, J. 2017. Effect of chlorides and curing duration on the hydration and strength development of plain and slag blended cements. *Journal of Civil Engineering Research, 7*(1), 9-16.

Oh, B. H., & Jang, S. Y. 2007. Effects of material and environmental parameters on chloride penetration profiles in concrete structures. *Cement and Concrete Research*, *37*(1), 47-53.

Oliveira, R. W. H., Fernandes, G., Sousa, F. C., & Barreto, R. A. 2017. Chemical and mineralogical characterization of silicon manganese iron slag as railway ballast. *REM-International Engineering Journal*, *70*(4), 385-391.

Olsen, S., & Tangstad, M. 2004. Silicomanganese production - Process understanding. *Proceedings: Tenth International Ferroalloys Congress*, pp. 231-238.

Oner, A., Akyuz, S., & Yildiz, R. 2005. An experimental study on strength development of concrete containing fly ash and optimum usage of fly ash in concrete. *Cement and Concrete Research, 35*(6), 1165-1171.

Otsuki, N., Saito, T., & Tadokoro, Y. 2011. Possibility of sea water as mixing water in concrete. *36th Conference on Our World in Concrete & Structures, Singapore, 36*, 131-138.

Padavala, A. B., Potharaju, M., & Kode, V. R. 2021. Mechanical properties of ternary blended mix concrete of fly ash and silica fume. *Materials Today: Proceedings, 43*, 2198-2202.

Papadakis, V., Pedersen, E., & Lindgreen, H. 1999. An AFM-SEM investigation of the effect of silica fume and fly ash on cement paste microstructure. *Journal of Materials Science, 34*(4), 683-690.

Papadakis, V. G. 1999. Effect of fly ash on Portland cement systems: Part I. Low-calcium fly ash. *Cement and Concrete Research, 29*(11), 1727-1736.

Paul, S. C., van Zijl, G. P., Babafemi, A. J., & Tan, M. J. 2016. Chloride ingress in cracked and uncracked SHCC under cyclic wetting-drying exposure. *Construction and Building Materials, 114*, 232-240.

Ponikiewski, T., & Gołaszewski, J. 2014. The influence of high-calcium fly ash on the properties of fresh and hardened self-compacting concrete and high performance self-compacting concrete. *Journal of cleaner production, 72*, 212-221.

Pratolongo, P., Leonardi, N., Kirby, J. R., & Plater, A. 2019. Temperate coastal wetlands: morphology, sediment processes, and plant communities *Coastal Wetlands* (pp. 105-152). New York: Elsevier.

Qi, B., Gao, J., Chen, F., & Shen, D. 2017. Evaluation of the damage process of recycled aggregate concrete under sulfate attack and wetting-drying cycles. *Construction and Building Materials, 138*, 254-262.

Qi, B., Gao, J., Chen, F., & Shen, D. 2018. Chloride penetration into recycled aggregate concrete subjected to wetting–drying cycles and flexural loading. *Construction and Building Materials, 174*, 130-137.

Radlinski, M., & Olek, J. 2012. Investigation into the synergistic effects in ternary cementitious systems containing portland cement, fly ash and silica fume. *Cement and Concrete Composites, 34*(4), 451-459.

Rao, S., Reddy, B., & Muttharam, M. 2001. The impact of cyclic wetting and drying on the swelling behaviour of stabilized expansive soils. *Engineering Geology, 60*(1-4), 223-233.

Ratnayake, N., Puswewala, U., Chaminda, S., Ekanayaka, E., & Jayawardene, M. 2014. Evaluation of the potential of sea sand as an alternative to river sand for concrete production in Sri Lanka. *Journal of Geological Society of Sri Lanka, 16*, 109-117.

Rezaifar, O., Hasanzadeh, M., & Gholhaki, M. 2016. Concrete made with hybrid blends of crumb rubber and metakaolin: optimization using response surface method. *Construction and Building Materials, 123,* 59-68.

Rezazadeh, M., & Carvelli, V. 2018. A damage model for high-cycle fatigue behavior of bond between FRP bar and concrete. *International Journal of Fatigue, 111,* 101-111.

Rodriguez, C. N., & Doehne, E. 1999. Salt weathering: influence of evaporation rate, supersaturation and crystallization pattern. *Earth Surface Processes and Landforms: The Journal of the British Geomorphological Research Group, 24*(3), 191-209.

Rosenqvist, M., Pham, L. W., Terzic, A., Fridh, K., & Hassanzadeh, M. 2017. Effects of interactions between leaching, frost action and abrasion on the surface deterioration of concrete. *Construction and Building Materials, 149,* 849-860.

Roshavelov, T. 2005. Prediction of fresh concrete flow behavior based on analytical model for mixture proportioning. *Cement and Concrete Research, 35*(5), 831-835.

Rostami, M., & Behfarnia, K. 2017. The effect of silica fume on durability of alkali activated slag concrete. *Construction and Building Materials, 134,* 262-268.

Roziere, E., Loukili, A., El Hachem, R., & Grondin, F. 2009. Durability of concrete exposed to leaching and external sulphate attacks. *Cement and Concrete Research, 39*(12), 1188-1198.

Ryu, D. W., Ko, J. W., & Noguchi, T. 2011. Effects of simulated environmental conditions on the internal relative humidity and relative moisture content distribution of exposed concrete. *Cement and Concrete Composites, 33*(1), 142-153.

Safi, B., Saidi, M., Daoui, A., Bellal, A., Mechekak, A., & Toumi, K. 2015. The use of seashells as a fine aggregate (by sand substitution) in self-compacting mortar (SCM). *Construction and Building Materials, 78,* 430-438.

Sahmaran, M., Erdem, T., & Yaman, I. 2007. Sulfate resistance of plain and blended cements exposed to wetting–drying and heating–cooling environments. *Construction and Building Materials, 21*(8), 1771-1778.

Saillio, M., Baroghel-Bouny, V., & Barberon, F. 2014. Chloride binding in sound and carbonated cementitious materials with various types of binder. *Construction and Building Materials, 68,* 82-91.

Samimi, K., Kamali-Bernard, S., & Maghsoudi, A. A. 2018. Durability of self-compacting concrete containing pumice and zeolite against acid attack, carbonation and marine environment. *Construction and Building Materials, 165,* 247-263.

Sankar, L. P., Sivasankar, S., Shunmugasundaram, M., & Kumar, A. P. 2020. Investigation on binder and concrete with fine grinded fly ash and silica fume as pozzolanic combined replacement. *Materials Today: Proceedings, 27,* 1157-1162.

Sargent, P. 2015. The development of alkali-activated mixtures for soil stabilisation *Handbook of alkali-activated cements, mortars and concretes* (pp. 555-604). New York: Elsevier.

Schafer, N., Gudzulic, V., Timothy, J. J., Breitenbucher, R., & Meschke, G. 2019. Fatigue behavior of HPC and FRC under cyclic tensile loading: Experiments and modeling. *Structural Concrete, 20*(4), 1265-1278.

Shareef, U., Cheela, V. S., & Raju, S. G. 2015. Study on Physical and Mechanical Properties of Quartzite and Silico-Manganese Slag as Alternative Material for

Coarse Aggregate. *International Journal for Scientific Research and Development, 3*, 72-74.

Shi, C., Hu, X., Wang, X., Wu, Z., & Schutter, G. d. 2016. Effects of chloride ion binding on microstructure of cement pastes. *Journal of Materials in Civil engineering, 29*(1), 04016183.

Shi, Z., Shui, Z., Li, Q., & Geng, H. 2015. Combined effect of metakaolin and sea water on performance and microstructures of concrete. *Construction and Building Materials, 74*, 57-64.

Siddique, R. 2004. Performance characteristics of high-volume Class F fly ash concrete. *Cement and Concrete Research, 34*(3), 487-493.

Siddique, R. 2011a. Properties of self-compacting concrete containing class F fly ash. *Materials & Design, 32*(3), 1501-1507.

Siddique, R. 2011b. Utilization of silica fume in concrete: Review of hardened properties. *Resources, Conservation and Recycling, 55*(11), 923-932.

Siddique, R., Aggarwal, P., & Aggarwal, Y. 2011. Prediction of compressive strength of self-compacting concrete containing bottom ash using artificial neural networks. *Advances in Engineering Software, 42*(10), 780-786.

Simcic, T., Pejovnik, S., De Schutter, G., & Bosiljkov, V. B. 2015. Chloride ion penetration into fly ash modified concrete during wetting–drying cycles. *Construction and Building Materials, 93*, 1216-1223.

Sonebi, M. 2004. Medium strength self-compacting concrete containing fly ash: Modelling using factorial experimental plans. *Cement and Concrete Research, 34*(7), 1199-1208.

Song, H. W., Lee, C. H., & Ann, K. Y. 2008. Factors influencing chloride transport in concrete structures exposed to marine environments. *Cement and Concrete Composites, 30*(2), 113-121.

Song, P., Wu, J., Hwang, S., & Sheu, B. 2005. Assessment of statistical variations in impact resistance of high-strength concrete and high-strength steel fiber-reinforced concrete. *Cement and Concrete Research, 35*(2), 393-399.

Standard Australia. 2018. *Concrete structures* (AS 3600). SAI Global Limited.

Standard, C. 2009. *Test Methods of Long-Term Performance and Durability of Ordinary Concrete* (GB/T 50082–2009). National Standard of The People's Republic of China.

Steiger, M., & Asmussen, S. 2008. Crystallization of sodium sulfate phases in porous materials: the phase diagram Na2SO4–H2O and the generation of stress. *Geochimica et Cosmochimica Acta, 72*(17), 4291-4306.

Sumer, M. 2012. Compressive strength and sulfate resistance properties of concretes containing Class F and Class C fly ashes. *Construction and Building Materials, 34*, 531-536.

Sun, W., Mu, R., Luo, X., & Miao, C. 2002. Effect of chloride salt, freeze–thaw cycling and externally applied load on the performance of the concrete. *Cement and Concrete Research, 32*(12), 1859-1864.

Suryavanshi, A., & Swamy, R. N. 1996. Stability of Friedel's salt in carbonated concrete structural elements. *Cement and Concrete Research, 26*(5), 729-741.

Tan, C. L., Wong, N. H., & Jusuf, S. K. 2014. Effects of vertical greenery on mean radiant temperature in the tropical urban environment. *Landscape and Urban Planning, 127*, 52-64.

Tang, J., Cheng, H., Zhang, Q., Chen, W., & Li, Q. 2018. Development of properties and microstructure of concrete with coral reef sand under sulphate attack and drying-wetting cycles. *Construction and Building Materials, 165*, 647-654.

Tang, W., Li, S., Lu, Y., & Li, Z. 2020. Combined effects of wetting–drying cycles and sustained load on the behaviour of FRP-strengthened RC beams. *Engineering Structures, 213,* 110570.

Tang, Z., Hu, Y., Tam, V. W., & Li, W. 2019. Uniaxial compressive behaviors of fly ash/slag-based geopolymeric concrete with recycled aggregates. *Cement and Concrete Composites, 104*, 103375.

Tanyildizi, H., & Coskun, A. 2008. Performance of lightweight concrete with silica fume after high temperature. *Construction and Building Materials, 22*(10), 2124-2129.

Thaulow, N., & Sahu, S. 2004. Mechanism of concrete deterioration due to salt crystallization. *Materials Characterization, 53*(2-4), 123-127.

Tjaronge, M. W., & Irfan, U. R. 2015. Porosity, pore size and compressive strength of self compacting concrete using sea water. *Procedia Engineering, 125*, 832-837.

Tjaronge, M. W., Irmawaty, R., Adisasmita, S. A., & Amiruddin, A. 2014. Compressive Strength and Hydration Process of Self Compacting Concrete (SCC) Mixed with Sea Water, Marine Sand and Portland Composite Cement. *Advanced Materials Research, 935*, 242-246.

Torres-Luque, M., Osma, J. F., Sanchez-Silva, M., Bastidas-Arteaga, E., & Schoefs, F. 2015. Electrical characterization of Calcium Aluminate (CA) in presence of chloride ions. *14th International Congress on the Chemistry of Cement, 14*, 1-8.

Trenhaile, A. S. 2011. Cliffs and rock coasts. *Treatise on Estuarine and Coastal Science, 3*, 171-191.

Tripathi, D., Kumar, R., Mehta, P., & Singh, A. 2020. Silica fume mixed concrete in acidic environment. *Materials Today: Proceedings, 27*, 1001-1005.

Val, D. V., & Stewart, M. G. 2003. Life-cycle cost analysis of reinforced concrete structures in marine environments. *Structural safety, 25*(4), 343-362.

Valipour, M., Shekarchi, M., & Arezoumandi, M. 2017. Chlorine diffusion resistivity of sustainable green concrete in harsh marine environments. *Journal of cleaner production, 142*, 4092-4100.

Wahalathantri, B., Thambiratnam, D., Chan, T., & Fawzia, S. 2011. A material model for flexural crack simulation in reinforced concrete elements using ABAQUS. *Proceedings of the first international conference on engineering, designing and developing the built environment for sustainable wellbeing*, 260-264.

Wang, H., & Song, Y. 2011. Fatigue capacity of plain concrete under fatigue loading with constant confined stress. *Materials and structures, 44*(1), 253-262.

Wang, Y., Li, J., Deng, J., & Li, S. 2018a. Bond behaviour of CFRP/steel strap joints exposed to overloading fatigue and wetting/drying cycles. *Engineering Structures, 172*, 1-12.

Wang, Y., Wu, L., Wang, Y., Liu, C., & Li, Q. 2018b. Effects of coarse aggregates on chloride diffusion coefficients of concrete and interfacial transition zone under experimental drying-wetting cycles. *Construction and Building Materials, 185*, 230-245.

Wang, Z., Zeng, Q., Wang, L., Yao, Y., & Li, K. 2014. Corrosion of rebar in concrete under cyclic freeze–thaw and Chloride salt action. *Construction and Building Materials, 53*, 40-47.

Wegian, F. M. 2010. Effect of seawater for mixing and curing on structural concrete. *The IES Journal Part A: Civil & Structural Engineering, 3*(4), 235-243.

Whitcomb, P. J., & Anderson, M. J. 2004. *RSM simplified: optimizing processes using response surface methods for design of experiments*. New York: CRC press.

Wong, J. (2018, June 25). Pertama eyes full capacity in October for smelting plant. *The Star Online*. Retrieved from https://www.thestar.com.my/business/business-news/2018/06/25/pertama-eyes-full-capacity-in-october-for-smelting-plant/

Wu, B., & Jin, H. 2019. Compressive fatigue behavior of compound concrete containing demolished concrete lumps. *Construction and Building Materials, 210*, 140-156.

Wu, J., Li, H., Wang, Z., & Liu, J. 2016. Transport model of chloride ions in concrete under loads and drying-wetting cycles. *Construction and Building Materials, 112*, 733-738.

Wu, J. Y., Li, J., & Faria, R. 2006. An energy release rate-based plastic-damage model for concrete. *International Journal of Solids and Structures, 43*(3-4), 583-612.

Wu, Z., Wong, H., & Buenfeld, N. 2017. Transport properties of concrete after drying-wetting regimes to elucidate the effects of moisture content, hysteresis and microcracking. *Cement and Concrete Research, 98*, 136-154.

Xiao, J., Li, H., & Yang, Z. 2013. Fatigue behavior of recycled aggregate concrete under compression and bending cyclic loadings. *Construction and Building Materials*, *38*, 681-688.

Xiao, J., Qiang, C., Nanni, A., & Zhang, K. 2017. Use of sea-sand and seawater in concrete construction: Current status and future opportunities. *Construction and Building Materials*, *155*, 1101-1111.

Xiao, K., Zhang, Q., & Jia, B. 2016. Cyclic behavior of prefabricated reinforced concrete frame with infill slit shear walls. *Frontiers of Structural and Civil Engineering, 10*(1), 63-71.

Xiao, Y. C., Li, S., & Gao, Z. 1998. A continuum damage mechanics model for high cycle fatigue. *International Journal of Fatigue, 20*(7), 503-508.

Xu, Q., Ji, T., Yang, Z., & Ye, Y. 2019. Preliminary investigation of artificial reef concrete with sulphoaluminate cement, marine sand and sea water. *Construction and Building Materials, 211*, 837-846.

Yadav, I. N., & Thapa, K. B. 2020. Fatigue Damage Model of Concrete Materials. *Theoretical and Applied Fracture Mechanics, 108*, 102578.

Yang, E. I., Kim, M. Y., Park, H. G., & Yi, S. T. 2010. Effect of partial replacement of sand with dry oyster shell on the long-term performance of concrete. *Construction and Building Materials, 24*(5), 758-765.

Yang, K. H., Mun, J. H., Cho, M. S., & Kang, T. H. 2014. Stress-strain model for various unconfined concretes in compression. *ACI Structural Journal, 111*(4), 819.

Yang, S., Xu, J., Zang, C., Li, R., Yang, Q., & Sun, S. 2019. Mechanical properties of alkali-activated slag concrete mixed by seawater and sea sand. *Construction and Building Materials, 196*, 395-410.

Yao, Y., Wang, L., Wittmann, F. H., De Belie, N., Schlangen, E., Alava, H. E., . . . Yunus, B. M. 2017. Test methods to determine durability of concrete under combined environmental actions and mechanical load: final report of RILEM TC 246-TDC. *Materials and structures, 50*(2), 1-13.

Yazici, S., & Arel, H. S. 2012. Effects of fly ash fineness on the mechanical properties of concrete. *Sādhanā, 37*(3), 389-403.

Ye, H., Jin, N., Jin, X., Fu, C., & Chen, W. 2016a. Chloride ingress profiles and binding capacity of mortar in cyclic drying-wetting salt fog environments. *Construction and Building Materials*, *127*, 733-742.

Ye, H., Jin, X., Fu, C., Jin, N., Xu, Y., & Huang, T. 2016b. Chloride penetration in concrete exposed to cyclic drying-wetting and carbonation. *Construction and Building Materials, 112*, 457-463.

Yeh, I. C. 2007. Computer-aided design for optimum concrete mixtures. *Cement and Concrete Composites, 29*(3), 193-202.

Yepez, F., & Yepez, O. 2017. Role of construction materials in the collapse of R/C buildings after Mw 7.8 Pedernales–Ecuador earthquake, April 2016. *Case Studies in Structural Engineering, 7*, 24-31.

Yılmaz, B., & Olgun, A. 2008. Studies on cement and mortar containing low-calcium fly ash, limestone, and dolomitic limestone. *Cement and Concrete Composites, 30*(3), 194-201.

Younis, A., Ebead, U., Suraneni, P., & Nanni, A. 2018. Fresh and hardened properties of seawater-mixed concrete. *Construction and Building Materials, 190*, 276-286.

Younis, A., Ebead, U., Suraneni, P., & Nanni, A. 2020. Performance of seawater-mixed recycled-aggregate concrete. *Journal of Materials in Civil engineering, 32*(1), 04019331.

Yu, X. T., Chen, D., Feng, J. R., & Zhang, Y. 2018. Behavior of mortar exposed to different exposure conditions of sulfate attack. *Ocean Engineering, 157*, 1-12.

Yu, Z., Chen, Y., Liu, P., & Wang, W. 2015. Accelerated simulation of chloride ingress into concrete under drying–wetting alternation condition chloride environment. *Construction and Building Materials, 93*, 205-213.

Yuan, J., Liu, Y., Tan, Z., & Zhang, B. 2016. Investigating the failure process of concrete under the coupled actions between sulfate attack and drying–wetting cycles by using X-ray CT. *Construction and Building Materials, 108*, 129-138.

Zeng, Q., Li, K., Fen-chong, T., & Dangla, P. 2012. Determination of cement hydration and pozzolanic reaction extents for fly-ash cement pastes. *Construction and Building Materials, 27*(1), 560-569.

Zhang, D., Zhao, Y., Ueda, T., Li, X., & Xu, Q. 2016a. CFRP strengthened RC beams with pre-strengthening non-uniform reinforcement corrosion subjected to post-strengthening wetting/drying cycles. *Engineering Structures, 127*, 331-343.

Zhang, H., Ji, T., & Liu, H. 2019. Performance evolution of the interfacial transition zone (ITZ) in recycled aggregate concrete under external sulfate attacks and dry-wet cycling. *Construction and Building Materials, 229*, 116938.

Zhang, J., Gao, Y., & Han, Y. 2011. Interior humidity of concrete under dry-wet cycles. *Journal of Materials in Civil engineering, 24*(3), 289-298.

Zhang, J., Sun, M., Hou, D., & Li, Z. 2017. External sulfate attack to reinforced concrete under drying-wetting cycles and loading condition: numerical simulation and experimental validation by ultrasonic array method. *Construction and Building Materials, 139*, 365-373.

Zhang, R., Castel, A., & François, R. 2010. Concrete cover cracking with reinforcement corrosion of RC beam during chloride-induced corrosion process. *Cement and Concrete Research, 40*(3), 415-425.

Zhang, Z., Zhang, B., & Yan, P. 2016b. Comparative study of effect of raw and densified silica fume in the paste, mortar and concrete. *Construction and Building Materials, 105*, 82-93.

Zhao, S., & Zhang, Q. 2019. Effect of Silica Fume in Concrete on Mechanical Properties and Dynamic Behaviors under Impact Loading. *Materials, 12*(19), 3263.

Zhongya, Z., Xiaoguang, J., & Wei, L. 2019. Long-term behaviors of concrete under low-concentration sulfate attack subjected to natural variation of environmental climate conditions. *Cement and Concrete Research*, *116*, 217-230.

Every reasonable effort has been made to acknowledge the owners of copyright material. I would be pleased to hear from any copyright owner who has been omitted or incorrectly acknowledged.

Appendix

A. Mix Design Calculation

The concrete mix design has been developed using the ACI 211.4-93 (1998) guideline. Mix design calculation for two types of concrete, concrete containing silicomanganese (SiMn) slag, marine sand and seawater and concrete incorporating fly ash (FA) and silica fume (SF), is presented below.

A.1. Concrete with SiMn Slag, Marine Sand and Seawater

Material properties

$\mathrm{DRUW_{limestone}} = 1419\ \mathrm{kg/m^3}$

$\mathrm{DRUW_{SiMn\ slag}} = 1640\ \mathrm{kg/m^3}$

$\mathrm{SG_c} = 3.15$

$\mathrm{SG_{limestone}} = 2.64$

$\mathrm{SG_{SiMn\ slag}} = 2.97$

$\mathrm{SG_{river\ sand}} = 2.67$

$\mathrm{SG_{marine\ sand}} = 2.7$

$\mathrm{SG_{quarry\ dust}} = 2.07$

Step 1: Target slump and strength

$\mathrm{Target\ slump} = 50\ \mathrm{mm}$

$\mathrm{f_c'} = 55\ \mathrm{MPa}$

$$\mathrm{f_{cr}}' = \frac{\mathrm{f_c}' + 9.65}{0.9} = \mathrm{f_{cr}}' = \frac{50 + 9.65}{0.9} = 71.83\ \mathrm{MPa}$$

Step 2: Calculation of coarse aggregate content

For coarse aggregate having 25 mm nominal size,

$\mathrm{CAF} = 0.68$

For limestone aggregate,

$\mathrm{W_{ca}} = (\mathrm{CAF} \times \mathrm{DRUW_{limestone}}) = 0.68 \times 1419 = 965\ \mathrm{kg/m^3}$

For SiMn slag aggregate,

$\mathrm{W_{ca}} = \left(\mathrm{CAF} \times \mathrm{DRUW_{SiMn\ slag}}\right) = 0.68 \times 1640 = 1115\mathrm{kg/m^3}$

Step 3: Calculation of water and cement contents

For target slump = 50 mm and coarse aggregate size = 25 mm,

$\mathrm{W_w} = 176\ \mathrm{kg/m^3}$

For $\mathrm{f_{cr}}' = 71.83$ MPa at 28 days,

$\mathrm{w/c} = 0.32$

$$\mathrm{W_w} = \frac{\mathrm{W_w}}{\mathrm{w/c\ ratio}} = \frac{176}{0.32} = 550\ \mathrm{kg/m^3}$$

Step 4: Calculation of fine aggregate content

$$\mathrm{V_{fa}} = 1 - \frac{1}{1000}\left(\frac{\mathrm{W_c}}{\mathrm{SG_c}} + \frac{\mathrm{W_{ca}}}{\mathrm{SG_{SiMn\ slag}}} + \frac{\mathrm{W_w}}{\mathrm{SG_w}}\right)$$

$$= 1 - \frac{1}{1000}\left(\frac{550}{3.15} + \frac{1115}{2.97} + \frac{176}{1}\right)$$

$$= 0.275\ \mathrm{m^3}$$

To produce concrete with comparable workability, 29.5% of river sand and 30.5% of marine sand are replaced with quarry dust.

For river sand,

$\mathrm{W_{fa,sand}} = 0.705 \times \mathrm{V_{fa}} \times \mathrm{SG_{river\ sand}} \times 1000$

$$= 0.705 \times 0.275 \times 2.67 \times 1000$$

$$= 520\ \mathrm{kg/m^3}$$

$$\mathrm{W_{fa,quarry\ dust}} = 0.295 \times \mathrm{V_{fa}} \times \mathrm{SG_{quarry\ dust}} \times 1000$$

$$= 0.295 \times 0.275 \times 2.07 \times 1000$$

$$= 167\ \mathrm{kg/m^3}$$

For marine sand,

$$\mathrm{W_{fa,sand}} = 0.695 \times \mathrm{V_{fa}} \times \mathrm{SG_{marine\ sand}} \times 1000$$

$$= 0.695 \times 0.275 \times 2.7 \times 1000$$

$$= 515\ \mathrm{kg/m^3}$$

$$\mathrm{W_{fa,quarry\ dust}} = 0.305 \times \mathrm{V_{fa}} \times \mathrm{SG_{quarry\ dust}} \times 1000$$

$$= 0.305 \times 0.275 \times 2.07 \times 1000$$

$$= 173\ \mathrm{kg/m^3}$$

A.2. Concrete with Fly Ash and Silica Fume

The ACI standard provides guideline for proportioning the concrete mix design containing supplementary cementitious material. A sample mix design calculation using FA40SF30, which includes the use of 40% FA and 30% SF, is shown below.

Material properties

$\mathrm{SG_{FA}} = 2.98$

$\mathrm{SG_{SF}} = 2.43$

Extra Step: Addition of Supplementary Cementitious Material

$\mathrm{RL_{FA}} = 0.4$

$\mathrm{RL_{SF}} = 0.3$

Content of cement, FA and SF,

$$\mathrm{W_{FA}} = \mathrm{RL_{FA}} \times \mathrm{W_c} = 0.4 \times 550 = 220\ \mathrm{kg/m^3}$$

$$\mathrm{W_{SF}} = \mathrm{RL_{SF}} \times \mathrm{W_c} = 0.3 \times 550 = 165\ \mathrm{kg/m^3}$$

$$\mathrm{W_{c,new}} = \mathrm{W_c} - \mathrm{W_{FA}} - \mathrm{W_{SF}} = 550 - 220 - 165 = 165\ \mathrm{kg/m^3}$$

Volume of cement FA and SF,

$$\mathrm{V_{c,new}} = \frac{\mathrm{W_{c,new}}}{1000 \times \mathrm{SG_c}} = \frac{165}{1000 \times 3.15} = 0.0524\ \mathrm{m^3}$$

$$\mathrm{V_{FA}} = \frac{\mathrm{W_{FA}}}{1000 \times \mathrm{SG_{FA}}} = \frac{220}{1000 \times 2.98} = 0.0738\ \mathrm{m^3}$$

$$\mathrm{V_{SF}} = \frac{\mathrm{W_{SF}}}{1000 \times \mathrm{SG_{SF}}} = \frac{165}{1000 \times 2.43} = 0.0679\ \mathrm{m^3}$$

Volume and content of fine aggregate,

$$\mathrm{V_{fa,new}} = 1 - \frac{1}{1000}\left(\frac{\mathrm{W_{ca}}}{\mathrm{SG_{ca}}} + \frac{\mathrm{W_w}}{\mathrm{SG_w}}\right) - \mathrm{V_{c,new}} - \mathrm{V_{FA}} - \mathrm{V_{SF}}$$

$$= 1 - \frac{1}{1000}\left(\frac{1115}{2.97} + \frac{176}{1}\right) - 0.0524 - 0.0738 - 0.0679$$

$$= 0.256\ \mathrm{m^3}$$

$$\mathrm{W_{fa,sand}} = 0.695 \times \mathrm{V_{fa}} \times \mathrm{SG_{marine\ sand}} \times 1000$$

$$= 0.695 \times 0.256 \times 2.7 \times 1000$$

$$= 481\ \mathrm{kg/m^3}$$

$$\mathrm{W_{fa,quarry\ dust}} = 0.305 \times \mathrm{V_{fa}} \times \mathrm{SG_{quarry\ dust}} \times 1000$$

$$= 0.305 \times 0.256 \times 2.07 \times 1000$$

$$= 161\ \mathrm{kg/m^3}$$

B. Composition of Seawater

The determination of anion and cation compositions of seawater used in the research is presented in this section. Atomic absorption spectroscopy (AAS) analysis was used to measure the cation composition of seawater, which included sodium (Na^+), magnesium (Mg^{2+}), calcium (Ca^{2+}) and potassium (K^+) ions. For the anion, the chloride (Cl^-) ion content was calculated using the Mohr's titration method, and the sulphate (SO_4^{2-}) ion content was determined through turbidimetric method. The calculation for the cation and anion compositions of seawater is shown below.

B.1. Cation Composition of Seawater

After a standard acid digestion and filtration of seawater, the AAS analysis was performed to determine the contents of Na^+, Mg^{2+}, Ca^{2+} and K^+ ions. The AAS test results for Na^+, Mg^{2+}, Ca^{2+} and K^+ ions are shown in Figure B.1, Figure B.2, Figure B.3 and Figure B.4 respectively. Based on the results, the cation compositions are:

$$\mathrm{C_{Na}} = 4.027\ \mathrm{mg/l}$$

$$\mathrm{C_{Mg}} = 3.184\ \mathrm{mg/l}$$

$$\mathrm{C_{Ca}} = 1.948\ \mathrm{mg/l}$$

$$\mathrm{C_{K}} = 4.621\ \mathrm{mg/l}$$

For each tested cation, seawater was diluted to a concentration of less than 5 mg/l. The following is the dilution factor and the actual compositions for each cation.

$$\mathrm{DF_{Na}} = 4430$$

$$\mathrm{DF_{Mg}} = 145$$

$$\mathrm{DF_{Ca}} = 315$$

$$\mathrm{DF_{K}} = 99$$

$$\mathrm{C_{Na,actual}} = 4.027\ \times 4430 = 17840\ \mathrm{mg/l}$$

$$\mathrm{C_{Mg,actual}} = 3.184 \times 145 = 460\ \mathrm{mg/l}$$

$$\mathrm{C_{Ca,actual}} = 1.948\ \times 315 = 613\ \mathrm{mg/l}$$

$$C_{K,actual} = 4.621 \times 99 = 456 \text{ mg/l}$$

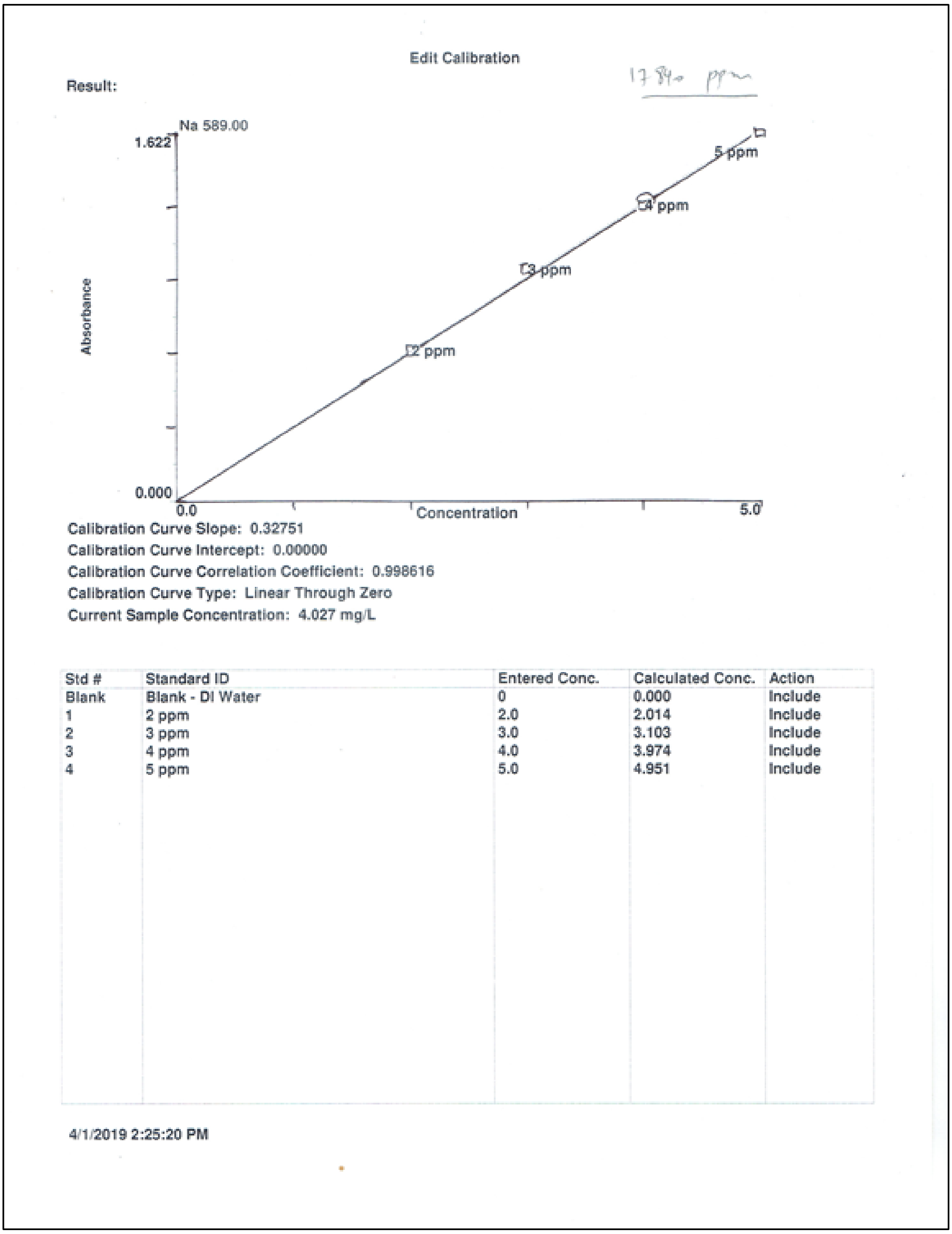

Edit Calibration

Result:

17840 ppm

Calibration Curve Slope: 0.32751
Calibration Curve Intercept: 0.00000
Calibration Curve Correlation Coefficient: 0.998616
Calibration Curve Type: Linear Through Zero
Current Sample Concentration: 4.027 mg/L

Std #	Standard ID	Entered Conc.	Calculated Conc.	Action
Blank	Blank - DI Water	0	0.000	Include
1	2 ppm	2.0	2.014	Include
2	3 ppm	3.0	3.103	Include
3	4 ppm	4.0	3.974	Include
4	5 ppm	5.0	4.951	Include

4/1/2019 2:25:20 PM

Figure B.1: AAS results for Na^+ in seawater

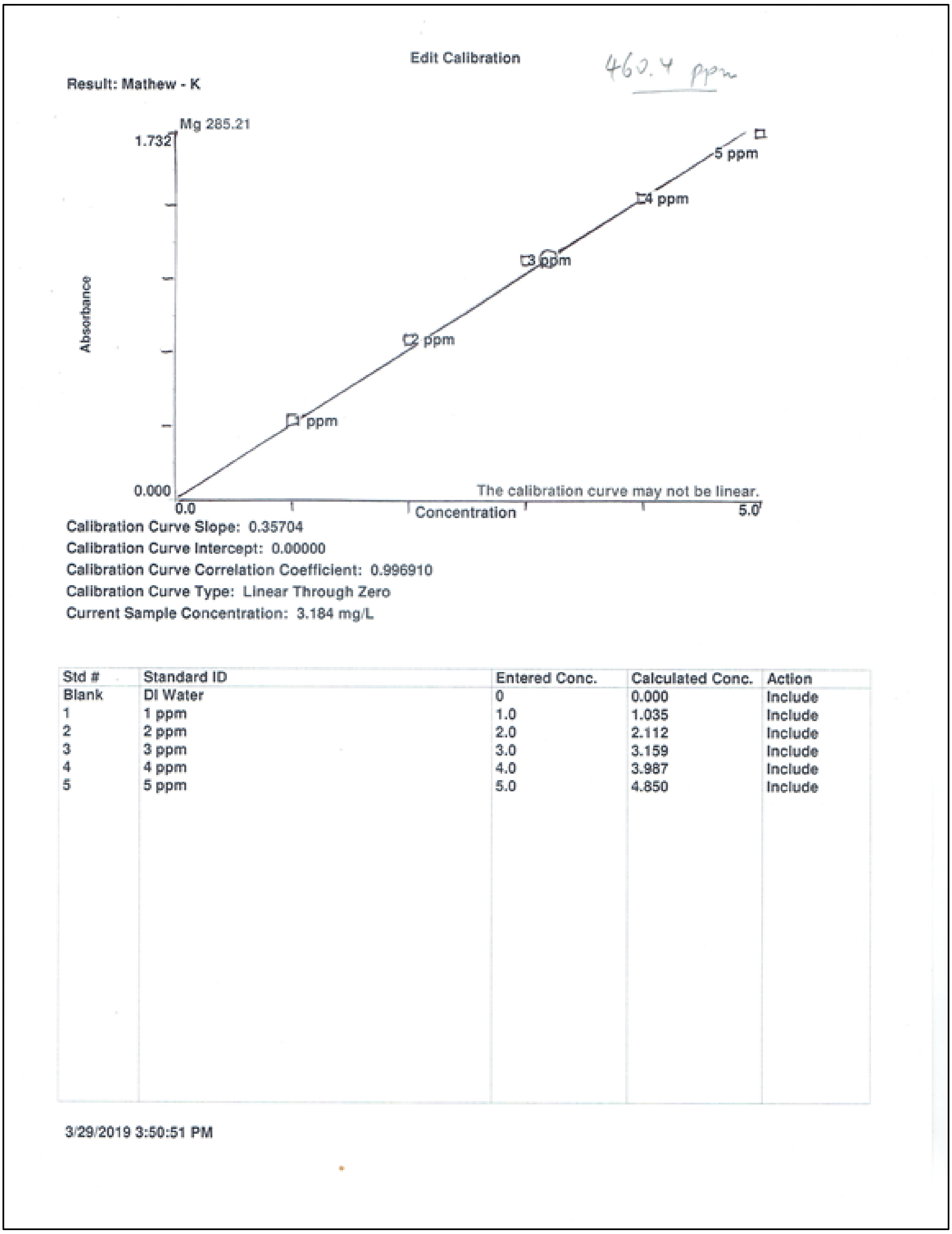

Edit Calibration

460.4 ppm

Result: Mathew - K

The calibration curve may not be linear.

Calibration Curve Slope: 0.35704
Calibration Curve Intercept: 0.00000
Calibration Curve Correlation Coefficient: 0.996910
Calibration Curve Type: Linear Through Zero
Current Sample Concentration: 3.184 mg/L

Std #	Standard ID	Entered Conc.	Calculated Conc.	Action
Blank	DI Water	0	0.000	Include
1	1 ppm	1.0	1.035	Include
2	2 ppm	2.0	2.112	Include
3	3 ppm	3.0	3.159	Include
4	4 ppm	4.0	3.987	Include
5	5 ppm	5.0	4.850	Include

3/29/2019 3:50:51 PM

Figure B.2: AAS results for Mg^{2+} in seawater

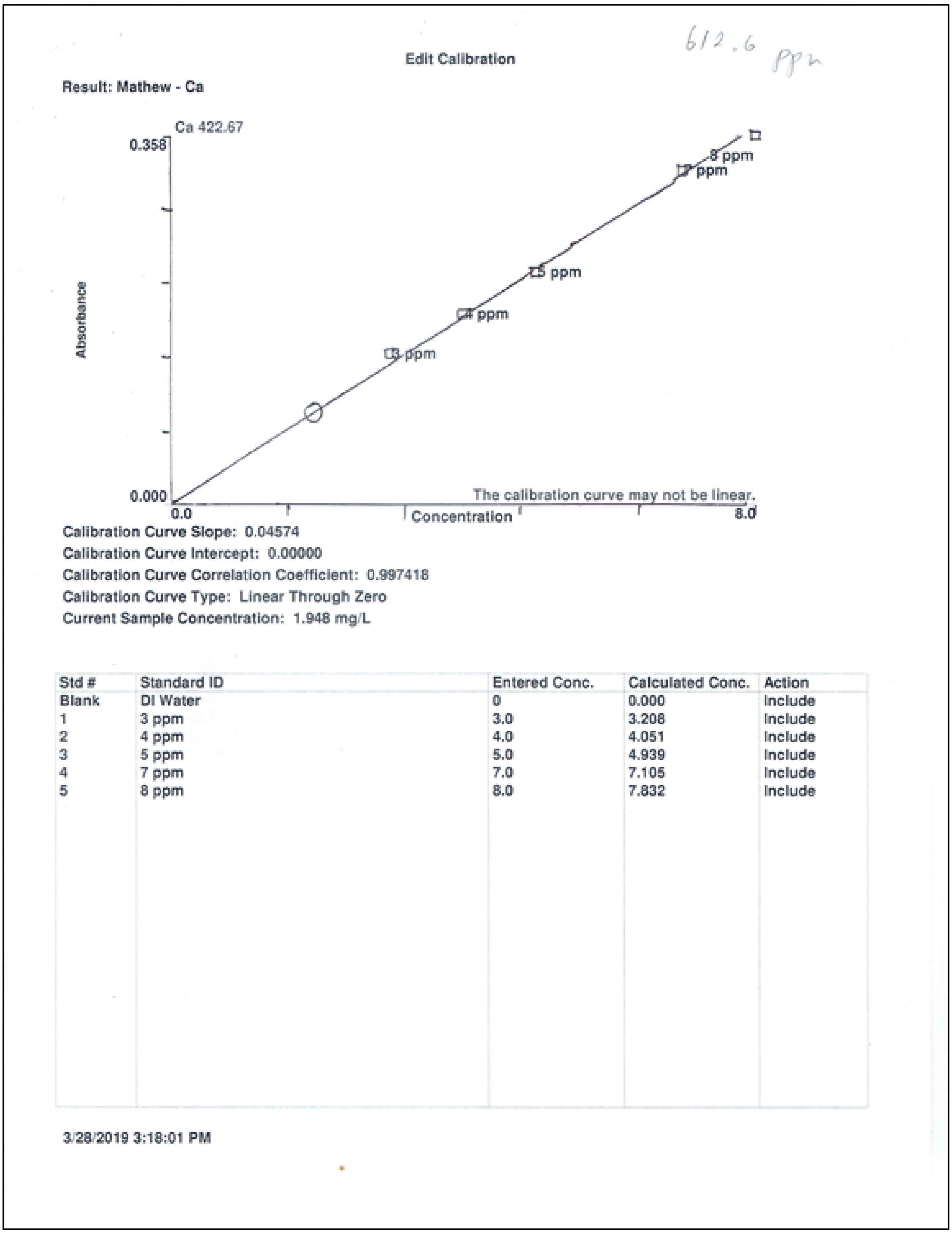

612.6 ppm

Edit Calibration

Result: Mathew - Ca

The calibration curve may not be linear.

Calibration Curve Slope: 0.04574
Calibration Curve Intercept: 0.00000
Calibration Curve Correlation Coefficient: 0.997418
Calibration Curve Type: Linear Through Zero
Current Sample Concentration: 1.948 mg/L

Std #	Standard ID	Entered Conc.	Calculated Conc.	Action
Blank	DI Water	0	0.000	Include
1	3 ppm	3.0	3.208	Include
2	4 ppm	4.0	4.051	Include
3	5 ppm	5.0	4.939	Include
4	7 ppm	7.0	7.105	Include
5	8 ppm	8.0	7.832	Include

3/28/2019 3:18:01 PM

Figure B.3: AAS results for Ca^{2+} in seawater

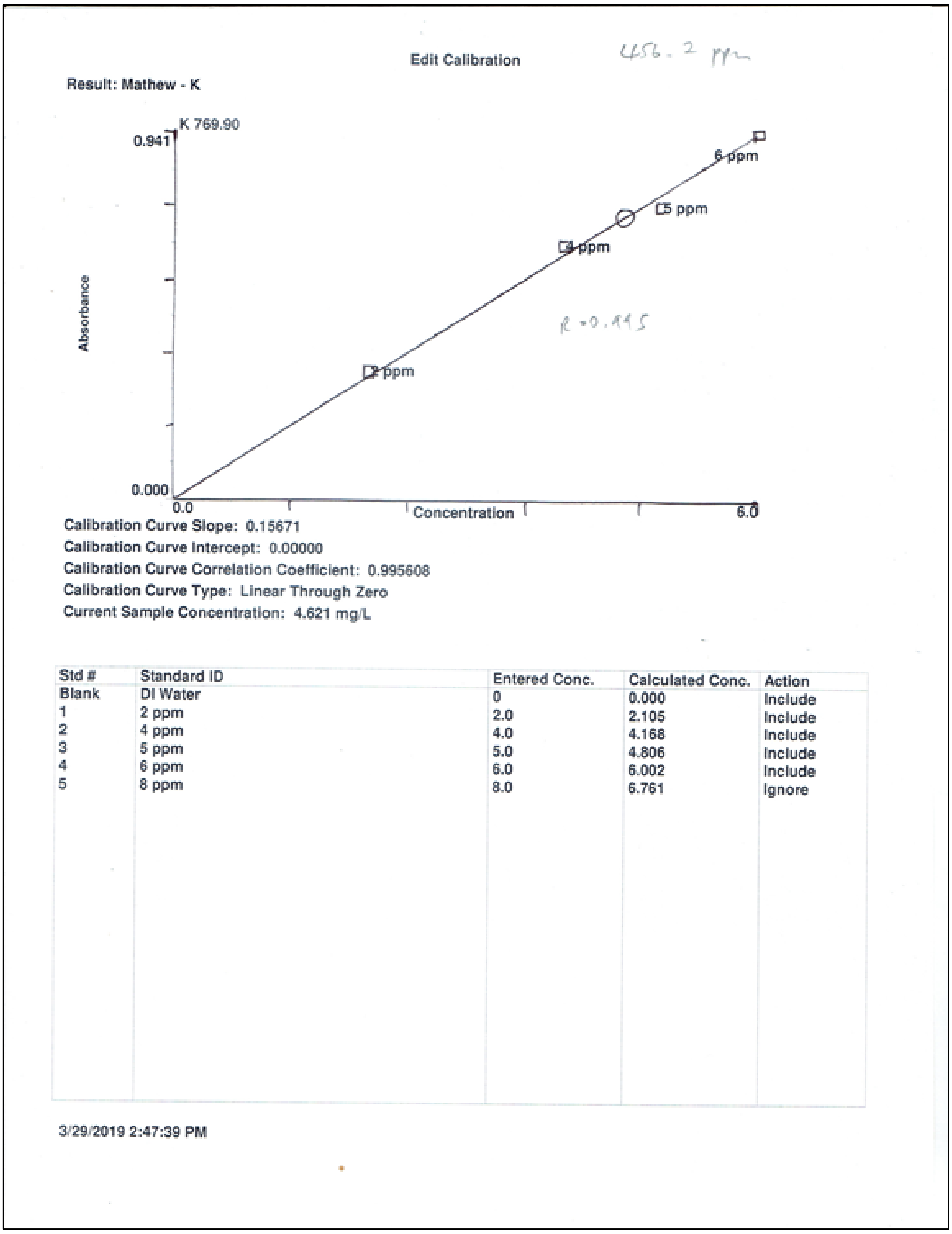

Edit Calibration

456.2 ppm

Result: Mathew - K

R = 0.995

Calibration Curve Slope: 0.15671
Calibration Curve Intercept: 0.00000
Calibration Curve Correlation Coefficient: 0.995608
Calibration Curve Type: Linear Through Zero
Current Sample Concentration: 4.621 mg/L

Std #	Standard ID	Entered Conc.	Calculated Conc.	Action
Blank	DI Water	0	0.000	Include
1	2 ppm	2.0	2.105	Include
2	4 ppm	4.0	4.168	Include
3	5 ppm	5.0	4.806	Include
4	6 ppm	6.0	6.002	Include
5	8 ppm	8.0	6.761	Ignore

3/29/2019 2:47:39 PM

Figure B.4: AAS results for K^+ in seawater

B.2. Anion Composition of Seawater

Chloride ion composition:

The Mohr's titration method was used to measure the Cl^- ion content of seawater. Prior to the test, the seawater was vacuum filtered through a 0.45 μm membrane filter. A 0.05 N silver nitration ($AgNO_3$) solution and a potassium chromate indicator were prepared for the titration. The seawater was diluted by factor of 20 using distilled water. In the test, $AgNO_3$ solution was gradually added from a burette into the 20 ml seawater sample until it turned reddish brown in colour. One sample calculation of Cl^- ion content of seawater is shown below. Three tests were carried out, and the average result is shown in Table B.1.

For Test Run 1,

$$\text{Volume of } \mathrm{AgNO_3} \text{ required for sample, } \mathrm{A} = 11.4 \text{ ml}$$

$$\text{Volume of } \mathrm{AgNO_3} \text{ required for blank, } \mathrm{B} = 0.2 \text{ ml}$$

$$\text{Normality of } \mathrm{AgNO_3}, \mathrm{N} = 0.05 \text{ mol/L}$$

$$\text{Diluted chloride content, } \mathrm{C_{cl}} = \frac{(\mathrm{A} - \mathrm{B}) \times \mathrm{N} \times 35.45}{20} \times 1000$$

$$= \frac{(11.4 - 0.2) \times 0.05 \times 35.45}{20} \times 1000$$

$$= 992.6 \text{ mg/l}$$

$$\mathrm{C_{cl,actual}} = 20 \times 992.6 \text{ mg/l} = 19852 \text{ mg/l}$$

Table B.1: Chloride content of seawater

Test	Volume of $AgNO_3$ (ml)	Diluted chloride content (ml/g)	Chloride content (ml/g)
1	11.4	992.6	19852
2	11.0	957.15	19143
3	11.5	1001.5	20030
Average value			19675

Sulphate ion composition:

The sulphate content of seawater was measured by using the turbidimetric approach. Seawater sample was similarly vacuum filtered through a 0.45 μm membrane filter before the test. The seawater sample was diluted 50 times with distilled water. A conditioning reagent was prepared by combining 50 ml of glycerol, 30 ml of concentrated hydrochloric acid, 100 ml of 95% ethyl alcohol, 75 g of sodium chloride and 300 ml of distilled water. In the test, 5 ml of conditioning reagent was added into 20 ml of seawater sample. The turbidity of the solution was then measured using a spectrophotometer with a colorimeter set at 420 nm. Based on the measured turbidity, the sulphate content of seawater was determined using the standard curve as shown in Figure B.5. The standard curve was plotted by determining the turbidity for standard sodium sulphate solution at concentration ranging from 10 mg/l to 50 mg/l. The sulphate content is computed as follows:

From the standard curve,

$\text{Absorption} = 0.22$

$\text{Diluted sulphate content}, C_{SO4} = 34.6\ \text{mg/l}$

$C_{SO4,actual} = 50 \times 34.6\ \text{mg/l} = 1730\ \text{mg/l}$

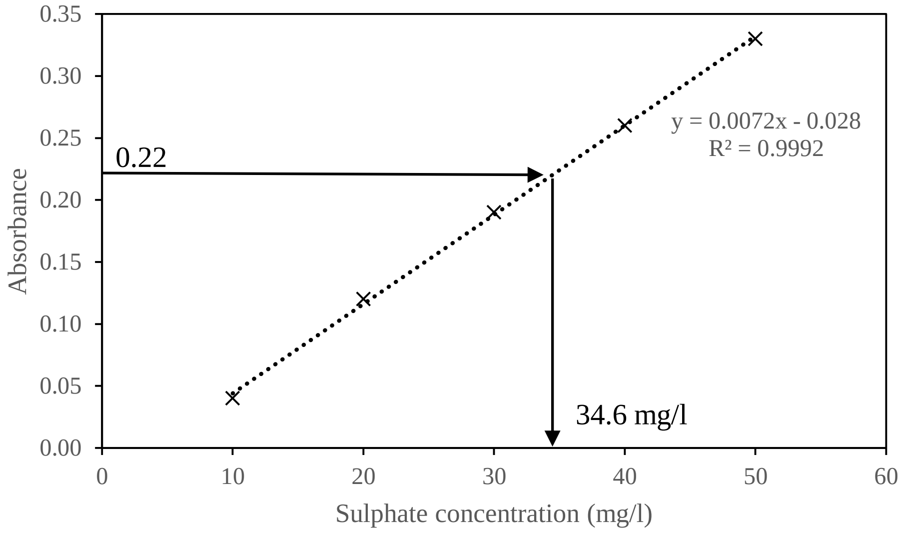

Figure B.5: Standard curve for sulphate solution at 420 nm

C. Analysis of Variance Result

The analysis of variance (ANOVA) results for concrete strength, durability and workability is shown in Table C.1 to Table C.5.

Table C.1: ANOVA of prediction model for compressive strength

Response	Source	Sum of square	Mean square	F-value	p-value	Significance
7-day compressive strength	Model	902.76	180.55	25.86	0.0001	Yes
	FA/B	214.70	214.70	30.75	0.0001	Yes
	SF/B	382.63	382.63	54.81	0.0001	Yes
	(FA/B)(SF/B)	37.50	214.70	30.75	< 0.0001	Yes
	$(SF/B)^2$	262.95	37.50	5.37	0.0350	Yes
	$(FA/B)^2$	9.55	262.95	37.67	< 0.0001	Yes
	Lack of fit	94.53	8.59	3.37	0.1257	No
	Pure Error	10.19	2.55	-	-	-
28-day compressive strength	Model	959.97	191.99	17.38	0.0001	Yes
	FA/B	49.78	49.78	4.51	0.0508	No
	SF/B	419.87	419.87	38.01	0.0001	Yes
	(FA/B)(SF/B)	40.3	40.3	3.65	0.0755	No
	$(SF/B)^2$	370.62	370.62	33.55	< 0.0001	Yes
	$(FA/B)^2$	62.05	62.05	5.62	0.0316	Yes
	Lack of fit	156.10	14.19	5.91	0.0504	No
	Pure Error	9.61	2.40	-	-	-
90-day compressive strength	Model	1060.03	212.01	25.58	0.0001	Yes
	FA/B	33.78	33.78	4.08	0.0618	No
	SF/B	404.32	404.32	48.78	0.0001	Yes
	(FA/B)(SF/B)	52.48	52.48	6.33	0.0237	Yes
	$(SF/B)^2$	410.97	410.97	49.58	< 0.0001	Yes
	$(FA/B)^2$	132.15	132.15	15.94	0.0012	Yes
	Lack of fit	112.64	10.24	3.51	0.1185	No
	Pure Error	11.68	2.92	-	-	-

Table C.2: ANOVA of prediction model for splitting tensile strength

7-day splitting tensile strength	Model	4.90	0.98	32.85	0.0001	Yes
	FA/B	1.63	1.63	54.78	0.0001	Yes
	SF/B	1.21	1.21	40.70	0.0001	Yes
	(FA/B)(SF/B)	0.119	0.119	3.99	0.0643	No
	$(SF/B)^2$	1.86	1.86	62.35	< 0.0001	Yes
	$(FA/B)^2$	0.0392	0.0392	1.31	0.2699	No
	Lack of fit	0.40	0.04	3.19	0.1369	No
	Pure Error	0.05	0.01	-	-	-
28-day splitting tensile strength	Model	5.38	1.08	39.50	0.0001	Yes
	FA/B	0.08	0.08	2.86	0.1117	No
	SF/B	1.60	1.60	58.89	0.0001	Yes
	(FA/B)(SF/B)	0.0551	0.0551	2.02	0.1753	No

	$(SF/B)^2$	2.87	2.87	105.29	< 0.0001	Yes
	$(FA/B)^2$	0.6218	0.6218	22.84	0.0002	Yes
	Lack of fit	0.35	0.03	2.32	0.2168	No
	Pure Error	0.06	0.01	-	-	-
90-day splitting tensile strength	Model	6.35	1.27	44.18	0.0001	Yes
	FA/B	0.12	0.12	4.14	0.0598	No
	SF/B	1.66	1.66	57.78	0.0001	Yes
	(FA/B)(SF/B)	0.0468	0.0468	1.63	0.2214	No
	$(SF/B)^2$	3.43	3.43	119.31	< 0.0001	Yes
	$(FA/B)^2$	0.8955	0.8955	31.14	< 0.0001	Yes
	Lack of fit	0.37	0.03	2.36	0.2111	No
	Pure Error	0.06	0.01	-	-	-

Table C.3: ANOVA of prediction model for sorptivity

Response	Source	Sum of square	Mean square	F-value	p-value	Significance
28-day sorptivity	Model	199.38 x10^{-7}	22.15 x10^{-7}	34.15	0.0001	Yes
	FA/B	0.01 x10^{-7}	0.01 x10^{-7}	0.14	0.7109	No
	SF/B	8.08 x10^{-7}	8.08 x10^{-7}	12.46	0.0047	Yes
	(FA/B)(SF/B)	7.88 x10^{-7}	7.88 x10^{-7}	12.15	0.0051	Yes
	$(SF/B)^2$	59.8 x10^{-7}	59.8 x10^{-7}	92.22	< 0.0001	Yes
	$(FA/B)^2$	22.8 x10^{-7}	22.8 x10^{-7}	35.14	< 0.0001	Yes
	$(SF/B)^2(FA/B)$	18.4 x10^{-7}	18.4 x10^{-7}	28.29	0.0002	Yes
	$(SF/B)(FA/B)^2$	0.59 x10^{-7}	0.59 x10^{-7}	0.9034	0.3623	No
	$(SF/B)^3$	1.47 x10^{-7}	1.47 x10^{-7}	2.26	0.1608	No
	$(FA/B)^3$	3.25 x10^{-7}	3.25 x10^{-7}	5	0.0469	Yes
	Lack of fit	6.24 x10^{-7}	0.89 x10^{-7}	4.00	0.0993	No
	Pure Error	0.89 x10^{-7}	0.22 x10^{-7}	-	-	-
90-day sorptivity	Model	23.20 x10^{-7}	13.69 x10^{-7}	63.42	0.0001	Yes
	FA/B	0.10 x10^{-7}	0.10 x10^{-7}	0.49	0.5003	No
	SF/B	5.15 x10^{-7}	5.15 x10^{-7}	23.85	0.0005	Yes
	(FA/B)(SF/B)	0.81 x10^{-7}	0.81 x10^{-7}	3.76	0.0787	No
	$(SF/B)^2$	35.3 x10^{-7}	35.3 x10^{-7}	163.64	< 0.0001	Yes
	$(FA/B)^2$	8.20 x10^{-7}	8.20 x10^{-7}	37.98	< 0.0001	Yes
	$(SF/B)^2(FA/B)$	3.74 x10^{-7}	3.74 x10^{-7}	17.32	0.0016	Yes
	$(SF/B)(FA/B)^2$	0.27 x10^{-7}	0.27 x10^{-7}	1.26	0.2848	No
	$(SF/B)^3$	0.43 x10^{-7}	0.43 x10^{-7}	1.99	0.1857	No
	$(FA/B)^3$	0.25 x10^{-7}	0.25 x10^{-7}	1.13	0.31	No
	Lack of fit	1.87 x10^{-7}	0.27 x10^{-7}	2.11	0.2450	No
	Pure Error	0.51 x10^{-7}	0.13 x10^{-7}	-	-	-
180-day sorptivity	Model	134.21 x10^{-7}	14.91 x10^{-7}	208.91	0.0001	Yes
	FA/B	0.01 x10^{-7}	0.01 x10^{-7}	1.13	0.3115	No
	SF/B	2.91 x10^{-7}	2.91 x10^{-7}	40.73	0.0001	Yes
	(FA/B)(SF/B)	0.57 x10^{-7}	0.57 x10^{-7}	7.96	0.0166	Yes
	$(SF/B)^2$	45.1 x10^{-7}	45.1 x10^{-7}	631.73	< 0.0001	Yes
	$(FA/B)^2$	4.52 x10^{-7}	4.52 x10^{-7}	63.36	< 0.0001	Yes
	$(SF/B)^2(FA/B)$	2.00 x10^{-7}	2.00 x10^{-7}	28.01	0.0003	Yes
	$(SF/B)(FA/B)^2$	0.18 x10^{-7}	0.18 x10^{-7}	2.56	0.1376	No

	$(SF/B)^3$	0.01 x10^{-7}	0.01 x10^{-7}	0.0913	0.7682	No
	$(FA/B)^3$	0.11 x10^{-7}	0.11 x10^{-7}	1.5	0.2469	No
	Lack of fit	0.67 x10^{-7}	0.01 x10^{-7}	3.40	0.1271	No
	Pure Error	0.11 x10^{-7}	0.03 x10^{-7}	-	-	-

Table C.4: ANOVA of prediction model for chloride permeability

28-day chloride permeability	Model	2.76 x10^6	1.97 x10^5	468.51	0.0001	Yes
	FA/B	20955.03	20955.03	49.80	0.0004	Yes
	SF/B	4808.75	4808.75	11.43	0.0148	Yes
	(FA/B)(SF/B)	15087.74	15087.74	35.86	0.001	Yes
	$(SF/B)^2$	9365.12	9365.12	22.26	0.0033	Yes
	$(FA/B)^2$	2818.52	2818.52	6.7	0.0413	No
	$(SF/B)^2(FA/B)$	193500	193500	459.81	< 0.0001	Yes
	$(SF/B)(FA/B)^2$	192000	192000	456.23	< 0.0001	Yes
	$(SF/B)^3$	29919.68	29919.68	71.11	0.0002	Yes
	$(FA/B)^3$	37432.13	37432.13	88.97	< 0.0001	Yes
	$(SF/B)^2(FA/B)^2$	69922.84	69922.84	166.19	< 0.0001	Yes
	$(SF/B)^3(FA/B)$	41568.96	41568.96	98.8	< 0.0001	Yes
	$(SF/B)(FA/B)^3$	41059.92	41059.92	97.59	< 0.0001	Yes
	$(SF/B)^4$	8859.48	8859.48	21.06	0.0037	Yes
	$(FA/B)^4$	2611.01	2611.01	6.21	0.0471	No
	Lack of fit	1130.85	565.42	1.62	0.3048	No
	Pure Error	1393.63	348.41	-	-	-
90-day chloride permeability	Model	1.01 x10^6	72242.33	283.09	0.0001	Yes
	FA/B	351.70	351.70	1.38	0.2849	No
	SF/B	10236.72	10236.72	40.11	0.0007	Yes
	(FA/B)(SF/B)	925.01	925.01	3.62	0.1056	No
	$(SF/B)^2$	780.01	780.01	3.06	0.131	No
	$(FA/B)^2$	5.76	5.76	0.0226	0.8855	No
	$(SF/B)^2(FA/B)$	22620.62	22620.62	88.64	< 0.0001	Yes
	$(SF/B)(FA/B)^2$	11522.29	11522.29	45.15	0.0005	Yes
	$(SF/B)^3$	230.25	230.25	0.9023	0.3789	No
	$(FA/B)^3$	6366.98	6366.98	24.95	0.0025	Yes
	$(SF/B)^2(FA/B)^2$	14.4	14.4	0.0564	0.8201	No
	$(SF/B)^3(FA/B)$	2979.24	2979.24	11.67	0.0142	Yes
	$(SF/B)(FA/B)^3$	10662.96	10662.96	41.78	0.0007	Yes
	$(SF/B)^4$	2368.18	2368.18	9.28	0.0226	Yes
	$(FA/B)^4$	304.59	304.59	1.19	0.3165	No
	Lack of fit	142.55	71.27	0.21	0.8225	No
	Pure Error	1388.59	347.15	-	-	-
180-day chloride permeability	Model	4.66 x10^5	51760.64	226.18	0.0001	Yes
	FA/B	3125.99	3125.99	13.66	0.0035	Yes
	SF/B	6135.65	6135.65	26.81	0.0003	Yes
	(FA/B)(SF/B)	65662.65	65662.65	286.93	< 0.0001	Yes
	$(SF/B)^2$	5552.53	5552.53	24.26	0.0005	Yes
	$(FA/B)^2$	5095.9	5095.9	22.27	0.0006	Yes
	$(SF/B)^2(FA/B)$	5234.79	5234.79	22.88	0.0006	Yes
	$(SF/B)(FA/B)^2$	3370.42	3370.42	14.73	0.0028	Yes

	$(SF/B)^3$	9.54	9.54	0.0417	0.842	No
	$(FA/B)^3$	125.69	125.69	0.5492	0.4742	No
	Lack of fit	1594.74	227.82	0.99	0.5380	No
	Pure Error	922.53	230.63	-	-	-

Table C.5: ANOVA of prediction model for slump value

Response	**Source**	**Sum of square**	**Mean square**	**F-value**	**p-value**	**Significance**
Slump value	Model	59691.43	6632.38	84.26	0.0001	Yes
	FA/B	231.80	231.80	2.94	0.1142	No
	SF/B	478.86	478.86	6.08	0.0313	Yes
	(FA/B)(SF/B)	5635	5635	71.59	< 0.0001	Yes
	$(SF/B)^2$	3115.72	3115.72	39.58	< 0.0001	Yes
	$(FA/B)^2$	127.4	127.4	1.62	0.2295	No
	$(SF/B)^2(FA/B)$	1666.29	1666.29	21.17	0.0008	Yes
	$(SF/B)(FA/B)^2$	1.88	1.88	0.0238	0.8801	No
	$(SF/B)^3$	197.87	197.87	2.51	0.1412	No
	$(FA/B)^3$	2.82	2.82	0.0358	0.8534	No
	Lack of fit	727.09	103.87	2.99	0.1531	No
	Pure Error	138.80	34.70	-	-	-

D. Supplementary Detail for Binder Optimization

This section presents the optimization of fly ash (FA) and silica fume (SF) using the Response Surface Method (RSM). In Chapter 6, two sets of optimization are used: concrete with SF only and concrete with both FA and SF.

Optimization for concrete with both FA and SF

Table D.1 presents the optimization criteria for concrete containing FA and SF. By using the RSM, the combination of FA and SF contents that give the maximum strength and minimum permeability of concrete is determined as 16.3% and 11.5%, respectively, as shown in Figure D1. As shown in Figure D2, the optimization has a desirability of 0.896, which is close to 1.

Table D.1: Optimization criteria for concrete with FA and SF

Variable and response	Optimization target	Lower limit	Upper limit
FA/B	Within range	0	0.4
SF/B	Within range	0	0.3
7-day compressive strength (MPa)	Maximize	35.46	63.73
28-day compressive strength (MPa)	Maximize	53.66	78.39
90-day compressive strength (MPa)	Maximize	66.50	94.76
7-day splitting tensile strength (MPa)	Maximize	1.99	3.97
28-day splitting tensile strength (MPa)	Maximize	3.64	5.56
90-day splitting tensile strength (MPa)	Maximize	4.19	6.28
28-day sorptivity (mm/sec$^{0.5}$ x10^{-3})	Minimize	2.713	5.493
90-day sorptivity (mm/sec$^{0.5}$ x10^{-3})	Minimize	2.604	4.812
180-day sorptivity (mm/sec$^{0.5}$ x10^{-3})	Minimize	2.415	4.636
28-day chloride permeability (C)	Minimize	739.30	2475.45
90-day chloride permeability (C)	Minimize	529.85	1467.90
180-day chloride permeability (C)	Minimize	362.40	966.50
Slump value (mm)	Within range	80	210

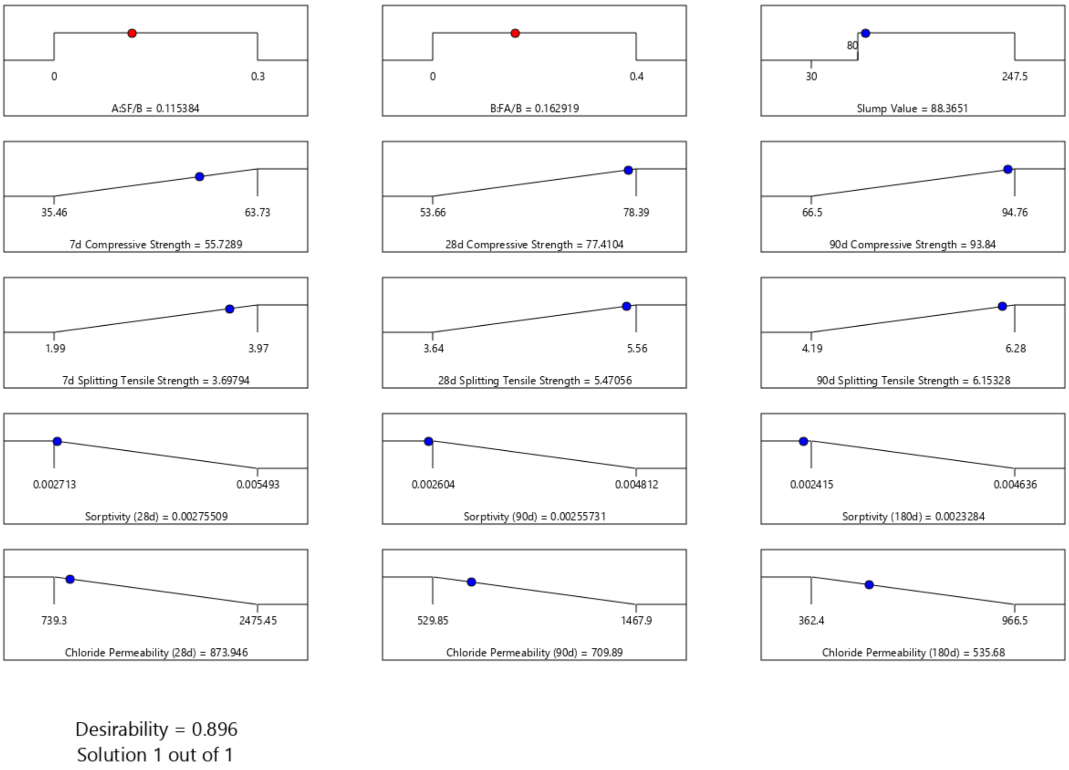

Figure D.1: Optimization outcomes for concrete with FA and SF

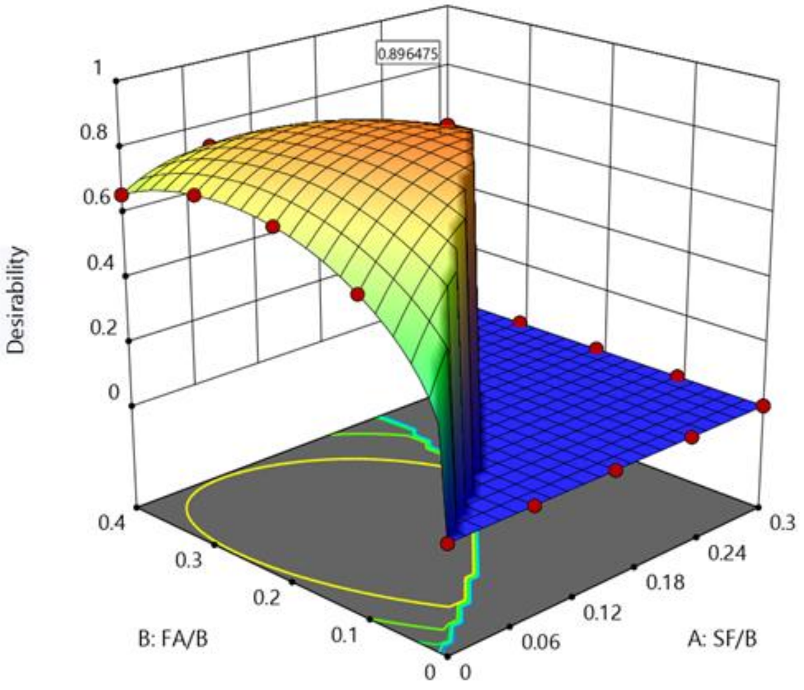

Figure D.2: Desirability function for optimization of concrete with FA and SF

Optimization for concrete with SF

The optimization criteria for concrete containing only SF are shown in Table D.2. The variable FA/B is set to to 0 in the RSM. According to the optimization an SF content of 14.2% provides the maximum strength and durability of concrete, as depicted in Figure D3. Besides, Figure D4 shows that the desirability of optimization is 0.823.

Table D.2: Optimization criteria for concrete SF

Variable and response	Optimization target	Lower limit	Upper limit
FA/B	Equal to 0	-	-
SF/B	Within range	0	0.3
7-day compressive strength (MPa)	Maximize	35.46	63.73
28-day compressive strength (MPa)	Maximize	53.66	78.39
90-day compressive strength (MPa)	Maximize	66.50	94.76
7-day splitting tensile strength (MPa)	Maximize	1.99	3.97
28-day splitting tensile strength (MPa)	Maximize	3.64	5.56
90-day splitting tensile strength (MPa)	Maximize	4.19	6.28
28-day sorptivity (mm/sec$^{0.5}$ x10^{-3})	Minimize	2.713	5.493
90-day sorptivity (mm/sec$^{0.5}$ x10^{-3})	Minimize	2.604	4.812
180-day sorptivity (mm/sec$^{0.5}$ x10^{-3})	Minimize	2.415	4.636
28-day chloride permeability (C)	Minimize	739.30	2475.45
90-day chloride permeability (C)	Minimize	529.85	1467.90
180-day chloride permeability (C)	Minimize	362.40	966.50
Slump value (mm)	Within range	80	210

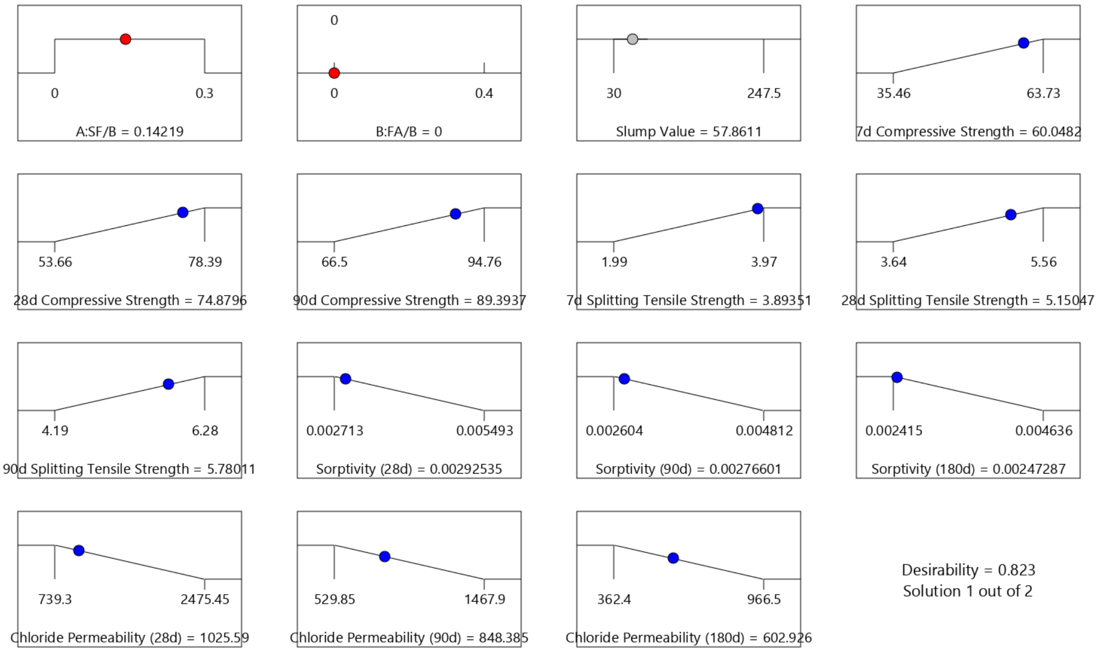

Figure D.3: Optimization outcomes for concrete with SF

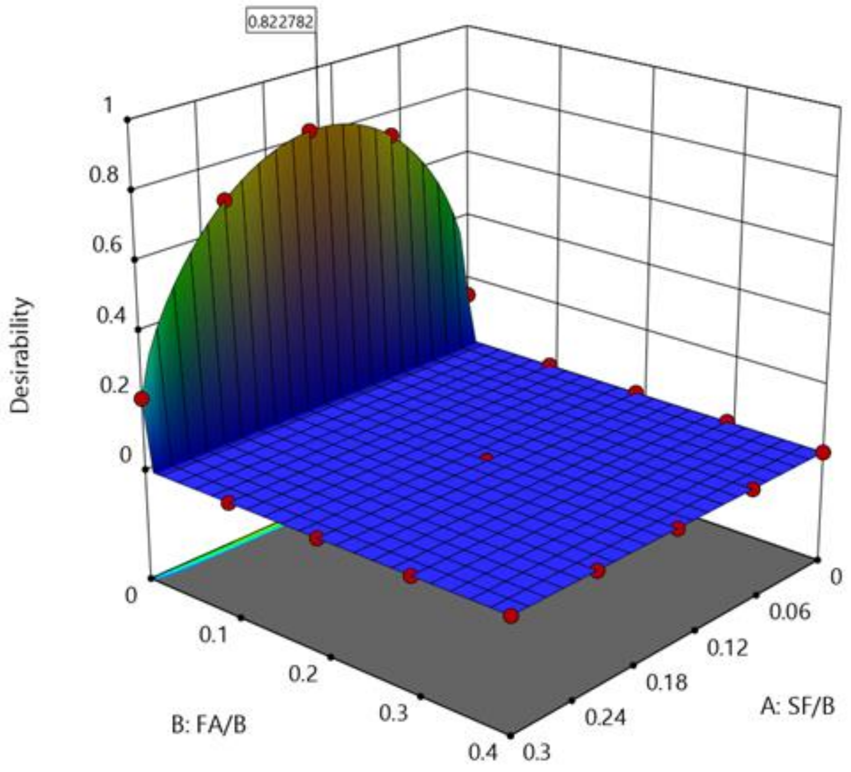

Figure D.4: Desirability function for optimization of concrete with SF

E. Copyright Permissions

The copyright of published journal articles in this thesis belongs to ELSEVIER. According to the policy of ELSEVIER, the publisher permits the awarding institution to post publicly the theses and dissertations that contains the embedded published journal article.

“*Theses and dissertations which contain embedded Published Journal Articles as part of the formal submission can be posted publicly by the awarding institution with DOI links back to the formal publications on ScienceDirect*”

(https://www.elsevier.com/about/policies/sharing)